

Structural, electronic and transport properties of amorphous/crystalline silicon heterojunctions

vorgelegt von
Diplom-Physiker
Tim Ferdinand Schulze
aus Berlin

Von der Fakultät II - Mathematik und Naturwissenschaften
der Technischen Universität Berlin
zur Erlangung des akademischen Grades

Doktor der Naturwissenschaften
- Dr. rer. nat. -

genehmigte Dissertation

Promotionsausschuss:

Vorsitzender: Prof. Dr. Thomas Möller
Gutachter: Prof. Dr. Mario Dähne
Gutachter: Prof. Dr. Bernd Rech
Gutachter: Prof. Dr. Pere Roca i Cabarrocas

Tag der wissenschaftlichen Aussprache: 21. Juni 2011

Berlin 2011

D83

Abstract

Solar cells based on heterojunctions between hydrogenated amorphous (a-Si:H) and crystalline silicon (c-Si) are an active field of research. a-Si:H/c-Si heterojunction solar cells combine the high efficiency potential of wafer-based photovoltaics (PV) with simple and low-temperature processing using thin-film deposition with PECVD. The company Sanyo has reached a conversion efficiency of 23 % with this concept, which is considerably more than delivered by typical 'classical' c-Si based homo-junction solar cells (< 19 %), with a potentially simplified processing. Also from a scientific point of view, a-Si:H/c-Si heterojunctions are of great interest, as fundamental properties of the heterojunction remain under dispute. This e.g. concerns the lineup of the electronic bands, the charge carrier transport across the heterojunction, or the outstandingly effective passivation of c-Si surface defects by a-Si:H.

The present dissertation is concerned with the physical aspects of the a-Si:H/c-Si heterojunction in the context of PV research. In a first step, the technological development which took place in the framework of the thesis is summarized. Its main constituent was the development and implementation of ultrathin (≤ 10 nm) undoped a-Si:H [(i)a-Si:H] layers to improve the passivation of the c-Si surface with the goal of increasing the open-circuit voltage of the solar cell. It is shown that the effect of (i)a-Si:H interlayers depends on the c-Si substrate doping type, and that challenges exist particularly on the technologically more relevant (n)c-Si substrate. A precise optimization of (i)a-Si:H thickness and the doping level of the following a-Si:H top layers is required to realize an efficiency gain in the solar cell. In this chapter, the key scientific questions to be tackled in the main part of the thesis are brought up by the technological development.

In the next chapter, the charge carrier transport through a-Si:H/c-Si heterojunctions is investigated making use of current-voltage (I/V) characteristics taken at different temperatures. The dominant transport mechanisms in a-Si:H/c-Si heterojunctions are identified, and the relevance for solar cell operation is discussed. It is found that in the bias regime relevant for solar cell operation, the theoretical framework for the description of carrier transport in classical c-Si solar cells applies as well, which enables to use I/V curves for a simple characterization of a-Si:H/c-Si structures.

The next chapter deals with the microscopic characterization of ultrathin a-Si:H layers. Employing infrared spectroscopy, spectroscopic ellipsometry, photoelectron spectroscopy and secondary ion mass spectroscopy, the structural, electronic and optical properties of (i)a-Si:H are analyzed. It is found that ultrathin a-Si:H essentially behaves like layers of 10 . . . 100 times the thickness. This represents the basis for the application of established concepts for the physical description of a-Si:H in the following chapters. Further, the impact of the PECVD deposition parameters on the properties of the re-

sulting layers is explored and discussed.

Next, the lineup of the electronic bands at the heterojunction is elucidated in device-relevant a-Si:H/c-Si heterostructures. To this end, a novel method combining photoelectron spectroscopy and surface photovoltage measurements is developed and employed. It is found that upon widening the a-Si:H optical band gap by controlling its hydrogen content, predominantly the valence band offset is increasing while the conduction band offset stays constant. This result is consistent with established theories on the a-Si:H electronic structure, but was not experimentally observed to date to the author's knowledge. The significance of the valence band offset for solar cell operation and possible pathways for tailoring the electronic properties of the heterojunction are discussed.

In the last chapter, the microscopic properties of the a-Si:H layers are linked with the resulting passivation of c-Si surface states, which limit the obtainable open-circuit-voltage in a heterojunction solar cell. It is found that in case of ideal processing, the heterojunction does not possess particular properties but can be described by the a-Si:H bulk properties projected onto the actual heterojunction. Based on this conclusion it is possible to comprehend the complex phenomenology of c-Si surface passivation by a-Si:H from the properties of the amorphous silicon passivation layer. The principal limit of c-Si surface passivation follows naturally, as does the explanation of passivation degradation effects from the metastability inherent to a-Si:H. The amorphous network has the propensity to adapt upon changes in externally controllable parameters like the Fermi energy, which was seldom taken into account so far when interpreting phenomena of the a-Si:H/c-Si heterojunction.

Zusammenfassung

Solarzellen auf der Basis von Heterostrukturen aus hydrogeniertem amorphem (a-Si:H) und kristallinem Silizium (c-Si) sind ein aktuelles Forschungsfeld in der Photovoltaik (PV). Sie vereinen das hohe Wirkungsgrad-Potential von c-Si Wafern mit einfacher Prozessierung bei niedrigen Temperaturen durch die Gasphasendeposition von a-Si:H mittels PECVD. Die Firma Sanyo hat mit diesem Konzept einen Wandlungs-Wirkungsgrad von 23 % erreicht, der deutlich über dem aktueller 'klassischer' c-Si-Solarzellen liegt (< 19 %), bei potentiell vereinfachter Herstellung. Auch wissenschaftlich ist das Feld von großem Interesse, da fundamentale Eigenschaften der Heterostruktur bislang unverstanden sind. Unter anderem betrifft dies die genaue Anordnung der elektronischen Bänder, den elektronischen Transport, und die höchst effektive Absättigung der c-Si-Oberflächendefekte ('Passivierung') durch a-Si:H.

Die vorliegende Dissertation befasst sich mit den physikalischen Fragen zum amorph-kristallinen Silizium-Heteroübergang im Kontext der PV. Zunächst wird die technologische Weiterentwicklung der Heterosolarzellen, die im Rahmen der Dissertation stattfand, zusammengefasst. Diese bestand aus der Entwicklung und dem Einsatz sehr dünner (≤ 10 nm) undotierter a-Si:H Schichten [(i)a-Si:H], um die Passivierung des c-Si weiter zu verbessern und somit die offene-Klemmen-Spannung der Solarzelle zu vergrößern. Es zeigt sich, dass die Wirkung des (i)a-Si:H je nach Dotiertyp des c-Si-Substrats unterschiedlich ist, und vor allem auf dem (technologisch wichtigeren) n-dotierten c-Si-Substrat Herausforderungen bestehen. Eine genaue Einstellung der (i)a-Si:H Dicke und der Dotierung der weiteren a-Si:H-Schichten ist vonnöten, um das Verbesserungspotential in der Solarzelle umzusetzen. In diesem Kapitel werden aus der technologischen Optimierung heraus die wesentlichen physikalischen Fragen gesammelt, die im weiteren Verlauf der Arbeit als Leitlinie für die Grundlagen-Untersuchungen dienen.

Im nächsten Kapitel wird der elektronische Transport durch a-Si:H/c-Si Heterostrukturen mit Hilfe von Strom-Spannungs-Kennlinien (I/V) bei verschiedenen Temperaturen untersucht. Die elektronischen Transportmechanismen in a-Si:H/c-Si Heterostrukturen werden identifiziert, und deren Bedeutung für die Funktion der Solarzelle diskutiert. Es zeigt sich, dass im für den Betrieb der Zelle relevanten Regime die Beschreibung von klassischen c-Si-Solarzellen angewandt werden kann, was eine einfache Charakterisierung von Zellstrukturen mittels I/V-Messungen ermöglicht.

Das nächste Kapitel beschäftigt sich mit der mikroskopischen Charakterisierung von ultradünnen (i)a-Si:H-Schichten. Mit Hilfe von Infrarotspektroskopie, Spektralellipsometrie, Photoelektronenspektroskopie und Sekundärionen-Massenspektroskopie werden die strukturellen, elektronischen und optischen Eigenschaften des a-Si:H untersucht. In der Gesamtschau zeigt sich, dass auch ultradünne a-Si:H Schichten sich ähnlich wie

10...100-fach dickere Schichten verhalten. Dies ist die Grundlage für die Anwendbarkeit etablierter Konzepte der physikalischen Beschreibung von a-Si:H in den folgenden Kapiteln. Im Weiteren wird die Wirkung verschiedener Parameter der Herstellung der a-Si:H-Schichten auf ihre Eigenschaften untersucht und diskutiert.

Im nächsten Kapitel wird die relative Anordnung der elektronischen Bänder in der a-Si:H/c-Si-Heterostruktur an Bauteil-relevanten Proben untersucht. Hierzu wird ein neuartiges Verfahren entwickelt, welches Photoelektronen-Spektroskopie und die Messung der Oberflächen-Photospannung kombiniert. Es zeigt sich, dass bei einer Aufweitung der a-Si:H-Bandlücke durch Kontrolle des Wasserstoff-Gehalts nur der Sprung im Valenzband variiert, während derselbe im Leitungsband konstant bleibt. Dieses Ergebnis ist konsistent mit etablierten Theorien, wurde jedoch noch nie experimentell nachgewiesen. Die Bedeutung des Valenzband-Sprungs für die Heterosolarzelle und die Möglichkeit dessen gezielter Kontrolle werden diskutiert.

Im letzten Kapitel wird die Verbindung zwischen mikroskopischen Eigenschaften der a-Si:H-Schichten und der resultierenden Passivierung von c-Si-Oberflächendefekten gezogen, welche die realisierbare Spannung in Heterosolarzellen bestimmt. Es zeigt sich, dass im Falle einer idealen Prozessierung die Heterogrenzfläche keine ausgezeichneten Eigenschaften besitzt, sondern sich als Projektion des a-Si:H-Volumens auf die Grenzfläche beschreiben lässt. Auf dieser Grundlage lässt sich die komplexe Phänomenologie der c-Si-Passivierung durch a-Si:H verstehen. Die Bestimmung der maximal möglichen Defekt-Absättigung folgt daraus ebenso wie die Erklärung von Degradationseffekten aus der inhärenten Metastabilität des amorphen Siliziums. Dessen Eigenschaften können sich als Reaktion auf externe Parameter wie z.B. die Fermi-Energie verändern, was bislang in der Analyse der a-Si:H/c-Si Heterostruktur nur selten berücksichtigt wurde.

Contents

| | |
|--|------------|
| Abstract | iii |
| Zusammenfassung | v |
| Table of Contents | vii |
| 1. Introduction | 1 |
| 1.1. General introduction | 1 |
| 1.2. Amorphous/crystalline silicon heterojunction solar cells | 2 |
| 1.3. This thesis | 4 |
| 2. Fundamentals | 5 |
| 2.1. Amorphous Silicon | 6 |
| 2.1.1. General properties | 6 |
| 2.1.2. Hydrogen in a-Si:H | 11 |
| 2.1.3. Defect reactions and thermal equilibrium | 15 |
| 2.1.4. a-Si:H growth | 17 |
| 2.2. Recombination and Passivation | 21 |
| 2.2.1. Bulk recombination processes in crystalline silicon | 22 |
| 2.2.2. Specifics of amphoteric dangling bonds in a-Si:H | 26 |
| 2.2.3. Surface/interface recombination | 27 |
| 2.2.4. Semiconductor physics | 27 |
| 2.2.5. From minority carrier lifetime to V_{oc} — a simple test case | 28 |
| 2.2.6. Looking further: The presence of band bending | 32 |
| 2.3. Electronic transport | 33 |
| 2.3.1. From the semiconductor equations to the ideal diode | 33 |
| 2.3.2. The diode under illumination | 35 |
| 2.4. The a-Si:H/c-Si heterojunction: A very brief introduction | 36 |
| 3. Experimental Techniques | 39 |
| 3.1. Sample preparation | 40 |
| 3.1.1. c-Si cleaning and surface conditioning | 40 |
| 3.1.2. Growth of a-Si:H films with PECVD | 40 |
| 3.1.3. Low-temperature annealing | 41 |
| 3.1.4. TCO and metal deposition | 41 |
| 3.2. Film characterization | 41 |
| 3.2.1. Structural properties: IR spectroscopy, H effusion and SIMS | 41 |
| 3.2.2. Electronic structure: (Near-)UV photoelectron spectroscopy | 42 |

| | |
|--|------------|
| 3.2.3. Optical characterization: Spectroscopic ellipsometry | 49 |
| 3.3. Heterostructure analytics | 49 |
| 3.3.1. Measurement and analysis of c-Si minority carrier lifetime | 49 |
| 3.3.2. Surface photovoltage measurements | 51 |
| 3.4. Solar cell diagnostics | 52 |
| 3.4.1. Spectral response and quantum efficiency | 52 |
| 3.4.2. I/V characteristics | 53 |
| 4. Development and assessment of a-Si:H/c-Si solar cell technology | 55 |
| 4.1. Introduction | 56 |
| 4.2. Inclusion of undoped a-Si:H buffer layers | 57 |
| 4.2.1. Phenomenology of c-Si surface passivation by (i)a-Si:H | 57 |
| 4.2.2. Doped a-Si:H layers | 63 |
| 4.2.3. Development of doped/undoped a-Si:H emitter stacks | 64 |
| 4.2.4. Implementation of buffer layers and solar cell performance | 70 |
| 4.3. Technological issues | 77 |
| 4.3.1. Analysis of the solar cell process flow | 77 |
| 4.3.2. The impact of metalization on V_{oc} | 78 |
| 4.4. Discussion | 79 |
| 4.5. Summary and key scientific questions | 80 |
| 5. Analysis of electronic transport in a-Si:H/c-Si solar cells | 83 |
| 5.1. Introduction | 84 |
| 5.2. Heterojunction transport models | 84 |
| 5.2.1. Brief history of semiconductor transport models | 84 |
| 5.2.2. Transport in a-Si:H/c-Si heterostructures | 85 |
| 5.3. Results of dark-I/V curve fitting | 86 |
| 5.3.1. High forward bias | 86 |
| 5.3.2. Low forward bias | 91 |
| 5.4. 2D effects under low forward bias | 95 |
| 5.5. Discussion | 98 |
| 5.5.1. Discussion of transport mechanisms | 98 |
| 5.5.2. Application of dark-I/V fitting for passivation assessment | 100 |
| 5.6. Chapter conclusion | 100 |
| 6. The material properties of ultrathin a-Si:H layers | 103 |
| 6.1. Introduction | 104 |
| 6.2. a-Si:H hydrogen content and microstructure: Infrared spectroscopy | 104 |
| 6.2.1. FTIRS results | 104 |
| 6.2.2. Comparison to pertinent data | 106 |
| 6.3. Optical properties | 108 |
| 6.3.1. Optical band gap | 108 |
| 6.3.2. Refractive index and mass density | 109 |
| 6.4. Electronic structure | 111 |
| 6.4.1. He-I UPS valence band spectra | 111 |

| | | |
|-----------|--|------------|
| 6.4.2. | Constant-final-state yield spectroscopy results | 113 |
| 6.5. | Hydrogen/deuterium profiling by SIMS | 117 |
| 6.5.1. | Depth profiling — the choice of samples | 118 |
| 6.5.2. | a-Si:H versus a-Si:D layers | 118 |
| 6.5.3. | Features of SIMS raw data | 119 |
| 6.5.4. | Deconvoluting SIMS spectra from measurement artifacts | 122 |
| 6.5.5. | Intermediate discussion of SIMS results | 126 |
| 6.6. | Discussion of a-Si:H bulk properties | 130 |
| 6.6.1. | Structural properties | 130 |
| 6.6.2. | Electronic properties | 132 |
| 6.7. | Chapter conclusion | 134 |
| 7. | The a-Si:H/c-Si band lineup in device-relevant structures | 135 |
| 7.1. | Introduction | 136 |
| 7.2. | Methods for the determination of band offsets | 137 |
| 7.3. | Revisiting a-Si:H valence band edge and band gap | 138 |
| 7.4. | The a-Si:H/c-Si band offsets | 139 |
| 7.5. | Discussion I: The fundamental origin of the band lineup variations | 140 |
| 7.5.1. | Comparison to previous works | 140 |
| 7.5.2. | Impact of disorder and hydrogen microstructure | 144 |
| 7.6. | Discussion II: Impact of band offsets on carrier transport | 146 |
| 7.6.1. | Phenomenology in solar cell I/V curves | 146 |
| 7.6.2. | Interpretation | 147 |
| 7.7. | Chapter conclusion | 151 |
| 8. | The interplay of a-Si:H properties with a-Si:H/c-Si interface passivation | 153 |
| 8.1. | Introduction | 154 |
| 8.2. | Correlation of a-Si:H bulk properties with a-Si:H/c-Si interface defects | 154 |
| 8.3. | Low-temperature annealing | 156 |
| 8.3.1. | Microscopic reaction of the a-Si:H bulk | 156 |
| 8.3.2. | Sensitivity of FTIRS | 159 |
| 8.3.3. | Annealing dynamics | 161 |
| 8.3.4. | Hotplate- versus microwave annealing | 162 |
| 8.3.5. | Microscopic preconditions for the annealing effect | 166 |
| 8.4. | The as-deposited state of the heterointerface | 167 |
| 8.4.1. | Limits of the as-deposited interface defect density | 168 |
| 8.5. | Properties of the equilibrated heterointerface | 170 |
| 8.5.1. | The annealed interface defect density | 170 |
| 8.5.2. | Intermediate discussion | 174 |
| 8.6. | Impact of a-Si:H chemical potential on the passivation | 175 |
| 8.6.1. | Phenomenology and possible origins | 175 |
| 8.6.2. | Looking for E_F -dependent Si-H bond breaking | 177 |
| 8.6.3. | Modeling E_F -dependent interface defect equilibration | 180 |
| 8.6.4. | Possible issues and consequences | 185 |
| 8.7. | Discussion | 187 |

| | |
|--|---------------|
| 8.8. Chapter conclusion | 189 |
| 9. Conclusions and Outlook | 191 |
| 9.1. Main conclusions of this thesis | 191 |
| 9.2. Outlook | 194 |
| A. Experimental details | 197 |
| A.1. Fourier-transform infrared spectroscopy | 197 |
| A.2. Photoelectron spectroscopy | 202 |
| A.3. Spectroscopic ellipsometry | 205 |
| B. Hydrogen effusion experiments | 211 |
| B.1. Hydrogenated a-Si:H samples | 211 |
| B.2. Deuterated a-Si:D samples | 213 |
| List of Figures | I |
| List of Tables | V |
| List of Symbols and Abbreviations | VII |
| Bibliography | XV |
| Publications | XXXVII |
| Acknowledgment | XLI |

1. Introduction

1.1. General introduction

The ever increasing markedness of man-made climate change and the drastic economic and political consequences of our dependence on a diminishing stock of fossil fuels have underlined the urgency to shift our energy supply towards renewable sources in recent years. The environmental catastrophe unfolding in Japan has illustrated in a drastic manner that nuclear energy does not range among the sustainable technologies, further intensifying the need for a paradigm shift. In the last decade, photovoltaics (PV) have proven to be a promising building block for a future sustainable energy supply, and worldwide production of PV panels is on the rise. In 2010, a worldwide total production output of over 25 GW_p ¹ was reported (Fig. 1.1), and the total annual production capacity operational at the end of 2010 amounted to over 36 GW_p [98]. The worldwide installed PV capacity already cumulated to $> 20 \text{ GW}_p$ by the end of 2009 [10].

Despite the sunny picture of an exponential increase in both PV panel production capacity and installed power, a closer look reveals several challenges: First of all, the major part of worldwide installed PV power is located in Germany ($>50\%$ by the end of 2009 [10]), which is primarily due to a generous incentive policy and not due to its share of sunlight. Other countries with a much higher potential harvest like Spain or in recent days Italy have drastically cut their feed-in tariffs after excessive installation drove the costs, which caused the local PV markets to collapse. This highlights the fact that PV is still not competitive without subsidies, which of course hinders a true worldwide market breakthrough. On the other hand, already at the stage reached up to now, material availability is becoming an issue. Indium and Tellurium which are found in thin-film solar cells, and Silver which is contained in contact pastes are currently candidates for a potential future shortage.

Thus, the challenge faced in PV research and development nowadays is twofold: To further decrease production costs and increase module efficiencies, while at the same time to develop technologies with lower material consumption and using easily scalable processes with a small environmental footprint.

At the moment, there are two competing mainstreams in applied PV research and development. Firstly, the classical silicon wafer-based PV, close to being technically saturated, is currently pushed to even higher efficiencies by sophisticated device concepts

¹The quasi-unit W_p denotes the power delivered by a solar cell (SC) under standard test conditions, which means at 25°C upon irradiation with the so-called 'AM1.5 standard spectrum' at a power density of 1000 Wm^{-2} . This spectrum describes the average spectral irradiance relevant to solar cell operation at European or North-American latitudes, and is equivalent to the solar spectrum after passing through 1.5 times the average atmospheric airmass ($\text{AM} = \text{'air mass'}$). It is defined in the norm IEC 904-3 (1989), part III.

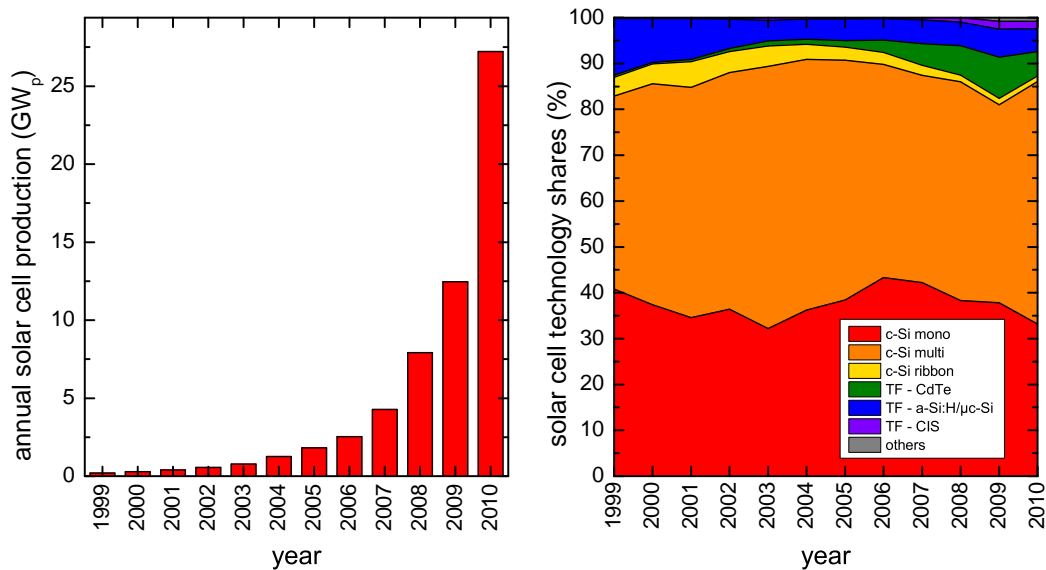


Figure 1.1.: Annual output of worldwide solar cell production including all technologies, expressed as the potential electrical power output under standard test conditions (left). Share of different solar cell technologies in percent (right). 'c-Si' denotes technologies based on crystalline silicon, which can be either monocrystalline ('mono'), multicrystalline ('multi') or made by the ribbon technique ('ribbon'). 'TF' stands for thin-film technologies such as cadmium telluride ('CdTe'), amorphous/microcrystalline silicon thin-film tandem cells ('a-Si:H/ μ c-Si')[159], or Cu(In,Ga)(S,Se)₂ solar cells ('CIS'). Data taken from Photon International [98].

like selective emitter/passivated rear-side solar cells and back-contacted solar cells². These concepts require excessive structuring and are difficult to manufacture. Secondly, several different device concepts are currently being developed or entering production which use thin films instead of wafers to absorb the sunlight, thus requiring less material and making use of large-area coating techniques for processing. The small thicknesses loosen the constraints with respect to material reserves and thus allow to use more 'exotic' compounds like CdTe, CuInGaSe or SiGe, among others. However, with the exception of CdTe, currently being the cheapest solar cell in terms of \$/Watt, and to a lesser extent the amorphous-/microcrystalline-silicon tandem cell, these concepts are still not as efficient or cheap enough to be competitive which is reflected in a market share <20%.

1.2. Amorphous/crystalline silicon heterojunction solar cells

A hybrid concept incorporating aspects of both wafer-based and thin-film solar cells are amorphous silicon/crystalline silicon (a-Si:H/c-Si) heterojunction (HJ) solar cells — also sloppily termed 'silicon heterojunctions' (SHJ)—, being the focus of this thesis: While a-Si:H/c-Si HJ solar cells are a high-efficiency concept based on silicon wafers,

²The ultimate efficiencies of these concepts are represented by the PERL cell that yielded a record 25% conversion efficiency on the lab scale [289] for the former concept, and 24% with a back-contacted solar cell recently shown on large area [44]

they use thin-film processing techniques and can be made using only highly abundant materials. For allowing to reach more than 23% conversion efficiency [264], which has to be compared with the physical limit of 29% conversion efficiency in a c-Si solar cell [123], the process to make the cell is comparably simple: Starting with a clean c-Si surface, full-area coating with 10 nm of hydrogenated amorphous silicon by chemical-vapour deposition suffices to create the p/n junction. The structure is then terminated with roughly 100 nm of a transparent conductive oxide (TCO) deposited by physical vapor deposition, and a screen-printed metal contact, while no structuring is required. All processing can be done around 200°C, which reduces the energy consumption in making the cells.

SHJ solar cells were first developed by Sanyo, starting research on this device structure in 1990. In 1992, 18.1% conversion efficiency were demonstrated on 1 cm² cell area with a SHJ cell on an n-type silicon wafer [(n)c-Si] comprising undoped a-Si:H buffer layers [(i)a-Si:H] [254]. This concept was termed 'heterojunction with intrinsic thin layer' (HIT), and successively developed further over the next 20 years. Mass production of HIT modules was launched in 1997, and until now Sanyo is the only company producing SHJ solar cells. The independently confirmed record efficiency reported so far by Sanyo is 23.0% on 100.4 cm² with $V_{oc} = 729$ mV, $j_{sc} = 39.5$ mA/cm² and $FF = 80.0$ %, presented in 2009 [146, 264]. In mass production, the best HIT cells have 21.6% conversion efficiency, leading to 19.0% module efficiency [205].

The Helmholtz-Center Berlin (HZB) is conducting research on a-Si:H/c-Si heterojunction solar cells since 1997. As the expiry of Sanyo's most important patents in 2010 came closer, including the most important on undoped buffer layers, the interest in the industry for HIT-type solar cells rose and research on a-Si:H/c-Si HJ solar cells was started at several institutes³. Currently, there is a devoted competition in terms of efficiencies between institutes, several research projects aiming at developing HJ solar cells, and an increasing number of industrial partners are considering commercialization.

While the solar cell itself contains only silicon, material reserves may become an issue concerning the contacts: Sanyo's HIT cell comprises Ga-doped InSn-oxide (ITO) TCOs and requires screen-printed silver contacts as contact firing is incompatible with the cell concept. Both technologies are expensive already now and prices will most likely increase further. While competitive production is obviously possible nowadays with the original HIT concept, the replacement of ITO by ZnO and a hypothetical solution of the screen-printing issue, e.g. by electroplating, could yield an additional decrease of production costs by 20% [207]. Thus it is obvious that the a-Si:H/c-Si heterojunction cell concept is one of the most attractive alternatives to the classical c-Si based solar cell technology.

On the other hand, and quite surprising given the success of the HIT solar cell in terms of reached efficiencies and early industrialization, there is still a plethora of open questions concerning the detailed physical mechanisms at work in SHJ solar cells, which determine the final conversion efficiency. These include the c-Si surface passivation mechanism by

³Nowadays there are activities at NREL and University of Delaware in the USA, EPFL in Switzerland, the universities of Utrecht and Delft in the Netherlands, national research labs in France (CEA-INES, CNRS) and Italy (ENEA), and the Institute for Solar Energy Research Hameln (ISFH) as well as the Fraunhofer institute for solar energy systems (ISE) in Germany, to name just a few.

(i)a-Si:H, the size and impact of the a-Si:H/c-Si band offsets and the charge carrier transport mechanisms.

This situation sets the stage for the present thesis which is located at the intersection of solar cell technological optimization and detailed physical understanding of the constituents and their interplay.

1.3. This thesis

In the present thesis it will be attempted to reconcile the technological and physical aspects by the following approach: After giving brief introductions into the involved physics and the methods used throughout this thesis, the previous a-Si:H/c-Si solar cells made at HZB will be analyzed, and a technological strategy will be outlined with the goal to overcome the shortcomings of the current solar cell processing in chapter 4. The main component of this strategy is the development and implementation of (i)a-Si:H buffer layers which aims at improving the passivation of the c-Si surface defect states and thus increasing the output voltage of the solar cell. The analysis of the results of this *technological* optimization will highlight some technical issues specific to the cell processing at HZB and, more importantly, identify several *physical* questions which are addressed in detail in the remaining chapters of the thesis.

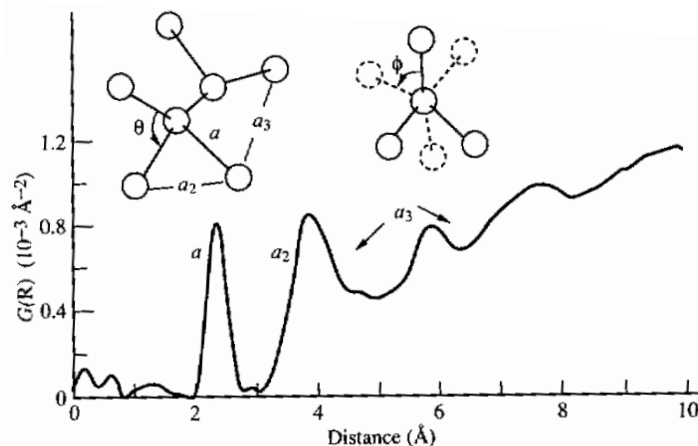
First, the transport through a-Si:H/c-Si heterojunctions will be analyzed in the presence and absence of (i)a-Si:H buffer layers in chapter 5, employing an analysis of current/voltage curves taken in the dark at different temperatures. In the following chapter 6, the structural and electronic properties of thin (i)a-Si:H layers (thickness ≤ 10 nm) on c-Si substrates will be analyzed. The microscopic insight gained in this chapter will be used in the following chapter 7 to analyze the dependence of the heterojunction band lineup on the microscopic a-Si:H properties. Finally, in chapter 8 the bulk properties of the (i)a-Si:H layers will be linked to their passivation potential on c-Si substrates, and the dependence of the passivation on post-treatment (thermal annealing and/or deposition of doped top layers) will be analyzed and explained by a microscopic model. While the focus of this second part of the thesis is clearly on the physics of a-Si:H/c-Si heterojunctions, it will recur to the technological issues raised in the first part at several points to establish a connection between the solar cell development and the underlying physics. The thesis concludes with a short summary of the main findings and a brief outlook in chapter 9.

2. Fundamentals

In this chapter, some fundamental aspects and textbook knowledge on which the analysis of experimental data is based in the course of this thesis shall be briefly reviewed. The scope of the present chapter is to provide the background necessary to comprehend the discussion in the following chapters. While readers familiar with the field may skip parts of this chapter, standard textbooks such as Refs. [88, 192, 244, 253] may provide a more thorough and detailed insight into the topics for the interested reader.

In the first section, amorphous silicon is introduced with emphasis on the role of hydrogen, a short introduction in the a-Si:H metastability and a description of the growth by PECVD. In the second section, recombination of photogenerated charge carriers in c-Si is discussed. Particularly, the role of interface recombination and the resulting task of interface or surface passivation is emphasized, as this aspect is most prominent in a-Si:H/c-Si HJ solar cells. The last sections briefly deal with electronic transport in semiconductor p/n junctions, and the basic features of a-Si:H/c-Si heterojunctions.

Figure 2.1: Radial atomic distribution function $G(r)$ of a-Si as obtained by x-ray diffraction and schematic of a-Si:H short-range order. While bond length a and tetrahedral angle θ are approximately preserved, there is considerable variation in the dihedral angle ϕ which defined the second-next nearest neighbor distance a_3 . Figure taken from Ref. [244] showing data of Schülke *et al.* [213].



2.1. Amorphous Silicon

This section is based on the textbooks by Street [244] and Tanaka [253].

2.1.1. General properties

Structure

The defining property of amorphous silicon in contrast to its well-known crystalline form is the absence of long-range order in the atomic positions. Firstly, on very fundamental ground, this aspect alone leads to the prominent electronic features such as dangling bonds in the band gap and exponentially decaying band tails, as will be discussed in the following. Secondly, the amorphous state, which does not represent the energetically most favorable condition, introduces a structural degree of freedom unknown in crystalline materials. The presence of hydrogen in hydrogenated amorphous silicon (a-Si:H) further increases this structural indetermination as H can be bound in different configurations. On the one hand, this means that nominally identical materials in terms of stoichiometry can possess different properties based on differences in the microscopic arrangement of the amorphous network (H microstructure, topological statistics), on the other hand these degrees of freedom lay the foundation for the metastability of amorphous silicon¹.

As atomic long-range order (LRO) is completely absent in an amorphous material, \vec{k} is not a good quantum number and thus a discussion of the structural features in terms of reciprocal space — as common for crystalline materials — is meaningless. However, an instructive approach towards understanding the basic structural features of a-Si:H is a statistical description of the atomic distribution in real space, as provided by the radial distribution function (RDF), a function describing the probability of finding an atom at a given distance to another atom. This function (schematically depicted in Fig. 2.1), which is determined by x-ray or neutron diffraction, reveals a 'hierarchy of disorder' in

¹This includes the a-Si:H defect equilibration by interconversion of weak bond into dangling bonds, to be explained later.

a-Si. The first peak corresponds to the average distance to the nearest neighbor atom from any given atom, and there is only marginal deviation from the c-Si signal. This signifies that the bond lengths are essentially the same as in c-Si. The second peak marks the distance to the next-nearest neighbor and involves the bond angle θ as can be seen from the sketched model network in the figure. This peak shows some broadening as compared to c-Si, still the bond angle is about the same as in c-Si, i.e. the tetrahedral angle of $\theta = 109^\circ$. The third-nearest neighbor peak however is significantly broadened and rises only slightly out of an increasing background continuum from overlapping shells of neighboring atoms, indicating that there is considerable disorder in the so-called dihedral angle.

The RDF analysis reveals that the short-range order is preserved as compared to c-Si, while there is considerable disorder already on the intermediate-range such as variations in the dihedral angle, and the LRO is absent. As the RDF provides only information integrated over all directions, no further insight can be gained into more subtle aspects of medium-range order (MRO) such as ring statistics², which are closely connected to the structural topology of the amorphous network. It has to be noted here that although hydrogenated a-Si:H is essentially a binary material, its RDF closely resembles the function discussed above. In the following, the discussion will be restricted to a-Si:H.

Based on the finding that the SRO is tetrahedral, some basic considerations concerning the average coordination can be made: In a three-dimensional solid, three constraints are necessary to make a continuous random network (CRN) well-defined. Taking into account that a Si-Si bond constrains two atoms, an ideal coordination number C of 2.45 results [182]. Thus, a fourfold CRN is over-coordinated which leads to considerable strain in the network and deviations from the local tetrahedral symmetry that can only be lifted by breaking Si-Si bonds or increasing the number of Si-H bonds. However, a H content exceeding 50% would be necessary to obtain $C = 2.45$. Therefore it is to be expected from the coordination argument alone that a balance between strain, H incorporation and structural defect concentration exists in a-Si:H. Indeed it is observed that such a balance exists in the form of the a-Si:H metastability. Additional consequences are the propensity towards an inhomogeneous structure as e.g. the formation of voids locally relieves the structural constraints, and the rigid nature and inherent stress of a-Si:H films.

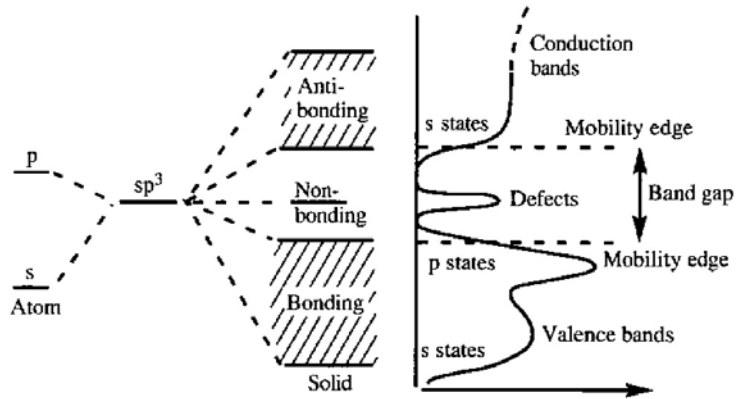
The density of states

Due to the absence of LRO, the strict periodicity of the potential landscape assumed in the derivation of the Bloch wave functions used to describe electrons on a lattice is not given. The perturbations of the periodic potential imposed by the disorder effectively lead to permanent scattering of the electrons from one Bloch state into another, which leads to a large uncertainty in the \vec{k} vector. However, it is important to note that the wave function is still extended in real space. There are several important consequences:

- a) If the disorder potential surpasses a threshold level, the wave function is restricted

²This refers to the statistical distribution of the number of atoms in the amorphous network which are connected in rings.

Figure 2.2: Molecular orbitals and schematic of the resulting density of states for hydrogenated amorphous silicon. Taken from Ref. [244].



to a defined volume ('localization'), whose extent depends on the amount of disorder. This effect can be described with the Anderson theory of localization [5].

- b) There are no momentum selection rules for optical transitions. Thus, there is no distinction between direct and indirect gap any more, a-Si:H is effectively a direct semiconductor resulting in an absorption coefficient significantly higher than that of c-Si. Transitions occur between states that overlap in real space, be them extended or localized.
- c) The $E\vec{k}$ band dispersions used in crystalline solid state physics are not applicable to describe the electronic states in a-Si:H. However, the concept of a density of electronic states (DOS) is still useful.

There are three essential contributions to the DOS, which are 1) the bands, 2) the band tails and 3) the defect states deep in the band gap, as depicted in Fig. 2.2.

The bands. Due to the slight variations in local symmetry and coordination, the electronic structure of the bands is similar to a 'smoothened' version of a c-Si DOS integrated over the \vec{k} space. Additional features in the valence band arise from Si-H bonds and will be discussed in Section 6.4.1. As in tetrahedral bonding in the c-Si crystal, the s and p orbitals combine to a sp^3 hybrid orbital, whose bonding states form the valence band while the anti-bonding states constitute the conduction band. Important to note is that the p states lie energetically higher than the s states in the broadened sp^3 hybrid-derived bands, which leads to the states at the top of the valence band having p character and the states at the bottom of the conduction band being s -like. The non-bonding Si states are not split by the bonding interaction and thus lie in the middle of the band gap (see below).

The band tails. It can be shown *a priori* that any disorder in the atomic lattice of a solid leads to an exponentially decaying density of localized states extending into the band gap, the so-called 'band tail' [234]. The density of localized states — and in consequence the slope of the tail in the DOS — depends on the amount of disorder. In the microscopic picture drawn above it is obvious that these localized states will be located in real space at topological configurations in the amorphous network

that deviate most from the ideal c-Si topology (cf. the discussion in section 7.5.2). The localized states of the band tails gradually merge into the extended states of the band, rendering the definition of a band edge complicated. An electronically distinguished point is the so-called 'mobility edge', which is the demarcation energy between extended and localized states in terms of electronic transport. The difficulty of defining a band edge will be discussed in more detail in Section 3.2.2. The localized band tail states heavily impact the electronic transport- and optical behavior of a-Si:H: Due to frequent trapping of charge carriers in the tail states, the effective mobility is further reduced³ and becomes temperature-activated, as thermal energy is needed to re-excite the trapped carriers. The optical absorption has an exponential dependence on the photon energy in the vicinity of the band edge due to optical transitions involving the localized tail states. This leads to subtleties in the definition of the optical band gap, similar to the band edge in the DOS. These will be discussed in detail in Section 6.3.

The density of the localized tail states is described by the width of the tail, or the slope of the exponential decay. The slope parameter (also termed Urbach energy, E_{0V}) characterizes the band tail, and is thus closely connected to the size of the effects described above. It was found that for the valence band, its value is directly connected to the structural disorder, as would be assumed based on the microscopic discussion presented above), with typical values being 40...80 meV. The conduction band tail slope on the other hand is dominated by the thermal disorder.

The dangling bonds. The defect states deep in the band gap are of structural origin. The most general category of a structural defect would be an anomaly of the covalent bond with respect to the SRO. The simplest possible configurations are three- or fivefold coordinated Si atoms (leading to 'dangling' or 'floating' bonds, respectively), weak/heavily strained bonds and bond-centered hydrogen. Based on electron spin resonance (ESR) measurements it was concluded that the dangling bond (DB), i.e. an unpaired electron in a distorted sp^3 hybrid orbital, is the most important defect type in a-Si:H. Apart from this configuration, the orbital can in principle accommodate a second electron or lose its electron/'capture a hole'. Thus, the DB can be found in three charge states, which is termed 'amphoteric behavior'. The energy needed or gained when adding or removing an electron from the DB depends on its charge state, with the effective Coulomb correlation energy U separating the two possible electronic states⁴. In the following, U denotes the true correlation energy, i.e. the Coulomb energy needed to fit the two electrons in the localized DB orbital, corrected by lattice relaxations, electron-phonon interactions and orbital rehybridization. In the case of a-Si:H, U is positive and generally assumed to be of order 0.2 eV. Concerning the energetic position of the DB, the D^- defect in (n)a-Si:H was doubtlessly located at about 0.8...0.9 eV below the conduction band. However, no consistent picture exists for the other

³Note that the disorder already causes a reduction from the c-Si value also for the extended states.

⁴In a one-electron picture, the DB is usually thought to produce two energy levels separated by U , as no electron can be added to D^- or removed from D^+ .

configurations based on experimental data, and it is uncertain if the DB energies shift with doping. Experimentally one typically observes a continuum of dangling bonds forming an approximately Gaussian distributions deep in the band gap with a width of about 0.2 eV.

Doping

Unlike in crystalline semiconductors with their well-defined atomic positions and thus fixed coordinations, doping in amorphous semiconductors is not trivially achieved: Impurity doping would require the dopant atoms to be incorporated with the same coordination as the host lattice atoms to create occupied antibonding states that are easily emptied by emitting carriers into the bands. In principle, the structural freedom of the amorphous network allows to incorporate each atom with its optimal valency, thus spoiling this doping mechanism. Theory clearly predicted such behavior based on the so-called ' $Z = 8 - N$ ' rule, stating that the energetically optimal number of covalent bonds Z is defined by the maximizing the number of saturated orbitals for a given number of valence electrons N . Surprisingly however, LeComber and Spear demonstrated experimentally that impurity doping actually *can* be achieved in a-Si:H [42]. Indeed, the majority of the B or P atoms incorporated to achieve impurity doping are threefold coordinated and thus inactive, some however are fourfold coordinated which suffices to make a-Si:H electronically controllable. The doping efficiency⁵ is of order 10^{-2} . A detailed analysis of the doping characteristics by Street led to the conclusion that the 8-N rule is in effect in a-Si:H as well, acting however on *charged* impurity atoms: If the Fermi level lies deep enough in the band gap, energy can be gained by the reaction $Si_4^0 + P_3^0 \rightarrow DB^- + P_4^+$ thus forming an ionized donor P_4^+ and a dangling bond from neutral Si_4^0 and P_3^0 atoms⁶. P_4^+ has the same valence state as Si and is thus incorporated according to the 8-N rule with fourfold coordination. The energy gain from the charge transfer to form the DB leads to the total energy being only slightly higher than for the P_3^0 incorporation, therefore the doping-active P_4^+ is present in small but significant fractions. With the Fermi level approaching the conduction band, the energy needed to form the active donor state increases, leading to a self-compensating effect which prevents the Fermi level to enter the band tail. The model explains the increase of the DB concentration with doping [250], which is shown to be intimately connected to the doping mechanism itself. The same principle was found to be at work for p-type doping with boron as well. The doping mechanism in a-Si:H is a first example of a metastable phenomenon, as the Fermi level position determines the energy needed to form an active donor state, leading to an equilibrium situation. In Section 2.1.3 it will be shown that the DB defect concentration is also subject to an equilibrium reaction.

⁵defined as the ratio of mobile carriers emitted into the bands and the incorporated concentration of donors/acceptors

⁶ P_4^+ denotes a fourfold coordinated phosphorous atom which is positively charged and the other symbols are defined accordingly.

Electronic transport

Electronic transport in amorphous semiconductors comprising localized tail states and a significant disorder potential dephasing the charge carrier wave function even in the extended states is highly nontrivial. As this thesis is concerned with a-Si:H conduction only to a small extent, no detailed introduction shall be given. Basically, three main conduction mechanisms are present in a-Si:H, whose relative importances change primarily with temperature and defect concentration. These mechanisms are hopping conduction at the Fermi level, hopping conduction in the band tail and extended state conduction. The latter is the most important mechanism, and it is important to be aware that the transport takes place at the lowest possible energy, i.e. right at the mobility edge, which renders its properties most important for electronic transport.

In principle, a thermally activated conductivity is observed which has the form

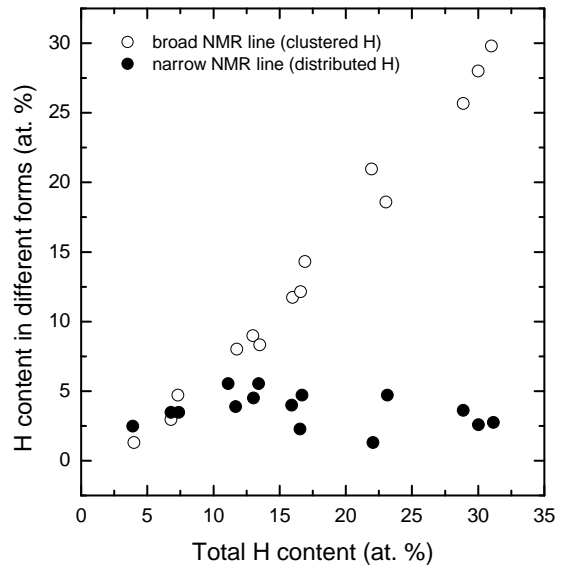
$$\sigma = \sigma_0 \exp\left(-\frac{(E_{\text{tr}} - E_F)}{kT}\right), \quad (2.1)$$

with the absolute temperature T and Boltzmann's constant k . This equation implies that the conductivity is defined solely by the Fermi level. However, there are two problems: Firstly, the transport energy E_{tr} is not equal to the conduction band mobility edge energy, and in addition also temperature-dependent. The more problematic fact is the variation in the conductivity prefactor σ_0 , which was found to be varying over 7 orders of magnitude depending on temperature, doping, and processing details of the a-Si:H samples [235, 255]. Although for most samples the variation of σ_0 is within 2 orders of magnitude, particularly the systematic shift in σ_0 with a-Si:H doping prevents an accurate determination of the Fermi level position from DC conduction experiments alone. Therefore it is refrained from comparing conductivity data e.g. with photoelectron spectroscopy data taken in the course of this thesis. Further details on the conduction mechanism go beyond the scope of this thesis and can be found in Refs. [244, 253].

2.1.2. Hydrogen in a-Si:H

Hydrogen is introduced into a-Si helping to lift the inherent over-coordination by the formation of Si-H bonds and to saturate the defects arising from Si dangling bonds. However, the role of H in a-Si:H is subtle and reaches beyond the simple DB saturation picture: Device-grade a-Si:H contains about 10-15% hydrogen and not the >50% necessary to decrease the average coordination to the optimal $C = 2.45$. Additionally, there is experimental evidence that H can be incorporated into a-Si:H in a variety of topological configurations, introducing the 'H microstructure' as additional parameter alongside the mere stoichiometry. It will be discussed in the first of the following sections. The manifold of Si-H bonds can be viewed in terms of a 'hydrogen DOS' [248], where available states are filled up to the H chemical potential. In consequence, the H found at different sites is not energetically equivalent and some of it is easily excited to a transport level, which leads to a plethora of phenomena related to H redistribution and transport. A brief introduction into H transport is found in the second of the following sections.

Figure 2.3: Contributions of distributed and clustered hydrogen to the total a-Si:H hydrogen content as implied by nuclear magnetic resonance measurements on thick a-Si:H specimens. Data reproduced from Knights [127].



Microstructure

The silicon-hydrogen bonding structure can best be accessed experimentally with infrared- (IR) and Raman spectroscopy. As IR spectroscopy will extensively be employed in the course of this thesis, the discussion will be focused on this technique here. The Si-H bonds in three-dimensional space can perform wagging-, bending- and stretching motions leading to IR modes in the wavenumber range 630 cm^{-1} , $850\text{--}900\text{ cm}^{-1}$ and $2000\text{--}2100\text{ cm}^{-1}$, respectively. The possible topological configurations of hydrogen in a-Si:H cover isolated monohydrides, the termination of dangling Si bonds in mono-, multi-vacancies and platelets, as well as polysilane chains and H-decorated nano- or even micro-sized voids. The experimental signatures of these structures in the IR spectra and their respective significance for structural and electronic properties of a-Si:H have been widely discussed (see e.g. Refs. [26, 86, 139, 149, 230, 286] and references therein). The most prominent and common distinction in the IR spectra is between the SiH and SiH₂ modes. The stretching modes allow for easiest discrimination of these modes as the SiH and SiH₂ peaks are well separated, the total H content however can best be estimated from the 630 cm^{-1} wagging signal as all modes contribute to the same peak. However, this can be experimentally challenging, and there are well-calibrated proportionality factors which allow to determine the H content from the stretching modes, as well. There is one important ambiguity in the interpretation of the IR spectra which concerns the signal at $2090\text{--}2100\text{ cm}^{-1}$ which is classically attributed to SiH₂ [26, 127, 147]: SiH can also yield a mode in that range when present in a clustered form as e.g. on the inner surfaces of voids, and newer works point out that interpreting this signal as clustered SiH helps to reconcile contradictory H evolution results and the mass density of a-Si:H [113, 230, 275]. Details of this issue will be discussed in section 6.3.2.

Nuclear magnetic resonance (NMR) yields complementary insight by probing the spatial distribution of H in a-Si:H: The line width of the NMR signal is directly related to the dipole interaction of the H nuclei and scales with the distance of the nuclei r to

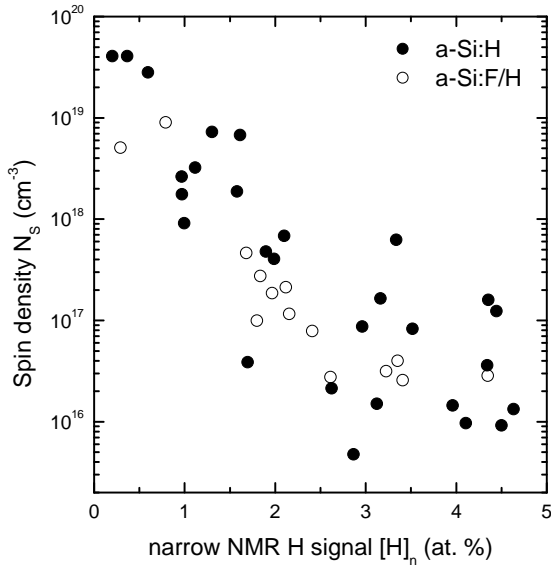


Figure 2.4: Dependence of the spin density, being a measure for the density of dangling bond defects in a-Si:H, on the distributed hydrogen content. While the spin density is measured with ESR, the distributed H is reflected the narrow contribution to the NMR signal. Data reproduced from Shimizu *et al.* [223].

the power of r^{-6} . It was found that each NMR spectrum can be deconvoluted into two contributions, indicating a two-phase nature of a-Si:H in terms of spatial distribution of H atoms. There is one phase of distributed H and another of H with only 2...3 Å distance to the next H atom. Integration over the deconvoluted signals allows to determine the H content found in each of the two phases. The results of Knights, which are prototypical for a-Si:H, are shown in Fig. 2.3.

There is a constant concentration of distributed H over the range of total H content, while the contribution of concentrated H increases along with the total H content. The similarity of this figure to the intensity of the IR modes at 2000 cm⁻¹ and 2090...2100 cm⁻¹ (Ref. [230] and cf. Fig. 6.4 in section 6.2.1) suggests to associate the distributed H with the Si-H bonds resonating at 2000 cm⁻¹ and the concentrated H with the 2090...2100 cm⁻¹ signal. To fulfill the requirement of a distance of 2...3 Å to the next H atom, this mode can only be indicative of SiH₂ (chains) or SiH in small voids. Thus, the NMR results are not decisive but restrict the IR analysis to these two structural candidates⁷.

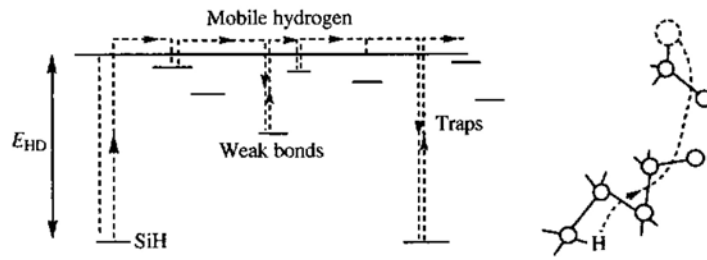
Connection to a-Si:H defect density

It is interesting to relate the H microstructure to the defects in a-Si:H. The introduction of H reduces the DB density from 10²⁰ cm⁻³ in a-Si to about 10¹⁶...10¹⁸ cm⁻³, which is the foundation of the usability of a-Si:H for electronics applications. However, the relationship between DB density and H microstructure is less straightforward than could be anticipated.

It was established that a clear correlation exists between the defect density and the distributed H (Fig. 2.4 showing data of Shimizu *et al.* [223]), while the clustered H

⁷It can be noted that NMR also detects a small fraction (<1 at.%) of molecular H, irrespective of growth conditions.

Figure 2.5: Schematic picture of hydrogen transport in a-Si:H. The mobile hydrogen emerges from Si-H bonds forming a dangling bond upon release, its transport is affected by shallow traps (weak Si-Si bonds), and it gets immobilized at dangling bonds. Taken from Ref. [244].



does not seem to help in eliminating defects. At first glance paradox, this can result in the defect density to increase with the total H content for higher H concentrations, as for $C_H > 10 \dots 15\%$ the distributed H slightly declines (Fig. 2.3). In samples prepared at low temperature, the defect density can be decreased by 1-2 orders of magnitude upon annealing at $200 \dots 300^\circ\text{C}$, while at the same time clustered H is converted into distributed H [287], supporting the picture drawn above. There is, however, no direct quantitative connection between distributed H and the DB density — obviously the H does not directly eliminate defects but helps to prevent the structural conditions leading to unsaturated Si bonds, i.e. facilitating structural relaxation. Reversely, it may be concluded that the clustered H favors structural conditions which are prone to defect creation by introducing additional strain or disorder into the amorphous network. This highlights structural relaxation to be intimately connected with the defect density, a fact that will become more obvious later.

Migration and dynamics

The mobility of H in a-Si:H and its dynamics have been studied predominantly by H evolution and H profiling after defined annealing. It was found that for $T > 300^\circ\text{C}$, H is successively removed from a-Si:H leading to irreversible changes in the amorphous network, while the onset of its mobility already around 100°C promotes the metastability phenomena to be described in Section 2.1.3. The motion of H occurs by thermally activated diffusion, i.e. a diffusion coefficient following $D_H = D_0 \exp(-E_d/kT)$, with the diffusion energy $E_d = 1.5 \text{ eV}$, and the diffusion prefactor D_0 of order $10^{-2} \text{ cm}^2/\text{s}$. Thermally activated diffusion usually occurs when trapping is present. The obvious trapping sites are the DBs and the transport sites may be the bond-centered position as is the case in c-Si. However, the detailed analysis of the prefactor behavior shows that there must be far more trapping sites than DBs. Obviously, the weak/strained Si-Si bonds act as shallow traps in the H diffusion, as schematically depicted in Fig. 2.5. The trapping occurs by breaking of the weak Si-Si bond while a stable Si-H bond and a DB are created. It has to be noted that samples featuring a large void volume may contain a network of interconnected voids through which H *molecules* can easily migrate without the need of bulk diffusion⁸. In conclusion it can be stated that H migrates comparably easy as it is only weakly bound, even in the covalent Si-H bond. Therefore,

⁸This leads to a low-temperature peak in H evolution spectra, occurring due extensive reconstruction of the Si network which creates H molecules from two adjacent Si-H bonds at the void surface. Details of this effect will be discussed in appendix B.

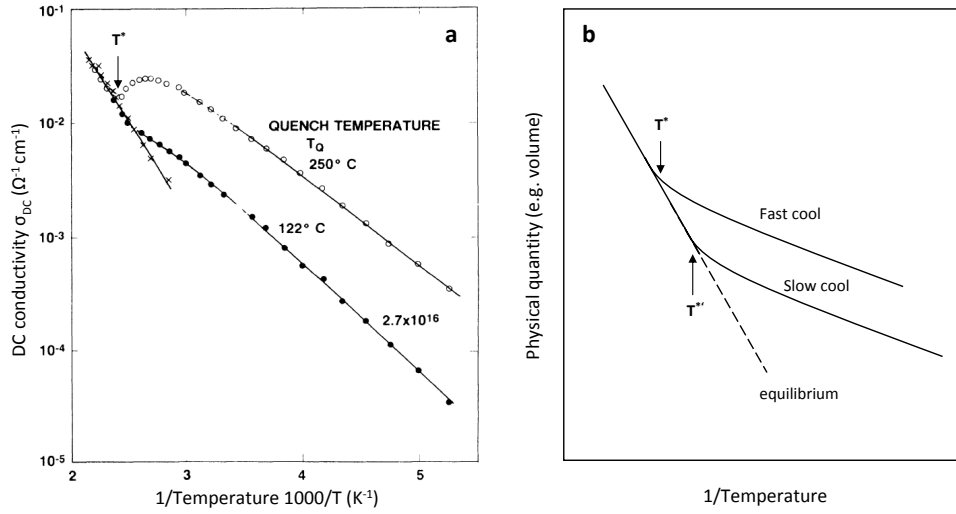


Figure 2.6.: (a) First experimental evidence for glass-like behavior in a-Si:H as reflected in the DC conductivity σ_{DC} [245]. $\sigma_{DC}(T)$ below the glass temperature $T^* \approx 500$ K depends on the thermal history of the sample: In the case of fast thermal quenching, the equilibrium state at $T_{\text{initial}} > T^*$ is frozen in, and relaxes slowly at $T_Q < T^*$. The rate of relaxation depends on the distance of T_Q from the glass temperature. (b) Prototypical picture of glass-like behavior: Below the glass temperature, which depends on the cooling rate, the equilibration processes are not fast enough to maintain the equilibrium corresponding to the actual temperature. As an effect, the state corresponding to T^* is frozen in and a much slower relaxation follows.

in comparison to the rigid over-coordinated Si network with its inherent frustrated non-equilibrium state, it is to be expected that the H distribution is closer to an equilibrium situation, at least concerning the distributed hydrogen.

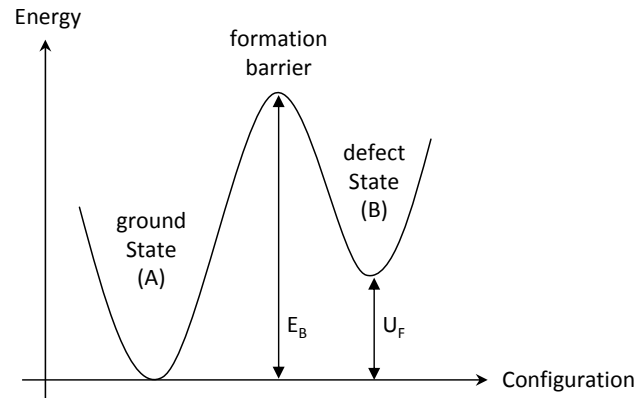
2.1.3. Defect reactions and thermal equilibrium

Experimental indications

In the light of the large spectrum of deposition conditions and post-treatment options, it is a puzzling fact that no a-Si:H films with defect concentrations below 10^{15}cm^{-3} have been reported. The most convincing attempts to explain this finding have one common foundation: They predict (near-)equilibrium processes to determine the defect density in a-Si:H, although the amorphous structure itself is in a non-equilibrium state. Thus, the defect concentration and other material properties can be described with thermodynamic models. In the following, the experimental foundation of these models shall be briefly outlined.

The first striking evidence for thermodynamic equilibration processes ruling the properties of a-Si:H was observed in the analysis of the temperature-dependent DC conductivity $\sigma_{DC}(T)$ in (n)a-Si:H [245]. It was found that below a certain temperature, $\sigma_{DC}(T)$ depends on the thermal history of the sample after annealing: It is largest for the samples quenched from the highest annealing temperature at the fastest rate, while it is lowest for slow cooling, long relaxation times and lower annealing temperatures (Fig. 2.6a).

Figure 2.7: Preconditions for metastable behavior: A reaction of the type $A \leftrightarrow B$, where the configuration A is energetically separated from B by some formation energy U_F , while the reaction is subject to a potential energy barrier of height E_B , and E_B is significantly larger than U_F . In the case of the a-Si:H metastability, B corresponds to a dangling bond defect.



The explanation of this observation was the decay of the carrier concentration in the bands, which is temperature-dependent and frozen in upon thermal quenching at a value corresponding to a freeze-in temperature which depends on the cooling rate. Below the freeze-in temperature, a slow relaxation process takes place, with the time constant depending on the relaxation temperature.

Such behavior is well-known from glasses and is generally observed if the following condition applies: There is a reaction of the type $A \leftrightarrow B$, where the configuration A is energetically separated from B by some formation energy U_F , while the reaction is subject to an potential energy barrier of height E_B , and E_B is significantly larger than U_F (Fig. 2.7). Any reaction of this type exhibits a high-temperature equilibrium situation, when kT is large enough to facilitate overcoming the potential barrier at a sufficient rate and the population of the two states is governed by Boltzmann statistics. At lowering the temperature, there is a 'glass temperature' T^* when the reaction rate drops below the level necessary to maintain equilibrium and the present population is frozen in. T^* depends on the cooling rate, as a fast rate requires a higher reaction rate to maintain equilibrium, thus the freeze-in happens at higher a temperature. The resulting behavior of any quantity depending on the products of the reaction looks like the one depicted in Fig. 2.6b. Below the glass temperature however, the reaction still takes place with a much reduced rate, leading to the system slowly deviating from the equilibrium state frozen in at T^* .

The processes underlying the trends in the DC conductivity shown above in doped a-Si:H are complex, as the carrier density is given by the difference of active dopants and defects, which both show a temperature-dependence. Most importantly in the framework of this thesis, it was found that the (i)a-Si:H defect density is indeed ruled by an equilibrium process similar to that just outlined. The fundamental reason for this shall be outlined in the next paragraph.

The weak Si-Si bonds and the defect pool

According to the similarity of the trends observed in the (i)a-Si:H defect density to the prototypical glass behavior, an equilibrium reaction between intact Si-Si bonds and

dangling bonds is suggested. In the light of the nature of the amorphous network with its different topological configurations one must assume not a single defect creation energy but a site-dependent distribution of energies. The defect reaction will of course preferably involve states with a minimum defect formation energy, which are the bonds farthest away from the c-Si equilibrium configuration, i.e. the strained Si-Si bonds. Thus one can see the valence band tail states as the reservoir for defect creation. For a known density of weak bonds N_{wb} and a fixed formation energy U , the defect density N_d at a given temperature would be given by $N_d \approx N_{wb} \exp(-U/kT)$ for $U > kT$. In reality, there is a distribution of formation energies as there is a continuum of both weak bonds found in the VB tail states and DBs in the band gap as final states of the reaction, leading to the generalized equation

$$N_d = \int \frac{N_0(U) \exp(-U/kT)}{1 + \exp(-U/kT)} dU. \quad (2.2)$$

Here, $N_0(U)$ is the distribution function of the formation energies, whose origin is the disorder in a-Si:H⁹. In the most simple case of absent ion interactions, the formation energy for neutral defects U_{d0} is given by the difference in energy of the defect state E_d and the weak bond in the valence band tail E_{wb} , thus $U_{d0} = E_d - E_{wb}$. As the variation in E_d is small, the formation energy distribution follows the valence band tail state density.

The inclusion of H, which was shown to be comparably mobile in a-Si:H, alters some details of the defect reaction description. If H is allowed to saturate the defect created by breaking a dangling bond¹⁰, then a DB will remain at the original site of the H atom, and thus the two DBs have effectively drifted apart. This leads to a different entropy and thus equilibrium defect density than for defects that stay close together. One could also think of H-mediated bond breaking, i.e. the breaking of the weak Si-Si bond by inclusion of a mobile H atom. Thus, several models can be formulated differing in the details of the defect reaction on which they are based, but not in the general concept. There is an ongoing debate for more than two decades now concerning the validity of the different approaches. The common feature however — the foundation on the glass-like defect equilibration reaction — is not questioned.

Some of the most prominent models were formulated by Smith and Wagner [232], Winer [281], Street [246, 247] and Stutzmann [249], among others. In chapter 8, the 'defect pool model' formulated by Powell and Deane [184–186] will be used to describe the a-Si:H defect equilibration.

2.1.4. a-Si:H growth

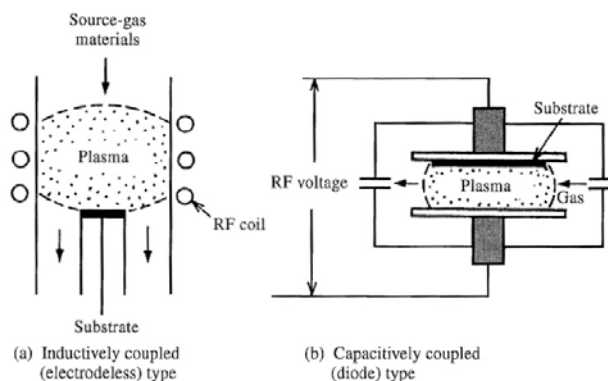
How to grow amorphous solids

As outlined above, the structure of an amorphous solid like a-Si:H is characterized by a non-equilibrium state. Thus, the different preparation methods for a-Si:H are firstly

⁹This is strictly true only for undoped a-Si:H, while the involvement of dopants render the matter more complicated for doped a-Si:H.

¹⁰Note that this corresponds to the deep trapping event in the description of H diffusion.

Figure 2.8: Schematic of PECVD deposition chambers employing (a) inductive coupling of the plasma to the RF source, and (b) capacitive coupling. A setup of the latter type was used to grow the a-Si:H samples analyzed throughout this thesis. Taken from Ref. [253].



methods to impose a non-equilibrium state. The propensity of a material towards forming a stable amorphous structure depends on the mean atomic coordination number. As stated in section 2.1.1, the most stable configuration is obtained with $C = 2.45$ ¹¹. In the case of a-Si with $C = 4$, there is a considerable tendency towards crystallization, which prevents the amorphous structure when quenching from the liquid state¹². The presence of H somewhat lifts the constraints by effectively reducing C , still the formation of a-Si(:H) is only possible by quenching from the gas phase. While a-Si can be grown by sputtering, which is a physical vapor deposition technique, it was found that high-quality hydrogenated amorphous silicon requires chemical processes in the gas phase to facilitate a favorable growth process. This requirement is met by either reactive sputtering or chemical vapor deposition (CVD). The films analyzed in this thesis were made by plasma-enhanced CVD (PECVD).

In this method, silane — often diluted by hydrogen and eventually with an added dopant source such as diborane or phosphine — is decomposed in the gas phase by the help of a low-temperature plasma, which leads to the growth of an a-Si:H film on the substrate usually held at a substrate temperature $T_{\text{sub}} = 150 \dots 250^\circ\text{C}$. Two of the most common means to form the plasma are radio-frequency (RF) excitation and electron-cyclotron resonance (ECR)¹³. Further aspects of the growth setup concern the distance between plasma and substrate, and the eventual use of chemically inert species (such as argon) which are introduced to 'host' the plasma but to not contribute to the a-Si:H growth. The technical details of the growth apparatus used in this study will be presented in section 3.1.2. Here, the general chemical processes common in PECVD growth shall be discussed.

¹¹Consequently, materials close to this value such as amorphous As_2S_3 readily turn into a glass and are difficult to crystallize. Materials with $C < 2.45$ are characterized by an increased configurational entropy and are closer to a liquid state, while for $C > 2.45$ the network is rigid and frustrated, containing an increased enthalpy in the form of strain energy.

¹²In fact this is true for all materials with $C > 3$.

¹³In the former case a diode-like configuration is mostly used, i.e. the plasma being confined between two parallel electrode plates. Alternatively, inductive coupling can be employed, i.e. the plasma burning in a RF-coil (cf. Fig. 2.8). The ECR technique is based on subjecting the precursor gases to a magnetic field while at the same time irradiating microwaves at the ECR frequency to obtain excitation of the precursor molecules. Further CVD methods are the expanding thermal plasma, hot-wire CVD or photo-CVD.

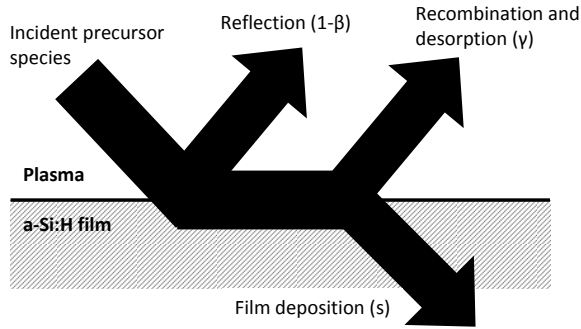


Figure 2.9: Balance of species at the a-Si:H growth front. Precursor molecules are either reflected or get adsorbed at the a-Si:H surface. In the latter case, they can either contribute to growth, recombine with other precursors or desorb from the surface.

Plasma chemistry

The defining property of the plasma used in a-Si:H growth is its non-equilibrium nature. In this context, this term refers to the disproportionality of electron energies being in the 1...10 eV range (corresponding to $T = 10^4 \dots 10^5$ K), and ion/atomic energies in the range of the ambient temperature of the plasma chamber (≈ 500 K). This stems from the fact that due to the high frequency of the exciting RF field, the heavy ions cannot follow the rapid reversal of the \vec{E} field¹⁴, so that the RF energy is only effectively transmitted to the electrons. At the same time, the usual pressures in the millibar range do not suffice to create thermal equilibrium in the gas phase by means of collisions. Therefore the plasma is mainly an electron plasma, while the ions and atoms are close to the ambient temperature equilibrium gas state.

The most important gas phase reaction in the PECVD plasma is the dissociation of SiH_4 by electron impact. The cross sections for the different possible reactions¹⁵ have a threshold electron energy of 8...9 eV, so only the highest-energy electrons contribute. The main reaction is the dissociation, while ionization has a lower cross section. The efficiency of the dissociation channels for the formation of SiH_2 , SiH_3 , SiH and Si product species decreases in that order. However, due to the mean free path being small, collisions of these reaction products occur, most probably with SiH_4 molecules as the overall fraction of ionized/dissociated molecules is small. Due to the formation of larger molecules by the reaction $\text{SiH}_4 + \text{SiH}_2 \rightarrow \text{Si}_2\text{H}_6$ (among others), the SiH_2 is quickly removed, while SiH_3 is more stable concerning secondary reactions. Detailed considerations of primary and secondary reactions and their chemical equilibrium are needed to consistently describe the plasma chemistry, which in addition are varying considerably depending on RF power, H dilution and chamber pressure [152, 154, 201]. However, it was found that for a large range of deposition conditions, SiH_3 is the dominant growth precursor as it is most stable against secondary reactions by collision with SiH_4 [80].

The growth mechanism

The growth process itself comprises two distinct mechanisms: The adsorption of precursor molecules onto the substrate/film surface and the release of atoms or molecules from the surface. As for SiH₃ being the dominant precursor the initial H content is 75% while in typical films 10...20% H content is found, it is obvious that there must be an efficient mechanism for H elimination from the film during growth.

The adsorption properties can best be analyzed in terms of a balance equation, which reads $\beta = s + \gamma$, with the sticking coefficient s and the recombination/desorption coefficient γ add up to the loss probability β [153, 180]. Experimentally, β was found to be ≈ 0.25 , which means that 3/4 of the incident SiH₃ radicals are directly reflected (probability $1 - \beta$). For the sticking coefficient s , a pronounced increase is observed when the H content of the film drops below 10% at very high substrate temperatures. This leads to the conclusion that SiH₃ is captured by dangling Si bonds which increasingly populate the surface for the highest T_{sub} . For $T_{\text{sub}} < 300^\circ\text{C}$ however, the a-Si:H surface was found to be entirely decorated by Si-H bonds, leading to a constant growth rate. Concerning the microscopic mechanism of the amorphous silicon growth, there is still considerable dispute (see e.g. Refs [107, 124, 195] and references therein). Particularly the vertical extent of the growth zone and the connection between growth parameters and resulting a-Si:H bulk properties are matters of discussion [34, 81].

However, there is agreement on the role of the surface diffusion of growth precursors in order to promote a dense film: SiH₃ radicals, adsorbed at Si-H bonds can undergo surface diffusion by hopping motion to adjacent sites. During this process SiH₃ can either encounter a DB with which a covalent bond is formed, and through successive cross-linking with other surface species H₂ is released, or encounter a second SiH₃ molecule to form Si₂H₆ which desorbs, or extract a superficial H atom from a Si-H bond forming a DB and SiH₄ which desorbs. In the common substrate temperature range (150...250°C), the formation of DBs at the surface (the SiH₃ sticking sites) is almost entirely due to H abstraction by SiH₃, while the energy for this endothermic reaction is provided by the exothermic covalent bonding of SiH₃ at DBs occurring in conjugation [180, 196]. Thus, the thermal activation energy is very low and in consequence, the growth rate does not strongly depend on the substrate temperature. For higher substrate temperatures, other processes come into play which are not discussed here.'

How to obtain high-quality a-Si:H

To promote the formation of a dense and structurally relaxed network, a long diffusion pathway of the growth precursors is desirable to facilitate encountering the energetically most favorable sticking sites [152]. The mean surface diffusion length l is given by $l = \sqrt{2D_s\tau_s}$, with the surface diffusion coefficient D_s and the precursor lifetime τ_s . The latter is determined by the growth rate and approximately equal to the time required for deposition of a monolayer. This reduces the problem to maximizing the diffusion

¹⁴The cutoff frequency for the ions lies in the 1...100 kHz range.

¹⁵Possible reactions are the dissociation with different product species, the ionization, or the electronic excitation.

coefficient D_s and illustrates that increasing the growth rate alone will in general lead to inferior film quality. SiH_2 radicals stick with a much higher probability as they can directly insert via $\text{SiH} + \text{SiH}_2 \rightarrow \text{Si-SiH}_3$, meaning that only SiH_3 can have considerable surface diffusion lengths. This leads to the following two requirements for a dense and structurally relaxed film: First, the domination of SiH_3 radicals as growth precursors, and second a high surface diffusion coefficient D_s , most effectively obtained by ensuring a dense coverage of the surface by H atoms. While the former depends on the suited choice of plasma conditions, the latter can be realized by diluting the silane with hydrogen. The extreme case of structural relaxation is the transition from amorphous to microcrystalline growth which is obtained for very high H dilution ratios. Consistent with this (much simplified) discussion, the best quality of a-Si:H films is obtained at conditions close to the microcrystalline transition, which is therefore a target zone for optimized a-Si:H growth. Problematic in the context of a-Si:H as passivation layer is the appearance of undesired epitaxial growth in the plasma regimes close to the transition, particularly on the c-Si{100} surface [51, 84]. This means that in terms of passivation by a-Si:H, two competing aspects have to be balanced: An increased network quality by H dilution, but at the same time an increased propensity towards epitaxy. In practice, this balance is dependent on both surface orientation and topology, rendering the search for optimized passivation a delicate task (see Section 4.2.1).

2.2. Recombination and Passivation

Having discussed the structural and electronic properties of amorphous silicon which is present as an emitter layer in a-Si:H/c-Si heterojunction solar cells, the fundamental aspects of the crystalline silicon absorber shall be introduced now as far as they are important in the context of this thesis. As the thin a-Si:H layers only marginally absorb sunlight, the photogeneration of excess charge carrier pairs will mainly take place in the c-Si. In order to maximize the harvesting of charge carriers which can be extracted and thus contribute to the externally retrievable current, the recombination properties of the crystalline absorber are most important. Note that the amorphous silicon layers contribute to these properties as they provide efficient chemical passivation of the c-Si surface states.

In thermal equilibrium, the carrier density in a semiconductor obeys the fundamental equation $pn \equiv p_0n_0 = n_i^2$. A solar cell operates under non-equilibrium conditions, as the sunlight imposes a certain concentration of charge carriers in excess of the equilibrium densities p_0n_0 . The system approaches equilibrium conditions by recombination of excess electron-hole pairs through different mechanisms, and a steady-state is reached when the generation rate through photon absorption and the sum of the recombination rates cancel. The generation rate is limited by the fixed properties of the solar spectrum and the absorber material, and can only be marginally influenced by means of optical adjustments¹⁶. The recombination rate on the other hand has contributions

¹⁶These include the incorporation of light trapping features and the careful control of thickness and absorption properties of electronically 'dead' layers and contacts in front of the absorber, namely the amorphous silicon and the TCO layer.

from different physical origins and can vary over orders of magnitude. In the following, the mechanisms important in silicon solar cells shall be briefly introduced.

2.2.1. Bulk recombination processes in crystalline silicon

The recombination originating from the silicon bulk comprises intrinsic effects — i.e. processes that also take place in a pure and defect-free semiconductor — and extrinsic contributions stemming from contaminants and defects which act as recombination centers. The two important intrinsic effects are radiative and Auger recombination, while the extrinsic recombination is involving defect states in the band gap and is commonly described by the Shockley-Read-Hall formalism.

Radiative recombination

Radiative recombination is the inverse absorption process, i.e. the conversion of the energy of a conduction band electron into light by relaxation into its ground-state in the valence band. The total radiative recombination rate is proportional to the product of electron and hole concentrations and reads [251]

$$R_{\text{rad}} = Bnp. \quad (2.3)$$

The rate constant B is a property of a given semiconductor material and is fundamentally connected to the absorption coefficient due to the similarity of these two processes. Under equilibrium conditions, the radiative recombination rate is canceled by thermal generation. Thus, the effective radiative recombination is

$$R_{\text{rad,eff}} = B(np - n_i^2). \quad (2.4)$$

For silicon, $B = 10^{-14} \text{ cm}^3\text{s}^{-1}$, which is 4 orders of magnitude smaller as compared to GaAs due to the indirect band gap and the required involvement of a phonon in the recombination process to fulfill momentum conservation [269].

Substituting $n = n_0 + \Delta n$ and $p = p_0 + \Delta p$, one gets

$$U_{\text{rad,eff}} = B(n_0 + p_0)\Delta n + B\Delta n^2. \quad (2.5)$$

With the general equation transforming a recombination rate into a mean 'lifetime' of excess charge carriers,

$$\tau_i = \frac{\Delta n}{U_i}, \quad (2.6)$$

one obtains the radiative lifetime τ_{rad} to be

$$\tau_{\text{rad}} = \frac{1}{B(n_0 + p_0) + B\Delta n}. \quad (2.7)$$

Depending on injection conditions, either of the two summands in the denominator dominates. For the conditions of interests for the operation of solar cells (doping- and excess carrier concentration $< 10^{17} \text{ cm}^{-3}$), $\tau_{\text{rad}} > 10^{-3} \text{ s}$ is always true. Thus other recombination mechanisms are usually more important as will be seen.

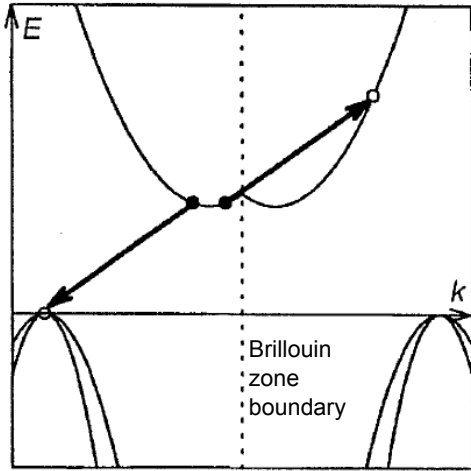


Figure 2.10: Schematic of a direct band-band *eeh*-Auger processes in an indirect semiconductor. Figure taken from Ref. [209].

Auger recombination

The second, and more important, intrinsic recombination mechanism in silicon is the band-band Auger recombination. In this process, the excess energy *and* momentum resulting from a recombination event involving an electron and a hole is transferred to a third (quasi)particle, either electron or hole. The latter particle successively transfers the energy to the lattice, thus converting it into heat (thermalization). Note that in the case of indirect semiconductors, the excitation of the third particle may cross a Brillouin zone boundary (Fig. 2.10). The corresponding net recombination rate (again including the corresponding thermal generation) reads [63]

$$U_{\text{Aug,eff}} = C_n (n^2 p - n_i^2 n_0) + C_p (np^2 - n_i^2 p_0), \quad (2.8)$$

with the two summands accounting for recombination events with two electrons and one hole (*eeh*-Auger processes), and two holes and one electron (*ehh*-Auger processes), respectively. It is obvious that substituting $n = n_0 + \Delta n$ and $p = p_0 + \Delta p$ will result in first and second order terms in n_0 , p_0 and Δn for the Auger lifetime τ_{Aug} . However, it was found in practice that this relationship is only approximately fulfilled, e.g. due to Coulomb-correlation enhanced recombination rates. Details about these phenomena can be found e.g. in Ref. [208]. For practical applications, there are empirical parametrizations of the Auger recombination rate in c-Si. One of the most widespread numerical equations was proposed by Kerr and Cuevas [122], and reads

$$\tau_{\text{Aug}} = \frac{1}{(n_0 + p_0 + \Delta n) (1.8 \times 10^{-24} n_0^{0.65} + 6 \times 10^{-25} n_0^{0.65} + 3 \times 10^{-27} \Delta n^{0.8})}. \quad (2.9)$$

This equation will be used throughout this thesis to quantify the Auger lifetime at a given doping- and injection density.

Shockley-Read-Hall recombination

Besides the two intrinsic recombination mechanisms discussed above, there is an important extrinsic recombination process mediated by defect states in the band gap of

extrinsic origin. These are mainly contaminants, but also lattice defects contribute. The recombination event is a two-step process with successive capture of electron and hole into the defect state, or vice versa. The excess energy is transferred either to phonons or to other charge carriers, or emitted as a photon. It was shown that detailed knowledge about the microscopic mechanism is not necessary and a statistical treatment yields a satisfactory description. A model was first presented by Shockley, Read and Hall (SRH) in 1952 [93, 225], and is widely accepted. It is based on the assumption of a single defect energy level, and each defect state is assumed to be isolated, i.e. no interaction between different trap states is allowed. The latter assumption is sometimes violated in real devices, which will become apparent later in this thesis in chapter 5. The net recombination rate reads

$$U_{\text{SRH,eff}} = \frac{(np - n_i^2)}{\tau_{h0}(n + n_{1,\text{SRH}}) + \tau_{e0}(p + p_{1,\text{SRH}})}, \quad (2.10)$$

where $\tau_{h0} = (\sigma_p v_{\text{th}} N_t)^{-1}$ and $\tau_{e0} = (\sigma_n v_{\text{th}} N_t)^{-1}$ are the characteristic capture times of holes and electrons into the defect state, which depend on the density of traps N_t and the capture cross sections for holes (σ_p) and electrons (σ_n). v_{th} is the thermal velocity of the charge carriers, and $n_{1,\text{SRH}}$ and $p_{1,\text{SRH}}$ are reference quantities for the calculation of the trap state occupation which read

$$n_{1,\text{SRH}} = N_C \exp(E_T - E_C/kT) \quad \text{and} \quad p_{1,\text{SRH}} = N_V \exp(E_V - E_T/kT). \quad (2.11)$$

They are equal to the electron and hole densities that would be present if the Fermi level was at the trap energy level E_T and contain the effective conduction and valence band DOS N_C and N_V . It is important to note that for similar values of the capture cross sections, the recombination rate is highest if the trap state lies in the middle of the band gap. For the SRH lifetime τ_{SRH} one obtains the equation

$$\tau_{\text{SRH}} = \frac{\tau_{h0}(n + n_{1,\text{SRH}}) + \tau_{e0}(p + p_{1,\text{SRH}})}{p_0 + n_0 + \Delta n}. \quad (2.12)$$

Over the 6 decades since the formulation of the SRH theory, a plethora of different possible trap levels was identified in crystalline silicon, of which the most prominent is the donor state resulting from iron contamination ($E_T = 0.375$ eV, $\sigma_n = 1.3 \times 10^{-14}$ cm⁻² and $\sigma_p = 7.0 \times 10^{-17}$ cm⁻² with typical concentrations N_t in the 10^{11} cm⁻³ range [148]). Another very important SRH recombination center is the boron-oxygen complex in Czochralski-grown (CZ) (p)c-Si [23], which however is not relevant in the framework of this thesis and will not be discussed further.

Significance of bulk recombination mechanisms

It is interesting to assess the contribution of these different recombination mechanisms to the overall bulk recombination rate. As the rates corresponding to the different recombination mechanisms add up, it follows from equation 2.6, that

$$\frac{1}{\tau_{\text{bulk}}} = \sum_i \frac{1}{\tau_i} = \frac{1}{\tau_{\text{SRH}}} + \frac{1}{\tau_{\text{Auger}}} + \frac{1}{\tau_{\text{rad}}}. \quad (2.13)$$

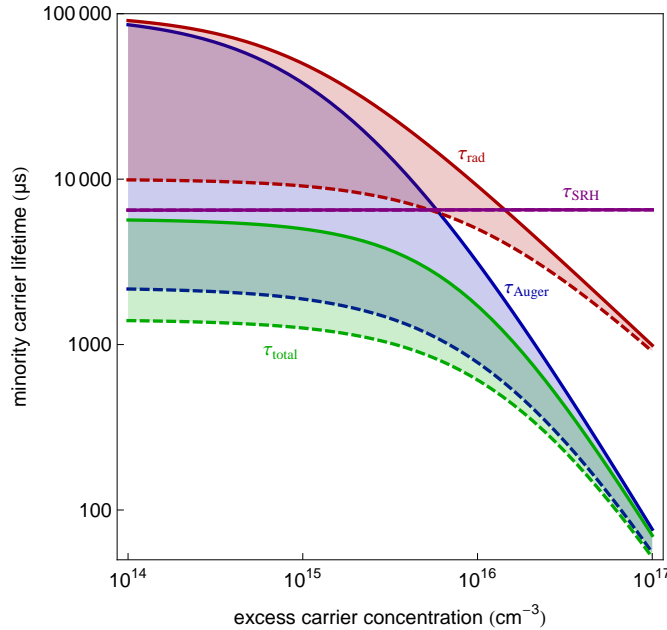


Figure 2.11: Injection dependence of the excess carrier lifetime in an (n)c-Si wafer resulting from different bulk recombination mechanisms. Red: Radiative recombination, blue: Auger recombination, purple: SRH recombination, green: Effective bulk lifetime involving all three mechanisms. The areas of different color denote the variation of the lifetimes with the doping level. Boundaries correspond to 10^{15} cm^{-3} (full lines) 10^{16} cm^{-3} (dashed lines) donor concentration.

From equations 2.7, 2.9 & 2.12 it is obvious that the three recombination rates depend on both doping concentration (controlling n_0 and p_0) and excess charge carrier density Δn . In Fig. 2.11, τ_{bulk} and its three contributions are plotted for an excess carrier range of $10^{14} \dots 10^{17} \text{ cm}^{-3}$ (abscissa) and a doping concentration range of $10^{15} \dots 10^{16} \text{ cm}^{-3}$ (filled areas in the plot, full lines represent the 10^{15} cm^{-3} boundary and dashed lines mark 10^{16} cm^{-3}) for an (n)c-Si wafer with an iron concentration of $N_t = 2 \times 10^{11} \text{ cm}^{-3}$. The Δn range relevant for c-Si solar cells is $10^{15} \dots 10^{16} \text{ cm}^{-3}$, as will be shown later. The plot reveals some important facts: The radiative lifetime (red) is always larger than the Auger lifetime, with the difference decreasing for lower doping- and excess carrier concentrations. However, in the Δn range of interest here, Auger recombination always dominates and therefore τ_{rad} will be omitted from here on¹⁷.

The SRH lifetime is injection- and doping-independent for the parameter range of interest here, it will therefore be considered to be constant in the following. The bulk lifetime (green) is in large parts of the parameter space dominated by the Auger lifetime, particularly for high injection- and doping levels. Typical substrates used in this study were (n)c-Si with $1 \Omega\text{cm}$ resistivity (corresponding to $5 \times 10^{15} \text{ cm}^{-3}$ dopant concentration) and a SRH lifetime of $> 10 \text{ ms}$ as specified by the vendor. It is found that for those substrates and an excess carrier density of 10^{16} cm^{-3} which is typical for well-passivated c-Si under 1 sun illumination, τ_{bulk} and τ_{Auger} differ by not more than 30%.

¹⁷Although this procedure is common and does not lead to large errors, it has to be noted that the radiative recombination rate is still a useful (and significant) quantity: By monitoring the radiative recombination leading to so-called 'photoluminescence' (PL), the contribution of the non-radiative recombination mechanisms to the overall recombination can be assessed [261].

2.2.2. Specifics of amphoteric dangling bonds in a-Si:H

In amorphous silicon, the SRH recombination statistics do not apply in their original form, as the dangling bond defects — representing the dominant share of recombination-active defects — can accommodate three charge states (positive, neutral and negative, termed D^+ , D^0 and D^-) [104, 212, 253]. In consequence, two different energy levels are relevant for the treatment of the recombination statistics: The processes involving only a singly occupied dangling bond ($D^+ + e \rightarrow D^0$, $D^0 \rightarrow D^+ + e$, $D^0 + h \rightarrow D^+$ or $D^+ \rightarrow D^0 + h$) have the reference energy level $E^{+/0}$, while the processes involving also a doubly occupied dangling bond ($D^0 + e \rightarrow D^-$, $D^- \rightarrow D^0 + e$, $D^- + h \rightarrow D^0$ or $D^0 \rightarrow D^- + h$) have a reference energy $E^{0/-} = E^{+/0} + U$ shifted upwards by the effective correlation energy U . There are probability distribution functions F^i for the occupancy of the three charge states, which read [212]

$$F^+ = \frac{P^- P^0}{N^0 N^+ + N^+ P^- + P^- P^0} \quad (2.14)$$

$$F^0 = \frac{N^+ P^-}{N^0 N^+ + N^+ P^- + P^- P^0} \quad (2.15)$$

$$F^- = \frac{N^0 N^+}{N^0 N^+ + N^+ P^- + P^- P^0}, \quad (2.16)$$

with the parameters of the occupation functions

$$N^0 = v_{\text{th}} \left[\sigma_n^0 n + \sigma_p^- N_V / 2 \exp [(E_V - E - U)/kT] \right] \quad (2.17)$$

$$N^+ = v_{\text{th}} \left[\sigma_n^+ n + 2\sigma_p^0 N_V \exp [(E_V - E)/kT] \right] \quad (2.18)$$

$$P^0 = v_{\text{th}} \left[\sigma_p^0 p + \sigma_n^+ N_C / 2 \exp [(E - E_C)/kT] \right] \quad (2.19)$$

$$P^- = v_{\text{th}} \left[\sigma_p^- p + 2\sigma_n^0 N_V \exp [(E + U - E_C)/kT] \right]. \quad (2.20)$$

This 'amphoteric nature' of the trap states facilitating recombination in amorphous silicon alters the recombination statistics, and leads to the following expression for the recombination rate $U_{\text{a-Si:H}}$:

$$U_{\text{a-Si:H}} = v_{\text{th}} N_D \frac{(np - n_i^2) (\sigma_n^0 \sigma_p^- N^+ + \sigma_p^0 \sigma_n^+ P^-)}{N^0 N^+ + N^+ P^- + P^- P^0}, \quad (2.21)$$

with the occupation parameters as defined above and the dangling bond defect density N_D . The a-Si:H bulk lifetime is lower by orders of magnitude than normal c-Si bulk lifetimes for typical dangling bond concentrations. Thus, the amorphous layers in the a-Si:H/c-Si structure can be considered 'dead' in terms of charge carrier generation without considering the recombination dynamics in detail: Excess charge carriers generated in the a-Si:H recombine before they can be extracted. However, the a-Si:H is important for the c-Si recombination properties as it determines the a-Si:H/c-Si interface recombination. In consequence, the amphoteric recombination statistics are involved in modeling the recombination properties of the heterointerface.

2.2.3. Surface/interface recombination

The discontinuity in the covalent bond network present at semiconductor surfaces is a dominant source of defect states. In the case of silicon, these states are found around the middle of the band gap and are therefore efficient recombination centers. The recombination through interface defects is calculated similar to the SRH formalism for bulk defects, but refers to a rate per unit area. As the traps are usually distributed across a certain energy range in the band gap, an integration is performed. However, for each individual interface defect it is assumed that interaction — i.e. trapping or emission of carriers — can only proceed with the bands, and not with the other interface defects, consistent with the SRH formalism. The net interface recombination rate reads [208]

$$U_S = v_{\text{th}} \left(n_S p_S - n_i^2 \right) \int_{E_V}^{E_C} \frac{D_{it}(E) dE}{(n_S + n_{1,\text{SRH}}(E)) / \sigma_p + (p_S + p_{1,\text{SRH}}(E)) / \sigma_n}, \quad (2.22)$$

with the electron- and hole concentrations at the surface n_S, p_S . It is important to note that the reference concentrations $n_{1,\text{SRH}}$ and $p_{1,\text{SRH}}$ are energy-dependent, while the capture cross sections are assumed to be energy-independent here. Instead of a lifetime, a 'surface recombination velocity' S is calculated from the net recombination rate:

$$S = \frac{U_S}{\Delta n} \quad (2.23)$$

In the case of amphoteric surface defect states, Eq. 2.22 would have to be modified accordingly, making use of equation 2.21 to implement the amphoteric formalism instead of SRH recombination statistics. This is done in detailed models for c-Si surface/interface recombination, based on the assumption that the surface/interface dangling bonds can also accommodate three charge states (Refs. [142, 173] and cf. section 2.2.6).

2.2.4. Semiconductor physics

In this section it will be briefly shown how the different contributions to the recombination of excess charge carriers are combined in a consistent way in order to model the behavior of a solar cell device. Only the open-circuit case shall be treated here, while transport equations under external bias are considered in the next section. First, the set of equations necessary to describe a general semiconductor in one dimension is given.

The basic semiconductor equations

The charge carrier dynamics in a semiconductor are governed by the following three basic equations:

1. The **current equations** for electrons and holes read

$$j_e(x) = en(x)\mu_e E(x) + eD_n \frac{dn(x)}{dx} \quad \text{and} \quad j_h(x) = ep(x)\mu_h E(x) + eD_p \frac{dp(x)}{dx}, \quad (2.24)$$

with the diffusion constants being related to the mobilities by Einstein's relation:

$$D_n = \frac{kT}{e} \mu_e \approx 30 \text{ cm}^2 \text{ s}^{-1} \quad \text{and} \quad D_p = \frac{kT}{e} \mu_h \approx 12 \text{ cm}^2 \text{ s}^{-1} \quad \text{for c-Si.} \quad (2.25)$$

The two summands in equation 2.24 are usually termed 'drift current' (caused by electric fields) and 'diffusion current' (caused by the gradient of the carrier concentration).

2. The electric field E driving the drift current results from the charges in the semiconductor, which is found in the electrons and holes as well as in the dopant ions. The balance of charges is the source term in **Poisson's equation** which yields the electric field:

$$\frac{dE(x)}{dx} = \frac{e}{\epsilon\epsilon_0} (p(x) - n(x) + N_D(x) - N_A(x)), \quad (2.26)$$

with N_D and N_A being the densities of donor and acceptor ions.

3. Lastly, the **continuity equation** balances the gain and loss of charge carriers at a given point due to current flow, generation and recombination:

$$\frac{1}{e} \frac{dj_e(x)}{dx} = \frac{1}{e} \frac{dj_h(x)}{dx} = \sum_i U_i(x) - G(x), \quad (2.27)$$

with the generation rate $G(x)$ and the sum over the recombination rates $U_i(x)$, which are generally position-dependent. In a solar cell, the generation term is usually caused by absorption of light and then has the form

$$G(x) = - \int_{\lambda=0}^{\infty} \frac{d}{dx} \Phi_0(\lambda) \exp[-\alpha(\lambda)x] d\lambda = \int_{\lambda=0}^{\infty} \alpha(\lambda) \Phi_0(\lambda) \exp[-\alpha(\lambda)x] d\lambda, \quad (2.28)$$

with the wavelength-dependent photon flux $\Phi_0(\lambda)$ and the absorption coefficient $\alpha(\lambda)$. There are other equations for G in different situations, e.g. in the presence of back-side reflection or for the case of electron-beam-induced generation as used for solar cell device analytics.

2.2.5. From minority carrier lifetime to V_{oc} — a simple test case

In the following, a simple solution of the equations presented above shall be briefly discussed, allowing to assess the interplay of the different parameters. Further, the impact of different recombination parameters on the open-circuit voltage V_{oc} is highlighted.

Without loss of generality it is assumed that the semiconductor is n-doped. For p-doped materials, the equations have to be modified accordingly. The carrier concentrations are given by $n = n_0 + \Delta n$ and $p = p_0 + \Delta n$, while in a doped n-type semiconductor the equilibrium carrier concentrations n_0 and p_0 are given by [108]

$$\begin{aligned} n_0 &= 2N_D \left(1 + \sqrt{1 + 4N_D/N_C \exp[(E_{\text{don}} - E_C)/kT]} \right)^{-1} \underset{\text{at room } T}{\approx} N_D \\ p_0 &= n_i^2/n_0 \\ n_i &= \sqrt{N_C N_V} \exp\left[-\frac{E_g}{2kT}\right], \end{aligned} \quad (2.29)$$

with the band gap of crystalline silicon $E_g = 1.12$ eV and the energy of the donor state E_{don} . The semiconductor shall be field-free, thus $E = 0$. In the absence of electric fields

and thus band bending, $\Delta n(x) = \Delta p(x)$ holds in a large part of the parameter space. A possible violation of this condition can result from the unequal diffusion constants of electrons and holes, leading to the appearance of the so-called 'Dember voltage' [59] which can be significant if $\Delta n \gg N_{\text{dope}}$. Under the conditions considered here, $\Delta n(x) = \Delta p(x)$ is fulfilled and the problem is reduced to solving a differential equation valid for *both* carrier types, the so-called ambipolar transport equation, with an effective ambipolar diffusion constant D_{eff} containing the diffusion constants of electrons and holes 'lumped' into one quantity [198]. Equations 2.24 and 2.27 can be combined to yield a diffusion equation with source terms, which describes the dynamics of the excess carrier density Δn :

$$D_{\text{eff}} \frac{\partial^2 \Delta n(x, t)}{\partial x^2} - \frac{\partial \Delta n(x, t)}{\partial t} + G(x, t) - \Delta n(x, t) \left(\frac{1}{\tau_{\text{SRH}}} + \frac{1}{\tau_{\text{Auger}}} \right) = 0. \quad (2.30)$$

The steady-state solution for this equation can be obtained by numerically solving it with $\partial_t n(x, t) = 0$, and two boundary conditions which specify the recombination currents occurring at the surfaces:

$$\begin{aligned} j|_{x=0} &= eD_{\text{eff}} \left. \frac{d\Delta n(x)}{dx} \right|_{x=0} = eS_{\text{front}} \Delta n(x) \\ -j|_{x=d} &= eD_{\text{eff}} \left. \frac{d\Delta n(x)}{dx} \right|_{x=d} = eS_{\text{back}} \Delta n(x), \end{aligned} \quad (2.31)$$

with the two surface recombination velocities S_{front} and S_{back} . Note that the sign of the recombination current at the right surface has to be inverted to ensure that both surfaces act as sinks for excess carriers. The equations 2.28 through 2.31 represent a consistent set which can be solved for Δn when the irradiated spectrum Φ_0 and the absorption characteristics of the semiconductor are known. The excess carrier density $\Delta n(x)$ is a rather abstract quantity, but can be related to a fundamental parameter of the solar cell under certain conditions: Provided that 'ideal' contacts are used and $\Delta n(x)$ is spatially homogeneous, the maximum open-circuit voltage that can be realized with a given photovoltaic absorber and illumination situation ('implied V_{oc} ') is equal to the splitting of the electron- and hole-quasi-Fermi levels $E_{F,n}$ and $E_{F,p}$. From the definition of the Fermi function results immediately:

$$\begin{aligned} n &= n_0 + \Delta n = n_i \exp \left[\frac{E_{F,n} - E_i}{kT} \right] \Leftrightarrow \log \left[\frac{n_0 + \Delta n}{n_i} \right] = \frac{E_{F,n} - E_i}{kT} \\ p &= p_0 + \Delta n = n_i \exp \left[\frac{E_i - E_{F,p}}{kT} \right] \Leftrightarrow \log \left[\frac{p_0 + \Delta n}{n_i} \right] = \frac{E_i - E_{F,p}}{kT}, \end{aligned} \quad (2.32)$$

with the intrinsic Fermi level E_i . Combining these equations yields

$$eV_{\text{oc},i} = E_{F,n} - E_{F,p} = kT \log \left[\frac{(n_0 + \Delta n)(p_0 + \Delta n)}{n_i^2} \right], \quad (2.33)$$

which relates the maximum possible V_{oc} to the excess carrier density Δn provided the latter is homogeneous across the absorber.

As a test case, equations 2.28 through 2.31 were numerically solved with a varying τ_{SRH} and a varying $S = S_{\text{front}} = S_{\text{back}}$ for a situation typical for solar cell operation: The crystalline silicon absorption coefficient α was employed as well as Φ_0 according to the AM1.5 solar spectrum after passing through a 75 nm SiN dielectric¹⁸. The Auger lifetime τ_{Aug} was parametrized according to equation 2.9. An (n)c-Si wafer with 1 Ωcm resistivity and thickness $d = 200 \mu\text{m}$ was assumed, as typically used for a-Si:H/c-Si solar cells. Figure 2.12 shows the resulting steady-state excess carrier density at $x = d/2$ (upper left panel), the inhomogeneity of $\Delta n(x)$ across the wafer in % (upper right panel) and the implied V_{oc} as calculated with equation 2.33 (lower left panel). The lower right panel shows the so-called 'effective lifetime', which is defined as

$$\frac{1}{\tau_{\text{eff}}} = \frac{1}{\tau_{\text{SRH}}} + \frac{1}{\tau_{\text{Auger}}} + \frac{2S}{W}. \quad (2.34)$$

It can be shown that this equation is a good approximation (valid if $SW/D_{n/p} < 1/4$) for the empirical quantity $\tau_{\text{eff,meas}} = \Delta n(t)/\partial_t \Delta n(t)$, which can be measured by different 'minority carrier lifetime spectroscopy' methods, e.g. by photoconductance decay (cf. section 3.3.1).

From Figure 2.12 it is obvious that the assumption of a homogeneous excess carrier concentration Δn is approximately fulfilled for a large fraction of the parameter space. Only for the highest surface recombination velocities ($S \geq 100 \text{ cm/s}$), the surface concentration of Δn is significantly reduced resulting in inhomogeneities. Thus, the Δn and V_{oc} values in the case of $S < 100 \text{ cm/s}$ are trustworthy. It is obvious that the overall trends of Δn and V_{oc} are similar (as would be expected from equation 2.33). In addition, though not easily visible from Fig. 2.12, it is found that V_{oc} is approximately proportional to $\log(\tau_{\text{eff}})$.

Figure 2.12 allows to draw some important conclusions for the design of solar cell devices. First of all it can be noted that for bulk lifetimes $< 1 \text{ ms}$, V_{oc} is decreasing fast. The same is true for surface recombination velocities $> 10 \text{ cm/s}$. The stagnation of V_{oc} in the region of $\tau_{\text{bulk}} > 1 \text{ ms}$ and $S < 10 \text{ cm/s}$ on the other hand is caused by the domination of Auger recombination in this region, rendering it literally impossible to reach $\Delta n > 10^{16} \text{ cm}^{-3}$ under one sun illumination. It becomes obvious that in order to obtain V_{oc} values in the range of the Sanyo record HIT cell (displaying 729 mV), surface recombination velocities as low as the order of 1 cm/s have to be realized.

It is important that in real devices a band bending towards the boundaries of the c-Si absorber is usually present which reduces the impact of the surface defects, as will be explained in the following.

¹⁸This is a typical front-side anti-reflection coating and results in slight losses in the UV region

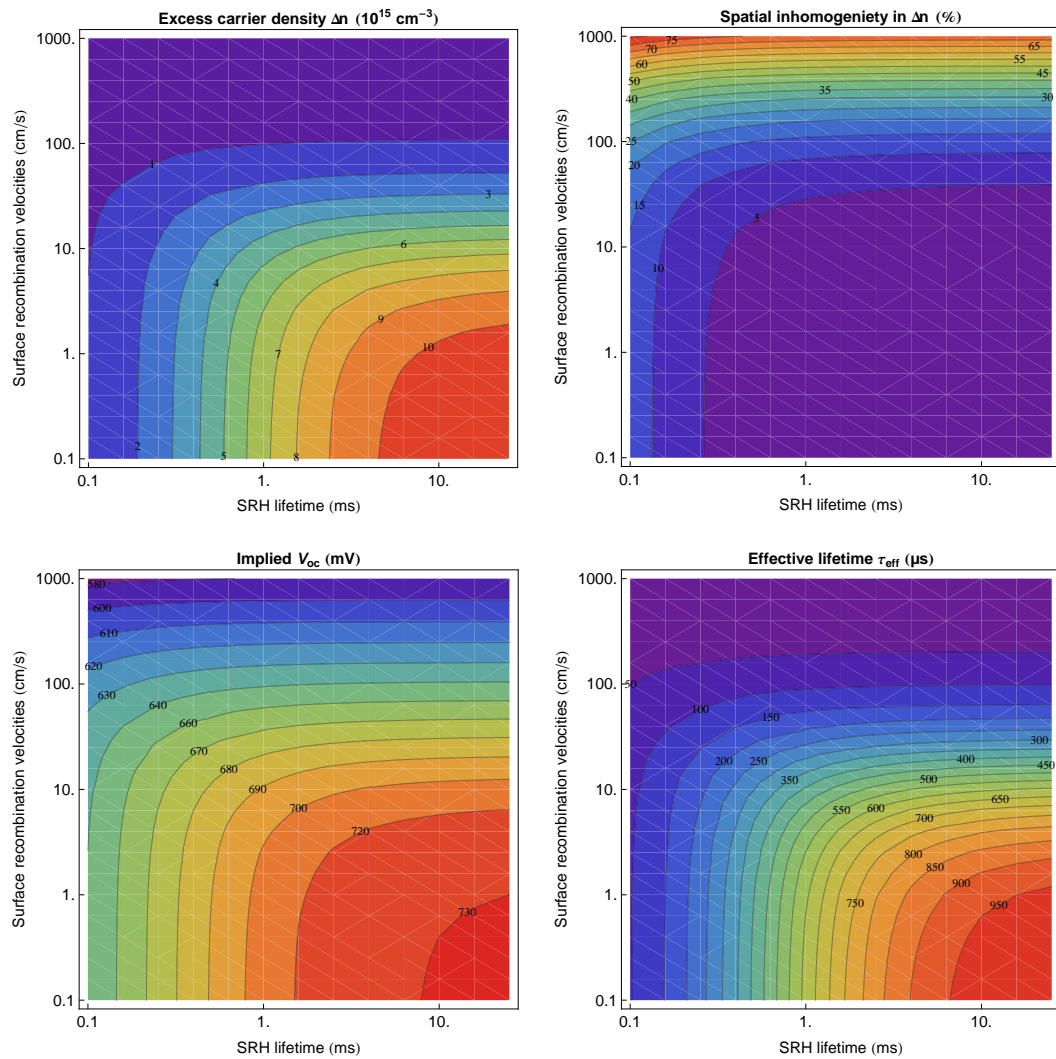


Figure 2.12.: Visualization of the numerical steady-state solution of the semiconductor equations under illumination. Parameters were the surface recombination velocity $S = S_{\text{front}} = S_{\text{back}}$ and the Shockley-Read-Hall lifetime τ_{SRH} . Upper left panel: Excess carrier density Δn ; upper right panel: Homogeneity in Δn ; lower left panel: Implied V_{oc} ; lower right panel: Effective lifetime τ_{eff} .

2.2.6. Looking further: The presence of band bending

Semiconductor modeling with band bending

In the calculation presented above, $E = 0$ was assumed. In reality however, even without external bias and in equilibrium, $E = 0$ is not true at every point and thus the energy bands in a semiconductor are most likely not constant: At unpassivated c-Si surfaces, the Fermi level is usually pinned in the abundant surface defect states near mid-gap. If the surfaces are covered by other materials, an electric field can result from fixed charges in dielectric top layers, or by the requirements of charge neutrality in a semiconductor heterojunction. The first scenario is very common in silicon semiconductor devices, where SiO_2 (carrying positive fixed charges in the 10^{11} cm^{-3} range) is used as gate dielectric in field-effect transistors. In classical c-Si solar cells, SiN_x (carrying positive fixed charges in the 10^{12} cm^{-3} range) is commonly used as a dielectric coating with anti-reflection properties, while Al_2O_3 (carrying negative fixed charges in the 10^{12} cm^{-3} range) is currently emerging as passivating dielectric in c-Si based solar cells. Further and most importantly, in a-Si:H/c-Si structures a c-Si band bending is found depending on the Fermi level position in the a-Si:H, which is defined by the a-Si:H doping concentration and/or the composition of an a-Si:H layer stack.

In all cases involving band bending, the assumption $\Delta n(x) = \Delta p(x)$ is violated in the region with bent bands, which significantly complicates the calculation of surface recombination rates. In principle, the Poisson- and continuity equations have to be simultaneously solved with boundary conditions, and a closed-form expression of $S(\Delta n)$ similar to equation 2.23 does not exist under those circumstances. However, there are simplified approaches which have proven useful for the calculation of surface recombination in the presence of band bending. Among these are the works of Grove and Fitzgerald [89] and Girisch [85], and newer works which extend the capabilities of the Girisch model by including amphoteric occupation statistics [142, 173]. These models share the implementation of a charge balance formalism, where the charge resulting from uncompensated dopants and charged interface defects balances an assumed fixed charge outside the c-Si. While this approach is well-tailored for the description of dielectrics actually *carrying* a fixed charge, difficulties may arise in the a-Si:H/c-Si system where the charge in the amorphous layer can be altered depending on injection conditions. There are current activities at HZB aiming at explicitly including the particular properties of the a-Si:H/c-Si system, which would require a self-consistent and injection-dependent calculation of the charge balance [142].

Impact on the effective lifetime

It is important to note that the presence of band bending introduces an additional degree of freedom which can be exploited in order to reduce the interface recombination rate. If the band bending is directed such that the minority carriers are repelled from the defective surface, a net decrease in the recombination rate results as compared to the flat band case. This is the case in the commonly employed 'back-surface field' at solar cell back sides, where a local increase in the absorber doping concentration creates an additional 'dip' in the band structure. For very high concentrations of fixed charges in a

dielectric layer, the polarity is not important as the c-Si can locally be driven into inversion, resulting in repelling the majority carriers. This effect is used in SiN_x coatings or Al₂O₃ films which are commonly employed providing so-called 'field-effect passivation'. Thus, a decrease in surface recombination velocity — and in consequence, an increase in effective lifetime — can be caused by either a low density of recombination-active surface defects or by an increase of the field effect repelling the right type of charge carrier.

In practice, the impact of both aspects can be distinguished with the help of the mentioned semiconductor models incorporating the field effect. The commonly employed 'lifetime spectroscopy' by transient photoconductance decay measurements yields a dataset of $\tau_{\text{eff,meas}}(\Delta n)$ values, which can be fitted with a suitable model. While the density of interface states D_{it} leads to a global up- or downward shift of the $\tau_{\text{eff,meas}}(\Delta n)$ curve, the impact of the field effect is injection-dependent: For high injection levels, the bands are flattened as the mobile excess charge carriers are relocated and thus effectively shield the fixed charges, which reduces the passivating field effect. Thus, a band bending will predominantly impact the low Δn range and leads to a tilting of the $\tau_{\text{eff,meas}}(\Delta n)$ curve. By fitting the $\tau_{\text{eff,meas}}(\Delta n)$, a discrimination of both effects and thus quantitative analysis of the contributions to the passivation is generally possible [141]. Details of the method employed to analyze the effective lifetime data in this thesis will be discussed in section 3.3.1.

2.3. Electronic transport

In this section, the semiconductor equations as presented and exemplarily solved for a non-contacted structure above shall be very briefly linked to the behavior of a solar cell device under external bias and illumination. The treatment will be rudimentary, as the derivation of the respective equations is textbook material. The interested reader shall be directed to e.g. Refs. [88, 251].

2.3.1. From the semiconductor equations to the ideal diode

The prototypical solar cell device is the silicon-based homojunction p/n diode. It is instructive to review the underlying assumptions and resulting properties, as they are important for solar cells. In addition it will be found that also in the presence of a space-charge region, the diffusion of carriers in the neutral bulk and thus the recombination properties of the material play an important role for carrier transport.

Near the actual junction of the p/n diode, the majority carriers of both parts of the diodes recombine when combining the two parts in a gedankenexperiment, leaving the fixed charge of the dopant ions in this region uncompensated. This leads to the built-in potential and the characteristic bending of the bands. In consequence, the device consists of large regions of flat bands in the bulk of both p- and n-material, and a small region where the bands are bent and the carrier concentrations change rapidly. In the quantitative treatment of p/n junctions, ideally sharp edges of this 'depletion region' are usually assumed. An externally applied voltage will only impact the potential drop over this depletion region. From the requirement of space-charge neutrality and the

continuity equation it is found that the minority carrier concentrations at the edges of the space charge region depend exponentially on the applied bias voltage V (indices denote the doping type of the respective region):

$$p_n|_{\text{edge}} = p_{n0} \exp\left[\frac{qV}{kT}\right] = \frac{n_i^2}{N_d} \exp\left[\frac{qV}{kT}\right], \quad (2.35)$$

$$n_p|_{\text{edge}} = n_{p0} \exp\left[\frac{qV}{kT}\right] = \frac{n_i^2}{N_a} \exp\left[\frac{qV}{kT}\right]. \quad (2.36)$$

The current which can flow through the device now depends on the diffusion of the carriers in the neutral regions. To calculate the current flow, the carrier concentrations have to be obtained by solving the diffusion equation without source terms (obtained again combining equations 2.24 and 2.27):

$$D_p \frac{d^2 \Delta p(x)}{dx^2} - \frac{\Delta p(x)}{\tau_p} = 0 \Leftrightarrow \frac{d^2 \Delta p(x)}{dx^2} - \frac{\Delta p(x)}{L_p^2} = 0, \quad (2.37)$$

$$D_n \frac{d^2 \Delta n(x)}{dx^2} - \frac{\Delta n(x)}{\tau_n} = 0 \Leftrightarrow \frac{d^2 \Delta n(x)}{dx^2} - \frac{\Delta n(x)}{L_n^2} = 0, \quad (2.38)$$

with the diffusion lengths $L_n = \sqrt{D_n \tau_n}$ and $L_p = \sqrt{D_p \tau_p}$. These equations have the general solutions for holes and electrons

$$p_n(x) = p_{n0} + p_{n0} \left(\exp\left[\frac{qV}{kT}\right] - 1 \right) \exp[-x/L_p], \quad (2.39)$$

$$n_p(x') = n_{p0} + n_{p0} \left(\exp\left[\frac{qV}{kT}\right] - 1 \right) \exp[-x'/L_n], \quad (2.40)$$

where x and x' are zero at the edges of the depletion region on the p- and n-side, respectively. Now, the current equation is solved for both holes and electrons:

$$j_h(x) = -eD_p \frac{dp(x)}{dx} = \frac{eD_p p_{n0}}{L_p} \left(\exp\left[\frac{qV}{kT}\right] - 1 \right) \exp[-x/L_p], \quad (2.41)$$

$$j_e(x') = -eD_n \frac{dn(x)}{dx} = \frac{eD_n n_{p0}}{L_n} \left(\exp\left[\frac{qV}{kT}\right] - 1 \right) \exp[-x'/L_n]. \quad (2.42)$$

The crucial step is now to obtain the electron and hole current at the same position $x = x'$. Under the assumption that the recombination in the space charge region is insignificant and thus $j_h(x) \approx j_h(x')$ and $j_e(x) \approx j_e(x')$, the previous two equations can be linked to yield:

$$\begin{aligned} j_{\text{total}} &= j_h(x=0) + j_e(x'=0) = \left(\frac{eD_p p_{n0}}{L_p} + \frac{eD_n n_{p0}}{L_n} \right) \left(\exp\left[\frac{qV}{kT}\right] - 1 \right) \\ &= \left(\frac{eD_p n_i^2}{N_d L_p} + \frac{eD_n n_i^2}{N_a L_n} \right) \left(\exp\left[\frac{qV}{kT}\right] - 1 \right) \equiv j_0 \left(\exp\left[\frac{qV}{kT}\right] - 1 \right), \end{aligned} \quad (2.43)$$

with the so-called saturation current density j_0 . As due to the continuity of charge carriers the total current must be constant across the device, this equation also described

the current density at the terminals. It is known as the 'ideal diode equation' and was first derived by Shockley [225]. Thus it is obvious that under the assumptions of an abrupt depletion region with small recombination rate¹⁹ the current through a p/n junction diode depends exponentially on the applied bias. Interestingly, the behavior of the diode is decisively affected by the recombination properties of the material, as the largest part of the semiconductor is field-free and thus transport proceeds only by diffusion. The recombination properties are reflected in the diffusion lengths L_n and L_p of the minority carriers in their respective regions. In the presence of interface- or surface recombination, the diffusion lengths can be substituted by effective diffusion lengths incorporating the effective lifetime and diffusion constant by $L_{\text{eff}} = \sqrt{D_{\text{eff}}\tau_{\text{eff}}}$ [112].

It has to be noted that the assumption of vanishing recombination in the space-charge region is often violated under realistic conditions. In this case, the forward current behavior is changed to a non-ideal type according to

$$j_{\text{total}}(V) = j_0' \left(\exp \left[\frac{qV}{n_d kT} \right] - 1 \right), \quad (2.44)$$

with the ideality factor n_d and the saturation current density j_0' . In the framework of the theoretical description by Sah, Noyce and Shockley [203], $n = 2$ holds and $j_0' \propto n_i$. Note that the temperature dependence of the saturation current density is different from the ideal diode due to the different power of n_i being involved. Therefore, these two cases in the charge carrier transport can be distinguished by analyzing temperature-dependent current-voltage curves, and the diode ideality factor n_d .

2.3.2. The diode under illumination

It can be shown that under typical illumination conditions, the dark current-voltage characteristics is, to a good approximation, shifted on the current axis by the value of the photogenerated current j_{phot} [88]:

$$j_{\text{total}}(V) = j_0 \left(\exp \left[\frac{qV}{n_d kT} \right] - 1 \right) - j_{\text{phot}}. \quad (2.45)$$

Here, the general equation comprising a diode ideality factor was used. In the simplest case of a homogeneous generation rate, $j_{\text{phot}} = eG(d_{\text{depl}} + L_n + L_p)$ holds, with d_{depl} being the width of the depletion region. As $d_{\text{depl}} \ll W$ is true in solar cells, it is obvious that diffusion lengths in the order of the wafer thickness W are mandatory in order to extract the photogenerated charge carriers. Although in realistic cases the generation rate is position-dependent as considered in the previous section, this conclusion stays valid.

Solar cell current-voltage characteristics ('I/V curves') under illumination are analyzed making use of three fundamental parameters: The short-circuit current density j_{sc} is

¹⁹An additional assumption is that minority carrier densities are much lower than majority carrier densities.

trivially found to be $j_{sc} \equiv j_{total}(V = 0) = j_{phot}$. The open-circuit voltage V_{oc} is obtained by solving $j_{total}(V_{oc}) = 0$ for V_{oc} :

$$V_{oc} = \frac{n_d k T}{e} \log \left[\frac{j_{phot}}{j_0} - 1 \right] \approx \frac{n_d k T}{e} \log \left[\frac{j_{phot}}{j_0} \right]. \quad (2.46)$$

Lastly, the fill factor is defined as the quotient of the area in the I/V plane defined by the point of maximum output power $\{V_{mpp}, j_{mpp}\}$ and the area spanned by $\{V_{oc}, j_{sc}\}$:

$$FF = \frac{V_{mpp} j_{mpp}}{V_{oc} j_{sc}}. \quad (2.47)$$

Consistently, the conversion efficiency of the solar cell can be calculated by

$$\eta = \frac{V_{mpp} j_{mpp}}{p_{in}} = \frac{V_{oc} j_{sc} FF}{p_{in}}, \quad (2.48)$$

with the incident power density of the light p_{in} .

2.4. The a-Si:H/c-Si heterojunction: A very brief introduction

The current work is concerned with heterojunctions consisting of amorphous silicon layers with a thickness of the order of 10 nm on crystalline silicon substrates. In this section, the state of knowledge on this structure and the fundamental questions related to it shall be briefly reviewed.

The resulting band lineup is sketched in Fig. 2.13, where the general features are visible: Due to the band gap of a-Si:H and c-Si differing by about 0.5 . . . 0.7 eV, offsets between the conduction- and valence bands of a-Si:H and c-Si are present. The state of knowledge is that the valence band offset is larger than the conduction band offset by a factor of 2 . . . 3 [20]. This asymmetry in the band lineup can be understood from a fundamental point of view employing the concept of so-called 'charge neutrality levels' for both a-Si:H and c-Si, which are aligned in forming the heterojunction [135, 167, 257, 258]. The band bending in the structure adjusts such that charge neutrality is fulfilled, just as for c-Si homojunctions. Due to the large density of rechargeable states in a-Si:H, the band bending supported on the a-Si:H side is small as the electric field stemming from the c-Si dopant ions is shielded already close to the heterointerface. Thus, the bands in the a-Si:H are comparably flat, while the c-Si supports most of the overall band bending [202].

In a homojunction, the built-in potential amounts to $\Psi_{bi} = kT/e \log [N_A N_D / n_i^2]$, as can be derived from equation 2.32, with N_A and N_D being the doping concentrations on both sides of the junction. It is obvious that in order to ensure efficient separation of excess charge carriers by imposing a large Ψ_{bi} , the doping concentrations would have to be maximized. This, on the other hand, increases the recombination in the c-Si bulk. The resulting bulk recombination in the highly doped emitter regions limits the V_{oc} to about 650 mV for c-Si homojunctions²⁰ [87].

²⁰Note that the recombination at the usually employed direct Al contacts also contributes significantly to the overall recombination in c-Si solar cells.

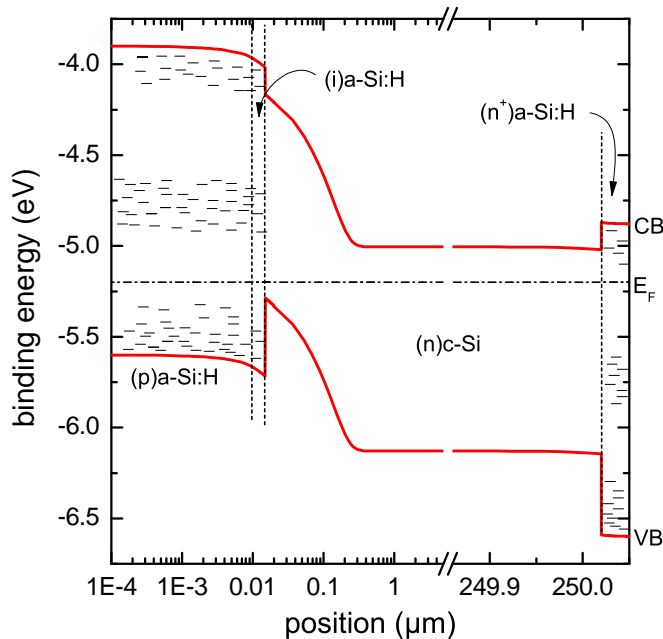


Figure 2.13: Band structure of an a-Si:H/c-Si heterojunction solar cell based on an (n)c-Si substrate as calculated with the numerical device simulator AFORS-HET [241, 242]. Small horizontal lines schematically indicate high densities of localized states. General features of the band lineup are a small fraction of the overall band bending found in the a-Si:H layers, asymmetric band offsets, and the functioning of the back-side a-Si:H as a back-surface field being mainly provided by the band offsets and not by a pronounced c-Si band bending.

In a heterojunction, the Fermi level in the wide-band gap material does not need to be brought as close to the bands to yield the same overall band bending, due to the band offsets. Although the a-Si:H Fermi level is pinned in the localized tail states already some 100 meV away from the band edges when increasing the doping level, this fact — together with the inherent asymmetry of the distribution of band bending in the heterojunction — leads to the possibility of imposing a larger c-Si band bending for a given c-Si dopant concentration as compared to the c-Si homojunction²¹. In SHJ solar cells, c-Si doping concentrations around $10^{15} \dots 10^{16} \text{ cm}^{-3}$ can be employed, leading to a much higher c-Si minority carrier lifetime, which contributes to a higher V_{oc} potential. The second crucial ingredient for the high V_{oc} potential is the outstandingly high potential for c-Si surface passivation by amorphous silicon, provided particularly by undoped a-Si:H. Surface recombination velocities well below 5 cm/s have been reported for (i)a-Si:H layers [51, 52, 55, 58, 166, 214, 218], and if made thin enough an undoped a-Si:H buffer layer seems not to significantly affect the charge carrier transport across the heterojunction [50]. Thus, combined with the advantageously low c-Si bulk recombination rates due to small doping concentrations, the surface passivation by a-Si:H yields a V_{oc} potential of SHJ solar cells exceeding 730 mV [60, 146, 264].

One aspect that has to be kept in mind is that the a-Si:H emitter is essentially a 'dead layer' in terms of excess carrier collection. This means that all the excess carriers generated in the a-Si:H recombine before they can be extracted²². This fact is reflected in a vanishing spectral response for small wavelengths (cf. Fig 4.13) which are absorbed in the thin a-Si:H layers, leading to a reduction in the short-circuit current j_{sc} . Thus,

²¹There are even reports on degenerate c-Si regions at the heterointerface due to the Fermi level locally entering the bands, which results in a two-dimensional electron gas [126].

²²Note that this situation is similar to the situation in classical c-Si homojunction cells in case of excessive emitter doping leading to e.g. phosphorous precipitates [88].

narrow constraints are posed on the maximum thickness of the a-Si:H emitter [76], and increasing the a-Si:H band gap is suggested in order to minimize this 'parasitic absorption', e.g. by alloying with carbon [188] or oxygen [74, 238].

As for c-Si solar cells, the formation of a back-surface field is suggested which prevents the minority carriers in the field-free bulk of the c-Si absorber from reaching the recombination-active back contact [240]. In a-Si:H/c-Si HJs, the band offsets can elegantly take over this function when a back-side a-Si:H layer is deposited. It is not necessary to impose a large band bending at the c-Si back side as the band offsets contribute to the blocking of minority carriers (Fig. 2.13).

A last aspect concerns the contacts of the solar cell. While classical c-Si solar cells comprise a highly doped emitter providing sufficient lateral conductivity, this is not the case for a-Si:H/c-Si HJs. Here, a TCO has to be deposited on top of the a-Si:H emitter to allow for charge carriers to reach the metal grid. Different materials can be principally employed of which indium-tin-oxide (ITO) and aluminum-doped zinc oxide (ZnO:Al) are the most promising. It has however to be kept in mind that the role of the TCO layer goes beyond the simple role as a 'metal' contact, as the TCO/a-Si:H heterojunction comprises some subtleties concerning band lineup and carrier transport. The band bending present at this junction can even penetrate the a-Si:H emitter and affect the a-Si:H/c-Si heterojunction as was recently invoked based on simulations [118]. In summary, the a-Si:H/c-Si heterojunction is promising for the application in solar cells particularly due to its high V_{oc} potential. While the processing is comparably simple, the physics involved in the heterostructure are rich and complex and many open questions persist, which concern the passivation mechanism of a-Si:H on c-Si surfaces, the band lineup and the charge carrier transport across the a-Si:H/c-Si heterojunction.

3. Experimental Techniques

In the present chapter, the techniques used throughout this thesis will be briefly introduced. In the first part, the sample preparation is described: Starting with cleaning and surface conditioning of the crystalline silicon substrates, the deposition of amorphous silicon layers by plasma-enhanced chemical vapour deposition will be treated, before annealing of a-Si:H/c-Si samples is described. The main part of this chapter contains the description of thin-film characterization techniques which will mainly be applied to undoped a-Si:H layers: To characterize the structural properties of the amorphous layers, infrared spectroscopy and hydrogen effusion measurements are used which allow to assess the concentration and bonding configuration of hydrogen, and secondary-ion mass spectroscopy is employed to profile the concentrations of hydrogen or deuterium along the depth axis of the layers. The electronic properties are determined with photoelectron spectroscopy: While far-UV excitation allows to monitor the structure of the valence band, near-UV light is used to excite electrons from electronic states in the band gap. The optical properties are measured with spectroscopic ellipsometry, being particularly suited to analyze ultrathin layers.

Further, techniques are described which are used to analyze a-Si:H/c-Si heterojunctions, representing precursor structures of high-efficiency solar cells. These comprise photoconductance decay which monitors minority carrier lifetimes in the crystalline absorber passivated by the a-Si:H layer, while surface photovoltage measurements allow to determine the equilibrium band bending in the crystalline silicon. Finally, the measurement and analysis of I/V curves of complete solar cells is described.

3.1. Sample preparation

3.1.1. c-Si cleaning and surface conditioning

The crystalline silicon wafers used as substrates for a-Si:H deposition have been cleaned by the procedure of the Radio Company of America (RCA clean) prior to deposition [121]. Random pyramid textures for light-trapping purposes were obtained on c-Si{100} surfaces by anisotropic etching in a potassium hydroxide/isopropyl alcohol (KOH/IPA) solution at 80°C [187] prior to RCA cleaning. Some wafers which initially had polished surfaces were subjected to a standard saw damage etch using diluted KOH to create surface conditions which are typical for industrial wafer processing after the saw damage removal step.

Immediately prior to loading into the PECVD system for a-Si:H deposition, the native oxide on the c-Si surfaces was removed by a short dip in diluted hydrofluoric acid (HF) with a concentration of 1% in deionized water. Tests were carried out to determine the necessary etching time for complete oxide removal on a given surface morphology. Typical HF dipping times were between 30 seconds and 2'. All substrates used within this thesis were float-zone grown silicon wafers.

3.1.2. Growth of a-Si:H films with PECVD

The a-Si:H layers were deposited in a six-chamber cluster tool, equipped with three parallel-plate plasma-enhanced chemical vapor deposition chambers, two load locks and a hydrogen passivation chamber. Samples are placed on 6" silicon wafers serving as carriers and reside on the lower electrode plate during PECVD deposition. Undoped a-Si:H is deposited in a conventional 13.56 MHz RF-PECVD system with a base pressure of 2×10^{-7} mbar, using silane and hydrogen as precursor gases. The substrate temperature T_{sub} was varied between 130°C and 210°C. The different deposition regimes developed in the course of this thesis are detailed in Table 4.2 in chapter 4. Boron-doped (p)a-Si:H layers were deposited either in a remote plasma ECR-CVD system, or in a parallel-plate PECVD system operating at 60 MHz excitation frequency (VHF), by decomposition of silane and hydrogen-diluted diborane (B_2H_6 , 0.5% in H_2). The base pressures for both chambers were in the low 10^{-7} mbar range. The silane flow rate was kept constant at 10 sccm, while the gas phase doping concentration was controlled by varying the $\text{B}_2\text{H}_6/\text{H}_2$ flow rate, the deposition pressure was 0.5 mbar and the substrate temperature was $T_{\text{sub}} = 130^\circ\text{C}$. (n)a-Si:H was deposited solely in the VHF-PECVD chamber and doped with hydrogen-diluted phosphine (PH_3), also at a constant silane flow rate of 10 sccm, a deposition pressure of 0.5 mbar and a substrate temperature of $T_{\text{sub}} = 190^\circ\text{C}$. The standard doping concentrations in the PECVD chambers for (n)a-Si:H were 1000 ppm if used as emitter layer, and 2000 ppm if used as BSF. For (p)a-Si:H 2000 ppm and 4000 ppm were employed. Emitter layers had 10 nm thickness and BSF layers 30 nm if not stated otherwise.

Deuterated undoped amorphous silicon [(i)a-Si:D] was deposited from D_2 -diluted deuterated silane (SiD_4) with purity 4.0 in the same RF-PECVD chamber as used for (i)a-Si:H deposition.

3.1.3. Low-temperature annealing

Annealing of the samples was done on a conventional temperature-controlled hotplate with a cleaned c-Si wafer as support under nitrogen flow. Cooling down of the sample was also performed under nitrogen. However, no purging of the hotplate box was possible, thus some remaining oxygen was present. An alternative annealing recipe employing a microwave oven as used for cooking was developed in the course of this thesis and is described in section 8.3.4.

3.1.4. TCO and metal deposition

To process a-Si:H/c-Si solar cells, a transparent front contact with sufficient conductivity and low reflectivity needs to be deposited. To this end, 80 nm of Al-doped zinc oxide was sputtered on the emitter side of the solar cell structure. TCO deposition was performed employing reactive DC sputtering under ultra-high vacuum (UHV) from a metallic Zn target containing 1 mass-% Al under argon and oxygen atmosphere. The metal contacts were made of aluminum, which was deposited by electron-beam evaporation under high vacuum. The front grid structure was obtained using a photolithographic lift-off process. Finally, the active solar cell area (1 cm^2) was defined by photolithographic mesa etching of the (metal/TCO/a-Si:H) stack down into the c-Si base region.

3.2. Film characterization

3.2.1. Structural properties: IR spectroscopy, H effusion and SIMS

Fourier-transform infrared spectroscopy

To quantify the H bonding configuration in the a-Si:H layers, Fourier-transform infrared absorption spectroscopy (FTIRS) was employed in Brewster-angle transmission mode to avoid internal reflections [12, 32]. To this end, polarized IR light is used and the sample is positioned at the correct angle versus the incident beam to avoid reflection at the a-Si:H/air surface. The setups used here were a Bruker IFS 66v/S for (i)a-Si:H/c-Si samples and a Bruker IFS 125HR for a-Si:D/c-Si and (p)a-Si:H/(i)a-Si:H/c-Si samples. All measurements were made employing 'double-side polished' (DSP) (n)c-Si{111} substrates with $2.5 \Omega\text{cm}$ resistivity, symmetrically coated with a-Si:H/D layers to allow for measurement of the effective carrier lifetime as well. The H content of the thin layers was determined from the integrated peak intensity of the Si-H stretching modes following the procedure of Langford *et al.* [139]. Further details on the FTIRS analysis are discussed in appendix A.1, and can also be found in Refs. [215, 216].

Hydrogen/deuterium effusion

A method aimed at gaining insight into a-Si:H hydrogen content and -microstructure which is complementary to infrared spectroscopy is hydrogen effusion or thermal desorption spectroscopy, as the method is also termed. To this end, a sample with precisely defined area is heated under UHV with a linear temperature ramp (usually several

K/min), while the desorbing species are detected with a mass spectrometer in the exhaust line of the vacuum setup.

Hydrogen effusion measurements were carried out by F. Einsele of Forschungszentrum Jülich on one-sided (i)a-Si:H/(n)c-Si{111} samples on DSP substrates. The samples are placed in a cylindrical quartz tube which is heated electrically. The heating system is calibrated to provide a constant heating rate which is controllable between 5...40 K/min, and the maximum sample temperature is 1050°C. A turbopump is connected to the sample space and provides a base pressure of $< 10^{-7}$ mbar. The effusing species are detected with a quadrupole mass spectrometer (QMS), which is calibrated in a separate measurement. To this end, the element sought for is introduced into the setup at a defined rate, and a calibration factor describing the sensitivity of the QMS is determined for the specific element. Further details on the particular setup and the analysis of H effusion spectra can be found in Ref. [64].

Additional measurements on one-sided (i)a-Si:D/(n)c-Si{111} samples on DSP substrates were performed by N. H. Nickel at HZB in a similar setup.

Secondary ion mass spectroscopy

Secondary ion mass spectroscopy (SIMS) was measured on a-Si:D samples to profile the deuterium concentration along the depth axis of the a-Si:D layer employing a Cameca IMS-4f system. Argon ions with a kinetic energy of 6.5 keV were employed and the mechanical angle between the ion optical axis and the sample normal was 28°. Due to the deflection of the ion beam at low sputtering energies, the impact angle is significantly larger. Depending on the calculation method, 55°...65° are expected [161]. Further information on the measurement and analysis of SIMS spectra can be found e.g. in Ref. [280] and are discussed in section 6.5.

3.2.2. Electronic structure: (Near-)UV photoelectron spectroscopy

The photoelectron setup

Photoelectron spectroscopy (PES) was measured in a UHV cluster tool consisting of a molecular-beam epitaxy chamber and a photoelectron analytics chamber where UPS, XPS and constant-final-state yield spectroscopy (CFSYS, [211, 219]) can be performed. The required sample size is a 2" wafer. PES was measured immediately after direct transfer of the samples from the high vacuum PECVD system to the UHV analytics chamber to avoid surface contamination. For the He-I UPS measurements, He-I radiation at $\hbar\omega = 21.2$ eV was used for the excitation which was produced in a He gas discharge lamp which is directly connected to the analytics chamber and differentially pumped. For CFSYS and near-UV UPS (NUVPES), light from a 100 W xenon short-arc gas discharge lamp (Osram XBO) was used that was monochromated with a double grating monochromator¹. The lamp spectrum is broad and limited on the high-energy side

¹1680 SpectraMate Double Spectrometer, Czerny-Turner type, manufactured by Yobin-Yvon/Spex. Gratings have a line density of 1200mm^{-1} and the resulting dispersion at the exit slit plane is 1.8nm/mm .

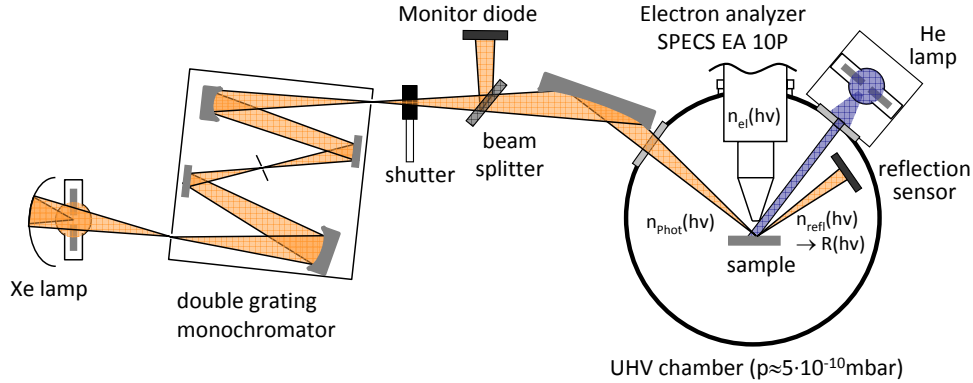


Figure 3.1.: Schematic of the (near-)UV photoelectron spectroscopy (PES) setup. Three measurement modes are possible: 1) Classical UPS with He-I excitation from a He gas discharge lamp (violet beam). 2) Near-UV PES with excitation at a constant adjustable energy provided by a combination of a Xe lamp and a monochromator (left, orange beam). 3) Measurement of the photoelectron yield (ratio of photoelectrons to incident photons) by sweeping the photon energy at constant photoelectron final state energy while measuring both incident and reflected photon flux (CFSYS mode, orange beam including the reflection sensor to calculate the yield). Figure adapted from Ref. [132].

at about 7.3 eV by the window layers made of suprasil or lithium fluoride. On the low-energy side, the work function cutoff of the sample is limiting at about 4 eV for a-Si:H, thus the usable spectral range is $\hbar\omega = 4 \dots 7$ eV or wavelengths from 310 ... 170 nm. To quantify the photon flux impinging on the sample, 10% of the incident beam are directed onto a monitor diode² by a suprasil beam splitter. To allow for yield measurements, the intensity reflected on the sample is measured by a second photodiode of the same type. Photoelectrons emerging from the sample are detected by a Specs EA 10 Plus photoelectron energy analyzer. The analyzer pass energy E_{pass} determines the energy resolution [200, 220]. The half width of the measured energy distribution ΔE_{an} is given by $\Delta E_{\text{an}} = 2.5 \times 10^{-2} E_{\text{pass}}$ for the present analyzer. All photoelectron spectra were taken with $E_{\text{pass}} = 5$ eV, thus $\Delta E_{\text{an}} = 125$ meV. In the present case, the limit of the energy resolution is given by the monochromator, which was operated with slit widths of 4 mm at both entry and exit slit, leading to an energy resolution of $\Delta E_{\text{mon}} = 93$ meV at $\hbar\omega = 4$ eV and $\Delta E_{\text{mon}} = 285$ meV at $\hbar\omega = 7$ eV. Thus, the finite energy resolution of the PES apparatus and the thus resulting broadening has to be taken into account as a 'transfer function' B_{PES} , which is the convolution of the constant energy resolution of the analyzer with the energy-dependent resolution of the monochromator.

Analysis of NUV PES data

While He-I UPS spectra were only analyzed qualitatively, the data were deconvoluted by a forward calculation procedure for the analysis of NUV PES and CFSYS spectra: The expected energy distribution of the photoelectrons is calculated based on a model

²Hamamatsu, calibrated at the Physikalische Technische Bundesanstalt.

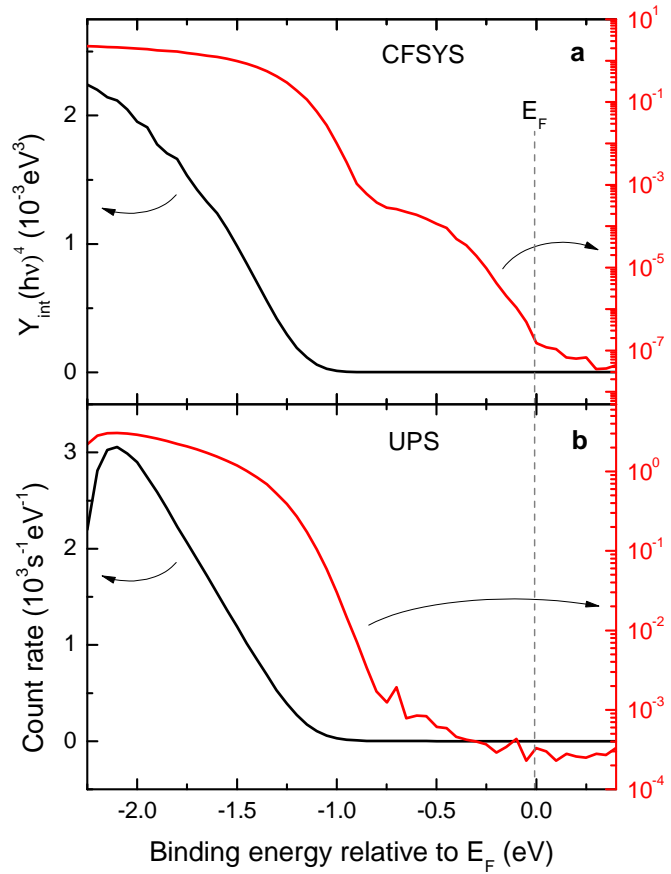


Figure 3.2: Comparison of UPS and CFSYS spectra taken on the same (i)a-Si:H sample. It is obvious that the dynamic range of the CFSYS method is larger by about four orders of magnitude, allowing to quantify the valence band tail *and* the defects deep in the band gap. The difference between the methods is explained in the text and in appendix A.2.

DOS (described in the next paragraph) and assumptions concerning the photoemission process (cf. appendix A.2), by convolution with the transfer function. The resulting calculated PES signal is fitted to the measured PES data by varying the parameters of the model DOS. It is important to note that two different modes of PES were employed in this thesis: For NUV-PES and He-I UPS, the excitation energy is kept constant while the energy distribution of the emerging photoelectrons is measured. For CFSYS on the other hand, the final state energy of the electrons is kept constant while the excitation energy is swept. This leads to different instrument transfer functions which have to be considered depending on the measurement method. The assets and drawbacks of these two methods are further described in appendix A.2. For more information on the particular setup and the PES data analysis, the reader is referred to Ref. [129].

The model DOS used to fit a-Si:H NUV-PES spectra

Typical spectra recorded with CFSYS and UPS are depicted in Fig. 3.2, on both linear (left) and logarithmic scales (right). It is obvious that the CFSYS technique yields data over a much larger dynamic range, resulting in the a-Si:H gap density of states being resolved up to the Fermi energy. This allows to determine the density of dangling bond defect states in a-Si:H, along with the localized states of the valence band tail.

The noise level in the UPS spectrum however prevents such effort as it covers the weak contribution of the dangling bonds, merging into the valence band tail on the low-energy side of the spectrum.

It is important to note that $Y_{\text{int}}\hbar\omega$ is directly proportional to the DOS [129, 219], as following from Eq. A.17 in appendix A.2³. The UPS spectra however can only be normalized to a DOS with additional assumptions concerning the density of unoccupied states and the emission function, yielding additive uncertainties (cf. appendix A.2).

The nature of the amorphous network leads to a rich electronic structure comprising exponential band tails, dangling bond defects and H-derived valence band features. The following quantities can principally be determined with near-UV PES:

The valence band edge. The band edges in amorphous semiconductors are not as well-defined as in their crystalline counterparts. The extended states of the valence and conduction band gradually merge into the localized states of the exponentially decaying band tails (resulting from the amorphous nature of the network as outlined in section 2.1.1), which renders the band edges inherently blurred. Thus, the energetic positions of the band edges have to be *defined* by choosing an extraction method for a given measurement technique. In consequence, different competing methods with more or less rigorous physical foundations have been used particularly to extract the band gap from optical data, which include extrapolations of the band region (e.g. the Tauc plot [256]) or artificially defined edges as the E_{04} gap. The validity of each of these approaches has been discussed extensively (see e.g. Refs. [39, 110] and references therein).

Principally, different definitions can be chosen in the analysis of PES spectra as well, such as the extrapolation of the valence band signal to zero or the choice of a distinguished point in the spectrum. In this thesis, two different techniques are compared: Firstly, the extrapolation of the valence band PES signal towards the abscissa using a square-root function, yielding $E_{V,a-Si:H}^{\text{ext}}$. This method is motivated by the common approximation of parabolic bands which leads to a square-root law for the DOS and corresponds to a fit of the valence band density of extended states while omitting the contribution of the exponentially decaying localized band tail states to the band edge. Secondly, the choice of a point 40 meV lower in energy than the transition energy between the exponentially decaying band tail and the valence band, $E_{V,a-Si:H}^t$, as found by fitting a model DOS convoluted with the instrument transfer function to the data [129, 132, 134]. This energy corresponds to the valence band mobility edge $E_{V,a-Si:H}^{\mu}$, i.e. the demarcation energy from extended to localized states in terms of electronic transport, and its definition relative to $E_{V,a-Si:H}^t$ was based on the comparison of internal photoemission data [285] with photoconductance data [129], consistent with other experimental works [260]. Note that for the band edge definitions used here, no normalization of the model-DOS is necessary. Most importantly, the proportionality of the CFSYS spectra to the DOS lays a physical foundation for the square-root fit of the spectrum. Thus one can avoid the uncertainties associated with normalization [283],

³Here, Y_{int} is the internal yield of photoelectrons and the multiplication with the photon energy accounts for the energy dependence of the optical matrix element [110].

which leads to a smaller systematic error for the obtained band edge values.

The valence band tail slope or Urbach energy. The valence band tail decays exponentially with a characteristic slope, which can be related to the slope in the exponential region in optical absorption spectroscopy (Urbach tail) [39, 137]. Therefore the terms 'valence band tail slope' referring to the exponential slope in PES data and 'Urbach energy' as commonly used to describe optical data will be used synonymously in the following. The tail can be described with

$$N_{V,a\text{-Si:H}}^{\text{tail}}(E) = N_{0V}^{\text{tail}} \exp\left(\frac{E_{V,a\text{-Si:H}}^t - E}{E_{0V}}\right) \quad (3.1)$$

with the Urbach energy E_{0V} determining the slope of the decay. The transition energy $E_{V,a\text{-Si:H}}^t$ and the prefactor N_{0V}^{tail} are chosen such that the combined DOS (valence band and valence band tail) is continuous and differentiable. Note that due to the exponential nature of the tail, E_{0V} is independent from the normalization of the DOS. Although at this point the term 'DOS' is used for convenience, which implies a normalization, E_{0V} can be determined without it as is also true for the valence band edge (see above).

The distribution of dangling bonds. Deeper in the band gap, the distribution of dangling bonds can be seen in the CFSYS spectra as a broad shoulder emerging from the band tail towards lower binding energy, while in the UPS spectra the noise level is reached. As usual for a-Si:H, a Gaussian distribution is assumed:

$$N_{d,a\text{-Si:H}}(E) = N_d \exp\left(-\frac{(E - E_d)^2}{2\sigma_d^2}\right) \quad (3.2)$$

It must be noted that this assumed distribution disregards the amphoteric nature of the dangling bonds. As pointed out e.g. by Powell and Deane [184, 185], due to the three charge states of the dangling bonds and the Coulomb correlation energy U relevant for doubly occupied states, six different Gaussians would be needed to correctly describe the gap state distribution in the one-particle picture. However, except for ideally intrinsic material⁴, two of the six Gaussians dominate the DB spectrum. With the correlation energy U separating these two Gaussians and their width typically assumed to be of the same magnitude (150...200 meV), the sum of both is almost indistinguishable from a single Gaussian in the DOS. Taking into account the broadening introduced by the finite energy resolution of the monochromator [129], it cannot be hoped to separate the contributions to the DB DOS with PES. Consequently, it is obvious that no structure is visible in the DB distribution observing Fig. 3.2. It therefore seems reasonable to assume the a *single* Gaussian as a basis for the fit. Care has to be taken, however, when extracting model parameters from PES data not to neglect the underlying structure.

There are three free parameters for the dangling bond distribution: While the

⁴which does not exist due to the slightly n-type nature of undoped a-Si:H

energetic position E_d and the width of the Gaussian distribution σ_d^2 can be obtained without normalizing the spectrum, obtaining the dangling bond density N_d requires a normalized DOS.

Normalization of NUV PES spectra

There are at least two different strategies for normalizing (near-)UV PES data, which shall be briefly introduced: When the Si 3p peak deeper in the valence band is completely visible with the given technique, a normalization can be performed based on a state-count argument [274]: The integration over the peak must yield the atom density multiplied by two to account for the spin degeneracy of electronic states. Thus, with a measured width of the peak (typically 4 eV), the peak DOS can be defined (typically $2 \times 10^{22} \text{ eV}^{-1} \text{ cm}^{-3}$).

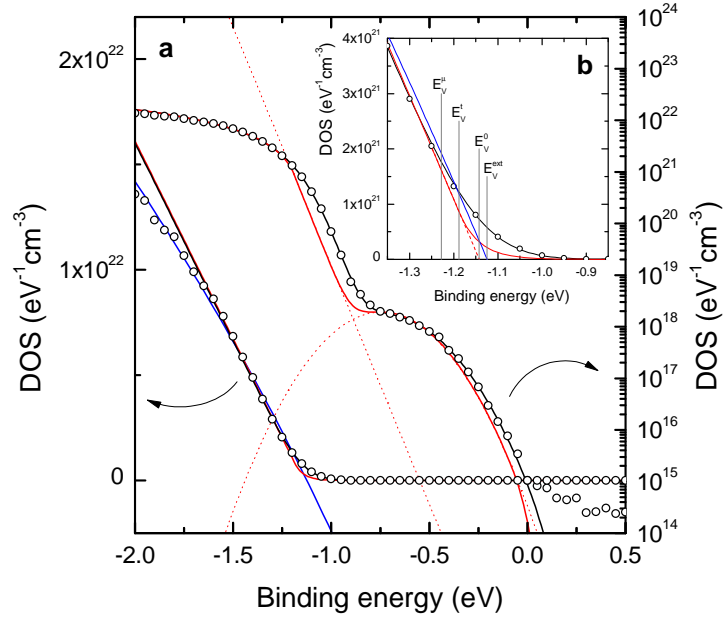
In the present case — as is true for all NUV PES studies — the Si 3p peak is not fully visible and another strategy has to be sought. Winer *et al.* based their normalization on the same argument as von Roedern and chose a point at 6.2 eV photon energy, „which corresponds to a point in the valence band about halfway down from the Si 3p maximum“, and consequentially assumed $1 \times 10^{22} \text{ eV}^{-1} \text{ cm}^{-3}$ [283].

This approach bears a certain risk when the Si 3p peak is not actually visible, as variations in the form of the valence band or — more importantly, as shall be demonstrated later on — a shift of the valence band edge relative to the core levels can affect the accuracy of this normalization. A different approach is based on the valence band mobility edge $E_{V,a-Si:H}^\mu$ as a reference point. Street [244, 245] found a density of $2 \times 10^{21} \text{ cm}^{-3} \text{ eV}^{-1}$ states at $E_{V,a-Si:H}^\mu$, which can be used to normalize the spectrum after localizing the mobility edge with the help of the procedure sketched above. As in the samples under study here a shift of the valence band edge with increasing H content is to be expected based on previous results [273], the latter method using the mobility edge as reference point will be used. A thorough discussion on the matter of the NUV PES normalization is contained in Ref. [129].

Discussion of an example spectrum

Fig. 3.3 shows a typical CFSYS spectrum (circles) and the results of different analysis steps. The black line is a fit of the model DOS as described above, convoluted with the instrument transfer function, to the data. Note that although no normalization is necessary for the band edge and tail slope determination as explained above, all fitting and extrapolation was done on the normalized spectrum in this case for simplicity of the figure. The red line is the DOS without convolution with the transfer function, the dotted lines are the contributions of the Gaussian dangling bond distribution and the valence band tail. Panel (a) allows to assess the overall quality of the DOS fit, which extends over six orders of magnitude (right axis logarithmically scaled). On the left side the linear scale brings up the structure of the valence band edge. Here, the fitted convoluted model DOS begins to deviate from the data, which is slightly better described

Figure 3.3: (a) Example for the analysis of CFSYS spectra as employed in this thesis. Open circles are measured data, the black line is a fitted model DOS folded with the instrument transfer function. The red line is the model DOS with the contributions of DBs and Urbach tail (dotted lines). The comparison of the red line to the data illustrates the broadening imposed by the finite resolution of the monochromator. There is a slight deviation of the linear model valence band from the data, which is better described by a square root function (blue). (b) Different methods for the estimation/definition of the valence band edge in a-Si:H, as explained in the text.



by a square root function (blue line) as could also be naïvely assumed⁵.

In panel (b), the important transition region between VB and exponential tail is magnified, again linearly scaled. It is visible that the DOS fit requires a continuous and differentiable transition, thus smoothly linking tail and VB parts of the DOS. Also included in panel (b) are the different definitions of the valence band edge, as discussed above: Starting at higher binding energies, the mobility edge $E_{V,a-Si:H}^{\mu}$ is found first, defined relative to the demarcation energy $E_{V,a-Si:H}^t$ which separates VB and VB tail as explained above. Further, $E_{V,a-Si:H}^0$ is the ordinate intercept of the model-DOS valence band (assumed to be linear), while $E_{V,a-Si:H}^{\text{ext}}$ is the extrapolation of the square-root fit to zero. The specific order of the different VB edge definitions ($E_{V,a-Si:H}^{\mu} < E_{V,a-Si:H}^t < E_{V,a-Si:H}^0 < E_{V,a-Si:H}^{\text{ext}}$) follows from the systematic differences in their determination. It is important to note that this order is valid for all spectra analyzed in the course of the study. Even more, the approximate energetic distances are also approximately constant⁶, thus trends in the VB edge do not depend on the choice of the definition. Additionally, it is obvious from the comparison of the square-root and the linear extrapolation, that the method of band edge extraction when applying a VB extrapolation does not significantly impact the result. Therefore, the exact functional form of the valence band assumed while extrapolating is not a crucial parameter. As stated above, for compatibility with transport results, the mobility edge will be used as reference point in this work.

The analysis of UPS spectra is performed accordingly, but without determination of the dangling bond parameters and with a different instrument transfer function according to the measurement details.

⁵This reasoning however disregards a possible non-parabolic structure in the valence band and the impact of the instrument transfer function.

⁶Note that $E_{V,a-Si:H}^{\mu} - E_{V,a-Si:H}^t = -40$ meV per definition.

3.2.3. Optical characterization: Spectroscopic ellipsometry

Spectroscopic ellipsometry (SE) was measured on a variable-angle SE (VASE) system by J. A. Woollam. Samples were either one-sided or symmetrical a-Si:H/(n)c-Si{111} structures. The measurements were performed at two angles (65° and 74°) with the excitation energy swept between 1...3.5 eV. A photon energy of 3.5 eV was the maximum achievable energy with the given combination of lamp and monochromator in the present setup. The SE data was analyzed with model-based fitting and the data taken at the two angles was fitted at once with a single set of parameters. The fits were done with the program *rig-vm*⁷ [181]. The fit model consisted of a crystalline wafer with known thickness and optical functions from literature [9], the a-Si:H layer parametrized either by the Tauc-Lorentz approach following Jellison *et al.* [114], or with the modified Tauc-Lorentz model of Ferlauto *et al.* [70], and a surface roughness layer with a-Si:H host matrix in the framework of the Bruggeman effective medium approach [30]. While the Jellison model for a-Si:H represents the *de-facto* standard in a-Si:H parametrization and comprises a minimum set of fit parameters, the Ferlauto model includes some specific aspects of amorphous semiconductors such as exponentially decaying band tails. Additionally, the Jellison model is based on the assumption of a constant momentum matrix element for optical transitions, while Ferlauto assumes a constant dipole matrix element.

The fits were done employing a Levenberg-Marquardt algorithm [144]. Although the thickness of the roughness layer was a free fit parameter, it was found to be almost independent of the particular sample, resulting in a mean thickness of 0.496 ± 0.03 nm. As most important fit parameter in the framework of this thesis, the a-Si:H optical band gap $E_{g,a-Si:H}^{\text{opt}}$ was extracted from both models, as well as further the long-wavelength limit of the dielectric constant for the calculation of the a-Si:H mass density [193]. The errors for the $E_{g,a-Si:H}^{\text{opt}}$ fit value were determined from the covariance matrices provided by the Levenberg-Marquardt fitting routine. To verify this estimation, the dielectric functions resulting from the two fit models were exemplarily calculated for some samples, stochastically varying all fit parameters within their 1σ intervals. Then, Tauc plots [256] of the resulting k functions were analyzed and verified that the minimum and maximum band gaps estimated from this procedure differed by not more than the error indicated by the fitting routine.

Further information on the SE analysis can be found in appendix A.3. For further reading on SE measurements and analysis the reader is referred to Ref. [4].

3.3. Heterostructure analytics

3.3.1. Measurement and analysis of c-Si minority carrier lifetime

Photoconductance decay measurements

The effective minority charge carrier lifetime in a-Si:H/c-Si structures was quantified employing photoconductance decay measurements on a WCT-100 by Sinton Instruments,

⁷Fraunhofer Institute for Surface Engineering and Thin Films, Germany

Table 3.1.: Parameters of the lifetime fit model [142] employed in this thesis.

| Name | Symbol | Value | Unit |
|--|----------------------|------------|------------------|
| c-Si bulk defect density | N_t | 1 | cm^{-3} |
| Center energy of interface defects ¹ | E_{center} | 0.1 | eV |
| Width of Gaussian interface defect density | σ | 0.18 | eV |
| Correlation energy of amphoteric defects | U | 0.15 | eV |
| Capture cross section for neutral defects ² | $\sigma_{n/p}^0$ | 10^{-17} | cm^2 |
| Capture cross section for charged defects | $\sigma_{n/p}^{+/-}$ | 10^{-16} | cm^2 |

¹ relative to the c-Si valence band edge.

² The choice of this capture cross section will be underpinned in chapter 8.

commonly known as the 'Sinton lifetime tester' [227]. In brief, the working principle is the following: The sample is placed near the coil of an oscillator circuit and excess charge carriers are generated by a short and intense light pulse provided by a photo flash equipped with an IR filter. Infrared light is chosen for excitation in order to yield a homogeneous generation rate. By the additional charge carrier density in the 10^{16} cm^{-3} range the conductance of the sample is changing which is detected as a detuning of the oscillator circuit due to eddy currents in the sample. The method is fast enough to obtain the temporal development of the conductance σ after the initial flash. The conductance is directly proportional to the excess carrier density by $\sigma = e(\mu_e + \mu_h)\Delta nW$, therefore the effective lifetime can easily be calculated employing $\tau_{\text{eff,meas}}(t) = \Delta n(t)/\partial_t \Delta n(t)$. Thus, a data set of $\tau_{\text{eff,meas}}(\Delta n)$ is obtained from the decay of the excess conductance. Further, by employing equation 2.33 the dependence of implied V_{oc} on the illumination density can be calculated. The underlying assumption of the analysis is the approximate homogeneity of the excess carrier density across the c-Si wafer (cf. section 2.2.5). Further, a so-called 'optical factor' is employed to quantify the fraction of light which is actually coupled into the semiconductor, thus calibrating the 'suns' axis. For all measurements within this thesis, a value of 0.7 was used which is a common assumption. The error in the $\tau_{\text{eff,meas}}(\Delta n)$ values was found to be about 8% in the transient decay mode employed here [157], which transforms into an error of about 0.6% in the implied V_{oc} as is found by analyzing the dependence of implied V_{oc} on τ_{eff} (cf. section 2.2.5). These error values will be used throughout this thesis.

Analysis of photoconductance decay data

The $\tau_{\text{eff,meas}}(\Delta n)$ data sets obtained by PCD can be analyzed by two means: The first and most simple approach is to quote τ_{eff} or implied V_{oc} at either a fixed excess carrier density or the Δn corresponding to 1 sun illumination. This is a valid approach if the potential of a given structure to be employed in a solar cell shall be evaluated as τ_{eff} is directly related to maximum V_{oc} which could be obtained. Note that with varying recombination properties of the structure, the Δn corresponding to 1 sun is different, as seen in section 2.2.5. In some cases, the 'Auger-corrected τ_{eff} ' is given, i.e. a value for the effective lifetime where the contribution of the Auger recombination was subtracted

using Eq. 2.34.

The second and more sophisticated approach is to fit the $\tau_{\text{eff,meas}}(\Delta n)$ curve with a model describing the recombination properties of the structure. By this means, the different contributions to the effective lifetime can be separated and — most importantly — a detailed insight in the recombination properties of the interfaces can be gained. Mostly, Auger recombination as parametrized with equation 2.9 is included and some reasonable assumptions concerning τ_{SRH} are made. Here, the model by Leendertz *et al.* is employed to fit the PCD data [142]. If not stated otherwise, the parameters used in the model were chosen as listed in Table 3.1. Further information about the lifetime fit model is contained in Refs. [140–142].

3.3.2. Surface photovoltage measurements

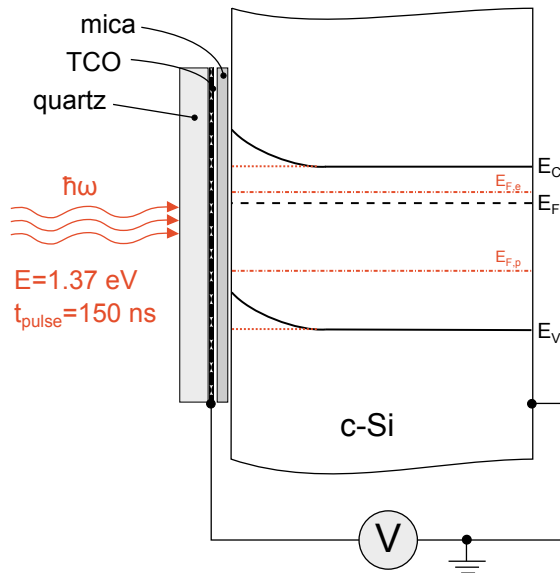


Figure 3.4: Schematic of the surface photovoltage (SPV) measurement setup. An MIS structure is formed between a transparent conducting oxide (TCO) on a glass plate serving as front contact, an insulating mica plate and the a-Si:H/c-Si sample. The crystalline silicon is driven into flat-band conditions by a short and intense laser pulse, while the change in surface potential is detected capacitively. After correcting the SPV signal for the Dember voltage, it equals the c-Si equilibrium band bending φ .

To quantify the c-Si band bending in equilibrium the surface photovoltage method [97] was employed. In a dedicated setup (sketched in Fig. 3.4), a metal-insulator-semiconductor (MIS) structure is formed between a transparent conducting oxide (TCO) on a glass plate serving as front contact, an insulating mica plate and the a-Si:H/c-Si sample, while a gold-plated chuck provides an Ohmic back contact. The sample is excited with a short laser pulse⁸ and the change in surface potential resulting from the redistribution of photogenerated charge carriers is detected via the change in capacitance of the MIS structure. As the photon energy is smaller than the a-Si:H band gap ($E_{\text{phot}} = 1.37 \text{ eV}$), the photogeneration takes place only in the crystalline part of the junction leading to a flattening of the bands and a split-up of the quasi-Fermi levels of electrons and holes ($E_{F,n}$ and $E_{F,p}$ in Fig. 3.4). The variation in surface potential measured as a photovoltage pulse V_{SPV} corresponds to a change in band bending supported by the c-Si, after correction for the Dember voltage resulting from the difference

⁸The laser parameters are: Wavelength 904 nm, pulse duration 150 ns, photon flux $10^{19} \text{ cm}^{-2} \text{ s}^{-1}$.

in mobilities of electrons and holes [59]. Ideally, the illumination intensity is chosen high enough to reach flat-band conditions in the sample and the system is in steady state when the laser pulse is switched off. Then, the maximum value of the Dember-corrected SPV signal right after the laser pulse, $V_{SPV,corr}(t=0)$, directly yields the c-Si band bending in the dark, φ . This is the case under high injection conditions, when charge carrier densities $n_{illum} p_{illum} \gg n_{dark} p_{dark}$. In the given setup, the initial excess charge carrier density is $> 2 \times 10^{17} \text{ cm}^{-3} \gg N_{doping}$, thus high injection conditions are fulfilled and $V_{SPV,corr}(t=0) = \varphi$ is assumed. As generation of electron-hole pairs takes place only in the c-Si, recharging of the a-Si:H defect states should mainly occur through injection of electrons and holes into the thin a-Si:H film, which is supposed to have a negligible effect on $V_{SPV,corr}(t=0)$, as these processes are comparably slow and thus only affect the form of the SPV decay transient [131].

3.4. Solar cell diagnostics

3.4.1. Spectral response and quantum efficiency

The spectral response (SR) is defined as the ratio of short-circuit current density j_{sc} and a monochromatic illumination power density E_λ , thus $SR = j_{sc}/E_\lambda$. The external quantum efficiency (EQE) can be calculated from the SR by

$$\eta_{EQE} = SR(\lambda) \frac{hc}{e\lambda}, \quad (3.3)$$

and has values between 0...1. It is measured in lock-in technique using chopped monochromatic light from a xenon lamp passing through a grating monochromator which is superimposed by white bias light from a halogen lamp to provide the background excess carrier concentration corresponding to 1 sun illumination. The bias light is important as the recombination properties are in general injection-dependent, thus it is imperative to provide realistic injection conditions. To calculate the internal quantum efficiency (IQE), the reflectance of the sample is measured ex-situ and the IQE is calculated by $\eta_{IQE} = \eta_{EQE}(1 - R(\lambda))^{-1}$. The relation to the solar cell output current is the following: j_{sc} depends on the intensity and spectrum of the light to which it is subjected, the reflection properties and the internal quantum efficiency, i.e. the fraction of photons being absorbed by the solar cell actually producing an electron-hole pair which can be extracted. The current can thus be calculated from the quantum efficiency by the formula

$$j_{sc} = \int_{\lambda=0}^{\infty} \frac{e\lambda E_{AM1.5}(\lambda)}{hc} [1 - R(\lambda)] \eta_{IQE}(\lambda) d\lambda = \int_{\lambda=0}^{\infty} \frac{e\lambda E_{AM1.5}(\lambda)}{hc} \eta_{EQE}(\lambda) d\lambda, \quad (3.4)$$

where $E_{AM1.5}$ is the spectral power density of the AM1.5 standard spectrum, $R(\lambda)$ the spectral reflectance, and η_{IQE} the internal quantum efficiency.

3.4.2. I/V characteristics

Measurement of temperature-dependent I/V curves

Temperature-dependent I/V curves were measured with a four-probe setup employing a Keithley source-measure unit with the sample being pneumatically fixed on a temperature-controllable chuck. Contact was made by gold wires pressed onto the Al contact patches of the solar cell. The accuracy of the temperature adjustment was ± 1 K and the range of temperatures was 240 K to 360 K. Illuminated I/V data was taken on the same setup employing a metal-halogenide lamp calibrated against a c-Si homojunction reference solar cell provided by the Fraunhofer Institute for Solar Energy Systems (Fraunhofer ISE), Freiburg. To calibrate the lamp of the sun simulator, the output current of the reference solar cell was matched to j_{sc} as measured under standardized conditions at Fraunhofer ISE by adjusting the electrical power fed into the lamp.

Fitting of I-V-curves

In order to elucidate on the electrical transport mechanisms in a-Si:H/c-Si solar cells, a general diode equation was fitted to dark I/V curves measured at different temperatures (see chapter 5). As series resistances become important in the high-forward-bias regime when considerable current flows through the device, and shunts can play a role depending on the details of device preparation, both series resistance R_S and shunt resistance R_P were included in the fit model.

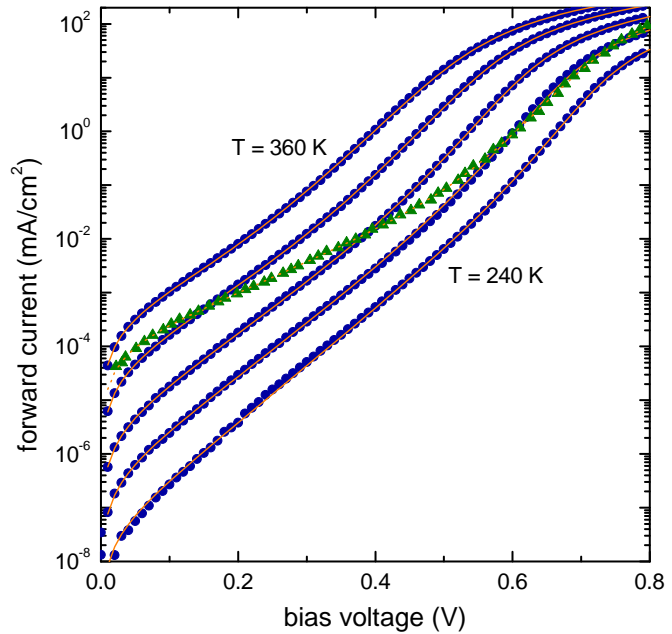
In most previous studies, two different current regimes have been observed in the forward bias direction. The high-forward-bias region was mostly interpreted in terms of a diffusion current (thus being characterized by a diode ideality factor), while in the low-forward-bias region tunneling was often invoked (reflected in a temperature-independent exponential factor). Thus, to be consistent with usual notation, the fit model of choice for the forward direction was

$$\begin{aligned}
 j_F &= j_{\text{diode1}} + j_{\text{diode2}} + j_{\text{shunt}} - j_{\text{phot}} \\
 &= j_{0,1} \left[\exp \left(\frac{q(V - j_F R_S)}{n_1 k T} \right) - 1 \right] \\
 &+ j_{0,2} [\exp(A(T)(V - j_F R_S)) - 1] \\
 &+ \frac{V - j_F R_S}{R_P} - j_{\text{Phot}}.
 \end{aligned} \tag{3.5}$$

Here, j_F is the forward current density through the solar cell, V the voltage at the cell electrodes, j_{Phot} is the photo-induced current present under illumination, $j_{0,1}/j_{0,2}$ denote the saturation current densities, n_1 is the ideality factor for the high-forward-bias region, $A(T)$ is the exponential factor for the low-forward-bias region, R_S is the series resistance and R_P denotes the parallel or shunt resistance.

The main goal of the fitting procedure was to ensure that the bias regions dominated by the different terms in Eq. 3.5 are fitted with equal accuracy. To this end, $\log(j_F)$ was fitted in regions where j_F is small. The fact that in those regions the series resistance R_S does not significantly influence the I/V curve can be benefited from as the simplification

Figure 3.5: Example of I/V data taken in the dark on a single sample at five different temperatures ($T = 240\text{ K} \dots 360\text{ K}$ in 30 K steps) and the respective fits with the two-diode model (lines) employing Eq. 3.5 in a semilogarithmic plot. A satisfactory agreement is observed between the data and fits across the whole bias range. For comparison the data of Taguchi et al. [252] taken at room temperature are shown together with the respective fits (green triangles and dashed line).



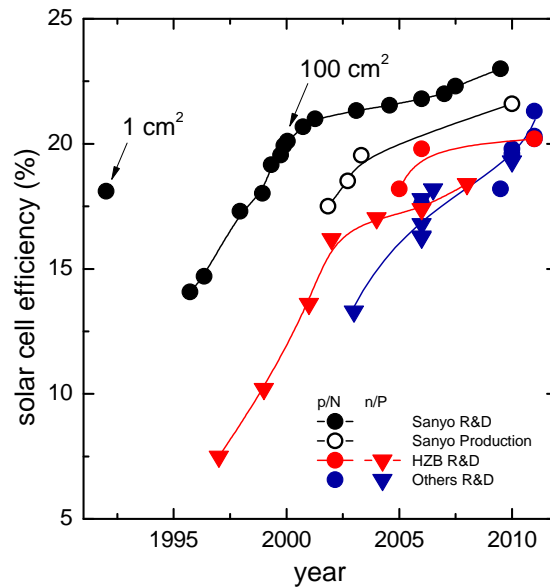
$R_S \rightarrow 0$ turns the transcendental Eq. 3.5 into an analytical expression, which considerably simplifies the fitting procedure. Consequently, for bias regions where the current density was below 1 mA/cm^2 , the simplified model was used to extract the parameters determining the I/V curve in this regime (R_P , $j_{0,2}$, A) from a fit of $\log(j_F)$ while the full model Eq. 3.5 was used for higher currents to yield the remaining parameters (R_S , $j_{0,1}$, n_1) from a fit of j_F . Care was taken to ensure convergence of the two partial fits in the transition regime and the procedure was then concluded by a fit of the full forward bias data taking the output values of the preceding partial fits as starting values. The quality of the resulting fit was usually satisfactory with R squared values of at least 0.999. A comparative study using different I/V fitting tools on the same dark I/V solar cell data performed at the French National Institute for Solar Energy Research (INES), revealed that the fit quality of the present implementation was competitive [46]. Thus, a consistent set of the six parameters modeling the I/V curve over the full forward bias range can be obtained by the outlined procedure. To allow for evaluation of the fit quality, an example of a typical fit of a single sample for five different temperatures is given in Fig. 3.5.

4. Development and assessment of a-Si:H/c-Si solar cell technology

In this chapter, the technological steps taken in order to optimize the a-Si:H/c-Si heterojunction solar cells made at HZB are described, and questions of fundamentally physical nature are identified which will be tackled in the following chapters of this thesis.

After briefly introducing the previous work on a-Si:H/c-Si solar cells at HZB, a survey of solar cell performance at the initial stage of this thesis is presented in the first section of this chapter. It is suggested that the HZB solar cells would benefit from undoped amorphous silicon buffer layers, shielding the crystalline absorber from the doped a-Si:H layers which comprise high defect densities as known from previous studies [254]. The main part describes the route towards implementation of such undoped a-Si:H buffer layers: First, the passivation properties of (i)a-Si:H on c-Si are analyzed depending on deposition conditions and thickness, and doped/undoped layer stacks to be used as emitter- and BSF units in a-Si:H/c-Si solar cells are developed. In a next step, the resulting solar cell performance after implementation of the buffer layers is analyzed. Thereby, fundamental questions concerning the passivation- and transport mechanism in a-Si:H/c-Si cells are raised. In the following section, the impact of TCO and metal contact deposition on the open-circuit-voltage are explored and a detrimental influence of the metalization step is highlighted. Finally, the results of the chapter are summarized and discussed, and the major scientific questions are formulated which will serve as the leitmotif for the remainder of the thesis.

Figure 4.1: Conversion efficiencies of solar cells based on a-Si:H/c-Si heterojunctions as reached by Sanyo, HZB and other research institutes for cells based on (n)c-Si and (p)c-Si.



4.1. Introduction

At HZB, the start of research on a-Si:H/c-Si heterojunction solar cells dates back to 1997. Unlike Sanyo, who published first results on (n)c-Si based cells already in 1992, primarily the doping-inversed structures¹ on (p)c-Si were investigated at HZB. There was a progressive learning curve for (p)c-Si-based cells, illustrated by the improvements in the conversion efficiencies over the years which are shown in Fig. 4.1. Importantly as well, HZB's excellence historically is on the fundamental research and -analytics side as compared to other solar energy research centers. Thus, a multitude of dedicated analytics tools was developed in the early years of HJ research, including photoelectron spectroscopy, surface photovoltage and photoelectrical characterization which are beyond the standard characterization capabilities in PV research.

The independently confirmed record solar cell conversion efficiencies reached at HZB are 19.8% on (n)c-Si and 17.4% on (p)c-Si. The illuminated I/V curves of the respective cells are shown in Fig. 4.2. Comparing the parameters to the Sanyo record HIT cell (23.0% efficiency with $V_{oc} = 729$ mV, $j_{sc} = 39.5$ mA/cm² and $FF = 80.0$ %), it is obvious that major room for improvement exists for the open-circuit voltage. The (p)c-Si-based solar cell is also inferior with respect to the short-circuit current. As outlined in Section 2.2.5, the open-circuit voltage V_{oc} is closely connected to the minority carrier lifetime, and thus the recombination properties of the device. Already in the original paper by Sanyo [254], it was highlighted that V_{oc} can be improved by inserting a thin undoped a-Si:H buffer layer (IBL) between the doped a-Si:H forming the emitter and the crystalline absorber. Based on the idea that the improved electronic properties of (i)a-Si:H as compared to (p)a-Si:H would lead to a better passivation of the crystalline absorber, the V_{oc} improvement was intuitively explained. As the a-Si:H/c-Si solar cell

¹'Doping-inversed' refers to a structure, where the doping type of all doped layers and the substrate is changed to the opposite type.

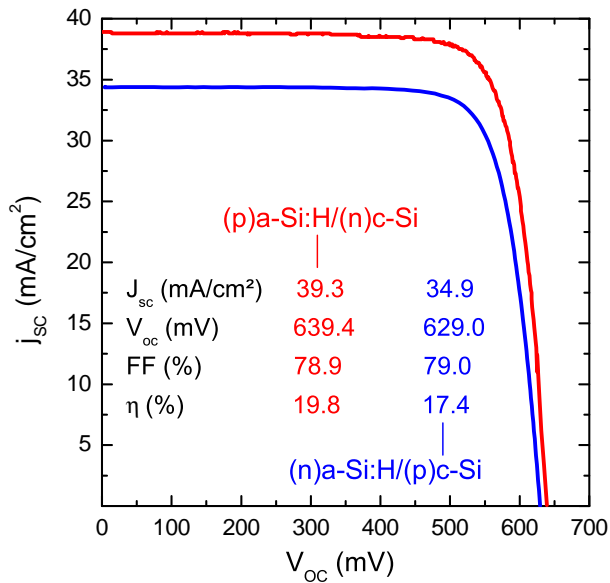


Figure 4.2: Illuminated I/V curves and cell parameters of the best a-Si:H/c-Si solar cells made at HZB (independently confirmed measurements at Fraunhofer ISE).

without IBLs as previously pursued by HZB appears to have reached its limits in terms of V_{oc} , developing undoped buffer layers seems to be a promising approach towards further increasing the cell efficiency.

In the following, the route towards implementation of (i)a-Si:H buffers into the cell concepts based on both (n)c-Si and (p)c-Si substrates shall be outlined. The analysis of this technology development will highlight some technical issues specific to the cell processing at HZB and — more importantly in the context of this thesis — identify fundamental physical questions which are addressed in the following chapters 5-8.

4.2. Inclusion of undoped a-Si:H buffer layers

4.2.1. Phenomenology of c-Si surface passivation by (i)a-Si:H

The first step in the development of passivating interlayers is the search for an optimized and robust PECVD deposition parameter set for (i)a-Si:H deposition which is suited to the given substrate. In previous studies, it was observed that the passivation quality of (i)a-Si:H depends on the PECVD deposition parameters (most notably the deposition temperature and hydrogen dilution) [32, 49, 55, 58, 128, 276], and collaterally also on the c-Si surface orientation which controls the propensity towards epitaxial growth for highly H-diluted plasmas [51, 277]. Depending on the targeted device structure, the relevant c-Si surface topology and -orientation is different: The usual random-pyramid surfaces used for classical HIT-type solar cells have predominantly $\{111\}$ orientation as the pyramid's facets are $\{111\}$ surfaces. Depending on the quality of the texture etching, defective regions of varying contribution are embedded (e.g. at the tips and edges of the pyramids, as well as in the 'valleys' between the pyramids). It was shown that at those regions, epitaxial growth can occur leading to a significant decrease of the passivation quality [174]. In the light of these previous results, it seems reasonable to

Table 4.1.: Passivation by different a-Si:H layer combinations on DSP (n)c-Si{111} and (p)c-Si{111}. Effective lifetime values were taken at the excess carrier density corresponding to 1 sun illumination, and the implied V_{oc} was calculated from the photoconductivity. It is obvious that the junction under (p)a-Si:H is most critical. Note that similar τ_{eff} values for different V_{oc} values are possible due to the different thickness of the two substrate types (cf. Section 2.2.5).

| Structure | DSP (n)c-Si{111} ¹ | | DSP (p)c-Si{111} | |
|-----------|-------------------------------|--------------------------|-----------------------------|--------------------------|
| | τ_{eff} (μs) | implied V_{oc} (mV) | τ_{eff} (μs) | implied V_{oc} (mV) |
| n/X/n | 918 | 683 | 950 | 710 |
| p/X/p | 183 | 616 | 42 | 625 |

¹ This substrate did not have a state-of-the-art bulk lifetime, therefore the reached V_{oc} values do not represent the full passivation potential of the respective layer combinations.

include double-side polished (DSP) c-Si{111} wafers into the considerations for passivation testing, representing the model system for an ideal texture-etched surface. Further, for back-contacted SHJ (BC-SHJ) solar cells, the relevant surface is the {100} (back-)surface as the front side of the wafer must also be texture-etched which requires a {100} surface. Again, a polished surface would be a model system, industrially relevant however is the KOH-etched {100} surface as occurring in the production processing after the KOH defect removal etch following the wafer sawing. This leads to four interesting surface orientations: Polished c-Si{111} and c-Si{100} as model systems for classical SHJ and BJSJ SCs, as well as the textured c-Si{100}, i.e. a pyramidal surface with {111} facets, and KOH-etched c-Si{100}.

Identification of the critical junction

It was demonstrated in numerous publications that the inclusion of (i)a-Si:H buffer layers has a positive effect on the passivation in a solar cell structure [48, 49, 76, 254, 277]. To identify the junction limiting V_{oc} in the present solar cells, symmetrical heterostructures comprising only the standard emitter- and BSF layers were processed on DSP (n)c-Si and (p)c-Si substrates with {111}-orientation. The effective lifetime of the samples was measured with PCD and is listed in Table 4.1 together with the implied V_{oc} at 1 sun illumination.

It is obvious that in the present solar cells, the (p)a-Si:H layer is responsible for the major part of the recombination. On both substrate types, the (p)a-Si:H layer leads to effective lifetimes well below 200 μs , and implied V_{oc} of < 625 mV. The (n)a-Si:H layer provides significantly better passivation, with implied V_{oc} > 680 mV. Thus, the junction under (p)a-Si:H is highlighted to be most delicate concerning passivation, needing to be shielded in order to reach higher V_{oc} values.

The following development of IBLs will be performed mainly on (n)c-Si, being the focus of current HZB activities and possessing the higher efficiency potential [239]. The task is now twofold: First, to identify a PECVD parameter set which leads to the

best passivation on a given surface with a reasonable (i)a-Si:H thickness. Secondly, to explore the interplay of the undoped and doped layer in terms of resulting passivation when thickness of the (i)a-Si:H layer and doping of the (p/n)a-Si:H layer are varied.

Choice of (i)a-Si:H deposition parameters

In the course of this work, the (i)a-Si:H parameter sets listed in Table 4.2 were developed, motivated by the following considerations: The starting point was defined by the LP parameter set being the standard at HZB. As one would intuitively assume that an increased electronic quality of the passivation layer leads to a better passivation, it seems reasonable to explore the PECVD deposition phase diagram searching for (i)a-Si:H recipes that yield a better layer quality than the LP standard parameter set. It is known that by diluting the silane deposition precursor with hydrogen, the quality of the resulting a-Si:H layers can be increased in terms of microscopic parameters such as the bulk defect density or hydrogen microstructure [82, 91, 155]. Therefore, a typical dilution ratio of $R_H = [H_2]/[SiH_4] = 10$ at a slightly higher pressure (necessary to ignite the plasma at low power densities) was chosen as a second deposition parameter regime, termed 'medium pressure' (MP). As the MP growth rate r_g is lower by roughly a factor of three as compared to LP which would heavily affect the applicability for industrial processes, a 'high pressure' (HP) regime was explored as the third choice, having $R = 10$ as well and yielding exactly the same growth rate as the LP parameter set.

Besides the combination of chamber pressure p_C and hydrogen dilution rate R_H , the substrate temperature T_{sub} was considered as a second parameter dimension: On the one hand, lowering T_{sub} decreases the propensity towards epitaxial growth, on the other hand it was shown that layers grown at low T_{sub} display a drastically reduced passivation potential in the as-deposited state which can be cured by annealing around 200°C [55, 58]. Thus, lowering T_{sub} from the usual 210°C standard at HZB is interesting to explore both suppression of epitaxy and annealing effects.

Note that in the following, the a-Si:H deposition parameter sets will be identified by their *nominal* deposition temperature T_{depo} which is not identical to the true substrate temperature T_{sub} ².

Passivation properties of (i)a-Si:H layers

In a first step, these parameters were applied to deposit 10 nm thick (i)a-Si:H layers on both sides of {111}-oriented DSP (n)c-Si substrates. The results are shown in Fig. 4.3. It is obvious that for each T_{depo} there is a trend LP → HP → MP in terms of lifetime in the as-deposited state, while for a fixed parameter set τ_{eff} increases with T_{depo} . The only notable anomaly is for the MP250 parameter set leading to a lower τ_{eff} than LP250 or HP250³.

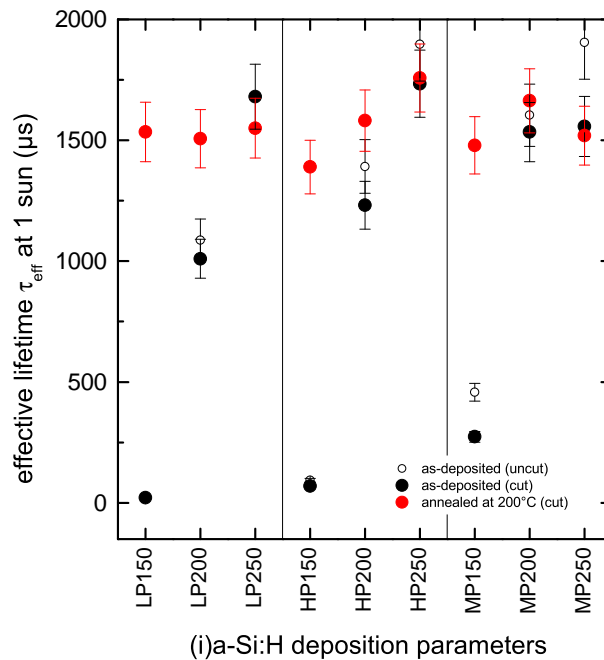
²For instance, 'LP250' denotes a nominal deposition temperature of $T_{depo} = 250^\circ\text{C}$, however the true substrate temperature is $T_{sub} = 210^\circ\text{C}$. This nomenclature is employed for consistency with the convention used at the author's institute.

³This may be due to the fact that the samples had to be cut for FTIRS measurements which were performed before the annealing step. The open circles in Fig. 4.3 show τ_{eff} values before cutting (which cannot be compared to the annealed data), showing a considerable decrease in τ_{eff} for the

Table 4.2.: PECVD deposition parameters of the (i)a-Si:H layers analyzed in this thesis. For each parameter set, three substrate temperatures were used ($T_{\text{sub}} = 210^\circ\text{C}$, 170°C or 130°C , corresponding to the nominal deposition temperatures $T_{\text{depo}} = 250^\circ\text{C}$, 200°C or 150°C) yielding a total of 9 different samples.

| Name | p_C (mbar) | R_H | d_{el} (mm) | P (mW/cm ²) | r_g Å/s |
|----------------------|-----------------|-------|-------------------------|------------------------------|--------------|
| low pressure (LP) | 0.5 | 0 | 30 | 9.4 | 1.8 |
| medium pressure (MP) | 1 | 10 | 30 | 9.4 | 0.53 |
| high pressure (HP) | 4 | 10 | 20 | 15.1 | 1.8 |

Figure 4.3: Effective lifetime at 1 sun obtained with 10 nm thick (i)a-Si:H passivation layers deposited at different PECVD parameter sets on {111}-oriented DSP (n)c-Si, in the as-deposited state (black) as well as after annealing for 5' at 200°C . The samples were used for FTIRS measurements and had to be cut to fit into the spectrometer. The open black circles show the as-deposited values, full symbols the values after cutting. There is a slight detrimental effect on most samples, which is most prominent for MP250.



Upon annealing, there is an increase in τ_{eff} for the samples deposited at 200 or 150°C , while the lifetime stays essentially constant for the 250°C -samples. All samples reach good passivation after annealing and thus the overall trends in terms of τ_{eff} visible in the as-deposited data are very much leveled out, but still mainly persist after annealing⁴. To summarize, there is a pronounced dependence of τ_{eff} on the (i)a-Si:H deposition conditions in the as-deposited state, which persists to a lesser extent after annealing when all samples reach good passivation. There is some indication that the (i)a-Si:H layer properties impact the final passivation, as e.g. the layer properties are expected to be better for the deposition with H dilution. Indeed, in chapter 8 it will be shown

MP250 sample upon cutting. This may be due to microscopic cracks introduced during the cutting procedure and explains the deviating behavior of the MP250 sample — indeed, the τ_{eff} value before cutting is highest for MP250, consistent with the trend just outlined.

⁴with the exception of LP150 and the MP250 sample which is supposedly affected by the cutting as discussed above

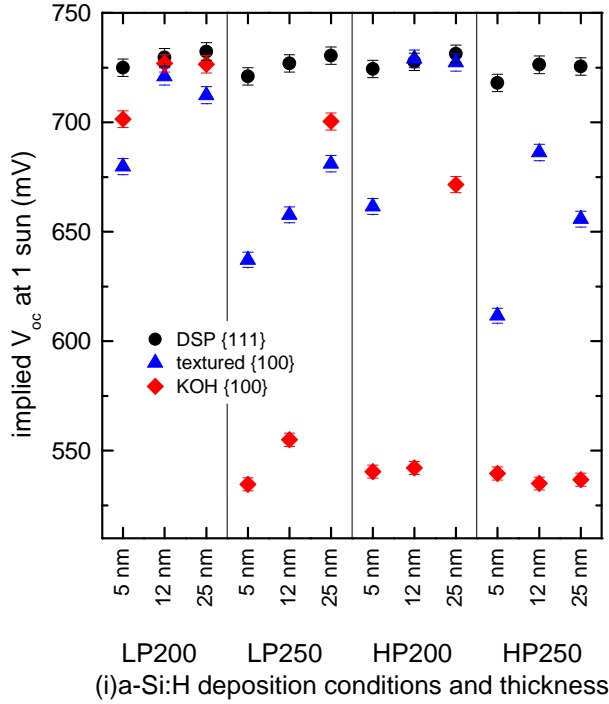


Figure 4.4: Implied open-circuit voltage V_{oc} at 1 sun obtained with (i)a-Si:H passivation layers of varying thickness, deposited with four different PECVD parameter sets on {111}-oriented DSP c-Si, texture-etched c-Si{100} and KOH-etched c-Si{100}. All samples have been annealed to reach saturation V_{oc} values.

that the (i)a-Si:H passivation depends on the microscopic properties of the passivation layers, which are elucidated in chapter 6.

Dependence of passivation on surface topology

In a next step, four exemplary deposition parameter sets are tested on different c-Si surfaces. These are the LP and HP parameter sets, having application-relevant growth rates, for $T_{depo}=170^{\circ}\text{C}$ and 210°C . The lifetime data are analyzed in terms of the implied open-circuit voltage, which is easiest to compare between substrates of different thickness (cf. section 2.2.5). The resulting implied V_{oc} are shown in Fig. 4.4 for annealed (i)a-Si:H layers with three different thicknesses on {111}-oriented DSP c-Si, texture-etched {100}-oriented c-Si and KOH-etched c-Si{100}. Note that the thickness values given in the figure are nominal thicknesses. For textured surfaces, the real thickness is smaller by a factor of 1.7 due to the geometrical surface area enhancement by the pyramidal structure, while the factor is unknown for the KOH-etched surface (but < 1.7). The resulting picture is quite diverse:

- For the DSP c-Si{111}, there is no pronounced difference in implied V_{oc} depending on the deposition parameter set (consistent with Fig. 4.3), and only a slight dependence on the (i)a-Si:H layer thickness. The resulting passivation is on an extremely high level with implied V_{oc} values of up to 732 mV.
- On textured c-Si{100}, the picture is more subtle: The highest implied V_{oc} are reached for the thicker layers deposited at $T_{depo} = 200^{\circ}\text{C}$. For these parameters and layer thicknesses ≥ 10 nm the implied V_{oc} is comparable to the DSP substrate.

For $T_{\text{depo}} = 250^\circ\text{C}$, the maximum implied V_{oc} is significantly lower, which may be taken as indication for partial epitaxy, e.g. at defect-rich regions [174]. The sudden increase of implied V_{oc} from 5 to 12 nm nominal layer thickness may be due to only partial surface coverage for the thinnest layers of effectively only 3 nm thickness.

- For KOH-etched c-Si{100}, the differences are most pronounced. While the LP200 parameter set seems to be robust (implied V_{oc} above 700 mV already for the lowest thickness, saturation values identical to the DSP reference), all other sets lead to very poor passivation with implied V_{oc} mainly below 550 mV. It is tentative to conclude that these layers grow epitaxially, which leads to an essentially depassivated c-Si surface. The comparably high V_{oc} values reached for the 25 nm thick LP250 and HP200 layers are surprising⁵.

Intermediate summary

From the results presented above it becomes obvious that the passivation properties of (i)a-Si:H on c-Si are manifold: There are dependencies on PECVD deposition parameters, layer thickness, surface orientation and -topology and post-treatment. The clearest picture emerges on the DSP reference surface: The differences in resulting τ_{eff} between different deposition parameter sets are obvious and there seems to be a connection to the bulk layer quality (to be discussed in detail in chapter 8). Annealing improves the passivation of the low- T_{depo} samples, and there is only a slight thickness dependence. On less ideal surfaces, the propensity towards epitaxy on {100}-oriented surfaces or at defective surface features comes into play, rendering the picture more subtle. Here, the best passivation can only be reached for a subset of deposition parameters. Additionally, a closed film — required for pronounced passivation — is only obtained above a certain threshold nominal thickness. Obviously, switching from an ideal to a device-relevant surface, a trade-off between optimum deposition conditions and tendency towards epitaxy is necessary and a naïve reasoning based purely on the results obtained on DSP substrates is misleading.

Thus, from a technological point of view it is obvious that the (i)a-Si:H deposition conditions have to be chosen according to the given task. While the KOH-etched surface requires the LP200 parameter set (out of the range of parameters explored here) and the resulting passivation is comparably insensitive to the layer thickness, the textured surface also allows the HP200 parameters but has a pronounced thickness dependence which has to be taken into account.

In the following, the technological optimization of the passivation layers will be restricted to the parameter sets that work best on the device-relevant surfaces, while the full set of parameters will be retained in the chapters 6,7 and 8 when the more fundamental questions related to the a-Si:H/c-Si heterointerface are treated.

⁵It may well be that the long deposition times lead to a breakdown into amorphous growth and thus the formation of a passivating heterojunction, although this is a somewhat speculative explanation. Note additionally that it was argued recently that the presence of epitaxy must not always be detrimental [47]. Microscopic information from e.g. transmission electron microscopy would be needed to explore the impact of epitaxy in the present case.

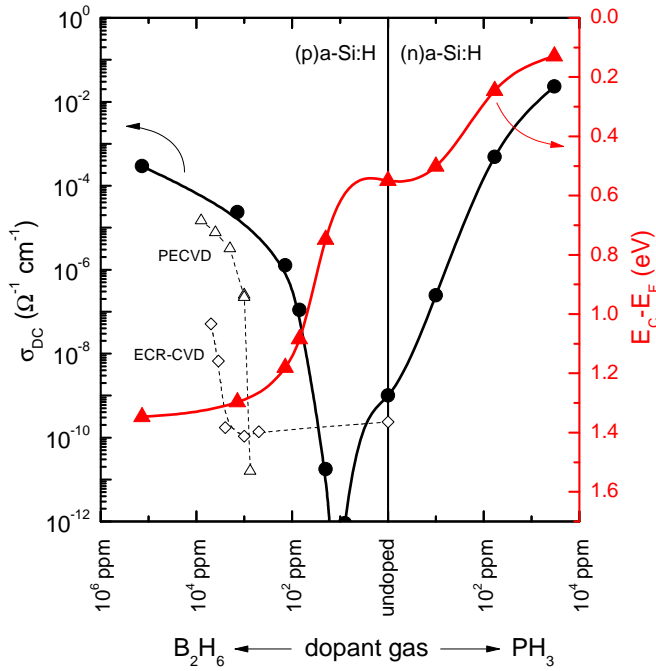


Figure 4.5: Doping efficiency for a-Si:H made by plasma-enhanced chemical vapor deposition. The figure shows the DC conductivity σ_{DC} and the Fermi level position E_F as deduced from activation energies of transport and reproduces data by Spear and LeComber from reference [236]. Additionally, conductivity data obtained at HZB for (p)a-Si:H made by VHF-PECVD and ECR-CVD is shown illustrating the inferiority of ECR-CVD-deposited a-Si:H in terms of external doping efficiency.

4.2.2. Doped a-Si:H layers

It is to be expected that the inclusion of an (i)a-Si:H buffer layer will affect the functioning of the doped top layer as an emitter or source of back-surface field. One aspect to be considered is a possible redistribution of band bending in the structure: As undoped a-Si:H comprises a smaller density of rechargeable defect states as compared to doped a-Si:H, it may not shield the electric field from the c-Si dopant ions immediately at the interface [202]. Further, the doping of the emitter layer in solar cells without IBLs is optimized by balancing the V_{oc} losses due to depassivation (increasing with doping) against FF losses due to insufficient c-Si band bending (decreasing with doping) [130]. This optimum is likely to be shifted upon inclusion of an IBL. Before stacks of doped and undoped a-Si:H are considered as a unit, the nature of the doped a-Si:H shall be briefly elucidated in this section.

In the original paper by Spear and LeComber where substitutional doping in a-Si:H was first demonstrated [42], the external doping efficiency was shown⁶ and an asymmetry between p- and n-doping became obvious. In Fig. 4.5, the original data on the conductivity σ and the Fermi level position relative to the conduction band edge is reproduced⁷. It is obvious that the (p)a-Si:H side is more critical in terms of gas phase doping efficiency. Additionally, a dependence of the doping efficiency on the details of the deposition (technique, setup, parameters etc.) is to be expected. To evaluate the

⁶defined as the ratio of charge carriers in the bands and dopant atoms provided in the gas phase upon deposition

⁷Note that the Fermi level position was deduced from the activation energy of the DC conductivity; a procedure which has to be seen with great care based on today's knowledge on a-Si:H as outlined in section 2.1.1.

doping efficiency of the (p)a-Si:H layers at HZB, the conductivity measured on layers prepared by two different techniques is plotted in Fig. 4.5 alongside the literature data. Initially, the (p)a-Si:H layers were made by ECR-CVD; it became obvious however that the doping efficiency was greatly inferior as compared to the expected textbook behavior⁸. Switching to the PECVD deposition system, the doping efficiency reflected in the conductivity data is much higher than for ECR-CVD, but still slightly lower than the literature data. The reached doping efficiency was considered sufficient, and further discussion shall be omitted here. Most importantly and consistent with textbook data, there is no 'optimum' doping to be determined from the conductivity data alone.

From the general mechanism of doping it is known that the electronic properties of doped layers change significantly with the doping concentration, most notably for (p)a-Si:H [250]. Thus, in order to find the optimum doping to be used in a device, the interplay of doped layers and IBLs must be considered, which will be discussed in the next section.

4.2.3. Development of doped/undoped a-Si:H emitter stacks

Impact of doped a-Si:H on effective lifetime

As shown above, the critical junction on (n)c-Si is the emitter junction, i.e. the junction under the (p)a-Si:H. Therefore, the effect upon insertion of IBLs into this critical junction was explored. To this end, lifetime data were taken on [(p)a-Si:H]/(i)a-Si:H/(n)c-Si samples with the most robust LP200 IBL parameter set and with varying thickness of the IBL on different substrate morphologies. The doping of the PECVD-deposited (p)a-Si:H top layer was 2500 ppm and the thickness 10 nm. Some (n)a-Si:H top layers at 1000 ppm doping concentration were exemplarily deposited on KOH-etched (n)c-Si{100} for comparison, representing the BSF side of the solar cell. The undoped layers have been annealed before (p)a-Si:H deposition. The results are shown in Fig. 4.6 in terms of Auger-corrected effective minority carrier lifetimes at $6 \times 10^{15} \text{ cm}^{-3}$ excess carrier density. It is obvious that starting from excellent lifetimes for the undoped layers alone⁹, τ_{eff} is significantly decreased by deposition of the (p)a-Si:H top layer. The overall trend versus IBL thickness for the different substrates is almost exactly reproduced, and the relative order of the different substrate morphologies stays the same. For almost all samples, the lifetime decrease is by a factor of 6...8.

Interestingly, for deposition of a (n)a-Si:H top layer, the lifetime degradation is less pronounced and shows no dependence on the (i)a-Si:H layer thickness (gray data points). For the set of data shown in Fig. 4.6 one could even conclude that the n/i stack lifetime is *decreasing* with IBL thickness, however this trend is weak and was not confirmed in successive sample series.

⁸Note that the ECR-CVD conductivity data was taken with a mercury probe setup which has a sensitivity limit of $10^{-10} \Omega^{-1} \text{ cm}^{-1}$, thus the layers with doping $< 10^3$ ppm most probably have even lower conductivity. The PECVD conductivity data was measured with a sensitive photoelectrical setup and is consistent with mercury probe measurements (not shown here), but accurate down to $10^{-12} \Omega^{-1} \text{ cm}^{-1}$.

⁹Note that the same order of τ_{eff} for different substrates and slight thickness dependence as for LP200 in Fig. 4.4 is visible

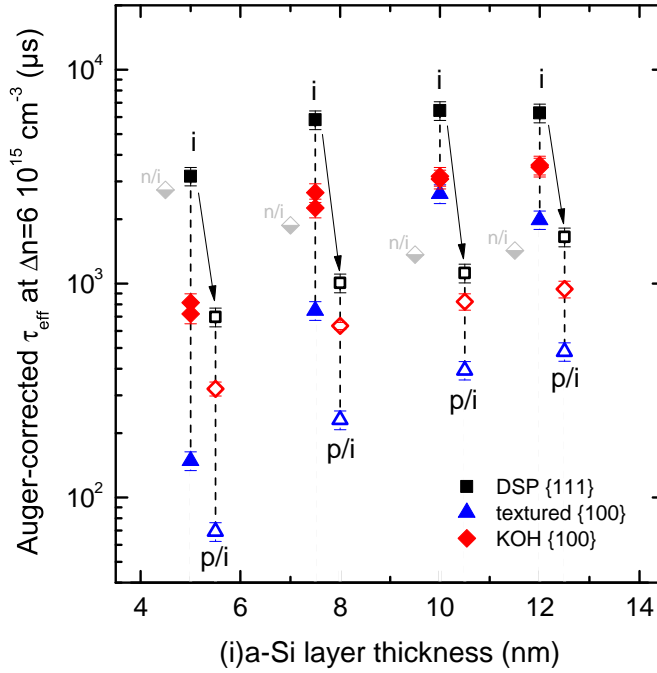


Figure 4.6: Effective Auger-corrected minority carrier lifetime evaluated at an excess carrier density of $6 \times 10^{15} \text{ cm}^{-3}$ for (i)a-Si:H of varying thickness on different c-Si surfaces. Additionally, the lifetime development upon deposition of (p)a-Si:H top layers of 4000 ppm gas phase doping and 10 nm thickness is shown, revealing a deteriorating passivation upon doped top layer deposition. In gray, the effect of an (n)a-Si:H top layer with 2000 ppm gas phase doping is shown.

The deterioration of passivation upon deposition of a (p)a-Si:H top layer is interesting and lends itself to further analysis. In the following it will be worked out which parameters govern this passivation loss. To this end, the impact of IBL deposition conditions, top layer doping and substrate morphology will be explored.

Dependence on (i)a-Si:H deposition conditions

It was tested whether the nature of the IBL, i.e. its deposition conditions, influence the final lifetime upon deposition of a doped top layer. The choice of (i)a-Si:H deposition parameters was restricted to those that were shown (or expected) to yield the highest τ_{eff} on substrate morphologies relevant for solar cells¹⁰. The (p)a-Si:H top layers had a doping concentration of 4000 ppm. The results are shown in Fig. 4.7 in terms of implied V_{oc} at the minority carrier density corresponding to 1 sun illumination. The IBLs alone display the same order in implied V_{oc} with respect to deposition conditions as previously found (Fig. 4.3), and approximately the same level of effective lifetime. Upon deposition of (p)a-Si:H, the lifetime is again decreased significantly, while the relative order is preserved. The results are consistent with the data shown in Fig. 4.6 and imply that for a fixed doping level of the top layer, the decrease in τ_{eff} or implied V_{oc} is effectively preserving trends which stem from the details of the buried heterointerface, such as the surface morphology or -orientation of c-Si and the nature of the undoped buffer layer.

¹⁰These were the LP200 parameter set and the three sets deposited at 150°C, complemented by HP250 which yielded the absolute best passivation on DSP c-Si{111} (cf. Fig. 4.3).

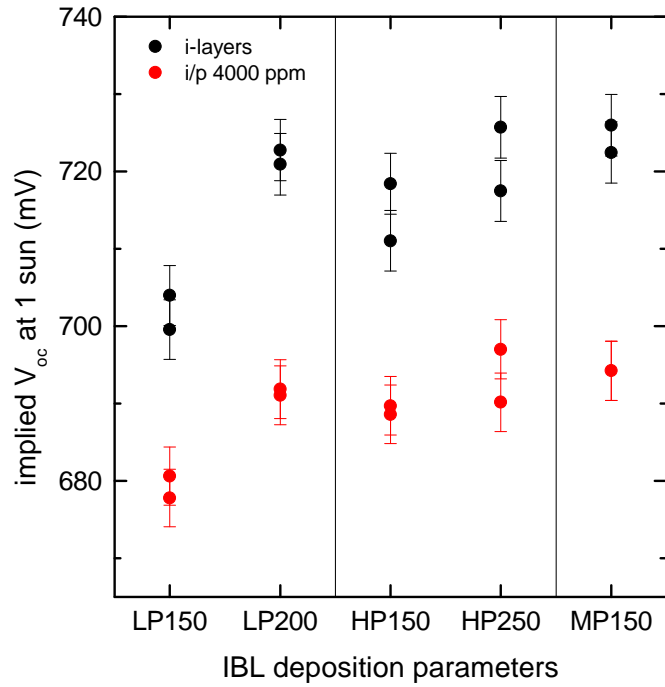


Figure 4.7: Implied V_{oc} for (i)a-Si:H passivation layers of varying deposition conditions (pressure, H dilution and substrate temperature), again evaluated at 1 sun (black data points). Additionally, the lifetime development upon deposition of (p)a-Si:H top layers of 4000 ppm gas phase doping and 10 nm thickness is shown (red data points). Again, the passivation deteriorates upon (p)a-Si:H deposition, preserving the relative order of the effective lifetime depending on (i)a-Si:H deposition conditions.

Role of (p)a-Si:H top layer doping and surface morphology

In the following, the impact of (p)a-Si:H layer doping on the passivation is explored for (p)a-Si:H layers and (p/i)a-Si:H stacks on {111}-oriented DSP wafers. Fig. 4.8 shows τ_{eff} and implied V_{oc} values for (p)a-Si:H/[(i)a-Si:H]/(n)c-Si stacks with varying (p)a-Si:H doping and IBL thickness. Without IBLs, both lifetime and implied V_{oc} decrease drastically when the (p)a-Si:H doping is increased, as would be expected from the deteriorating electronic quality of the (p)a-Si:H layers, which is known to occur with doping [250]. Indeed, this deterioration was also observed in this thesis as a collapse of (p)a-Si:H band gap and increase of HSM-related hydrogen upon increased B_2H_6 concentration.

When the thickness of the IBL is increased, the overall level of both τ_{eff} and V_{oc} is enhanced: Most pronounced is the step from 0 nm to 5 nm, a further slight increase is observed going to 7 nm and 10 nm, consistent with the results on single i-layers (Figs. 4.4 & 4.6). For each IBL thickness, the general trend that increased top layer doping leads to inferior passivation seems to hold, however with some scatter in the data. Although this statement is hard to make based purely on the data shown in Fig. 4.8, it seems to be a general trend as it is also present for other data sets, e.g. in those taken on varying substrate morphology which are described next: Fig. 4.9 again shows τ_{eff} and implied V_{oc} development upon changing the doping of an (p)a-Si:H top layer. This time, the thickness of the IBL is fixed to 6...7 nm, but the substrate morphology is varied. Again, besides the DSP c-Si{111} whose data are shown as well in Fig. 4.8, textured c-Si{100} and KOH-etched c-Si{100} were used as substrates. While the overall levels of τ_{eff} and V_{oc} are differing depending on the substrate morphology as also found for pure IBLs in Fig. 4.6, the general trend versus the top layer doping is the same: Both τ_{eff} and implied V_{oc} decrease upon increasing the doping level.

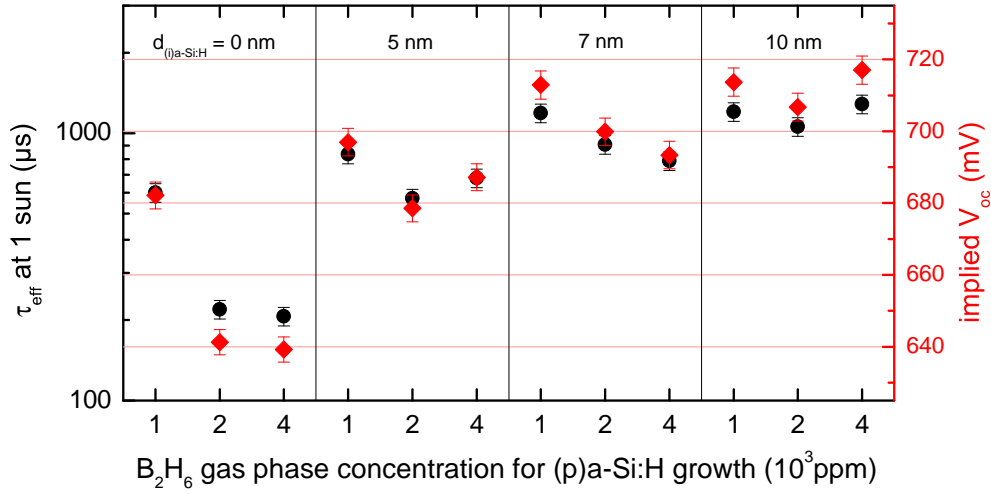


Figure 4.8.: Effective minority carrier lifetime and implied V_{oc} evaluated at the excess carrier density corresponding to 1 sun for (p/i)a-Si:H stacks with varying (i)a-Si:H thickness and (p)a-Si:H doping, detailing the phenomenon of passivation deterioration upon doped (p)a-Si:H top layer deposition. Substrates were double-side-polished (n)c-Si{111} wafers.

Doping-inversed structures

To complement the picture drawn above, the doping-inversed structures are analyzed as well. Note that it was found that (n)a-Si:H acting as BSF on (n)c-Si did not lead to a pronounced decrease in lifetime [57]. However, this could be different when employed as emitter layer on a (p)c-Si substrate. To this end, (n)a-Si:H with varying doping concentration was deposited on DSP (p)c-Si{111} with 1 Ωcm resistivity, with and without IBLs with varying thickness and the LP200 parameter set. The results are summarized in Fig. 4.10. Without IBLs, the behavior closely resembles the trend observed for (p)a-Si:H on (n)c-Si: τ_{eff} and thereby the implied open-circuit voltage decrease with increasing gas phase doping of the (n)a-Si:H layer. The decrease is not as drastic as for the doping-inversed structures which may be taken as evidence for the better electronic quality of (n)a-Si:H as compared to (p)a-Si:H¹¹ [250].

Most interesting is the trend for (n)a-Si:H deposited on IBLs, as shown in the middle and right panel of Fig. 4.10: In contrast to the results for the doping-inversed structures, the passivation does not monotonically deteriorate. Instead, starting from a very high level it rises steeply for the lowest gas phase PH₃ concentrations, reaches a maximum for about 1000 ppm PH₃ and decreases with a very small slope for the highest dopant gas phase concentrations. There is no notable difference between 4 nm and 7 nm, apart from an even smaller slope of the τ_{eff} decrease for highest PH₃ concentrations in the case of 7 nm IBL thickness.

¹¹Note that due to the higher external doping efficiency of PH₃ (cf. Fig. 4.5) the concentration of dopant atoms actually incorporated into the amorphous network as active dopants is expected to be much larger in the case of (n)a-Si:H. Nevertheless, the resulting passivation of (n)a-Si:H is better for a given gas phase doping concentration than that of (p)a-Si:H.

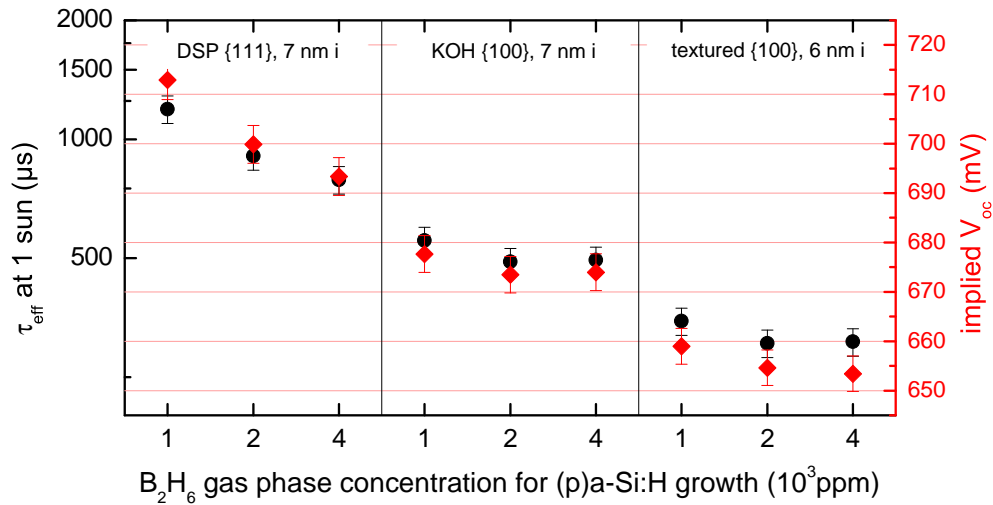


Figure 4.9.: Effective minority carrier lifetime and implied V_{oc} evaluated at the excess carrier density corresponding to 1 sun for (p/i)a-Si:H stacks with varying (p)a-Si:H doping on different c-Si surface morphologies. It is obvious that the passivation deterioration is of similar magnitude for the different c-Si surface types.

Intermediate summary

The results presented in this section have immediate significance for device optimization. The following has been shown:

- As compared to a direct deposition of doped a-Si:H layers onto the crystalline substrate, the presence of an undoped buffer layer always leads to a better passivation.
- Starting from an undoped passivation layer on an (n)c-Si substrate, deposition of a doped (p)a-Si:H top layer always leads to a considerable decrease of the passivation. This effect seems to be a general feature and always proceeds by about the same factor for a fixed (p)a-Si:H doping. Higher gas phase boron concentrations lead to stronger degradation of the IBL passivation. Trends in the passivation of the single IBLs, e.g. depending on IBL thickness or -deposition conditions, are preserved.
- For stacks of (n)a-Si:H and undoped passivation layers on (p)c-Si substrates, the passivation is *increased* for low gas phase phosphorous concentrations and slightly decreased for doping levels > 1000 ppm.

It is suggested that the electronic quality of the doped layers alone determines the passivation in the absence of IBLs. However, there is no intuitive explanation for the difference in the behavior of doping-inversed emitter structures which is observed *in the presence of undoped buffer layers*. Later it will be argued that for IBLs sandwiched between the doped a-Si:H and the c-Si absorber a Fermi level shift at the interface as imposed by the doped a-Si:H top layer causes the varying passivation, as recently

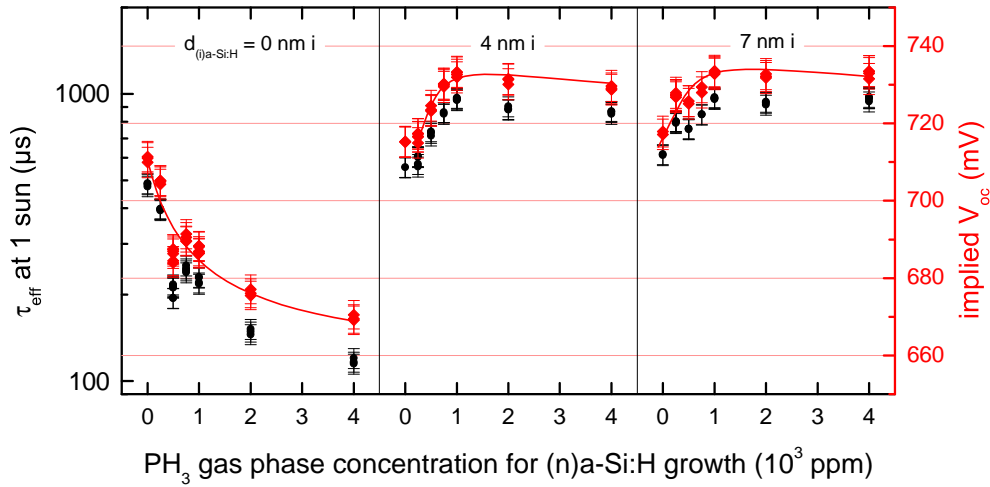


Figure 4.10.: Effective minority carrier lifetime and implied V_{oc} evaluated at the excess carrier density corresponding to 1 sun for (n/i)a-Si:H stacks with varying (i)a-Si:H thickness and (n)a-Si:H doping on double-side-polished (p)c-Si wafers. It is obvious that the lifetime development is different to the doping-inversed structures (shown in Fig. 4.8), with an increase of lifetime for the lowest doping concentrations with a successive decrease for higher doping levels.

invoked by de Wolf *et al.* [56, 57]. The differences observed in comparing (p)a-Si:H/(n)c-Si structures with their doping-inversed counterparts are caused by the fundamental asymmetries in the a-Si:H/c-Si properties (asymmetric band offsets, cf. chapter 7; and asymmetric defect creation energies in a-Si:H due to the amphoteric nature of dangling bond defects, cf. section 2.1.1) as will be shown in the later chapters of this thesis. Here it is proceeded drawing the technological conclusions from this section. It has become obvious that in order to fabricate an (n)c-Si based heterojunction solar cell with high V_{oc} , the following recipe seems to be appropriate:

- The back side is the less critical side. Employing an IBL here may have a positive effect (cf. Table 4.1 and Fig. 4.6), but a negligible thickness dependence would allow very thin IBLs to be used.
- The emitter side is most important. Employing an IBL has a positive effect, which depends on the IBL deposition conditions, the c-Si surface condition and the doping of the (p)a-Si:H emitter layer. As the lowest doping leads to the best passivation, a trade-off between passivation and photocarrier extraction efficiency has to be found in the device. The sensitivity towards the c-Si surface orientation and morphology seems to stem from the details of initial a-Si:H growth (being hard to predict *a priori*), and the impact of a-Si:H deposition conditions is suggested to be linked to the (i)a-Si:H electronic quality.

For the doping-inversed solar cell structure, it is to be expected that the back-side is more critical due to the detrimental impact of an unbuffered (p)a-Si:H BSF. In a next step, IBLs are tested in heterojunction solar cell devices based on the recipes developed in this section.

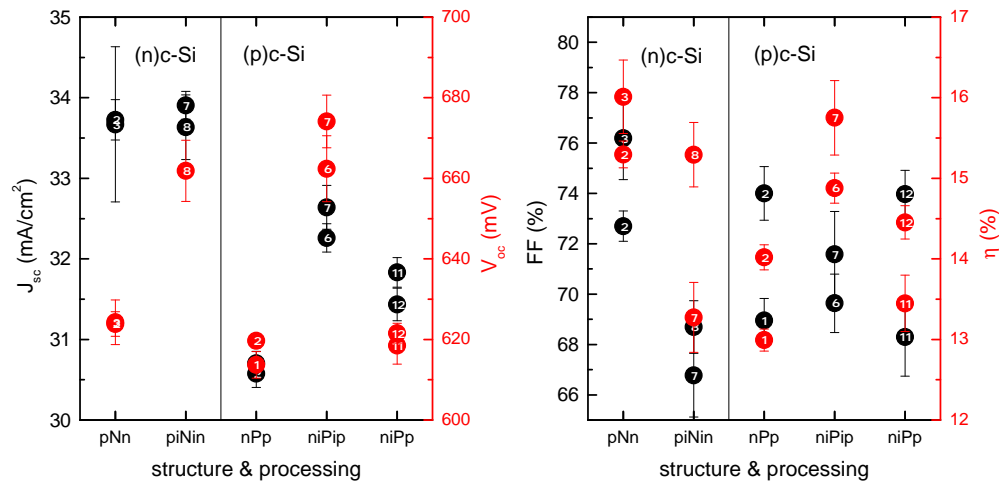


Figure 4.11.: Performance parameters as extracted from illuminated I/V curves at 1 sun of a-Si:H/c-Si heterojunction solar cells processed on textured (n)c-Si{100} and (p)c-Si{100} wafers. The data points correspond to the mean value of the respective parameter of the 5 cells of each wafer displaying the best conversion efficiencies, and the error bars show the standard deviation among these 5 best cells. The numbers in the data points identify the wafers within the series. Left panel shows V_{oc} and j_{sc} and the right panel FF and η .

4.2.4. Implementation of buffer layers and solar cell performance

Phenomenology on n-type wafers

Two solar cell series were processed on both (n)c-Si and (p)c-Si wafers comprising intrinsic buffer layers of 10 nm nominal thickness, i.e. 6 nm real thickness taking into account the geometric area enhancement factor of 1.7 on a textured surface. By the time of the processing, the results shown in Fig. 4.4 were not known yet, therefore the IBLs were deposited with the LP250 parameter set, which is not the optimum for the textured surface. The series consisted of 3" wafers, on each of which 13 separate solar cells were processed (cf. section 3.1). Here and in the following, solar cell results will be discussed in terms of the statistical mean values of illuminated I/V parameters of the 5 cells of each wafer displaying the highest conversion efficiencies. This procedure was chosen as a compromise between statistical significance and elimination of the impact of single pathological cells.

The left side of each panel in Fig. 4.11 shows the results for the series on (n)c-Si wafers. It is obvious that upon inclusion of IBLs, the open-circuit voltage is increased significantly, from around 630 mV being about the level of the current (n)c-Si record cell to around 660 mV with the best single cells approaching 680 mV¹².

There is no change in the values of the short-circuit current which is surprising at first glance as one would expect j_{sc} to decrease due to enhanced parasitic absorption in the

¹²Note that the LP250-IBL in this case yields a satisfactory passivation on most wafers in contrast to the expectation from Fig. 4.4, which underlines that the appearance of epitaxy depends on the exact topology of the texture-etched c-Si surface which was found to vary significantly from batch to batch.

IBL. Possible explanations would be that the added a-Si:H thickness does not significantly affect the absorption properties, or that the loss in the short-wavelength region by the additional a-Si:H thickness is compensated in other wavelengths regions due to better passivation. An IQE analysis will be performed later to decide the cause of this observation.

The right panel of Fig. 4.11 shows FF and conversion efficiency of the (n)c-Si based cells. It is obvious that upon inclusion of IBLs the fill factor is reduced significantly. The effect is as pronounced as to overcompensate the gain in V_{oc} , leading to an overall slight loss in conversion efficiency. This effect has been observed before [65, 252] and is commonly ascribed to the low conductivity of the undoped a-Si:H layers hindering charge carrier transport.

Phenomenology on p-type wafers

Next, the (p)c-Si based heterojunction solar cells are analyzed accordingly (results on the right side of the panels in Fig. 4.11). Here, also cells with IBLs only on the emitter side were processed. Interestingly, inclusion of IBLs leads to an increase in V_{oc} only if IBLs are incorporated on both sides. Buffering just the (n)a-Si:H on the emitter side leads to no change in V_{oc} , which further underlines the conclusion drawn above that (p)a-Si:H layers are most critical concerning passivation and thus require buffering from the c-Si absorber. Interestingly, the short-circuit current increases significantly with V_{oc} in contrast to the (n)c-Si based cells.

In the right panel it is seen that FF does not suffer markedly from inclusion of IBLs in the case of (p)c-Si substrates, comparing however to rather low FF values for the reference cells without IBLs in this series. Due to the overall low level of j_{sc} no improvement in conversion efficiency is reached compared to the (p)c-Si record cell although V_{oc} and j_{sc} were increased at approximately constant FF as compared to the reference cells in the same series. Reflectance and IQE data will be analyzed next to reveal the reason for the low j_{sc} values in the two cell series.

Cause for low j_{sc} values: Analysis of reflectance data

First, the reflectance of selected solar cells will be analyzed to find an indication for the low j_{sc} values observed in the two cell series presented above. Fig. 4.12 shows the spectral reflectance $R(\lambda)$ for the record solar cells on (p)c-Si and (n)c-Si substrates and exemplary $R(\lambda)$ data for two cells from the present cell series. It is obvious that $R(\lambda)$ qualitatively increases in the same order as the j_{sc} of the respective cells decreases (cf. values in the figure). To quantify the impact of $R(\lambda)$ the quantum efficiency is analyzed next:

In Table 4.3, the short-circuit current densities for the four cells whose $R(\lambda)$ was shown in Fig. 4.12 as obtained by different methods are listed: a) under illuminated I/V; b) by integrating over a textbook AM1.5 solar spectrum weighted by $\eta_{EQE} = (1 - R)\eta_{QE}$ (right part of equation 3.4); c) by taking the measured η_{QE} and assuming the reflectance properties of the record cell; or d) by assuming the η_{QE} of the record cell with respective doping type and taking the measured $R(\lambda)$. Note that for the (n)c-Si record cell, the

Figure 4.12: Spectral reflectance data for solar cells from selected wafers of the cell series on (n)c-Si and (p)c-Si analyzed above. The area fraction covered by the grids is identical for all cells, thus a quantitative comparison is possible. It is obvious that the overall level of the reflectance as judged by the eye correlates with the short-circuit current values reached by the respective cells. In the text, a quantitative analysis based on integrating over the reflectance data is discussed.

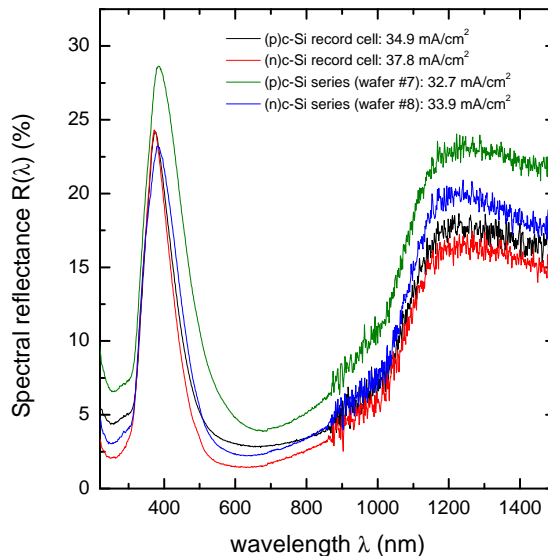


Table 4.3.: Short-circuit current values j_{sc} for the (n)c-Si and (p)c-Si record solar cells and two representative cells from the two series discussed above, as obtained by different methods. All values are in mA/cm^2 .

| Method | (n)c-Si based | | (p)c-Si based | |
|------------------------|------------------------|----------|---------------|----------|
| | record cell | wafer #8 | record cell | wafer #7 |
| a) illuminated I/V^2 | 37.8/39.3 ¹ | 33.9 | 34.9 | 32.7 |
| b) EQE | 36.4 | 35.7 | 34.1 | 34.4 |
| c) IQE + record R | 36.4 | 36.2 | 34.1 | 35.5 |
| d) record IQE + R | 36.4 | 35.9 | 34.1 | 33.1 |

¹ This value was measured at Fraunhofer ISE CalLab.

² Measured at HZB.

j_{sc} value measured at HZB will be considered in the following to be consistent with the illuminated cell parameters of the cell series measured on the same equipment.

First of all it is obvious that there is a discrepancy between the illuminated I/V data and the j_{sc} values deduced from the EQE data. While the EQE-derived j_{sc} are slightly lower than the I/V -measured j_{sc} for the record cells, they are by about $1.5 \dots 2 \text{ mA}/\text{cm}^2$ larger for the current cell series. This points towards a calibration problem with the sun simulator, e.g. drift in the Tungsten lamp characteristics over time affecting the spectral mismatch or changes in the reference solar cell. This $5 \dots 6\%$ error in the illumination density would lead to an underestimation of the overall cell efficiency by about 1% absolute, thus being relevant for the absolute classification of the solar cells. Here, we are interested in relative changes due to the insertion of IBLs, therefore the EQE-derived j_{sc} values will be compared in the following to circumvent errors arising from the (non-trivial) calibration of the sun simulator.

Judging from the EQE, the difference in j_{sc} between the present cells and the record cells are not that pronounced. On (n)c-Si, the current is lower by $0.7 \text{ mA}/\text{cm}^2$ while on

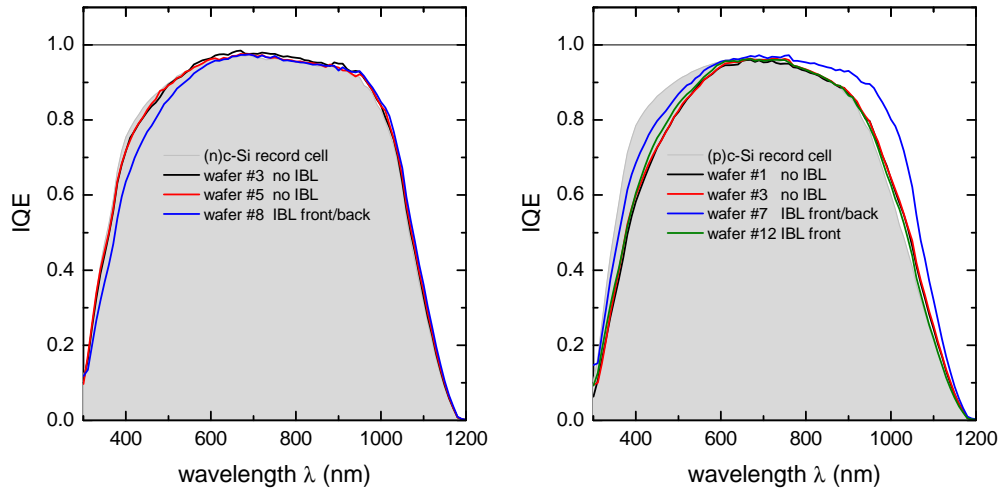


Figure 4.13.: Internal quantum efficiency (IQE) data measured on selected solar cells from the two series on (n)c-Si and (p)c-Si (lines), as well as the IQE taken on the respective record solar cells for comparison (gray area). The main findings are a loss of low-wavelength IQE upon increasing the a-Si:H thickness on the emitter side due to parasitic absorption, and a pronounced gain on the long- λ side due to the decrease in backside recombination upon inclusion of IBLs for (p)c-Si based cell. Further details are discussed in the text.

(p)c-Si it is even higher by 0.3 mA/cm^2 . This observation contrasts with the obviously inferior reflectivity properties seen in Fig. 4.12 and thus lends itself to further analysis. To this end, j_{sc} was calculated assuming the reflectivity properties of the record cells, leading to the values shown in the third line of Table 4.3: Indeed, it is shown that for the current cell series, j_{sc} could be increased by $0.5 \dots 1 \text{ mA/cm}^2$ with a more effective light-trapping. Thus, the inferior j_{sc} seen in the illuminated I/V data in Fig. 4.11 is partly due to a mis-calibrated I/V measurement and partly due to inferior light trapping properties of the substrates used.

Analysis of IQE data

Next, the impact of the IQE is highlighted by calculating j_{sc} with the measured R data but assuming the IQE of the record cells (fourth line in Table 4.3): While the (n)c-Si based cell j_{sc} increases by 0.2 mA/cm^2 , it decreases significantly by 1.3 mA/cm^2 for the (p)c-Si based cell. This highlights that the IQE of the present (n)c-Si-based cell is slightly inferior while it is significantly better for the (p)c-Si based cell. In the latter case, the poor reflectivity properties prevent an excellent current value.

In Fig. 4.13, the IQEs of the record cells are compared to representative IQEs of the current cell series. As compared to the (n)c-Si record cell, the (n)c-Si-based cells without IBLs show a similar behavior. While a slightly inferior IQE in the short-wavelength range is observed, these cells perform subtly better for large λ . Most prominent is the loss in the $300 \dots 600 \text{ nm}$ range upon inclusion of an IBL. This is most likely due to parasitic absorption in the additional a-Si:H thickness provided by the IBL, which un-

derlines the necessity to make the IBL as thin as possible¹³.

For the (p)c-Si cells it must be noted that irrespective of the existence of an IBL the low- λ IQE is always inferior as compared to the record cell. This is most likely due to the fact that the (n)a-Si:H emitter was only ≈ 7 nm thick in the (p)c-Si record cell as compared to 10 nm in the current cells. For the (p)c-Si based cells, the low- λ behavior is slightly *better* for the cells *with* IBL, opposite to the trend on (n)c-Si. The reason for this discrepancy is unknown.

Most striking in the comparison of the (p)c-Si based cells is the long-wavelength behavior of the cells comprising IBLs on the back side (e.g. wafer #7), which is very pronouncedly improved as compared to the record cell. This improvement for $\lambda > 800$ nm is the cause for the 1.3 mA/cm^2 gain as compared to the record cell that could be realized on substrates comprising good light trapping, resulting from the analysis shown in Table 4.3. Here, the improved back-side passivation is clearly seen in the IQE.

To summarize this paragraph it can be stated that (p)c-Si solar cells benefit from IBLs mainly on their backside which leads to an increase in V_{oc} through better passivation and collaterally in j_{sc} by IQE improvement while the FF is essentially unaffected. (n)c-Si based cells on the other hand benefit at the front side, leading to increased V_{oc} by better passivation but slightly lower j_{sc} most likely due to parasitic absorption losses and a significantly decreased FF .

Impact of buffer layer thickness

While (p)c-Si based cells were shown to widely benefit from IBLs, HJ cells on (n)c-Si seem to be much more critical: The crucial interface under the poor (p)a-Si:H layer is at the front side, in the middle of the space-charge region at the p/n junction. Therefore, the improved passivation is only effective under V_{oc} conditions (leading to a constant j_{sc}), the parasitic absorption poses narrow margins on the maximum IBL thickness and FF losses seem to play an important role, most likely due to transport barriers by the weakly conductive (i)a-Si:H. In the following, these interplays shall be elucidated in more detail.

Fig. 4.14 shows the illuminated I/V results of a cell series with varying IBL thickness (LP250 parameter set) on (n)c-Si, and two reference samples processed in the same series with 10 nm IBL thickness on (p)c-Si. The data from the cell series analyzed above are shown again (open symbols), and stars mark the record solar cell parameters. In the left panel it can be seen that on (n)c-Si the FF gradually decreases with increasing IBL thickness, as would also be expected based on the data shown in Fig. 4.11. The (p)c-Si based samples display reasonable fill factors also with 10 nm IBL, pointing towards a

¹³Note that for c-Si homojunction solar cells, one would expect a gain in the low- λ IQE from improved front-side passivation. Here, there is a net loss of current associated with short absorption lengths although the front side passivation is significantly enhanced by the passivating (i)a-Si:H, e.g. reflected in a V_{oc} increase by > 40 mV seen in Fig. 4.11. Note however that it is not to be expected *a priori* that the low- λ response is affected by the passivation of the heterointerface, as the dominant recombination in a-Si:H/c-Si solar cells takes place *in the space-charge region* and not at the front surface as for classical c-Si cells. It may well be that under the j_{sc} conditions at which IQE data are taken, the recombination properties of the front-side p/n junction are not affecting the output current.

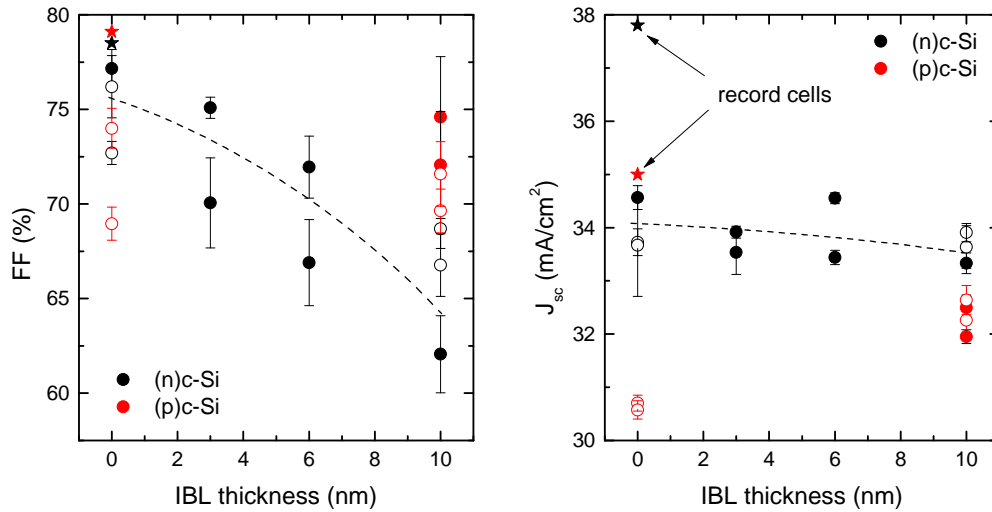


Figure 4.14.: Variation of solar cell fill factor FF and short-circuit current density j_{sc} with the (i)a-Si:H buffer layer thickness on (n)c-Si and (p)c-Si substrates. Open symbols reproduce the values from the solar cell series shown in Fig. 4.11, while stars mark the parameters of the record solar cells. It is obvious that increasing the IBL thickness leads to a significant decrease in the FF values on (n)c-Si, while FF is approximately constant with IBL thickness on (p)c-Si. This observation implies differences in the charge carrier transport between these structures. The difference in the reaction of j_{sc} upon IBL inclusion on the other hand is due to the different impact of a passivation improvement at the back-side (as on (p)c-Si) or at the front-side (as on (n)c-Si) on charge carrier collection.

much simpler charge carrier extraction also in the presence of an IBL. This aspect will be discussed in more detail in chapter 7, where the exact band alignment at the HJ is elucidated.

The right panel shows the j_{sc} development upon IBL thickness variation. The overall level of j_{sc} is of the order of the data presented above and the only slight decrease in j_{sc} is consistent with the trend seen in Fig. 4.11.

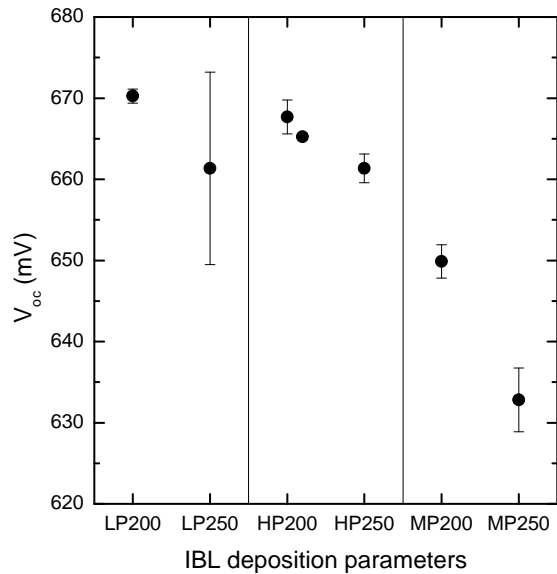
As shown in Fig. 4.4, textured c-Si{100} is critical concerning the choice of IBL deposition conditions, and the overall level of τ_{eff} is lower than on DSP c-Si{111}. To fully explore the passivation potential of the different IBLs in the solar cell device and to exclude a possible impact of the substrate morphology on the cell parameters it seems reasonable to process a solar cell series on DSP substrates. These cells will be described in the following paragraph.

DSP solar cells

The solar cell series on (n)c-Si DSP substrates (the same substrates as used for the passivation tests) comprised IBLs with 5 nm thickness deposited at six different (i)a-Si:H parameter sets¹⁴. The (p)a-Si:H was deposited using the ECR-CVD deposition system at 25000 ppm gas phase boron concentration for the emitter deposition, corresponding to ≈ 1000 ppm gas phase doping in PECVD-deposited layers (cf. Fig. 4.5). Fig. 4.15

¹⁴LP, MP and HP, each deposited at 210°C and 170°C.

Figure 4.15: Plot of solar cell V_{oc} versus (i)a-Si:H buffer layer deposition conditions. The absolute level of V_{oc} is much lower than expected from the implied V_{oc} values measured during the emitter stack development (cf. Figure 4.7). Additionally, the relative order of the V_{oc} values does not correspond to the one observed in the lifetime measurements. This points towards an extrinsic effect which deteriorates the passivation during the back-end steps of the cell processing.



shows the V_{oc} values reached for different IBL deposition conditions. The results are very surprising, if compared to the expectations based on the analysis of p/i stacks (cf. Figs. 4.7, 4.8 & 4.9). First of all, no V_{oc} values in excess of 680 mV are reached. Although the small short-circuit current densities resulting from the high reflection losses of the DSP substrates ($j_{sc} = 22 \dots 28 \text{ mA/cm}^2$) lead to smaller V_{oc} , this effect cannot explain the discrepancy. Even if subjected to an increased illumination density leading to $j_{sc} = 40 \text{ mA/cm}^2$ the best cell has only $V_{oc} = 700 \text{ mV}$, still lower than expected. Secondly, the order of the V_{oc} values is almost directly inverse to that expected from Fig. 4.7 and the 'IBL layer quality' argument: The IBLs deposited at the poorest conditions, requiring thermal post-treatment, lead to the highest V_{oc} .

These observations lead to the presumption of extrinsic effects to be co-determining the passivation and thus the open-circuit voltage which is reached in the current solar cells. It is suggested that there are effects in the processing scheme detrimental to the passivation of the heterointerface which become only apparent at a low D_{it} level. Note that in terms of D_{it} , the difference between $V_{oc} = 640 \text{ mV}$ (being the standard without IBLs) and 680 mV is a factor of 1/10, and between 640 mV and 710 mV a factor of $< 1/50$. Thus, there could be technological issues pinning D_{it} at a level corresponding to $V_{oc} = 680 \text{ mV}$ and therefore preventing to reach higher V_{oc} . In the next section, the process flow is checked for such detrimental effects. The cell series just presented will be returned to in section 7.6.1, when the microscopic properties of the IBLs are correlated with j_{sc} and FF .

Table 4.4.: Development of implied V_{oc} as obtained from PCD measurements upon successive deposition steps during heterojunction solar cell processing for three selected device structures. All values are in mV.

| Structure | (i)a-Si:H | | (p)a-Si:H | ZnO |
|---------------------|-------------|----------|-----------|-----|
| | before ann. | annealed | | |
| ZnO/p/N/n | — | — | 687 | 682 |
| ZnO/p/i/N/i/n | 718 | — | 710 | 713 |
| ZnO/p/i-LP150/N/i/n | 694 | 718 | 711 | 715 |

4.3. Technological issues

4.3.1. Analysis of the solar cell process flow

The impact of the different processing steps on the absorber passivation can be monitored conveniently with the PCD technique up to the metalization step¹⁵.

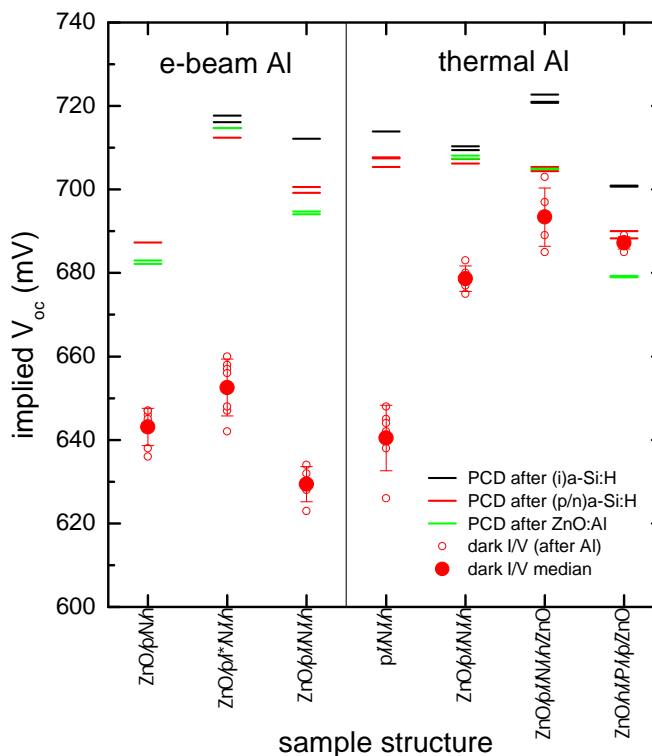
Table 4.4 exemplarily shows the development of implied V_{oc} values upon cell precursor processing. As commonly observed and discussed in detail above, the effective lifetime deteriorates upon (p)a-Si:H deposition on top of an IBL. During the successive ZnO:Al deposition, no prominent changes in implied V_{oc} are observed. Therefore the TCO deposition by sputtering can be excluded as a source of lifetime degradation¹⁶.

Thus, in terms of device processing, the 'back end' of the processing chain remains as a possible source of depassivation, most likely the metalization which is done by electron-beam evaporation of aluminum. Unfortunately, the metal contacts shield the excess charge carriers from detection by the PCD method, which can therefore not be applied to monitor the implied V_{oc} after metalization. In the course of this thesis, a method to determine V_{oc} based on the saturation current density measured in I/V curves in the dark was developed and validated. This method will be described and discussed in detail in the next chapter, dealing with the transport properties of a-Si:H/c-Si heterojunctions. Here, this method shall be applied in anticipation to decide the impact of the e-beam metalization on the passivation.

¹⁵As discussed above, a rigorous analysis in terms of D_{it} is only possible for symmetrical structures allowing to deconvolute the contributions of both interfaces and the bulk to the overall effective lifetime. However, for solar cell precursor structures comprising emitter and BSF (thus being asymmetric) the technique still provides qualitative insight into the development of the passivation during progressing technological processing. As shown above, (n)c-Si based SHJ solar cells possess *one* critical interface at the emitter side (under the (p)a-Si:H layer) determining the final passivation properties, thus the PCD method even yields quantitative information about this critical interface.

¹⁶Note that this is not intuitively so as DC sputtering leads to acceleration of Ar ions towards the substrate surface with an energy of some 10 eV, which could in principle lead to damage at the heterointerface due to ion implantation into the a-Si:H layer. However, the energy seems not to be sufficient for the ions to penetrate down to the heterointerface. In principle, looking only at the implied V_{oc} or τ_{eff} at 1 sun illumination density, a degradation of D_{it} could be hidden as a simultaneously imposed band bending could compensate the D_{it} increase by field effect passivation. However, it was found that after removal of the ZnO by etching, the implied V_{oc} still remains on a high level, definitely ruling out an impact of the TCO deposition [199].

Figure 4.16: Monitoring of minority carrier lifetime expressed as implied V_{oc} throughout the processing chain for a-Si:H/c-Si solar cells. The horizontal bars denote values measured with PCD before and after doped a-Si:H deposition and again after ZnO:Al deposition by reactive sputtering. The red circles correspond to the implied V_{oc} from dark I/V measurements on the resulting heterodiodes after full-area metalization and mesa etching to define a diode area of 1 cm^2 (identical to the usual active solar cell area). The full red circles are the mean value of the transport-deduced V_{oc} . It is obvious that with e-beam Al deposition, the lifetime degrades significantly during metalization, which can be prevented by using ZnO:Al as a buffer layer on both sides and by avoiding e-beam deposition. The error bars for the PCD-derived implied V_{oc} are omitted for clarity.



4.3.2. The impact of metalization on V_{oc}

Phenomenology of implied V_{oc} throughout the process chain

To monitor the impact of metalization on the passivation, diode structures were processed which possess a representative heterojunction structure with full-area metalization. Thus, no photolithography is needed before metalization which rules out any impact from this process step. The only post-processing is a wet-chemical mesa etch step to isolate single diodes with defined size, which cannot have an impact on the passivation as the semiconductor junctions are already buried under metal contacts at this stage. Additionally, different metals and metalization techniques can be tested as the requirement for the metalization setup to allow for samples with organic contamination (photoresist) is lifted¹⁷. The samples of this series were quarters of 4" wafers of both (n)c-Si and (p)c-Si, on which six diodes of $1 \times 1\text{ cm}^2$ can be processed. The implied V_{oc} was monitored through the a-Si:H- and ZnO process flow by PCD and by the dark-I/V technique after the metalization. Thus, a complete picture can be drawn comprising all thin-film deposition steps. The results are shown in Fig. 4.16 for different cell structures and full-area Al metalization by the standard e-beam evaporation and by thermal evaporation.

The horizontal bars in the figure represent the level of the implied V_{oc} as deduced from PCD measurements after a-Si:H and ZnO deposition. It is obvious that the passivation

¹⁷This aspect usually restricts the metalization options to e-beam-deposited Al as photoresist-coated samples can only be processed in this single setup at HZB.

provided by 5 nm thick IBLs always yielded implied V_{oc} between 710...720 mV for the (n)c-Si samples, and still above 700 mV for the (p)c-Si sample (black bars). Deposition of doped a-Si:H top layers leads to a small but systematic decrease of the implied V_{oc} as discussed above (red bars). With IBLs and on (n)c-Si, the implied V_{oc} remains above 700 mV, while it is around 690 mV without IBLs or on (p)c-Si. Deposition of ZnO mostly leads to a small additional decrease of implied V_{oc} , while in some cases no change or a slight increase is observed. Thus, after a-Si:H and ZnO deposition, no pronounced passivation losses were observed apart from the moderate V_{oc} decrease upon (p)a-Si:H deposition.

The subsequent metalization step however has a huge detrimental impact, depending on the deposition method, as becomes obvious from comparing the red bars with the red points representing the median implied V_{oc} value deduced from dark I/V curves of the six diodes. While e-beam evaporation leads to a decrease of implied V_{oc} down to as low as 630...660 mV, the resulting implied V_{oc} for thermally evaporated Al-contacts is sample-structure dependent. Omitting the ZnO layer (which is possible in a full-area metalized diode) also leads to a low V_{oc} (640 mV), ZnO at the front — being the standard processing — yields 680 mV and the existence of ZnO on both sides gives the highest implied V_{oc} values of up to 695 mV. Thus it is suggested that the final V_{oc} which is reachable after metalization depends on both the Al deposition technology and the existence of ZnO acting as buffer layer between the metal and the a-Si:H layer.

4.4. Discussion

Although the trends in Fig. 4.16 are quite pronounced, there are some questions which arise in the context of the diode series. First of all, it is tempting to ask why the e-beam Al-contacted diodes seem to be restricted to V_{oc} values < 660 mV while there are solar cells with e-beam Al contacts which actually reach > 680 mV. There is no definite answer to this question, but several hints: A lifetime mapping throughout the processing sequence is not desirable in general as it requires excessive handling of the sample and placing it on a potentially particle-contaminated surface (the PCD lifetime tester is not usually operated in the clean room). In both solar cell series and lifetime sample series it was observed that out of an arbitrary 'sample twin', usually the sample whose lifetime was monitored has the lower lifetime/ V_{oc} at the end (most likely due to contamination, scratches or cracks). Secondly, quarters of wafers generally display lower lifetimes as they slightly suffer from the cutting procedure (cf. section 4.2.1). Lastly, solar cells have the largest part of their delicate front side covered by photoresist with a thickness in the μm range during metalization which may provide an additional buffer protecting from the obviously detrimental effect of e-beam evaporation.

Based on experience from semiconductor processing it may be argued that this detrimental effect stems from the x-ray radiation which is produced upon impact of the electron beam in the Al-filled crucible [94, 171]. As the heterojunction lies in close proximity to the sample surface (under about 30 nm a-Si:H at the back side and under < 100 nm a-Si:H/ZnO at the front side), damage from radiation during e-beam evaporation may well occur. With thermally evaporated Al, this radiation is absent leading to signifi-

cantly higher remaining V_{oc} potential. The only possible detrimental effect in this case could stem from the thermal budget during metalization, however it is not likely that temperatures in excess of 200°C are present.

It is observed in the diode series that the preservation of initial V_{oc} potential not only depends on the choice of the Al deposition method but also on the device structure. Omitting the front TCO layer leads to a low V_{oc} irrespective of the metalization method which is most likely due to a detrimental influence of the Al on the thin (p)a-Si:H emitter¹⁸. Al/(p)a-Si:H is known to yield a particularly poor Ohmic contact and this combination is also prone to aluminum-induced crystallization of a-Si:H [95], the latter aspect being potentially detrimental for V_{oc} as well. Thus, the front side ZnO obviously has an important buffering function besides providing lateral conductance. Interestingly, a back side ZnO layer also seems to be beneficial for V_{oc} , as seen comparing the fifth and sixth data set. Only with ZnO on both sides, the implied V_{oc} values deduced from dark I/V on diode structures is (almost) the same as before the metalization¹⁹.

For the e-beam metalized samples, no diode structures were investigated with ZnO on both sides. In this context, the question arises if the missing TCO acting as a buffer between a-Si:H and metal on the back side is responsible for the low V_{oc} values in solar cells and diodes. However, this possibility can be ruled out from solar cell series comprising cells with one- and both-sided TCO deposition and e-beam Al evaporation. Although the highest V_{oc} values are again reached with IBLs, no clear advantage of using both-sided TCO deposition was observed and also those cells did not display V_{oc} values above 680 mV.

Thus, it can be concluded that in order to maintain highest V_{oc} potential throughout the metalization step, thermal evaporation of Al must be used and TCO layers on both sides have to be incorporated in order to best protect the delicate a-Si:H layers from detrimental influence of the metal. Unfortunately, it was not possible to test thermally evaporated Al on solar cells in the framework of this thesis²⁰.

4.5. Summary and key scientific questions

In this chapter, the technological route towards implementation of undoped a-Si:H buffer layers into HZB's a-Si:H/c-Si solar cells was described, and several physical questions were raised on the way.

In the first section it was found — in agreement with several previous studies — that (i)a-Si:H layers are well suited to passivate c-Si surface defects. However, the quality

¹⁸Note however that this structure has no technological significance as a-Si:H/c-Si solar cells require a front side TCO.

¹⁹It has to be noted that Sanyo's HIT cell is also comprising a backside TCO layer, possibly for the same reasons.

²⁰As the organic contamination from photoresist-coated samples brands an evaporation setup for years, it is literally impossible to have this task done externally on a commercial basis. A dedicated tool for thermal metal evaporation is currently being built for HZB and will be set up after submission of this thesis. Thus, the completion of the obvious task to test the hypothesis drawn above has to be left to my successor. A related task, which is highly important as well but was not touched in this thesis, is the optimization of the doped a-Si:H/TCO/metal stack for optimum band lineup and the ohmic nature of the contact.

of the passivation measured as the final effective lifetime τ_{eff} depends on a well-suited combination of PECVD deposition parameters, c-Si surface orientation and -topology, and thermal post-treatment. In addition, the thickness of the passivation layer plays a role.

The influence of the c-Si surface can be principally understood by geometrical arguments and the higher propensity towards epitaxial growth of c-Si{100} surfaces as compared to {111} [51, 277], and the thickness dependence may arise due to subsurface restructuring in the growing a-Si:H enhancing the quality of the interface-adjacent amorphous network as growth proceeds [96, 169, 243].

However, the mechanisms behind the other parameters governing τ_{eff} are not intuitively clear: Particularly the interplay between PECVD growth parameters, post-treatment, and resulting passivation is rich and puzzling. Microscopic insight into the bulk properties of the ultrathin (i)a-Si:H layers would help to understand the phenomenology shown above from a physical point of view. Thus, the questions arising from this section are the following:

1. **What is the relation between PECVD deposition conditions and the resulting structural and electronic properties of the (i)a-Si:H layers?**
→ chapter 6.
2. **How do the microscopic a-Si:H properties relate to the passivation potential of a given IBL?**
→ chapter 8.
3. **What is the microscopic effect of thermal post-treatment?**
→ chapter 8.

In the next section it was found that the passivation provided by (i)a-Si:H is changed by the deposition of doped a-Si:H top layers. The effect is most pronounced if top layer and c-Si substrate are of opposite doping type and the effect depends on the top layer doping. While (p)a-Si:H top layers always led to a derogation of the initial passivation, a complex picture emerged for (n)a-Si:H top layers, with either increase or decrease of the passivation being observed depending on the (n)a-Si:H doping level. Thus it is expected that there exists an optimum doping for (n)c-Si based solar cells, which balances FF and V_{oc} losses from undersized c-Si band bending for too small doping and V_{oc} losses for too high doping levels from the mentioned degradation. Solar cells on (p)c-Si substrates seem to be less critical in this regard. It is unknown so far what causes the detrimental effect of a doped top layer on the microscopic scale, and if such drawback can be avoided or diminished²¹. This leads to the following question:

4. **What causes the degradation of passivation by IBLs upon deposition of doped a-Si:H top layers and how can it be diminished?**
→ chapter 8.

²¹Note that recently a theory was presented which aims at linking the observed behavior to Si-H bond rupture upon shifting the Fermi level in the thin IBL [57]. This model will be critically reviewed and an alternative explanation will be presented in chapter 8.

In a next step, the IBLs were implemented into solar cells on both substrate doping types. Here again, a difference in behavior of the doping-inversed structures was found: While V_{oc} increases in both cell types upon inclusion of IBLs, the charge carrier transport seems to be much more critical for cells on (n)c-Si: The fill factor is very pronouncedly reduced upon inclusion of IBLs on (n)c-Si and depends markedly on the IBL thickness, while for (p)c-Si based solar cells FF is much less sensitive to the presence and thickness of an IBL²². Altogether, (p)c-Si based cells therefore seem to be more tolerant towards implementation of IBLs, while the physical origin of this effect is not trivially anticipated. To understand this effect, microscopic insight on the band lineup present in solar cells of both substrate doping type will be helpful in combination with a detailed investigation on carrier transport in a-Si:H/c-Si heterojunctions. Thus, the questions raised in this section are:

5. How does charge carrier transport proceed in a-Si:H/c-Si heterostructures, what is its relation to solar cell performance and what are the differences between the doping-inversed structures?

→ chapter 5.

6. How is the exact heterojunction band lineup in dependence on a-Si:H deposition conditions and how does it impact charge carrier transport?

→ chapter 7.

Lastly, it was seen in this chapter that none of the solar cells processed so far fully exploits the passivation potential provided by the undoped buffer layers. The metalization step at the back end of solar cell processing leads to a pronounced loss in passivation supposedly by radiation damaging of the heterointerface due to x-rays produced during e-beam evaporation [94, 171]. In a pilot experiment based on a newly developed approach to deduce implied V_{oc} values from dark I/V curves (to be described in chapter 5), the feasibility of using thermally evaporated Al was demonstrated. The implementation into solar cells will soon be possible with new equipment.

²²Further, systematic differences in FF and j_{sc} depending on the deposition conditions of the IBLs were observed, which will be presented and discussed in chapter 7.

5. Analysis of electronic transport in a-Si:H/c-Si solar cells

In this chapter, the mechanisms of electronic transport in a-Si:H/c-Si heterojunctions are elucidated by means of I/V curve analysis for data taken in the dark at varying temperatures. After briefly introducing the different transport mechanisms which principally could be present in the structure under study, the results of the dark I/V analysis are presented and discussed in terms of two different bias voltage regimes. It is found that for high-forward bias ($V > 0.5\text{ V}$), the classical Shockley diode model is well suited to describe the transport in a-Si:H/c-Si heterostructures. This establishes a fundamental connection between V_{oc} and the dark I/V parameters. It is validated that the latter can be used to accurately predict the open-circuit voltage under illumination from a dark I/V measurement alone, which is the foundation of the process flow analysis presented in the previous chapter. Under low forward bias, the dominant transport mechanism is suggested to depend on the substrate doping type, reflecting the differences in the transport seen in the cell results in the previous chapter. Additionally, the presence of low-dimensional defective regions in the active cell area strongly impact the transport signature in this regime, as is demonstrated by the use of lock-in thermography measurements.

As a result of this chapter, the dark I/V analysis is available as a simple means to deduce the passivation properties of a contacted structure from a dark I/V measurement, with potential for automation.

This chapter is based on the publications [B], [C] and [F] from the list in the appendix.

5.1. Introduction

Despite the long lasting efforts to elucidate on the physics of a-Si:H/c-Si heterojunctions and their successful application in solar cells and hetero-diodes, fundamental questions concerning the transport of charge carriers across the heterojunction still remain under dispute [111, 151, 156, 163, 168, 233, 252]. Amongst other methods, the analysis of solar cell I/V curves taken at different temperatures has been established to elucidate this issue. Note that the first transport measurement on a-Si:H/c-Si structures dates back to 1975 [73]. However, no consistent picture has emerged so far on the dominant transport mechanisms and their connection to the device performance of a-Si:H/c-Si solar cells. Previous studies either focused on model structures incorporating thick amorphous layers not suitable for solar cell application [151, 156, 163, 168], were limited to a certain device design, doping type and -level [233, 252] or reported on solar cells with a poor performance limiting the significance of the obtained results [111]. Thus, a systematic study varying a comprehensive set of parameters of state of the art a-Si:H/c-Si solar cells which are interpreted employing an extensive data analysis is suggested in order to unequivocally link microscopic transport mechanisms to device performance. In this chapter, I/V data from numerous a-Si:H/c-Si solar cell series are analyzed which comprise both substrate doping types, systematic variations of the surface morphology, back surface field parameters and presence of (i)a-Si:H buffer layers. I/V curves measured between 240 K and 360 K are fitted with a generalized two-diode model. The results obtained from the analytical model are analyzed in terms of activation energies, saturation current densities and diode ideality factors, discussed using prevalent transport models and connected to device parameters.

5.2. Heterojunction transport models

5.2.1. Brief history of semiconductor transport models

Depending on device structure, temperature and bias voltage, there are distinct physical mechanisms that can dominate the charge carrier transport in semiconductor devices comprising p/n junctions.

For homojunctions, besides the classical Shockley diode law, where the transport is limited by charge carrier diffusion in the neutral bulk [224] as discussed in section 2.3.1, a model formulated by Sah, Noyce and Shockley [203] describes I/V characteristics in case of dominating recombination in the space charge region.

In heterojunction p/n devices, band offsets acting as barriers, discontinuous bulk properties and the possible presence of interface states and dipole layers further complicate the issue. After the work of Anderson, who first described the transport in Ge-GaAs heterostructures with a model based on the Shockley diffusion theory [6], several authors presented modified analytical expressions for currents in the presence of band offsets [136, 179]. The impact of defect states at the heterointerface remained essentially untreated.

Bulk defect states in the band gap of one or both materials forming the heterojunction can give rise to trapping of charge carriers from the bands, hopping conduction at

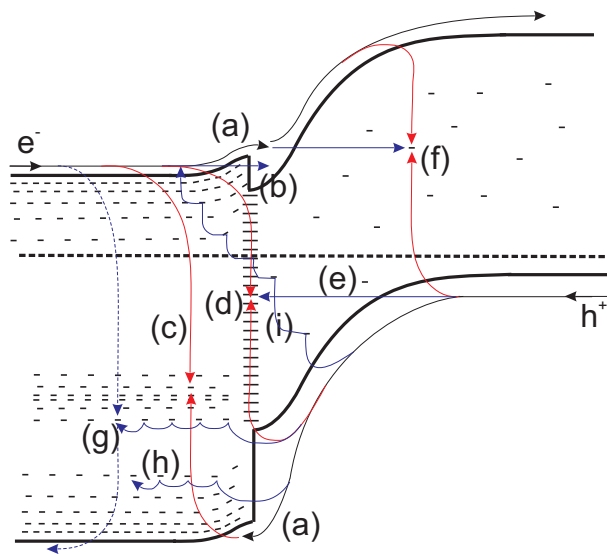


Figure 5.1: Schematic band lineup of a (n)a-Si:H/(p)c-Si heterojunction solar cell structure and possible transport paths for moderate forward bias. black: emission processes, red: recombination, blue: tunneling. (a) Emission of carriers across the barriers at the heterojunction imposed by band offsets. (b) Tunneling through a spike. (c) Recombination via the a-Si:H gap state density. (d) Recombination via interface states. (e) Tunneling into interface states and successive recombination. (f) Recombination via deep defects in the c-Si. (g) Multi-tunneling in the a-Si:H with successive recombination through carrier capture or reemission into the band ('multi-tunneling capture/emission'). (h) Tunnel hopping in the a-Si:H band tail. (i) Band-to-band 'multi-tunneling' process.

the Fermi level or in the localized states of the band tails and to tunneling processes¹. Heterojunctions comprising amorphous materials are especially prone to these effects because of the significant density of electronic states in the band gap found in exponentially decaying band tails and dangling bond states deep in the gap. Both trapping in tail states and a high density of localized states which facilitate hopping can lead to a transition from injection-limited transport (as in the models of Shockley, Sah *et al.*, Anderson and successors) to bulk-limited transport as e.g. reflected in the space-charge-limited current model [62, 197] and the variable range hopping model [27]. While the very small thickness of the a-Si:H layers in device-relevant a-Si:H/c-Si solar cell structures obviously reduces the propensity towards bulk-limited transport, there can be bias regimes in which tunneling transport modes dominate [111, 156, 163, 168, 252]. This is mainly the case in the low-forward-bias region where the current densities by diffusion/emission are small. To account for these currents, several authors presented analytical models based on tunneling or 'multi-tunneling' mediated by states in the band gap [156, 194]. In order to describe non-exponential forward currents, very detailed descriptions of tunneling processes were developed in recent times [105, 106] that serve mainly for numerical device simulation.

5.2.2. Transport in a-Si:H/c-Si heterostructures

As a-Si:H/c-Si solar cells combine the band-offset-derived barriers and emission processes of a heterostructure with the subtleties of transport in an amorphous material comprising gap states, competing transport mechanisms are to be expected. As an example, Fig. 5.1 shows possible transport paths for electrons and holes through a typical (n)a-Si:H/(p)c-Si structure. In consequence, several different transport models are in

¹Note that tunneling can proceed by a variety of different mechanisms, such as through a spike, from band to band in a staircase manner, or into trap states before reemission occurs or the opposing carrier type is captured which results in recombination.

Table 5.1.: Transport models and their functional form for $j_0(T)$ and $A(T)$. SD: Shockley diffusion [224]. G/R: generation/recombination (Sah/Noyce/Shockley [203]). TE: Thermionic emission. AND: Diffusion adapted to heterojunctions (Anderson [6]). MTCE: Multi-tunneling-capture/emission (Matsuura [156]).

| Model | Ref. | $j_0(T)$ | $A(T)$ | ideality n |
|------------------|-------|---|-----------------|-----------------------|
| SD ¹ | [224] | $T^{3+\gamma/2} \exp\left(-\frac{E_g}{kT}\right)$ | $\frac{e}{kT}$ | 1 |
| G/R | [203] | $T^{3+\gamma/2} \exp\left(-\frac{E_g}{2kT}\right)$ | $\frac{e}{2kT}$ | 2 |
| TE | [251] | $T^2 \exp\left(-\frac{\Phi_b}{kT}\right)$ | $\frac{e}{kT}$ | 1 |
| AND ² | [6] | $T^{3+\gamma/2} \exp\left(-\frac{eV_{bi}}{nkT}\right)$ | $\frac{e}{nkT}$ | $1 + \frac{N_D}{N_A}$ |
| MTCE | [156] | $\left[\exp\left(-\frac{E_T - E_V}{kT}\right) - \exp\left(-\frac{E_C - E_F}{kT}\right) \right]$ or $\left[\exp\left(-\frac{E_C - E_T}{kT}\right) - \exp\left(-\frac{E_F - E_V}{kT}\right) \right]$ | const. $ T$ | — |

¹ See section 2.3.1 for details.

² See section 5.3.1 for details.

principle applicable to the device structure and a surprisingly high number of these was indeed invoked in previous studies to describe the I/V characteristics.

As a starting point for the following discussion of charge carrier transport and its relation to solar cell performance, some analytical injection and tunneling models that have proven useful for the analysis of the I/V data are listed in Table 5.1. The functional form of the forward current can in all cases be described by a general diode expression

$$j = j_0(T) [\exp(A(T)U) - 1]. \quad (5.1)$$

The saturation current density $j_0(T)$ and the exponential factor $A(T)$ have different temperature dependencies according to the applicable model. For a full discussion of the different physical mechanisms, the reader is referred to the respective publications.

5.3. Results of dark-I/V curve fitting

An example result of the fitting procedure was already shown above in chapter 3, Fig. 3.5. In the following, the results will be discussed separately for the two distinct regions in terms of forward bias voltage which are visible in the I/V curves. The first section will be concerned with high forward bias (HFB) which is defined as $V > 0.5$ V. Later on, low forward bias (LFB) will be discussed, defined as $0 < V < 0.5$ V.

5.3.1. High forward bias

Under high-forward bias ($V > 0.5$ V) the dark I/V characteristics are dominated by the first term in Eq. 3.5:

$$\begin{aligned} j_F &\approx j_{0,1} \left[\exp\left(\frac{q(V - j_F R_S)}{n_1 kT}\right) - 1 \right] \\ &= j_{00,1} \exp\left(-\frac{E_{a,j01}}{kT}\right) \left[\exp\left(\frac{q(V - j_F R_S)}{n_1 kT}\right) - 1 \right] \end{aligned} \quad (5.2)$$

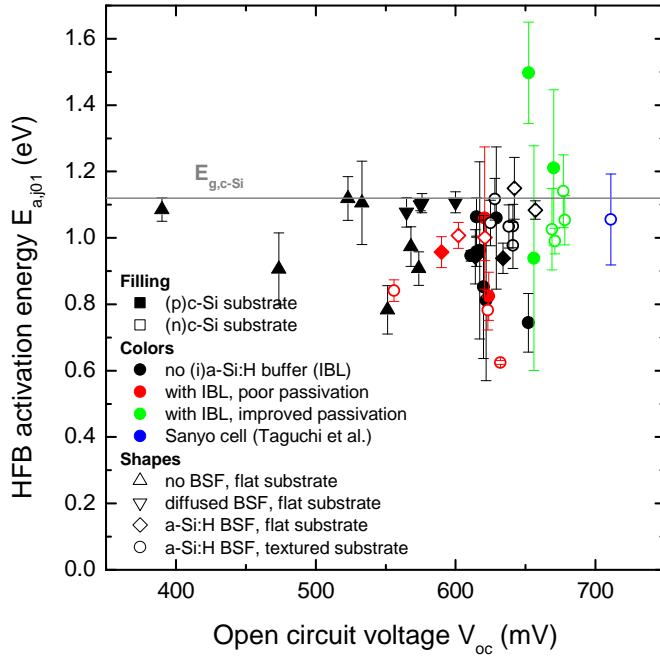


Figure 5.2: Activation energy of diffusion current density $E_{a,j01}$ as obtained from Arrhenius plots of the saturation current density $j_{0,1}$, plotted vs. the actual device V_{oc} as measured under illumination. The legend shown in the plot applies to all successive plots where fit results of different solar cells are compared. The blue data point is a HIT solar cell by Sanyo [252]. Concerning the categorization of IBLs, poor passivation is defined as no V_{oc} gain as compared to the reference solar cell without IBL.

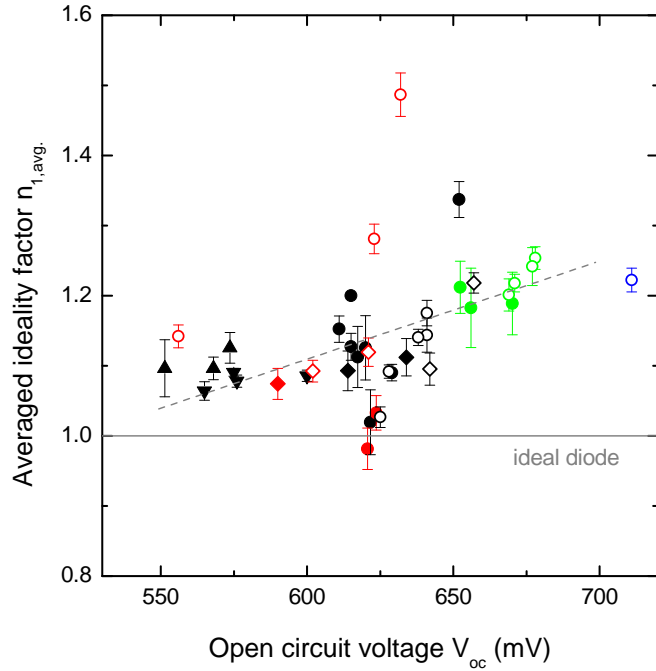
Useful means for the distinction of transport mechanisms are both the temperature dependence of the saturation current density $j_{0,1}$, from which an activation energy $E_{a,j01}$ can be deduced plotting $\log(j_{0,1})$ vs. $1/T$ (Arrhenius plot), and the value of the diode ideality factor n_1 . Further, the absolute value of $j_{0,1}$ can be used to anticipate the device performance under illumination as will be shown in the last part of the following section. The series resistance R_S is merely a technological device parameter and will not be discussed here. However, for almost all samples it was found to be in the range of state-of-the-art solar cells ($< 1 \Omega\text{cm}^2$).

Activation energy and diode ideality

The activation energy of the diffusion current density $E_{a,j01}$, obtained by a linear fit to the Arrhenius plot, is plotted against the device V_{oc} under illumination in Fig. 5.2. It is obvious that the activation energy scatters around the c-Si band gap value of 1.12 eV with most of the data being compatible with this value. Together with the ideality factor n_1 ranging mostly between 1 and 1.3 (Fig. 5.3, averaged values over all temperatures at which I/V curves were taken), this is a strong indication for diffusion in the neutral bulk governing the transport in the high-forward-bias regime. This means that HFB transport can well be described with Eq. 2.43 derived in section 2.3.1.

Further, there is some indication in Fig. 5.3 that the ideality factor n_1 increases away from the ideal value of one as the c-Si passivation is improved, which is reflected in a higher V_{oc} .

Figure 5.3: High-forward-bias diode ideality factor $n_{1,avg}$, as obtained by averaging over the values obtained from single fits at different temperatures plotted vs. the device V_{oc} under illumination. The gray line indicates the ideal value following from the Shockley theory while the dashed line describes the trend in the data and is intended as a guide to the eye.



Impact of the heterojunction on transport

This systematic enhancement of the ideality factor n_1 with the open circuit voltage V_{oc} is noteworthy and lends itself to further analysis. It is tempting to ascribe the obvious increase of n_1 away from the ideal behavior following the enhancement of the c-Si absorber passivation by improved a-Si:H layer quality and eventual inclusion of (i)a-Si:H buffer layers to the heterostructure aspects getting comparably more important for the transport. To corroborate this interpretation, heterojunction transport models were revisited in search for an explanation for the observed increase in n_1 which can be linked to microscopic aspects of the heterostructure.

One of the first models for the analytic description of heterojunction transport is the Anderson model [6]. It is based on a diffusion approach but incorporates barriers affecting transport via the band offsets present at the heterojunction. In the original paper, the model was proposed in order to interpret experiments on Ge-GaAs heterostructures. In those structures, the rather large offsets led the author to assume complete domination of one carrier type. In the case of a-Si:H/c-Si heterostructures the offsets are smaller and thus the circumstances of transport across the junction are more subtle. In Fig. 5.4 the schematic band lineup is depicted in equilibrium for a (p)a-Si:H/(n)c-Si structure. $\Psi_{bi} = V_{D1} + V_{D2}$ is the built-in voltage, $V = V_1 + V_2$ is the partition of an externally applied voltage and ΔE_C and ΔE_V are the conduction and valence band offsets. Due to the small fraction of band bending in the a-Si:H, an externally applied forward voltage will mainly reduce the band bending in the c-Si. It is easily seen that when a moderate forward bias V is applied, the electrons coming from the c-Si have to surpass a barrier of $(V_{D1} - V_1) + (V_{D2} - V_2) + \Delta E_C$. The holes coming from the a-Si:H side on the other hand have to surpass $(V_{D1} - V_1) + (V_{D2} - V_2) - \Delta E_V$ unless

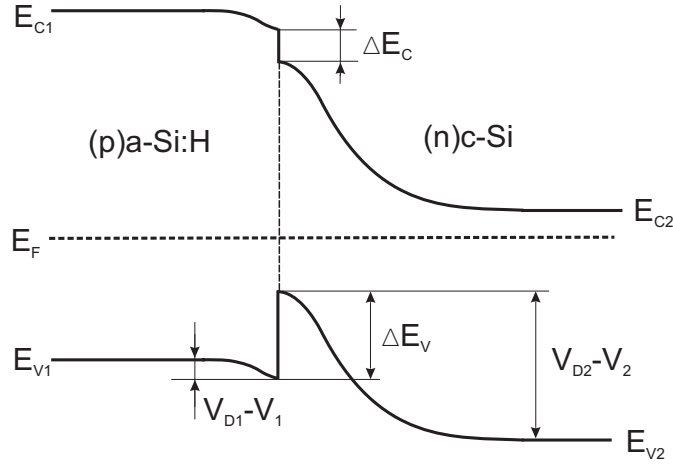


Figure 5.4: Band lineup of a (p)a-Si:H/(n)c-Si solar cell structure and distribution of built-in and applied voltage in both layers. Under forward bias, the barrier for electrons passing from c-Si to a-Si:H is $(V_{D1} - V_1) + (V_{D2} - V_2) + \Delta E_C$, the holes on the other hand have to surpass $(V_{D1} - V_1) + (V_{D2} - V_2) - \Delta E_V$ unless $V_{D2} - V_2 < \Delta E_V$. In that case, only $V_{D1} - V_1$ remains which changes the transport regime for hole transport.

the fraction of voltage drop supported in the c-Si (being $V_{D2} - V_2$) becomes less than ΔE_V with increasing V . From then on the barrier amounts to only $V_{D1} - V_1$ and the transport regime for holes changes. If both carrier types are considered, the equation for the current across the junction reads [6, 136, 162]

$$\begin{aligned}
 j_F &= \left[\frac{eD_{p,c-Si}}{L_{p,c-Si}} N_{A,a-Si:H} X_h \exp\left(-\frac{q\Psi_{bi} - \Delta E_V}{kT}\right) \right. \\
 &+ \left. \frac{eD_{n,a-Si:H}}{L_{n,a-Si:H}} N_{D,c-Si} X_e \exp\left(-\frac{q\Psi_{bi} + \Delta E_C}{kT}\right) \right] \\
 &\times \left[\exp\left(\frac{qV}{kT}\right) - 1 \right] \quad (5.3)
 \end{aligned}$$

if $V_{D2} - V_2 > \Delta E_V$. Here, $N_{D/A}$ is the donor/acceptor concentration, $D_{p/n}$ the diffusion constant and $L_{p/n}$ the diffusion length in the respective material. X_e and X_h are transmission coefficients for electrons and holes which express the fraction of carriers that overcomes the barriers represented by the band offsets. In this case, the diode ideality is always equal to one, while the activation energy is either $qV_{bi} - \Delta E_V$ or $qV_{bi} + \Delta E_C$, depending on which term dominates. The first term describes the contribution of holes crossing the junction from the amorphous side while the second term is for electrons originating from the c-Si side of the junction. If $V_{D2} - V_2 < \Delta E_V$ applies, the contribution of the holes to the current changes. Instead of the hole current related terms in Eq. 5.3, j_{hole} can then be described by [6, 136, 162]

$$\begin{aligned}
 j_{hole} &= \frac{eD_{p,c-Si}}{L_{p,c-Si}} N_{A,a-Si:H} X_h \exp\left(-\frac{qV_{D2} - \Delta E_V}{kT}\right) \\
 &\times \left[\exp\left(\frac{qV_2}{kT}\right) - \exp\left(\frac{-qV_1}{kT}\right) \right] \\
 &= \frac{eD_{p,c-Si}}{L_{p,c-Si}} N_{A,a-Si:H} X_h \exp\left(-\frac{q\Psi_{bi}}{(1+a)kT}\right) \\
 &\times \left[\exp\left(\frac{qV}{(1+a)kT}\right) - \exp\left(\frac{-aqV}{(1+a)kT}\right) \right] \quad (5.4)
 \end{aligned}$$

with $a = (V_{D1} - V_1)/(V_{D2} - V_2) = (N_{D2}\epsilon_2)/(N_{A1}\epsilon_1)$ being the ratio of the voltage drops supported by the two materials. Thus, according to the Anderson model, through bias-induced changes in the band alignment there can be a transition from ideal diode behavior with activation energy $qV_{bi} - \Delta E_V$ or $qV_{bi} + \Delta E_C$, Eq. 5.3, to a non-ideal diode with activation energy $V_{bi}/(1 + a)$ as follows from Eq. 5.4. The transition bias voltage is dependent on the partition of built-in voltage V_{bi} and bias voltage V between the two materials forming the heterojunction. Therefore, changes in the density of rechargeable states in the a-Si:H bulk within the space charge region (e.g. by inclusion of intrinsic interlayers) can shift the transition to lower bias voltages and affect the value of the non-ideal diode factor. Thus, a transition from ideal to non-ideal behavior through inclusion of intrinsic interlayers could be qualitatively understood in the simple framework of the Anderson model.

However, this theory is not able to satisfactorily reflect the whole set of experimental findings: Most importantly, no difference in behavior is found between the doping-inversed structures. As Eq. 5.4 is only applicable if the barrier for carriers coming from the a-Si:H involves only the a-Si:H side of junction (which means $V_{D2} - V_2 < \Delta E_V$ for (p)a-Si:H/(n)c-Si and $V_{D2} - V_2 < \Delta E_C$ for (n)a-Si:H/(p)c-Si), a much lower transition voltage is to be expected for the (n)a-Si:H/(p)c-Si combination. Experimentally however, these samples behave similarly to (p)a-Si:H/(n)c-Si. Also, in the Anderson model the diode ideality factor in Eq. 5.4 should *decrease* with increased voltage drop in the a-Si:H. This would mean that inclusion of an a-Si:H layer comprising less defects should reduce the ideality factor, although the opposite is observed. Lastly, the model has the severe deficiency of not taking into account the presence of interface states. As suggested by the smooth increase of n_1 with V_{oc} also for solar cells without (i)a-Si:H, the interface defect density, which is the main limit to V_{oc} in a-Si:H/c-Si cells as seen in the previous chapter, plays a major role also in determining n_1 . Therefore, the Anderson model seems not to provide a satisfactory description of transport in a-Si:H/c-Si structures. A consistent analytical model should contain both the barriers formed by band offsets and the interplay between rechargeable interface states and transport, and has yet to be formulated.

Linking the saturation current density with V_{oc}

The relevance of the diffusion current density $j_{0,1}$ as obtained from dark I/V curves for device characterization is highlighted by the estimation of device V_{oc} from the measured $j_{0,1}$ with the help of Eq. 2.46 while setting $n = n_1$ and $j_0 = j_{0,1}$. Comparing the values of V_{oc} as estimated by this procedure ($V_{oc,est.}$) with the actual device V_{oc} measured under illumination yields excellent agreement as can be seen in Fig. 5.5. The open-circuit voltage V_{oc} can be estimated with an accuracy of $> 95\%$ from the value of $j_{0,1}$ which again supports the interpretation of the high-forward-bias current as being dominated by diffusion. Further, this analysis establishes a convenient method to satisfactorily determine the value of the important device parameter V_{oc} from dark I/V curves. In the previous chapter, this procedure has already proven useful in the analysis of full-area metalized diode structures.

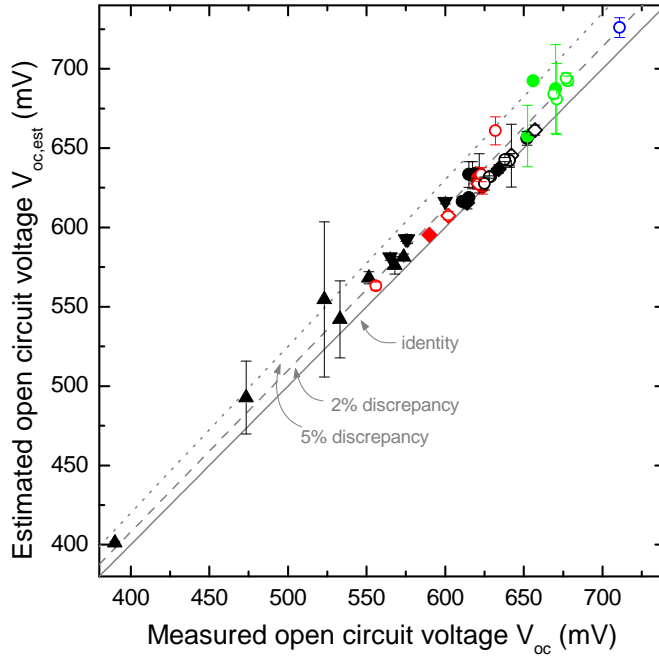


Figure 5.5: Device V_{oc} as implied from the absolute value of the high-forward-bias saturation current density $j_{0,1}$ obtained from dark I/V curve fits, compared to the actual V_{oc} as measured under illumination. For almost all solar cells within this study, the discrepancy is less than 2%.

5.3.2. Low forward bias

Activation energy and temperature dependence of A

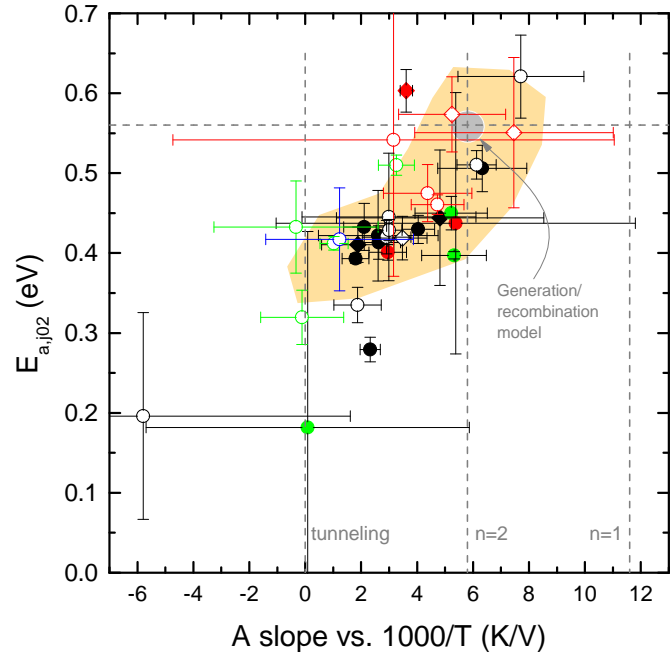
While previous studies on samples comprising thin amorphous silicon layers agree on the high-forward-bias current being a Shockley diffusion current² [112, 252], there is disagreement concerning the dominant transport mechanisms in the low-forward bias regime. While some studies claimed tunneling to be dominant as they observed a temperature independent exponent A [111, 156, 163, 168, 252], others found a recombination/generation current manifesting in a diode ideality factor around 2 and an activation energy of either $E_{g,c-Si}/2$ or $E_{g,a-Si:H}/2$ [150, 233] or a thermionic emission mechanism [151]. Even for nominally identical material combinations there is considerable inconsistency among the studies concerning the activation energies of the LFB transport process.

Under LFB, the series resistance has negligible impact and thus Eq. 3.5 with $R_S \rightarrow 0$ applies, the important parameters being $j_{0,2}$, $A(T)$ and the shunt resistance R_P . None of the solar cells analyzed here had a considerable current contribution from Ohmic shunts, therefore R_P was not significant — even though included in the fits — and will not be discussed. For the following analysis, the set of samples was restricted to the 'device-relevant' structures, i.e. a-Si:H/c-Si solar cells comprising BSFs and with at least acceptable passivation ($V_{oc} > 600$ mV).

The main result of the low-forward-current analysis is presented in Fig. 5.6 where the activation energy of the saturation current density $j_{0,2}$ is plotted against the slope of a linear fit to the exponential factor A vs. $1000/T$. A slope of zero corresponds to a

²This conclusion was based on the observation of $E_a \approx E_{g,c-Si}$ and $n \approx 1$. However, no thorough analysis of the ideality factor was done before to the author's knowledge.

Figure 5.6: Activation energy $E_{a,j02}$ of the low-forward-bias current $j_{0,2}$ vs. the slope of the exponential factor A when varying the temperature. A slope of 5.8 (11.6) corresponds to a diode ideality factor of 2 (1), while zero slope is an indication for tunneling. The orange area marks the range of the majority of data points and is intended as a guide to the eye, suggesting the systematic variation of $E_{a,j02}$ with the slope of A as discussed in the text.



temperature-independent exponential factor as expected for tunneling transport processes, a slope of $e/(1000 k) = 11.6 \text{ K/V}$ corresponds to a diode ideality factor of 1 and a slope of $e/(2000 k) = 5.8 \text{ K/V}$ to a diode ideality factor of 2.

Observing Fig. 5.6 one notes a grouping of most (p)c-Si based samples (filled symbols) with a very small slope of A vs. inverse temperature, i.e. close to zero slope, leading to a consistent picture: With or without intrinsic buffer layers, (p)c-Si based solar cells have activation energies of $E_{a,j02} = 0.4...0.45 \text{ eV}$ and very small to zero temperature dependence in the exponential factor A .

The (n)c-Si based samples show more scattering in both the slope of A and the activation energy. Nonetheless it can clearly be seen that the slope is generally higher and mostly consistent with a diode ideality of 2, while the activation energy ranges around $E_{a,j02} = 0.45...0.55 \text{ eV}$. However, some state-of-the-art devices including the Sanyo HIT cell (blue data point) show smaller slopes and lower activation energies and thus behave similarly to the (p)c-Si based samples. Although the scatter is rather large, one might get the impression that the (n)c-Si based samples with IBLs and high V_{oc} (green open data points) are tending towards a 'tunneling signature' while the samples without (or with defective) IBLs display $n_2 \approx 2$ and higher activation energies.

The most interesting feature of the plot is the apparently smooth transition from the generation/recombination regime ($n_2 \approx 2$, $E_{a,j02} = E_g/2 = 0.56 \text{ eV}$) to a tunneling signature (zero slope in A , activation energy $E_{a,j02} \approx 0.4 \text{ eV}$), as suggested by the orange region embracing the majority of data points as a guide to the eye. This observation can be interpreted in terms of two competing transport mechanisms being present in most of the solar cells, which correspond to both different A slopes and activation energies. It is suggested that a tunneling process comprising a temperature-independent A and activation energy around 0.4 eV coexists with a generation/recombination current involving a

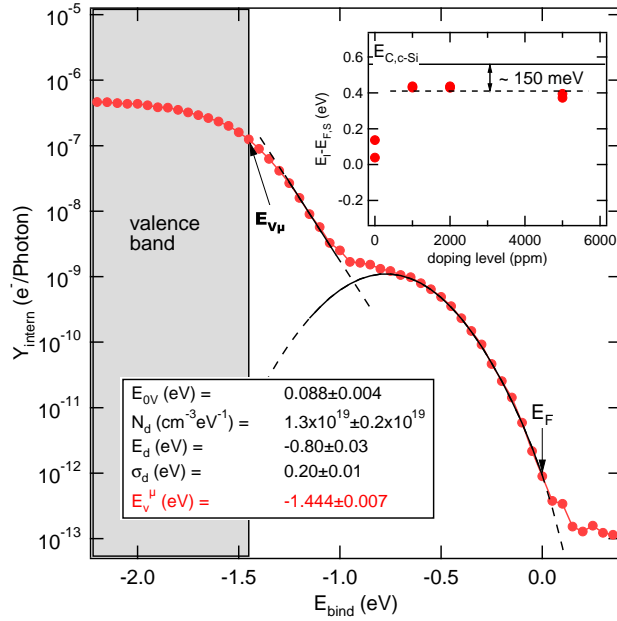


Figure 5.7: Constant-final-state-yield photoelectron spectrum taken on standard (n)a-Si:H as used in the emitters of (p)c-Si based cells. The fitting of a model DOS to the spectrum yields the shown defect- and valence band tail parameters. The distance of the valence band mobility edge from E_F is 1.44 eV, which results in 0.3...0.35 eV for the distance between E_F and the conduction band. This finding is supported by SPV measurements (shown in the inset for a (n)a-Si:H doping series, the 1000 ppm value being the same sample as for the CF-SYS measurement), which yield the energetic distance of E_F at the interface ($E_{F,S}$) from the c-Si conduction band. Adding the typical conduction band offset of $\Delta E_C \approx 0.2$ eV confirms $E_F - E_{C,a-Si:H} = 0.35...0.4$ eV.

diode ideality of 2 and an activation energy of $E_{a,j02} \approx 0.5...0.6$ eV $\approx E_{g,c-Si}/2^3$. Judging from the data in Fig. 5.6 it appears that tunneling clearly dominates in (n)a-Si:H/(p)c-Si structure while the (p)a-Si:H/(n)c-Si samples seem to be dominated by recombination in the space charge region. However, it has to be noted that the (p)a-Si:H/(n)c-Si samples with the highest V_{oc} and thus the best interface passivation also have the smallest slope in A with the HIT cell reaching even ≈ 0 slope. Therefore it is implied that in order to observe the tunneling mechanism present in these structures, excellent interface passivation is required [252].

Differences between doping-inversed structures

The suggested doping-dependent differences in the transport regime for samples *without* (i)a-Si:H interlayer can readily be explained from the a-Si:H electronic properties: The (p)a-Si:H bulk has in general a higher gap-state DOS and it forms highly defective interfaces leading to enhanced interface recombination. The first is commonly known from several previous studies (e.g. from ESR [250]), the latter from recent lifetime measurements (e.g. employing PCD [7]). Thus, eventual tunnel transport is likely to be inhibited by recombination at the heterointerface, or masked by a high level of the recombination current. The (n)a-Si:H bulk on the other hand is less defective and the

³Domination of one of the two mechanisms would be dependent on device structure, quality of the interface, nature and quality of the amorphous silicon which determines the density and energetic position of states facilitating hopping transport, and temperature. Consistently it would have to be expected that at lowest temperatures the tunneling contribution is enhanced. This is indeed observed for most of the samples when the A slope is determined only at 240...310 K, the fit errors however are significantly enhanced at the same time due to the smaller number of data points on which the fits are based [217].

interface to c-Si is usually better passivated, which allows to observe the tunneling of holes from the wafer across the heterojunction into the a-Si:H.

The fact that also some comparably well passivated (p,i)a-Si:H/(n)c-Si structures exhibit A slopes larger than zero implies band structure effects to be responsible for the preferential observation of tunneling transport in (n)a-Si:H/(p)c-Si samples. The tunneling probability scales exponentially with the overlap of the wave functions of involved states. Thus, both the density and nature of states play a role in determining the tunnel rate. To first order, the densities of accessible states in the a-Si:H are about the same for the c-Si conduction and valence band: While the conduction band offset is considerably smaller than the valence band offset, the a-Si:H conduction band tail slope is much higher (Urbach energies $E_{0V} = 30 \dots 50$ meV) than the valence band tail slope (Urbach energies $E_{0V} = 60 \dots 100$ meV). As a result, at both c-Si band edges, the a-Si:H gap DOS lies around 10^{19} cm^{-3} for state-of-the-art a-Si:H layers. Further, the Gaussian distribution of dangling bond defects in the a-Si:H is energetically close to the c-Si valence band edge, but amounts only to $10^{16} \dots 10^{17} \text{ cm}^{-3}$ in device quality a-Si:H, thus a dominant contribution to tunneling transport is less probable. Since the a-Si:H gap DOS in direct reach of the c-Si is approximately the same for both the valence and the conduction band, the cause for the dominant tunnel currents mainly in (p)c-Si based cells must be sought in the different band offsets and in the nature of the involved states. As the valence band offset is larger than the conduction band offset by a factor of three (cf. chapter 7), emission of holes across this barrier is impeded in (n)a-Si:H/(p)c-Si. Additionally, it is conceivable that the larger overlap of the p -orbital derived valence band tail states with their directional character can facilitate hopping transport more easily than that of the conduction band tail states, which have s -orbital character ⁴. Before analyzing the absolute level of $j_{0,2}$, the exact nature of tunnel transport shall be elucidated in the following section.

Nature of tunneling transport

As for the HFB transport it is instructive to analyze the activation energy of the saturation current density to identify the underlying tunneling transport mechanism. Within experimental errors, the activation energy of $j_{0,2}$ in the (p)c-Si based samples coincides with the energetic distance of the Fermi level from the a-Si:H conduction band as is implied by CFSYS photoelectron spectroscopy and surface photovoltage measurements on (n)a-Si:H layers. A CFSYS spectrum taken on a typical 10 nm (n)a-Si:H emitter layer is shown in Fig. 5.7. Fitting of a model DOS to the spectrum results in the parametrization of the defect distribution (maximum DB density N_d , energetic position E_d and -width σ_d) and the valence band tail. The distance between the Fermi level (binding energy zero) and the valence band mobility edge $E_{V\mu}$ is found to be 1.44 eV,

⁴Based on the above analysis one would anticipate an impact of the inclusion of intrinsic buffer layers on the absolute value of the forward tunneling transport contribution, as both the Urbach energies and the deep defect density are reduced in (i)a-Si:H as compared to (n)a-Si:H, which decreases the density of potentially tunnel-active states. Indeed, this effect is apparently present when observing the fit values for $j_{0,2}$. It will, however, be shown in section 5.4 that great care has to be taken when analyzing the absolute level of this second diode saturation current density as it is affected by low-dimensional defective structures in the active cell area.

which yields a distance of 0.3...0.35 eV for the distance between E_F and the conduction band⁵. The value is reasonably close to the activation energy of the low-forward-bias tunneling current of ≈ 0.4 eV. This finding is supported by SPV measurements yielding the energetic distance of the Fermi level at the a-Si:H/c-Si interface from its intrinsic value (inset in Fig. 5.7), from which the distance to the a-Si:H conduction band can readily be calculated knowing the conduction band offset which is $\Delta E_C \approx 0.2 \dots 0.25$ eV as will be shown in chapter 7 (cf. the compilation in Ref. [20]).

In a classic paper, Matsuura *et al.* [156] have derived a model for carrier transport in a-Si:H/c-Si heterojunctions based on I/V and C/V results they obtained on (i)a-Si:H/(p)c-Si structures. They invoked tunneling of holes from (p)c-Si into the a-Si:H emitter layer through the large valence band offset and, successively, either emission into the a-Si:H valence band or capture of electrons from the conduction band leading to recombination. The saturation current density in the framework of this so-called 'multi-tunneling capture/emission model' (MTCE) has the form

$$j_{0,\text{MTCE}} = B \left(\sigma_p v_{th} N_V \exp \left[-\frac{E_T - E_V}{kT} \right] + \sigma_n v_{th} N_C \exp \left[-\frac{E_C - E_F}{kT} \right] \right), \quad (5.5)$$

and domination of one of the two summands is to be expected. Invoking the MTCE model, the results obtained here are consistent with tunneling of holes from the (p)c-Si into a-Si:H VB tail states where successive tunnel hopping and electron capture with the typical activation energy of $E_a = E_{C,\text{a-Si:H}} - E_F$ occurs. Thus, the multi-tunneling-capture/emission model introduced by Matsuura [156] is thereby highlighted to consistently describe the dominant low-forward-bias transport contribution in (n)a-Si:H/(i)a-Si:H/(p)c-Si samples. These findings are consistent with other studies [168, 233, 252].

5.4. 2D effects under low forward bias

In the light of the extremely small current densities in the low-forward-bias range ($< 10^{-3}$ mA/cm² for typical solar cells), this regime is naturally prone to being affected by local excess currents occurring at edges or defective regions with lower dimensions, i.e. line- or point defects [88]. In order to assess the validity of the 1D approach underlying the whole of the above analysis, dark lock-in thermography (DLIT) [24, 25] was performed on some selected samples covering a typical range of solar cell structures and low-forward-bias characteristics. These measurements were done by O. Breitenstein at the Max-Planck Institute of Microstructure Physics, Halle. In the following, these results shall be analyzed to complement the picture for the low-forward-bias region drawn above.

Figure 5.8 shows DLIT images of four solar cells at two different forward voltages together with the respective position in the $E_{a,j02}$ vs. A slope plot (cf. Fig. 5.6) and in a plot showing the absolute level of the second diode saturation current density $j_{0,2}$ versus

⁵For this estimation, typical a-Si:H mobility band gap values of 1.75...1.8 eV are assumed, which are found for the present (i)a-Si:H layers as well (cf. Fig. 6.5), and 160 meV are added to account for the typical difference between optical and mobility band gap [285].

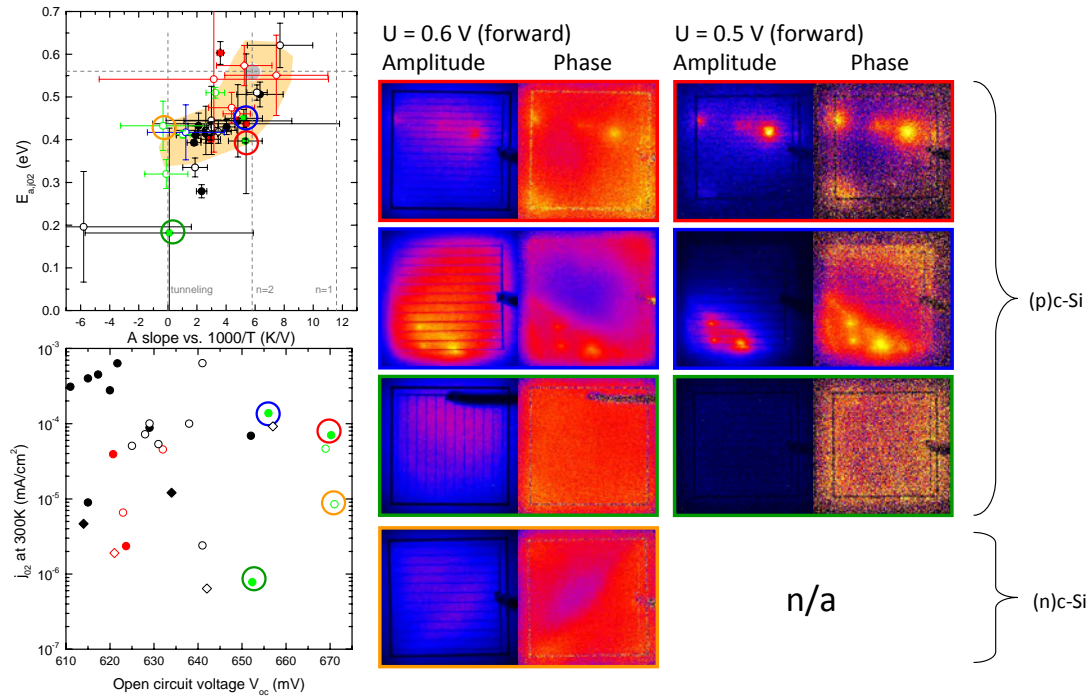


Figure 5.8.: Results of dark-lock-in thermography measurements on a-Si:H/c-Si solar cells. The pictures were taken at two different forward bias voltages and reveal the presence of local excess currents with high ideality factor for some cells. These cells, which display a recombination signature in the dark I/V transport analysis (Fig. 5.6 redrawn in upper left panel), have a high level of the LFB saturation current density $j_{0,2}$ (lower left panel). However, no detrimental effect of the locally enhanced currents on V_{oc} is observed as there is no correlation between V_{oc} and $j_{0,2}$ (lower left panel).

V_{oc} . The rectangles around the DLIT pictures color-code the position in the plots on the left side. It is obvious that the two (p)c-Si based solar cells which deviate from the conclusion drawn above by showing a recombination signature (A slope corresponding to $n_2 = 2$ in the upper left plot) are characterized by a pronouncedly inhomogeneous current distribution, with the peak currents flowing at a small number of low-dimensional regions which are mostly point-like bright spots. On the other hand, the two cells displaying a tunneling signature under low-forward-bias (temperature-independent A in the upper left plot), one of which is an (n)c-Si based solar cell, show a very homogeneous current distribution. Although the amount of data on which this conclusion is based is small, the lower left panel suggests that the homogeneity of the current distribution is correlated with the overall level of the second diode saturation current density $j_{0,2}$. This indicates a significant current contribution from the bright spots appearing in the DLIT pictures, consistent with intuition when one compares the images taken at $U = 0.6$ V and $U = 0.5$ V. While for $U = 0.6$ V, the pictures still show a significant area-related current, the active cell area besides the defective regions mainly displays the baseline noise of the measurement technique at $U = 0.5$ V, highlighting a significant current flow through those regions.

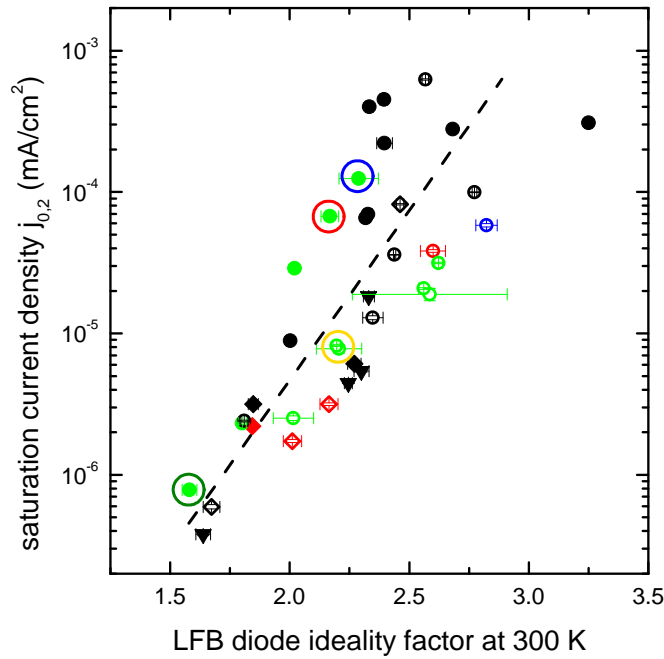


Figure 5.9: Correlation of the LFB saturation current density $j_{0,2}$ with the value of the effective second diode ideality factor $n_2 = e/(AKT)$. This graph implies that solar cells with potentially inhomogeneous current distribution, characterized by a large $j_{0,2}$, display a high ideality factor in the respective (low forward bias) region. This is consistent as the current peaks are most likely due to recombination in highly defective regions which is often characterized by ideality factors > 2 [24, 25, 206].

The fact that the bright spots gain in relative importance over the area-related current when lowering the bias voltage suggests a higher ideality factor of those local excess currents. Indeed it was found in previous works that a prototypical situation for most c-Si solar cells — particularly for multi-crystalline silicon solar cells — is the following: An area-related current with a low ideality factor (mostly close to one) is accompanied by an inhomogeneous current contribution which is localized at low-dimensional defect sites and displays a higher ideality factor (sometimes well in excess of 2). While the overall cell characteristics can be described well within the Shockley theory, peculiar behavior is often observed at low bias voltage which includes very large ideality factors or non-exponential forward currents (see e.g. Ref. [24, 25] and references therein). This behavior is commonly explained by so-called 'coupled defect-level recombination', which refers to a situation where the assumption underlying the SRH theory that each defect can be treated as isolated in terms of occupation statistics, breaks down: If an extremely high (local) defect concentration is present in a region of high built-in field, charge carriers can tunnel from the bands into defect states and undergo quick transfer to deeper defect levels if the respective wave functions overlap significantly, as is the case for high defect concentrations. This effectively enhances the recombination rate over the value expected from SRH theory and yields a saturation of the recombination rate with increasing bias voltage which is the prerequisite for an ideality factor in excess of 2 [24, 25, 206]. This situation seems to be present in some of the a-Si:H/c-Si cells as well, as implied by the DLIT analysis sketched above.

Additional evidence comes from Fig. 5.9, where the absolute level of the low-forward-bias current $j_{0,2}$ at 300 K is plotted versus an effective ideality factor of the LFB diode at 300 K, calculated by $n_2 = e/(AKT)$. It is obvious that for high levels of the LFB saturation current $j_{0,2}$, which may be taken as indication for a local excess current

contribution based on the assessment of the DLIT pictures, a higher ideality factor is observed at 300 K, being indicative of locally enhanced recombination which probably stems from low-dimensional defective regions.

In total, DLIT pictures were taken on 10 different cells at $U = 0.6$ V, all of which support the observed correlation between inhomogeneity and the absolute level of $j_{0,2}$. Additionally, DLIT was repeated at $U = 0.5$ V forward bias for 4 of these cells, with the results supporting the apparently enhanced local ideality factor of the defective regions. Of the 10 analyzed cells, 4 showed more or less pronounced current inhomogeneities which would identify $j_{0,2} \approx 5 \times 10^{-5}$ cm² as a 'threshold LFB saturation current density' separating the homogeneous from the inhomogeneous current distributions in terms of visibility with DLIT.

Thus, a consistent picture emerges if one assumes a prototypical character of the solar cells analyzed with lock-in thermography: The presence of low-dimensional defective regions leads to locally enhanced current contributions, a high level of the LFB diode saturation current density $j_{0,2}$ and a recombination signature, i.e. a slope of A versus T consistent with an ideality-factor-like T -dependence with $n_2 = 2 \dots 3$ and the respective activation energy being mostly compatible with $E_g/2$. The absence of inhomogeneities in the current distribution leads to a tunneling signature, i.e. no slope of A versus T and an activation energy around 0.4 eV for both substrate doping types, underpinning the observation sketched above that some (n)c-Si based cells which display good performance in terms of illuminated I/V parameters also show a tunneling signature.

Important to note, none of the illuminated cell parameters (including V_{oc}) seems to be affected by the low-dimensional excess current spots, as no correlation is observed between the level of the LFB saturation current density $j_{0,2}$ and V_{oc} . Consistently, both the cells showing such contributions and those that do not display V_{oc} values spreading across > 20 mV in the lower left panel of Fig. 5.8. This observation is consistent with previous reports indicating that the presence of LFB features such as local (in some cases even non-exponential) excess currents or high ideality factors does not affect the high-forward-bias range which determines the V_{oc} point [24]. Only for drastically enhanced $j_{0,2}$ or an Ohmic contribution from shunts, the fill factor deteriorates which affects the illuminated solar cell performance. However, in none of the cells analyzed here this was the case.

5.5. Discussion

5.5.1. Discussion of transport mechanisms

From the analysis presented above it is obvious that the transport signature of a-Si:H/c-Si heterojunction solar cells shows some subtle differences to the 'classical' c-Si homojunction solar cell. Two distinct regions are observed when analyzing dark I/V curves: In the high-forward-bias range, a Shockley-type diffusion current is observed as for homojunctions, however with the ideality factor slightly deviating from the ideal value of 1 and being dependent on the passivation of the c-Si absorber which is reflected in V_{oc} . The cause of this systematic deviation remains unclear, but a connection to the heterojunction aspects influencing the transport mechanism is suggested. In the high-

forward-bias region, a direct link between dark I/V fit values and device behavior can be established: The saturation current density $j_{0,1}$ allows for a remarkably precise estimation of device V_{oc} from its fit value, if the real ideality factor is taken into account. In the low-forward-bias range, the transport is more subtle: A naïve analysis in the framework of a 1D approach suggests a superposition of recombination and tunneling transport with the dominance of either mechanism being dependent on the substrate doping type. Most of the (n)c-Si-based samples exhibit a transport signature compatible with recombination in the space charge region, while most of the (p)c-Si-based samples reveal a dominating temperature-independent tunneling contribution to the forward current under low bias. The difference between the two substrate doping types may tentatively be explained by different band offsets, and seems to be supported by the quantum mechanical nature of states supporting the tunnel hopping process.

However, the analysis of dark lock-in thermography pictures reveals that the behavior under low forward bias is actually more complex: The recombination signature cannot *a priori* be connected to a certain device type but seems to be related to the appearance of lateral inhomogeneities in the current distribution, which appear to result from point- or stripe-like defective regions. The current originating from these regions displays a larger ideality factor, which points towards recombination through locally abundant coupled defects. Despite the small number of samples on which the conclusion is based, it appears that *all* the cells with a homogeneous current distribution show a temperature-independent A , i.e. a tunneling signature.

Thus it is suggested that the multi-tunneling-capture/emission processes seen in this case predominantly in (p)c-Si based samples represent the general case, which all the solar cells display in the case of well-passivated absorbers and a homogeneous current distribution. Then, the apparent domination of recombination-related signatures in (n)c-Si based cells would have to be seen as an indication for the fragility of (p)a-Si:H/(i)a-Si:H]/(n)c-Si passivation as compared to the doping-inversed case, as also suggested by the passivation phenomenology in section 4.2.3 (cf. Figs. 4.8 & 4.10). On the other hand, the dominant tunneling signature in (p)c-Si based structures may underline the importance of the valence band offset for charge carrier transport. Note that under forward bias majority carriers are injected, while the relevant transport situation for solar cell operation is the extraction of minority carriers. Thus, a crucial impact of the valence band offset under illuminated I/V could be expected for the *doping-inversed* structures: It may well be the case that the sensitivity of the fill factor in (n)c-Si based solar cells towards IBL thickness can be related to the valence band offset as well, which will be discussed in chapter 7.

The presence of defective regions in 4 out of 10 cells under study highlight the necessity to revisit the processing chain for possible origins of this finding⁶.

Interestingly, the low-forward-bias regime is much less intimately connected to relevant device parameters than the high-forward-bias transport. Although microscopic aspects of the heterojunction (band offsets, a-Si:H gap DOS etc.) indeed seem to influence the carrier transport in this regime, the interface passivation quality as reflected in V_{oc}

⁶One is tempted to blame this result on the manual handling and the excessive use of tweezers during the processing, however this is a handwaving explanation at this stage.

governs only the high-forward-bias current.

5.5.2. Application of dark-I/V fitting for passivation assessment

The main application of the dark I/V analysis results from the direct connection between the high-forward-bias saturation current density $j_{0,1}$ and the open-circuit voltage V_{oc} of the device via Eq. 2.46. It enables assessing the passivation of the c-Si absorber from transport properties of the a-Si:H/c-Si heterojunction through a measurement which can be performed in the dark. This allows to monitor the implied V_{oc} through the entire process chain: For structures without metal contacts, PCD provides a convenient method which can be complemented by the dark I/V technique after the stage in the process when metal contacts are deposited. In the last chapter in section 4.3.2, the method was employed to monitor the impact of aluminum deposition by e-beam evaporation revealing a detrimental effect of the x-ray exposure during this deposition step. In order to calculate an implied V_{oc} from Eq. 2.46, an estimated j_{sc} has to be used. If only relative comparison is desired, e.g. to compare different processing options, the j_{sc} value is not important and 'generic' values can be used e.g. obtained from Eq. 3.4 employing typical reflection properties and IQEs. If an absolute comparison to illuminated I/V data shall be done, the knowledge of typical j_{sc} for a given substrate morphology is necessary to achieve a thorough V_{oc} estimation.

Based on the DLIT analysis one could further imagine to employ the dark I/V analysis to deduce the presence of local excess currents from the low-forward-bias fit parameters, most prominently from the level of $j_{0,2}$ or the effective n_2 . However, more DLIT measurements would be needed to underpin the relation between $j_{0,2}$ and the current inhomogeneity, before such effort can be undertaken.

5.6. Chapter conclusion

The key question for this chapter was:

How does charge carrier transport proceed in a-Si:H/c-Si heterostructures, what is its relation to solar cell performance and what are the differences between the doping-inversed structures?

In conclusion, it was found that in the high-forward-bias range, a direct link between fit values and device behavior can be established: The saturation current density $j_{0,1}$ allows for a precise estimation of device V_{oc} from its fit value. While the transport signature is compatible with diffusion in the neutral bulk and thus ruled by the classical Shockley equation at first glance, a closer look reveals the heterojunction aspects of the a-Si:H/c-Si structures to become more pronounced with enhanced absorber passivation, as reflected in the ideality factor increasing with V_{oc} .

In the low-forward-bias range, the picture is subtle: In the ideal case, tunneling processes dominate the I/V characteristics particularly for (p)c-Si based cells, with the multi-tunneling-capture/emission model providing a promising explanation for the signature observed experimentally. This result reflects the impact of the large valence band

offset on the transport, representing a significant barrier for holes crossing from the c-Si into the a-Si:H and thus rendering alternative transport paths important — such as tunneling into the localized states of the a-Si:H valence band tail.

In practice however, a large fraction of a-Si:H/c-Si solar cells seems to be affected by the presence of point- or stripe-like defective regions which leads to an increased overall level of the low-forward-bias current and a recombination signature in the transport, which is superimposed on the tunneling signature.

Thus it was demonstrated that meaningful information can be extracted from fitting of dark I/V curves which allows for evaluation of interface passivation and thus accurate prediction of device open circuit voltage, alongside the determination of obvious technological parameters such as shunt and series resistance, and identification of the dominant transport mechanisms.

6. The material properties of ultrathin a-Si:H layers

In this chapter, the material properties of thin undoped a-Si:H layers on c-Si substrates are investigated. Characterization of amorphous silicon with thicknesses in the order of only 10 nm is challenging from an experimental point of view. Dedicated methods are employed to gain insight into structural, electronic and optical properties of the (i)a-Si:H films. First, the hydrogen concentration and bonding configuration is explored using infrared absorption spectroscopy. Then, the optical properties are investigated with spectroscopic ellipsometry and the mass density is inferred from the optical data. Photoelectron spectroscopy is used to evidence the Si-H bonds in the a-Si:H valence band and to quantify the density of localized electronic states in the a-Si:H band gap.

Further, secondary ion mass spectroscopy is employed on deuterated amorphous silicon layers (a-Si:D) to profile the deuterium distribution along the depth axis and thus obtain a quantitative picture of the homogeneity of the layers. A forward simulation based on a model of ion-beam assisted profiling is used to eliminate the impact of experimental broadening from the data.

At the end of the chapter, the elucidated a-Si:H properties are discussed in their entirety and in relation to previous data on thick a-Si:H layers. It is found that ultrathin a-Si:H films mostly behaves similarly to thick a-Si:H layers which lays the foundation for the assumption that the mechanisms and relations well-known from thick layers are at work as well in films consisting of about 50 monolayers only. This will help in the following chapters to understand the a-Si:H/c-Si band lineup and the passivation properties of thin (i)a-Si:H on crystalline silicon surfaces.

Note that hydrogen/deuterium effusion measurements which complement the infrared spectroscopy results presented here are described in appendix B.

This chapter is based on the publications [D], [E] and [G] from the list in the appendix.

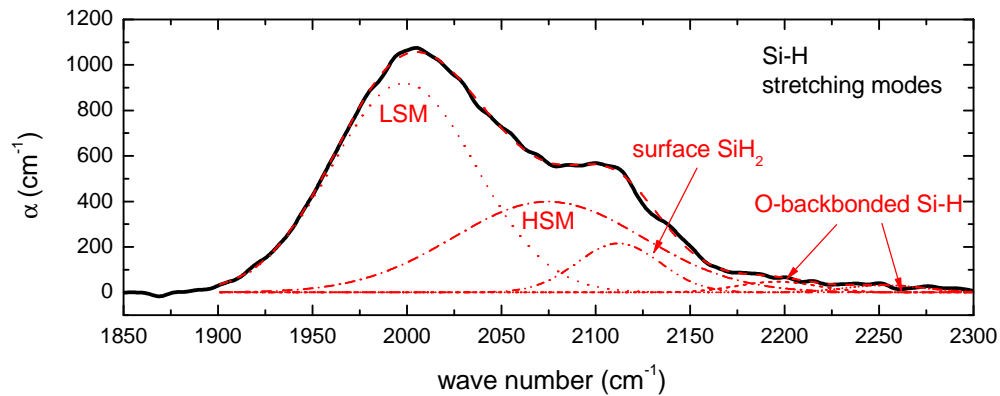


Figure 6.1.: Typical FTIR spectrum of a 10 nm thick a-Si:H layer in the wave number region of the Si-H stretching modes. The most important modes and their contributions as deduced from fitting are included: Low-frequency-stretching mode (LSM), high-frequency-stretching mode (HSM), surface-related SiH₂ and two oxygen-back-bonded Si-H modes. The dashed red line is the sum of the fitted modes, agreeing well with the measured data.

6.1. Introduction

Due to the structural and compositional degrees of freedom in the amorphous silicon-hydrogen network of a-Si:H, it is to be expected that the properties of the a-Si:H/c-Si heterojunction will depend to some extent on the microscopic aspects of the thin a-Si:H layer. This is concerning both the heterojunction band lineup, as well as the defect density at the heterointerface. Until now there is only limited knowledge on the interplay between a-Si:H properties and these aspects of the heterointerface. This gap shall be filled by gaining microscopic insight on undoped a-Si:H layers with device-relevant thickness — being of the order of 10 nm — by infrared spectroscopy, photoelectron spectroscopy and spectroscopic ellipsometry. Further, it is not given *a priori* that the layer properties are constant across the film thickness. For instance there have been reports of a layer of poor structural properties adjacent to the heterointerface [78, 84]. Making use of secondary-ion-mass spectroscopy (SIMS) on deuterated amorphous silicon, the homogeneity of (i)a-Si:D layers is assessed. The microscopic information gained in this chapter will prove useful in the later parts of this thesis when the properties of the heterojunction are analyzed.

6.2. a-Si:H hydrogen content and microstructure: Infrared spectroscopy

6.2.1. FTIRS results

The stretching mode spectra

As explained in Section 2.1.2, hydrogenated amorphous silicon contains hydrogen bound in different microscopic configurations and varying total atomic percentage. In the following, the H content and -microstructure is elucidated for the standard (i)a-Si:H de-

Table 6.1.: Silicon-hydrogen stretching modes as seen in FTIR spectra and the respective peak assignment, following the previous works indicated in the last column.

| Hydride type | Wavenumber cm ⁻¹ | FWHM cm ⁻¹ | Name | References |
|------------------------------------|--------------------------------|--------------------------|--------|---------------|
| SiH | 1980-2010 | 80 | LSM, A | [32, 78, 230] |
| SiH clustered | 2070-2100 | ? | HSM, B | [230] |
| SiH surface | 2080 | <30 | | [32] |
| SiH ₂ | 2085-2088 | 80 | HSM, B | [32, 78] |
| SiH ₂ surface | 2114 | <30 | C | [32] |
| SiH ₃ surface | 2135 | <30 | | [32, 78] |
| SiH ₂ (O ₂) | 2185-2210 | 80 | D | [32, 78] |
| SiH(O ₃) | 2250 | 80 | E | [32, 78] |

position conditions employed in this study, which are listed in Section 3.1.2, Table 4.2. To this end, FTIRS was applied to measure the vibrational response of the Si-H bonds in the frequency range of the stretching modes [26, 32] on quarters of 4" (n)c-Si wafers symmetrically passivated with (i)a-Si:H layers of 10 nm thickness [12]. Figure 6.1 shows a typical IR spectrum in the domain of the absorption coefficient, taking into account the layer thickness. A satisfactory deconvolution of the spectrum can be obtained with five Gaussian modes, which are compiled in Table 6.1, together with other possible hydride signals and the references for the respective assignments. Note that there is an ambiguity of the signals in the wave number range 2080 . . . 2090 cm⁻¹, which is assigned to bulk dihydrides by some authors [26, 147] and to clustered monohydrides by others [86, 229, 275]. It will be referred to this mode as the 'high-frequency stretching mode' (HSM) and its microscopic origin shall be discussed below. Observing the spectrum one notes that the most prominent modes are the HSM, the 'low-frequency stretching mode' (LSM) and surface SiH₂, while the oxygen-related signals are marginal. As the surface SiH₂ mode at 2114 cm⁻¹ involves the H at the free a-Si:H surface only¹, no impact on the heterointerface is to be expected and therefore this mode will not be analyzed in detail in the following.

In Fig. 6.2, the IR spectra of nine different (i)a-Si:H samples corresponding to the deposition parameter sets from Table 4.2 are given, again showing the absorption coefficient. The film thickness for the calculation of α was obtained from model-based fitting of SE data taken on the same samples using the parametrization of the optical functions by Jellison *et al.* [114] (cf. appendix 3.2.3).

It is obvious that the deposition conditions impose drastic differences in the H bonding configuration. Particularly, the contribution of the HSM varies significantly, with the layers deposited at higher temperatures at a given pressure regime having lower contributions of the HSM mode. In terms of the HSM dependence on the deposition regime, it can be stated that the HSM is always largest for LP at constant substrate temperature, and lowest for MP. The amplitude of the LSM changes to a lesser extent, however it ap-

¹Additional evidence for this assignment will be given in chapter 8 in the analysis of difference spectra before and after annealing of the samples.

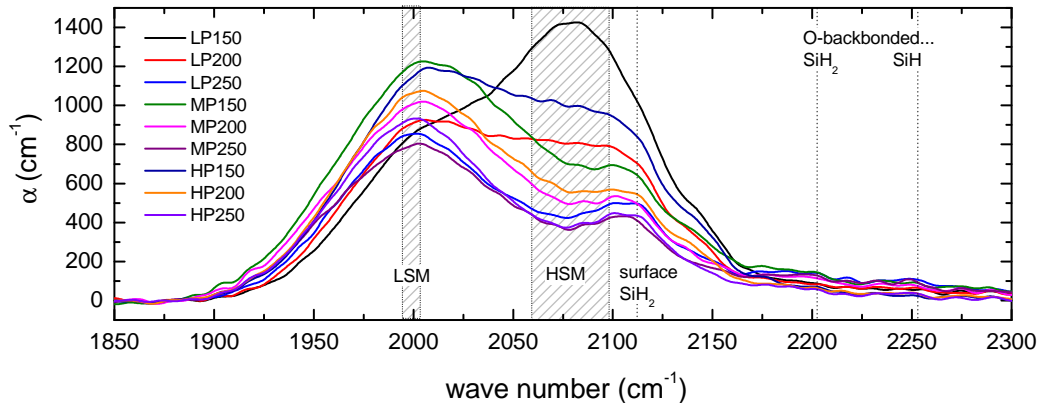


Figure 6.2.: FTIR spectra of (i)a-Si:H layers with 10 nm thickness deposited at different PECVD conditions. The gray lines and hatched areas mark the peak positions of the modes which were used to fit the spectra (example fit shown in Fig. 6.1).

pears that there is a reciprocal connection between LSM and HSM. The surface-bound SiH_2 mode is visible, however its size cannot be evaluated without a deconvolution. The oxide-related modes are marginal for all the samples.

Determination of H content

In a next step, the spectra were fitted with the five modes described above (A-E) and the hydrogen concentrations in atomic percent giving rise to the respective silicon-hydrogen stretching modes were calculated following the procedure of Langford *et al.* [139]. In Fig. 6.3, the contributions of the three significant modes to the total H content are plotted, distinguishing different deposition temperatures and pressure regimes. The qualitative discussion performed above on the spectra is confirmed here: The total H content decreases with increasing deposition temperature at constant pressure, or for constant temperature along the line LP \rightarrow HP \rightarrow MP. The most significant change occurs in the HSM, which can contain between 5 and 20 at. % hydrogen, while the LSM-content varies only between 3 and 9 at. % H. The fact that LSM and HSM are inversely connected leads to the total H content and the LSM being also reciprocal (i.e. the *lower* the LSM contribution, the higher the HSM and also the total H content as the HSM varies over a larger range). The surface-bound SiH_2 does not vary pronouncedly, however it appears that higher overall H content is connected with increased surface-bound H concentrations, as would be expected.

6.2.2. Comparison to pertinent data

Plotting the H concentrations found in LSM and HSM versus the total *bulk* H content $C_{\text{H,bulk}}$, defined as LSM- plus HSM-bound hydrogen, in Fig. 6.4a again highlights the large differences in total H content imposed by the deposition conditions, and the dom-

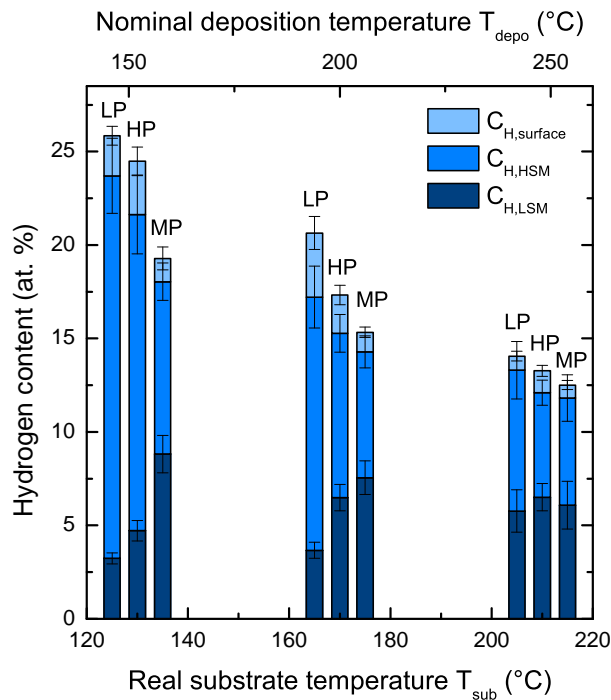


Figure 6.3: Hydrogen content found in the three dominant Si-H stretching modes (LSM, HSM and surface SiH_2) of (i)a-Si:H layers with 10 nm thickness, depending on PECVD deposition conditions. Layers were deposited at 130°C, 170°C and 210°C substrate temperature (horizontal offset of the bars for clarity) using parameter sets 'LP', 'HP' and 'MP'.

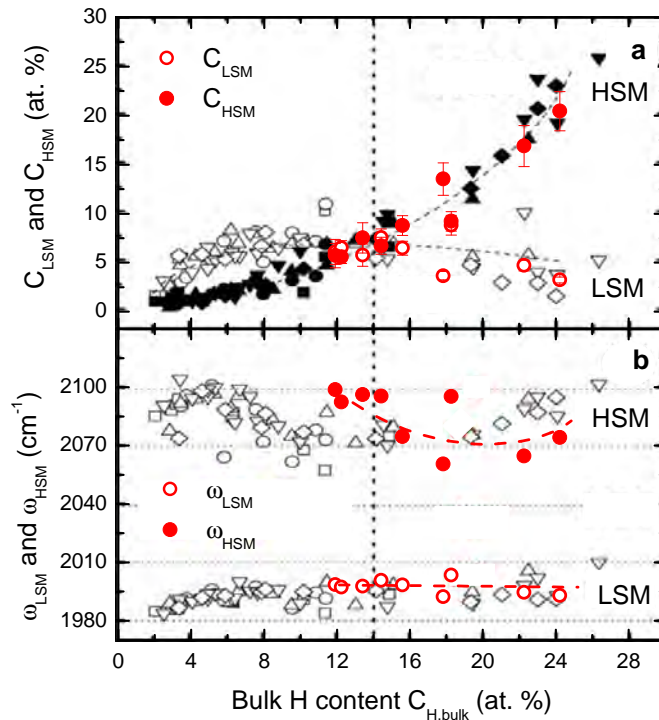
inating role of the HSM in determining the total H content. There is a smooth and systematic increase of the HSM with the total H content, while the contribution of the LSM slightly decreases, as seen also in Fig. 6.3. In Fig. 6.4b the peak positions are plotted versus the total H content, displaying no pronounced shifts. There is some scatter in the HSM peak position which is explainable by the close proximity to the surface dihydride mode, which introduces some cross-correlations between the position (and to a lesser extent the amplitude) of the HSM and the amplitude of the surface mode². One might see some small systematic shift in the HSM position, indicated by the dashed red line in Fig. 6.4b which is intended as a guide to the eye. More importantly, the observations in Fig. 6.4 are fully consistent with the results by Smets *et al.* [229, 230] on thick a-Si:H samples made by the expanding thermal plasma technique (data shown in the background of Fig. 6.4). This striking evidence underlines the compliant behavior of ultrathin a-Si:H in terms of H microstructure: There is no observable difference between the layers of 10 nm thickness and the μm range samples analyzed by Smets *et al.* in terms of H incorporation.

Additionally, the similarity of the data suggests the conclusion of Smets *et al.* and others to associate the HSM with the clustered Si-H phase on the inner surfaces of voids [86, 229, 275] to be valid in this case as well. Indeed, in the next section, additional evidence for an increasing void fraction along with the total H content will be presented, based on the analysis of the a-Si:H mass density.

Concerning the H microstructure, one can summarize the following: The samples are

²Additional evidence for this slight cross-correlation will be presented in chapter 8, section 8.3.1.

Figure 6.4: (a) Contributions of LSM and HSM to the total H content, and (b) the respective peak positions in terms of wave numbers. The data in the background of the figure is FTIRS data by Smets *et al.* [229, 230] taken on thick a-Si:H layers deposited by the expanding-thermal-plasma technique (thickness in the μm range). It is obvious that the trends observed here are consistent with existing data.



characterized by an essentially constant contribution of isolated monohydrides and a strongly varying fraction of the H configuration giving rise to the HSM, which are supposedly microscopic voids. Additionally, a SiH_2 -rich open surface of the a-Si:H is detected, while almost no oxide-related signal are present.

6.3. Optical properties

Now that the H content and -microstructure of the thin (i)a-Si:H have been elucidated, it seems reasonable to make use of the bulk H concentration $C_{\text{H,bulk}}$ as an ordering parameter when examining other structural and electronic features of (i)a-Si:H in the following.

6.3.1. Optical band gap

It is known that the a-Si:H band gap changes upon varying the bulk hydrogen concentration $C_{\text{H,bulk}}$. This effect has been observed experimentally in several studies on thick samples measuring the optical band gap with absorption spectroscopy [41, 72, 119]. In a first step it is aimed at reproducing this trend for (i)a-Si:H layers of 10 nm thickness. To this end, SE data is taken on the FTIRS samples to quantify $E_{g,\text{a-Si:H}}^{\text{opt}}$ with the two optical parameterizations explained above in section 3.2.3. Combining the SE data with the total bulk H content $C_{\text{H,bulk}}$ in Fig. 6.5, it is obvious that the band gap widening is also present in thin (i)a-Si:H. Note that while fitting the Ferlauto model to the SE data yields a slightly larger scatter in the $E_{g,\text{a-Si:H}}^{\text{opt}}$ fit value and systematically smaller band

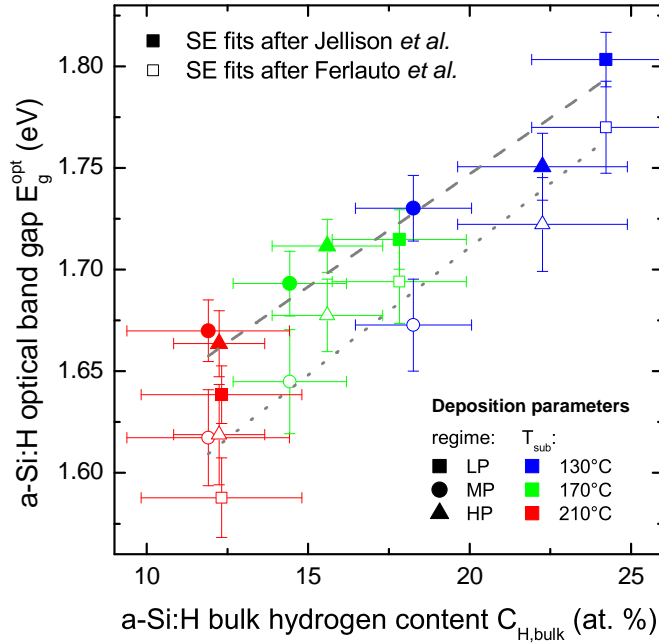


Figure 6.5: Optical band gap of (i)a-Si:H layers as derived from modeling of SE data, and linear fits (dashed lines). Full symbols: Tauc-Lorentz model of Jellison *et al.* [114]. Open symbols: Modified Tauc-Lorentz model of Ferlauto *et al.* [70]. The latter model leads to a less defined fit value for the band gap due to a higher number of fit parameters and the resulting interdependencies. The offset stems from the different definitions of $E_{g,a-Si:H}^{opt}$ in the framework of the two models. Note that the legend identifying the (i)a-Si:H deposition conditions applies in the following, as well.

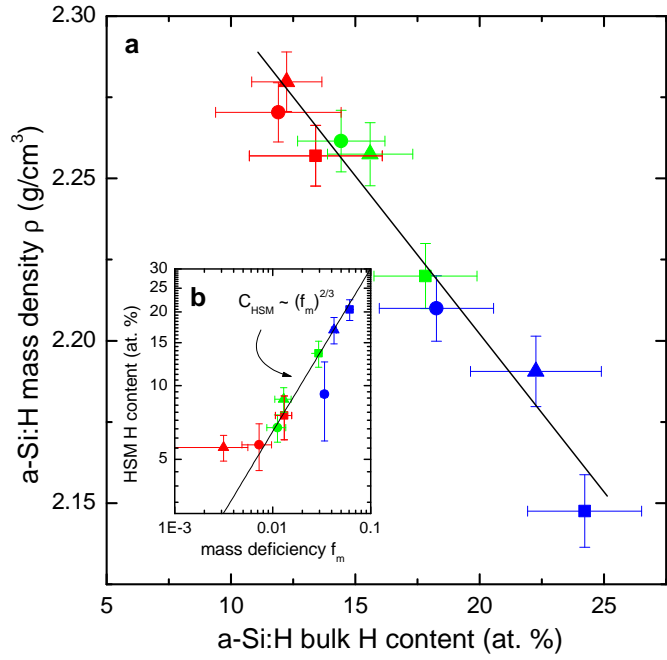
gaps, the two parameterizations agree well in terms of the overall trend: The a-Si:H band gap widens by approximately 150 meV when the bulk hydrogen content increases from 12% to 24%. Linear fits yield a slope of 11.1 ± 1.2 meV per at. % H for the Jellison model data (dashed line in Fig. 6.5), and 12.6 ± 1.5 meV per at. % H for the Ferlauto model (dotted line).

The differences in fitting results between the two models can be readily explained: The larger errors when employing the Ferlauto parameterization follow from a higher number of fit parameters and thus resulting cross-correlations. The vertical offset of ≈ 40 meV stems from the different definitions of $E_{g,a-Si:H}^{opt}$ in the framework of the two models. Ferlauto *et al.* themselves noticed systematically smaller band gap values obtained with their model as compared to the optical gaps from Tauc plots [256] of optical absorption spectroscopy data [70]. In the band gap range of our samples, this deviation amounted to about 55 meV, which is reasonably close to the difference between the two models observed here. Thus one can consider the Jellison model to yield band gap estimates compatible to those obtained from optical absorption spectroscopy. As the details of the band tail absorption, which is explicitly included only in the Ferlauto model, are not relevant for the present purpose and the band gap fit values obtained with the Jellison model are more robust and compatible with the Tauc gap (thus facilitating comparability to measurements on thick layers), the output of the latter model will be used for the remainder of this thesis. It is further noted that the *slope* of $E_{g,a-Si:H}^{opt}$ versus $C_{H,bulk}$ is found to be independent of the choice of a-Si:H optical parametrization.

6.3.2. Refractive index and mass density

In order to corroborate the interpretation of the HSM in the IR spectra to be indicative of H-decorated voids [86, 229, 275], the mass density ρ of the films is analyzed in the

Figure 6.6: (a) Mass density ρ of a-Si:H films as calculated from FTIRS and SE data vs. total bulk H content. The line is a guide to the eye. (b) HSM hydrogen content shown over the mass deficiency f_m and power law fit (line). The scaling of the HSM intensity with the mass deficiency to the power of 2/3 is consistent with the HSM being related to the clustered Si-H bonds at the inner surfaces of voids causing the loss in mass density.



following. It can be calculated using a Clausius-Mossotti approach from the refractive index in the long-wavelength limit n_∞ and the bulk hydrogen content $C_{H,bulk}$ by the following equation [193]:

$$\rho = \frac{n_\infty^2 - 1}{n_\infty^2 + 2} \times \frac{3m_{Si}}{4\pi \left[2\alpha_{Si-Si} + \frac{C_{H,bulk}}{1-C_{H,bulk}} (\alpha_{Si-H} - 0.5\alpha_{Si-Si}) \right]}. \quad (6.1)$$

Here, $\alpha_{Si-Si} = 1.87 \times 10^{-24} \text{ cm}^{-3}$ and $\alpha_{Si-H} = 1.36 \times 10^{-24} \text{ cm}^{-3}$ are the bond polarizability of Si-Si and Si-H bonds in a-Si:H, respectively, and a purely amorphous layer is assumed. The result of this analysis is shown in Fig. 6.6a: A pronounced loss in film density is observed with increased H incorporation. The slope of the decrease is much higher than what would be expected for the compact hydrogen configurations [230], which underpins the association of the HSM with Si-H decorating voids. Additional support comes from the analysis of the mass deficiency, i.e. the density loss relative to a-Si, defined as $f_m = 1 - \rho/\rho_{a-Si}$ with $\rho_{a-Si} = 2.287 \text{ g/cm}^3$. The decoration of the inner surfaces of microscopic voids in a-Si:H resulting in the HSM in the IR spectra must lead to an increase of the HSM signal with the void *volume*, which is proportional to the mass deficiency f_m , to the power of 2/3 [229]. Indeed, in Fig. 6.6b it can be seen that $C_{H,HSM}$ scales with f_m according to a power law with an exponent of 2/3.

Again, the general trends in the data are in very good agreement with the data of Smets *et al.* [229, 230]. The dominant HSM for a-Si:H films with higher H content and a pronounced loss in film density was also observed for PECVD films in the μm thickness range by Manfredotti *et al.* [149]. This and the fact, that the band gap widening per at. % hydrogen is of the same order as for several other studies [41, 72, 119], leads to the conclusion that the samples are typical for the higher H content range, despite their

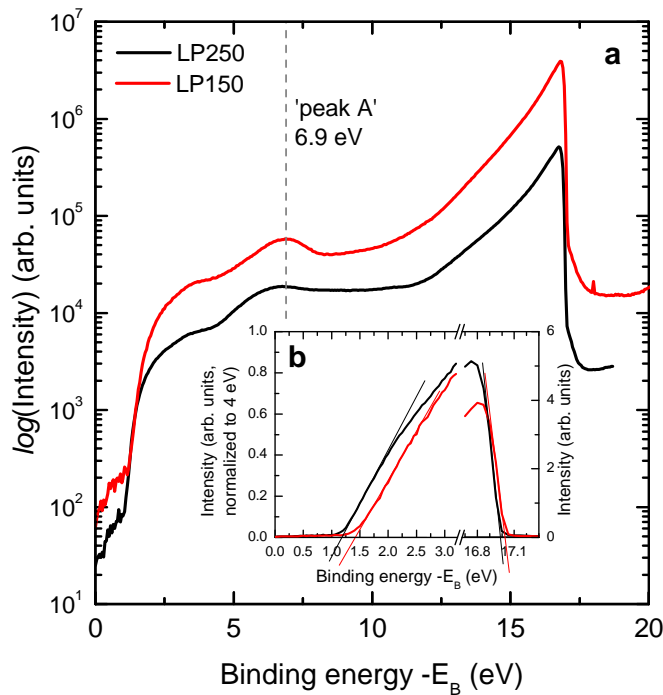


Figure 6.7: He-I UPS valence band spectra of two (i)a-Si:H layers (deposition parameter sets LP150 and LP250). (a) Overview on the spectra in the logarithmic domain (LP150 data is offset for clarity): Band edge at around 1 eV, Si-H bond-derived structure at approximately 7 eV, for > 10 eV a rising signal due to the increasing background of inelastically scattered electrons, before the work function cutoff is reached at 17 eV. (b) Details of the band edge and work function cutoff: Upon increasing the H content, the valence band edge moves down in energy.

small thickness.

Thus, to summarize the main result at this stage: The a-Si:H layers are characterized by an approximately constant contribution from distributed monohydrides and a strongly increasing phase of clustered-monohydride-decorated voids, while the band gap widens with the total H content consistent with previous studies. In the next section the accompanying changes in the electronic structure will be analyzed with photoelectron spectroscopy.

6.4. Electronic structure

To characterize the electronic structure of the undoped amorphous silicon layers, photoelectron spectroscopy was performed on layers nominally identical to those used for FTIRS and SE, however deposited on 2" substrates compatible with the UHV analytics chamber. Both UPS and CFSYS were measured on all layer types, He-I UPS spectra were exemplarily taken on two different layers representing the extreme cases of the spectrum in terms of H content to analyze the hydrogen-derived peaks deeper in the valence band [272].

6.4.1. He-I UPS valence band spectra

First, the He-I UPS valence band spectra are analyzed. Fig. 6.7a shows two spectra for the LP250 and LP150 samples (LP150 spectrum is offset for clarity), representative of the extreme ends of the range in H content (LP150: 24 %, LP250: 13 % as resulting from the FTIRS analysis). The energy axis has the Fermi energy as reference energy.

Fig. 6.7a provides an overview of the spectrum and allows to assess the general features: At about 1 eV, the leading edge of the valence band signal emerges from the noise level, and forms a plateau around 3...5 eV. At around 7 eV, there is a peak with a width of approximately 2 eV which is more pronounced for the LP150 sample. Above about 12 eV the spectrum begins to rise markedly, due to the increasing background of inelastically scattered electrons. At about 17 eV the count rate decreases sharply due to the work function cutoff of the secondary electron distribution.

In previous UPS studies on a-Si:H, the peak around 7 eV (commonly termed 'peak A') was observed as well and attributed to silicon-hydrogen bonds [231, 272, 278]. Thus it is consistent that its magnitude increases with the a-Si:H hydrogen content.

There is disagreement in the literature concerning the exact microscopic configuration of H giving rise to the 7 eV peak in the VB spectrum. Von Roedern *et al.* observed the combination of this 'peak A' and a second peak termed 'peak B' around 10.5 eV and identified both with SiH₃ groups [272, 274] based on theoretical and experimental results for H chemisorption on Si{111} surfaces [176]. Wesner *et al.* on the other hand took the peaks as indication for dihydrides *or* trihydrides [278]. This conclusion was supported by the pronounced decrease of peak A upon annealing [272], consistent with the standard interpretation of H effusion data which identified the elimination of higher hydrides with the low-temperature H evolution peak. This conclusion of higher hydrides causing the peak in the VB spectrum would directly contradict the association of the HSM IR mode with clustered monohydrides instead of higher hydrides, as made above. However, the *newer* works on a-Si:H VB UPS are more careful in giving definite peak assignments, based on two observations: Firstly, it was found in calculations by Ching *et al.* [37, 38] that different H configurations (including closely coordinated Si-H) can give rise to the same peak structure in the VB spectrum. Secondly, the identification of the low-temperature H evolution peak with dihydrides was questioned [172], alongside with the association of the HSM with SiH₂. Additionally, in our data 'peak B' is missing, as also observed for a-Si:H produced by sputtering in Ar/H atmosphere [231]. Thus, it is difficult to give definite assignments based on UPS spectra alone. Consequently, Smith *et al.* refrained from such effort and reasoned that in the light of the conflicting findings in previous studies, 'peak A' could also stem from H configurations different from di- or trihydrides [231]. As the limited data prevents further discussion at this point, the conclusion shall be restricted to the finding that the increase in intensity of 'peak A' associated with silicon-hydrogen bonds is consistent with the increased H incorporation found with FTIRS.

Despite the difficulties in interpreting the H contribution to the VB, there is a quantitative result which can be drawn from the UPS spectra, which is the position of the top of the valence band. As obvious in Fig. 6.7b, the leading edge of the VB moves down in energy upon increasing the H content. Extrapolating the band edges to the abscissa yields a retreat of 190 meV in the LP150 sample as compared to LP250. Later it will be shown that this value is consistent with the VB retreat found in near-UV PES. Note that in Fig. 6.7b it can also be seen that the work function cutoff slightly shifts by about 40 meV. Since in He-I UPS spectra the vacuum level is found at an energy 21.2 eV apart from the cutoff of the secondary electron tail, the 40 meV shift of the secondary electron cutoff would mean a 40 meV increase in the a-Si:H work function

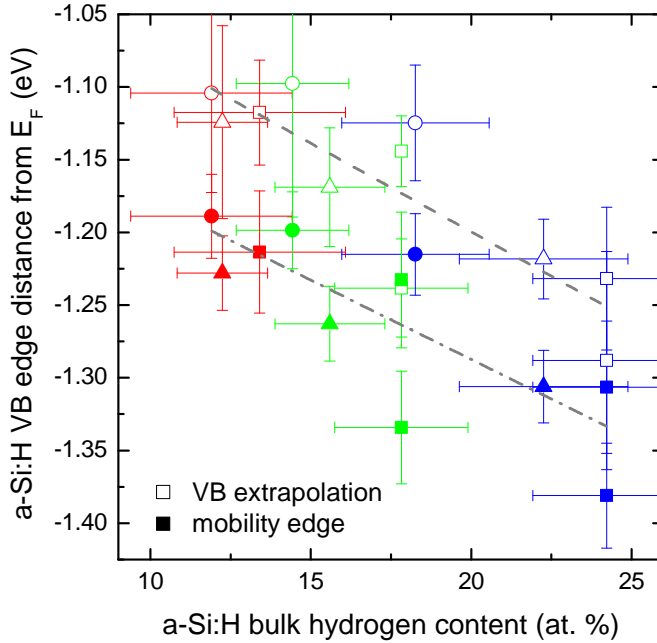


Figure 6.8: Energetic distance of a-Si:H valence band edges from E_F as determined from the analysis of CFSYS spectra, versus the bulk hydrogen content as measured with FTIRS on nominally identical samples. Open symbols: Extrapolation of a square-root fit to the a-Si:H valence band PES signal to zero. Closed symbols: Mobility edge as defined in the text, making use of an unnormalized a-Si:H model-DOS folded with the instrument's transfer function which is then fitted to the PES data. Both methods yield similar slopes as obtained from linear fits (dashed lines), and are offset by 90...100 meV which results from the definitions of the band edges.

of the LP150 sample as compared to the LP250 sample. This is slightly larger than the error of 30 meV assumed for the secondary electron cutoff value from reproducibility tests, and indeed it was confirmed in the NUVPEs spectra that the work functions of the different (i)a-Si:H layers are slightly different [134].

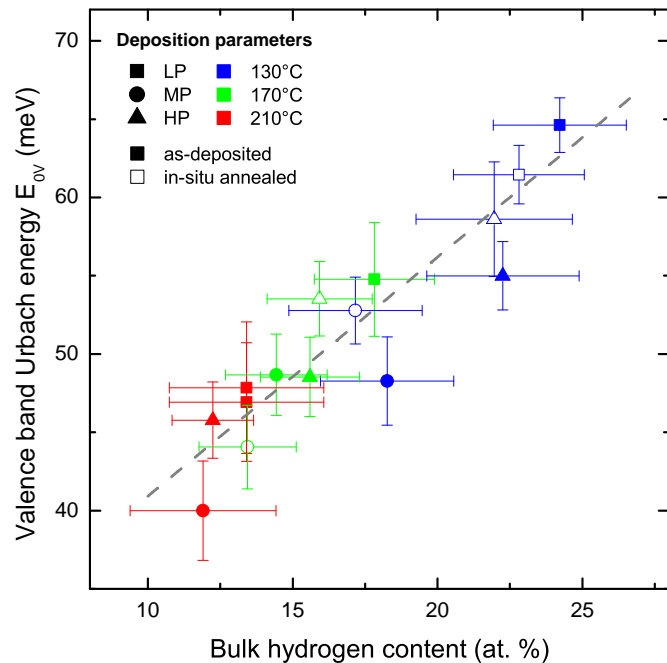
6.4.2. Constant-final-state yield spectroscopy results

In the following, the discussion will be restricted to the CFSYS data, as this method is optimally tailored for the analysis of thin a-Si:H layers in terms of information depth and resolution. The UPS data show the same trends in terms of VB edge and Urbach tail, however they are affected by a larger instrumental broadening and a much lower resolution, combined with the difficulties of normalization. Details go beyond the scope of this work, but are discussed in [129]. The CFSYS results will be discussed making use of the bulk H content $C_{H,bulk}$ from FTIRS as ordering parameter.

The valence band edge

The analysis begins with the valence band edge data, which are plotted in Fig. 6.8 versus the total bulk H content $C_{H,bulk}$, making use of the mobility edge definition (full symbols) and the extrapolated square root function (open symbols), as explained in section 3.2.2. Observing Fig. 6.8 one notes that the two definitions of the valence band edge lead to values which systematically differ by approximately 90...100 meV, consistent with the distance seen in Fig. 3.3. As mentioned above, the energetic distance of the two edges stays constant over the range of samples, therefore there is the same trend for the distance of the valence band edge from the Fermi level increasing by about 150 meV with the hydrogen content. The measured slopes are 11.1 ± 2.8 eV per at. %

Figure 6.9: Correlation between the valence band tail slope (Urbach energy, E_{0V}) and the bulk hydrogen content of 10 nm thick (i)a-Si:H layers. Note that the H content was measured with FTIRS on nominally identical samples. Open symbols denote samples that were annealed *in-situ* under UHV in the PES setup for 20' at 200°C and measured again, while the respective hydrogen concentration was inferred from ex-situ annealed FTIRS samples. It is suggested that E_{0V} stays constant upon annealing within experimental errors.



of H for the mobility edge (dash-dotted line) and 12.2 ± 2.6 eV per at. % of H for the extrapolated VB edge (dashed line), i.e. identical within experimental errors.

Interestingly, there is some scatter in the data which is not stemming from the method of VB edge determination, as it has the same form for both data sets. There are some possible reasons for this observation which shall be briefly discussed. Firstly, a possible charging of the sample during the PES measurement generally leads to a displacement of the valence band edge by shifting the reference energy. Although utmost care was taken to avoid such effect, an additional scatter may be introduced by a residual charge accumulating on the sample during measurement. Secondly, an eventual parasitic surface potential stemming from adsorbates collected during vacuum transfer could also vary from sample to sample as the base pressure in both the PECVD and PES tools is not entirely constant due to the particular chamber history or simultaneously running processes.

The valence band tail

In a next step, the valence band tail slope E_{0V} is plotted in Fig. 6.9 versus $C_{H,bulk}$. There is a pronounced and systematic increase of E_{0V} with the bulk H content with a slope of 1.5 ± 0.17 meV per at. % hydrogen. The absence of scatter as compared to Fig. 6.8 underlines the fact that the Urbach energy is the most robust fit parameter, as the slope of the exponential tail is well-defined, independent of normalization, and unaffected by shifts of the Fermi level due to charging or adsorbates. The origin of this pronounced increase will be discussed in chapter 7.

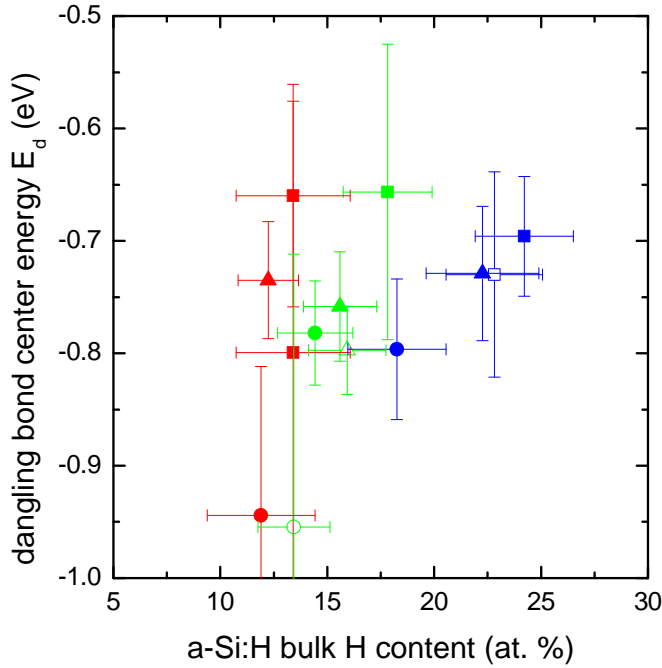


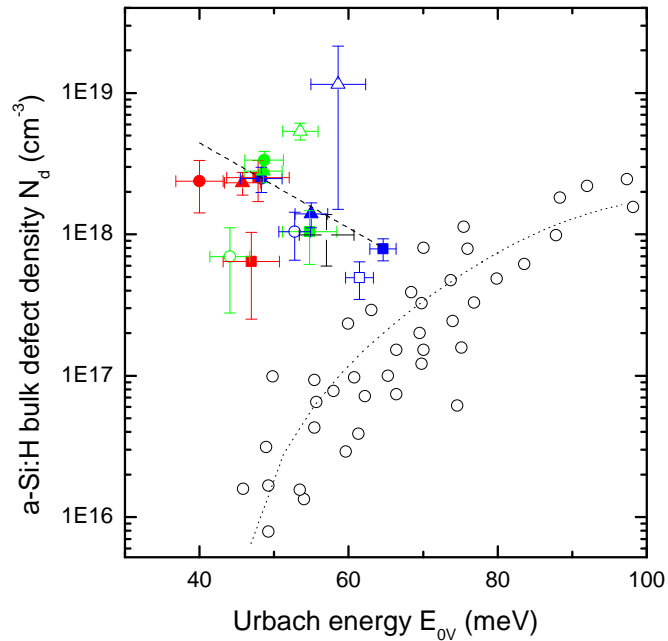
Figure 6.10: Energetic position of the Gaussian dangling bond distribution fitted to the CFSYS spectra, plotted versus the bulk H concentration. There is no pronounced systematic shift of the dangling bond center energy, implying that upon the downward shift in binding energy of the valence band edge with increasing H content, the deep defects stay at the same position relative to E_F .

The dangling bonds

In a last step, the defect parameters were analyzed. In Fig. 6.10, the center energy of the Gaussian dangling bond defect concentration is plotted. There is no trend with the H content and most of the data is compatible with $E_d = -0.75$ eV on the binding energy scale. Interestingly, as the valence band edge was found to retreat with $C_{H,bulk}$ this signifies that the dangling bonds are moving away from the VB edge upon increasing $C_{H,bulk}$. This would suggest that the valence band retreat and band gap widening are caused solely by removal of states at the top of the valence band, while the other features of the DOS (Si-H bonds deep in the VB and the dangling bonds in the band gap) stay at constant energies with respect to the Fermi level.

However, some doubt is shed on the analysis of the defect parameters when analyzing the defect density N_d . There is no known direct connection between the H content and N_d , however the Urbach energy — being indicative of the density of strained bonds in the amorphous network — and N_d are connected through the metastability of a-Si:H and the weak bond-dangling bond formation mechanism (cf. Section 2.1.3). There is a large amount of pertinent data on thick a-Si:H films available for comparison of the $\{E_{0V}, N_d\}$ data, thus is reasonable to plot N_d versus the Urbach energy E_{0V} as is done in Fig. 6.11. The empty circles denote $\{E_{0V}, N_d\}$ data on thick films from different authors compiled by Stutzmann [249] (both doped and undoped a-Si:H, several growth techniques). The dotted line is a guide to the eye and marks the obvious trend to higher defect densities upon increasing E_{0V} . Disregarding the details of the specific models of defect equilibration, there is consensus that the amount of strain or disorder in the amorphous network is connected to the defect density via a conversion of weak bonds from the band tails into dangling bonds, leading to the observed connection. The (i)a-Si:H

Figure 6.11: Amorphous silicon bulk defect density N_d as obtained from CFSYS fits plotted against the valence band Urbach energy E_{0V} , and comparison to previous data on thick a-Si:H films taken from literature [249]. While the literature data illustrate the fundamental connection between the density of strained Si-Si bonds reflected in E_{0V} and the defect density (cf. section 2.1.3), the CFSYS-measured data deviate markedly. This result is interpreted as a surface-related enhancement of the defect signal in PES, e.g. due to adsorbates.



CFSYS data show systematically higher defect concentrations than would be expected based on the E_{0V} values, and a trend of decreasing N_d upon increasing E_{0V} . The few outliers stem from annealed samples, which may be explained by increased adsorption of parasitic species in the UHV molecular-beam-epitaxy chamber where the in-situ annealing took place. Fitting an exponential function through the unannealed data (dashed line) highlights the surprising behavior which contradicts the well-established trend. A similar trend of N_d versus E_{0V} was observed already by Korte [129] analyzing data taken in the same setup. In his data, the Urbach energies were systematically higher (65...120 meV) while the overall level of the defect concentration was about the same. Overlooking both sets of data it seems that there is a lower limit for the defect density around $10^{18} \text{ eV}^{-1} \text{ cm}^{-3}$ which is almost independent of the Urbach energy. Other authors reported similarly high N_d values observed in total yield PES [226, 282, 283] and attributed this effect to a defect-rich layer at the surface, which over-proportionally contributes to the PES signal [283]. Evidence for the existence of a defect-rich surface was also found in optical absorption measurements [109]. It thus seems reasonable to assume that a similar contribution of a defect-containing surface layer is present in the samples analyzed here as well. This on the other hand also restricts the significance of the DB energetic positions obtained with CFSYS, as the nature of the states dominating the measured defect density is unknown. The resulting energetic position of the superposition from surface layer- and bulk defect densities may not be representative of the dangling bonds in equilibrated a-Si:H.

Summary of CFSYS analysis

Concluding this section it can be stated that the (i)a-Si:H layers are characterized by an Urbach energy displaying state-of-the-art values (40...65 meV) and increasing with

the total H content. At the same time, the valence band edge retreats by a value of ≈ 150 meV, which is about the same as the band gap widening observed in optical measurements. This result is independent of the choice of VB edge definition. The defect density measured with CFSYS is inconsistent with the E_{0V} values, as it is systematically enhanced and slightly decreases with increasing E_{0V} . This effect may be due to a surface-near damaged layer dominating the PES signal of the defect states in the a-Si:H band gap.

6.5. Hydrogen/deuterium profiling by SIMS

The analysis presented so far implicitly assumed a homogeneous a-Si:H layer, as all techniques yield signals integrated over the depth of the thin layer. However, it is not to be expected *a priori* that the structural and compositional parameters (H content and bonding, topological disorder, void density, etc.) are constant across the depth of the layer. This is e.g. due to the fact that the details of the a-Si:H growth process (cf. Section 2.1.4) impose certain structural inhomogeneities, particularly at the heterointerface and near the open surface. For instance, it was observed by real-time IR spectroscopy during growth, that the initial film growth³ leads to a significantly increased contribution of the HSM (attributed to SiH₂ in the respective paper) in the first 2...3 nm as compared to the bulk of the final layer with up to 40 % peak HSM-bound H concentration [75, 77, 78, 84]. Upon the successive bulk film growth, the HSM amplitude decreases and an increasing LSM signal is detectable, with a stationary growth reached at about 4 nm film thickness. These data suggest the existence of a void- or dihydride-rich interface layer of 2...3 nm thickness. In some publications, also indications for a HSM-rich surface layer were found [78].

Further, the growth mechanism itself requires film restructuring and relaxation taking place in the buried parts of the layer during deposition, which means that for a given volume element in the film the structure is not fixed at the moment when it is buried by the next monolayer of precursor particles⁴. Consequently, it was observed in minority carrier lifetime spectroscopy that the interface defect density decreases systematically during successive film growth, indicating a progressive improvement of the interface region in terms of electronic defects upon further growth, up to 30 nm thickness [169]. Indications for subsurface relaxation also come from other techniques [96].

For very thin layers, the impact of growth-induced inhomogeneities should be greater than for thick layers as the relative contribution to the bulk is larger and the time for equilibration of the network during growth is much smaller due to short deposition times. On the other hand, it was shown above that e.g. in terms of H incorporation there is no observable difference between the layers of 10 nm thickness and samples of the μm thickness range. Further, the passivation potential of (i)a-Si:H was shown to saturate around 10 nm thickness for the present samples (cf. Fig. 4.6). In the light of the

³The initial stages of a-Si:H growth are the creation of isolated islands on the substrate surface which then coalesce before the growth of a closed film begins.

⁴This effect is thought to stem from the flux of energy and particles, particularly atomic H, penetrating into the deeper layers from the film surface and the elimination of excess H from the subsurface layers by network reconstruction.

effects described above, this is an interesting observation which lends itself to further analysis.

6.5.1. Depth profiling — the choice of samples

Experimentally, the aspect of structural or compositional variations across the film thickness is hard to tackle directly, but a first and helpful step would be to profile the concentrations of the constituting species of a-Si:H, i.e. the silicon and hydrogen atoms, in layers of device-relevant thickness. This can be principally done using secondary-ion mass spectroscopy (SIMS), as described in section 3.2.1. Applying this technique on layers of the relevant thickness is extremely challenging, therefore the layout of the sample series has to be carefully chosen. First of all, the depth resolution is of the order of nanometers, and a trusted signal cannot be gained starting right from the open surface of the a-Si:H due to the details of the sputtering process [280]. To deposit a capping layer on top of the a-Si:H to avoid the blind spot of the transient initial SIMS sputtering phase was ruled out as interactions between the two layers are possible during deposition and sputtering. A test run revealed that (i)a-Si:H layers of 50 nm thickness had to be used to ensure an undisturbed signal in the region of interest, which are the first 10 nm of a-Si:H film starting from the heterointerface.

Further, hydrogen is abundant in vacuum chambers, limiting the achievable resolution on the concentration axis and lifting the noise level into the low percent range for hydrogen. Therefore, hydrogen was substituted for deuterium in the amorphous silicon layers, the latter being easily traceable down to relative concentrations of less than 10^{-4} . This was done by depositing a-Si:D with the usual deposition parameters from (D_2 -diluted) SiD_4 in the regular plasma chambers. It was thus implicitly assumed that the plasma chemistry is not dependent on the nuclear weight of the hydrogen atoms, and therefore the resulting a-Si:D layers were considered representative for a-Si:H as well. This assumption will be corroborated in the following paragraph. The thickness of the a-Si:D layers was measured by single-wavelength ellipsometry on co-deposited a-Si:D/ SiO_x /c-Si samples, as usually done for the a-Si:H layers. The effective lifetime of the a-Si:D-passivated c-Si substrates was checked with PCD which yielded values comparable to those of the respective (i)a-Si:H layers, suggesting similar conditions of the heterointerface under a-Si:D. It has to be noted that the HF dip employed to strip the native oxide off the crystalline substrates before loading them into the PECVD deposition system was performed with ordinary HF (instead of using deuterated hydrofluoric acid), therefore a monolayer coverage of hydrogen was introduced into the deposition system as c-Si surface bonds were H-terminated.

6.5.2. a-Si:H versus a-Si:D layers

A first phenomenological confirmation for the similarity of the SiD_4 and SiH_4 plasma chemistry is the similar growth rates which are observed during deposition. To test the assumption of compositional/structural similarity of the a-Si:H/a-Si:D layers, the integrated D content of the resulting a-Si:D layers was checked with FTIRS employing the identical analysis scheme as used for (i)a-Si:H. The results are shown in Figs. 6.12 & 6.13,

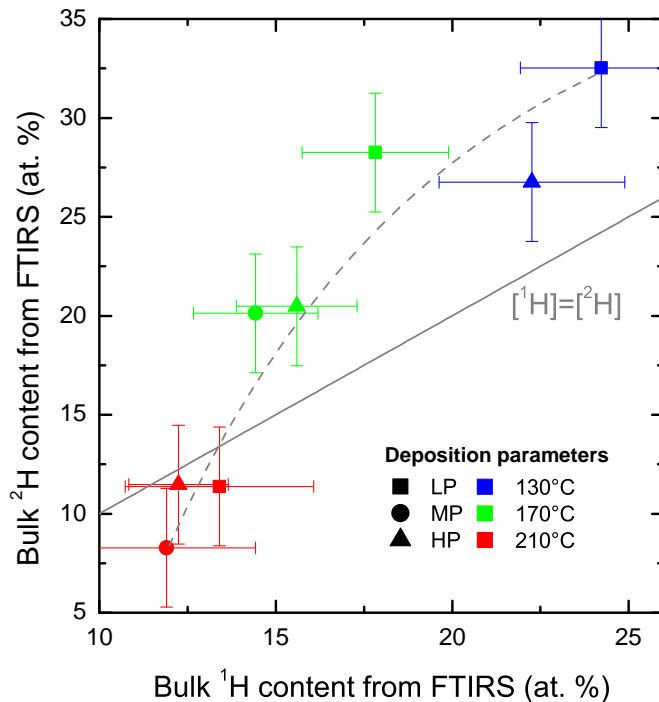


Figure 6.12: Comparison of bulk hydrogen/deuterium content as deduced from FTIRS measured on a-Si:H samples (abscissa) and a-Si:D samples (ordinate), which were deposited under identical plasma conditions with precursor gases (H_2 -diluted) SiH_4 , and (D_2 -diluted) SiD_4 , respectively. The approximate correspondence of the D/H content implies that the structural properties of a-Si:D are similar to a-Si:H, but not identical.

in comparison to the results on the a-Si:H layers. In Fig. 6.12, the resulting total D content is compared to the total H content for the same PECVD deposition conditions. It is obvious that the trends are qualitatively the same, with a larger variation of total D content than was observed for the H content. While the same deposition conditions mark the end points of the D/H content spectrum, the variation of D content is 8...32 at. %, while it was 11...25 at. % for the H concentration. For most deposition conditions the resulting a-Si:D deuterium concentration is higher than the hydrogen content in the respective a-Si:H sample, consistent with previous results [222]. Fig. 6.13 further allows to compare the hydrogen/deuterium microstructure and annealing behavior of the a-Si:D and a-Si:H layers, by showing the ratio of intensities for the LSM and HSM modes in the as-deposited and annealed state (after annealing for 5' at 200°C). The trends are very similar with the single exception of the MP250 layer. Thus, based on the comparison of the FTIRS analysis one can conclude that the a-Si:D layers behave quantitatively similar to the a-Si:H layers. While the total D content seems to be larger by up to 30% relative (7 at. %), the relative differences between the layers are very similar to the ones observed in a-Si:H layers. Thus, one can expect the SIMS results obtained on the a-Si:D layers to be significant for the interpretation of the results on (i)a-Si:H.

6.5.3. Features of SIMS raw data

Figure 6.14 shows a typical set of raw SIMS data for an a-Si:D layer of 50 nm thickness deposited with the LP250 parameter set. The left side of the spectra (approximately up to 5 nm nominal depth) is characterized by non-equilibrium initial sputtering conditions, which is indicated by a non-constant signal of the Si host matrix ('matrix signal'). In

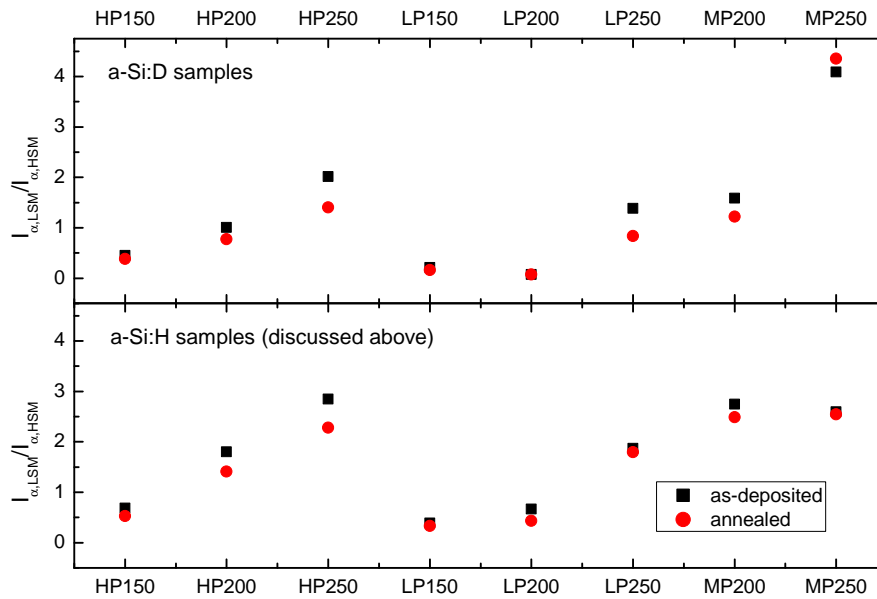


Figure 6.13.: Signature of the H/D microstructure of a-Si:H/a-Si:D samples, expressed via the ratio between LSM and HSM IR-intensities in the as-deposited and annealed state as obtained with FTIRS. It is obvious that the H/D microstructure is similar between a-Si:H and a-Si:D samples, ensuring the significance of the a-Si:D samples for the analysis of a-Si:H.

this case, ^{29}Si was used to monitor the host matrix as its concentration is about 4.7% in ordinary silicon and thus of the same order as the hydrogen or deuterium concentration, allowing to use the same detector settings. The ^1H and ^2H signals are calibrated using the ^{29}Si matrix signal by the means of an implantation standard which is measured under identical conditions immediately before the samples and contains well-defined concentrations of ^1H and ^2H in a c-Si matrix. Thus, in our case the assumption is needed that the matrix behavior of a-Si:D/H is the same as for c-Si, which is a usual procedure when analyzing a-Si:H samples and is also underpinned by the exact correspondence of the matrix signal level on both sides of the heterointerface. The interface itself can be conveniently identified by the 'matrix effect', manifesting as a peak in the ^{29}Si signal. This peak can be caused by both the presence of oxygen and by structural discontinuities [280]. In the case of a-Si:H/c-Si heterostructures the origin is supposedly a combination of both. It is obvious that both the ^1H and ^2H signals show pronounced features at exactly the same sputtering depth as the ^{29}Si matrix peak, consistent with the crossing of the heterointerface: The ^2H signal sharply kinks from a plateau into an exponential decay, while the ^1H signal peaks due to the presence of hydrogen left over from the HF dip and also decays exponentially on the c-Si side of the junction. An additional feature is a bump in the ^1H signal near the open surface which is supposedly due to ^1H from water vapor on the a-Si:D surface driven into the film by the sputtering process.

Interesting is the absolute position of the heterointerface at about 40 nm depth which significantly differs from the expected 50.2 nm measured with ellipsometry. This discrep-

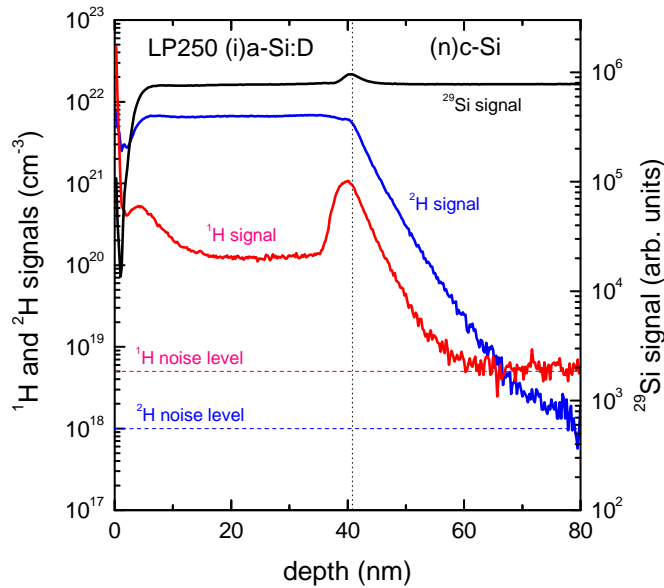


Figure 6.14: Typical SIMS raw data taken on a 50 nm thick (i)a-Si:D layer deposited with the LP250 parameter set. Blue: ^2H signal, red: ^1H signal, black: ^{29}Si signal. The peak in the ^{29}Si signal ('matrix peak') identifies the heterointerface by its chemical/structural discontinuity and thus enhanced sputtering rate. Note that the presence of hydrogen near the heterointerface is due to the Si-H surface coverage after the HF dip before loading of the substrate into the PECVD setup.

any stems from the calibration procedure of the depth axis. This is done in practice by measuring the depth of the sputtering crater after the SIMS sputter run and mapping the sputtering time onto a thickness based on a linear transformation. This implicitly assumes a constant sputtering rate at all times, which can however be violated under transient sputtering conditions, first of all at the beginning of the sputtering process. In the light of the shortcomings of the depth axis calibration it is important to note that the absolute concentrations measured with SIMS are calibrated using the implantation standard (i.e. the matrix signal) at every point in time and are therefore *not* dependent on the depth axis.

In Fig. 6.15, SIMS profiles from three different (i)a-Si:H layers are shown, with the zero point of the abscissa chosen to be the peak maximum of the ^{29}Si matrix peak. It is obvious that depending on the deposition conditions, both the ^1H and ^2H spectra change. While significant contributions of ^1H are confined to a narrow peak at the heterointerface with varying height for all samples, ^2H is (almost) homogeneously distributed while the level varies from sample to sample. However, it becomes obvious that some slight inhomogeneities are present: Most prominent is a dip in the ^2H spectra immediately before the interface is reached, which is supposedly due to the competition of ^2H and ^1H for the same atomic sites. Calculating the sum signal of ^2H and ^1H to eliminate the impact of this effect (green lines) reveals some interfacial H/D pileup for the layers deposited at lower temperatures. This pileup was observed before in combined ATR/in-situ SE measurements on a-Si:H during growth [75, 78, 84]. Here it is demonstrated that the appearance and distinctness of this feature depends on the deposition conditions of the a-Si:H layer. The implications of this finding and possible microscopic explanations will be discussed below. At this point, the quantitative significance of the spectra shall be discussed first.

In order to validate the SIMS results it would be desirable to compare the data to the FTIRS results, e.g. by integrating the SIMS spectra over the first 10 nm from the het-

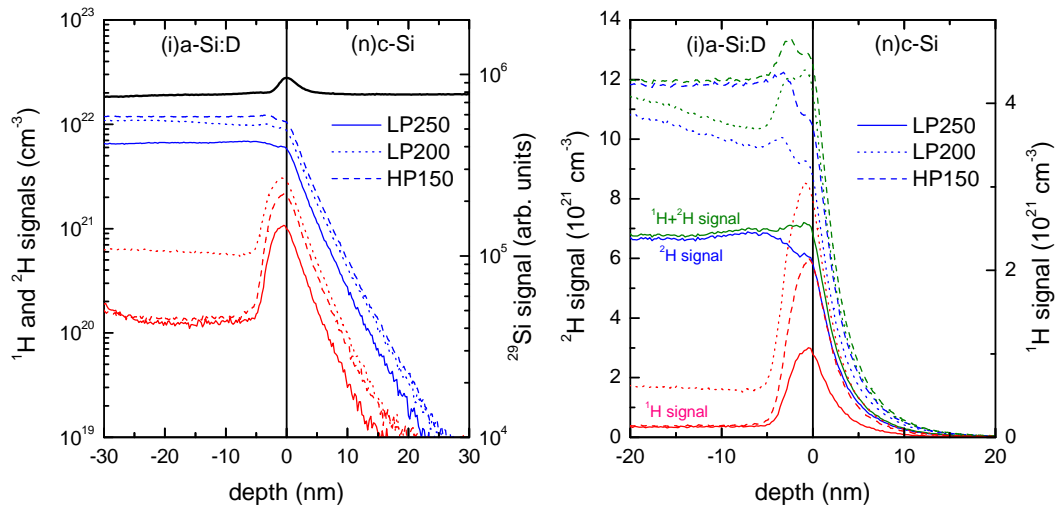


Figure 6.15.: SIMS spectra of three different (i)a-Si:D layers in the logarithmic and linear domain (colors as in the previous figure). The zero point of the abscissa was shifted to the position of the heterointerface. The right panel illustrates that D and H compete for the same atomic sites, thus suggesting to analyze the D+H sum in the following in order to assess the overall hydrogen distribution.

erointerface. This would require the spectrum as measured to represent the real-space distribution of H and D in the layers. However, based on the microscopic mechanism of sputtering this is not likely to be the case [280]. Most prominently, the mixing of species from the actual surface in the sputtering crater with subsurface material due to the impact of the ion beam will lead to a broadened distribution in the resulting spectrum as compared to the real-space distribution. The spectra contain one prominent feature which supposedly stems from this effect: The exponential decay of the ^2H and ^1H concentrations after crossing the interface into the c-Si. Naïvely, this tail could also be taken as indication for D or H in-diffusion into c-Si. However, it is puzzling that the slope of the tail is exactly identical for all ^2H and ^1H spectra. Based on the different diffusion coefficients for D and H and the diffusion times⁵ differing up to a factor of 3...4, one would expect different slopes. Thus, this feature is most likely resulting from an experimental broadening due to atomic mixing in the sputtering process.

This means that before the spectra can be quantitatively analyzed, a method must be found which allows for deconvolution of the experimental artifacts from the measured spectra. Such a method will be described and employed in the next section.

6.5.4. Deconvoluting SIMS spectra from measurement artifacts

The MRI model

Ion-beam-assisted profiling techniques such as SIMS, but also Auger electron spectroscopy or XPS if employed for layer-by-layer analysis in combination with sputtering,

⁵These are given by the PECVD deposition times as in-diffusion of H/D from the plasma is most effective.

are affected by profile distortions due to the ion-surface interaction [100, 268]. Prominent effects are the mixing of surface species with sub-surface material as already mentioned above, the roughness (evolution) of the sputtering crater and the significance of a finite information depth. The different effects are usually present in some non-trivial combination yielding a so-called 'depth-resolution function' (DRF), which is distorting the real-space distribution of the probed element. In principle, this function can be either determined by measuring a δ -function concentration of some typical element in a representative host matrix under identical conditions as used for analyzing the samples, or by inferring it from known parameters of both the setup and sample and some general considerations. The literature documents an extensive consecutive development of methods aiming at the description of the sputtering process and the deduction of a suitable DRF. Due to space constraints, these approaches shall not be summarized here, the interested reader however may find a comprehensive review in Ref. [103]. One widely used and well-grounded model is the so-called 'mixing length – roughness – information depth model' (MRI model) by Hofmann [101, 102]. It is based on a forward calculation starting from an assumed real-space distribution of an element which is convoluted with a physically motivated effective DRF. The effective DRF itself is composed of three different partial DRFs resulting from the three main distorting effects, which are successively convoluted with the assumed real-space profile to yield the expected measured profile. This expected profile is then fitted to the actually measured profile by varying the assumed real-space distribution in an iterative process. Thus, mathematically, the procedure of deconvolution is avoided which generally suffers from noise and seldom yields unambiguous results⁶. The MRI model can be formulated as follows [101]:

$$I_{\text{meas}}(z) = \iiint_{-\infty}^{\infty} I_{\text{real}}(z''') g_w(z'' - z''') dz''' g_{\lambda}(z' - z'') dz'' g_{\sigma}(z - z') dz' \quad (6.2)$$

$$g_w(z'' - z''') = \frac{1}{w} \exp\left(\frac{-z''(z'' - z''' + w)}{w}\right) \quad (6.3)$$

$$g_{\lambda}(z' - z'') = \frac{1}{\lambda} \exp\left(\frac{-z'(z' - z'')}{\lambda}\right) \quad (6.4)$$

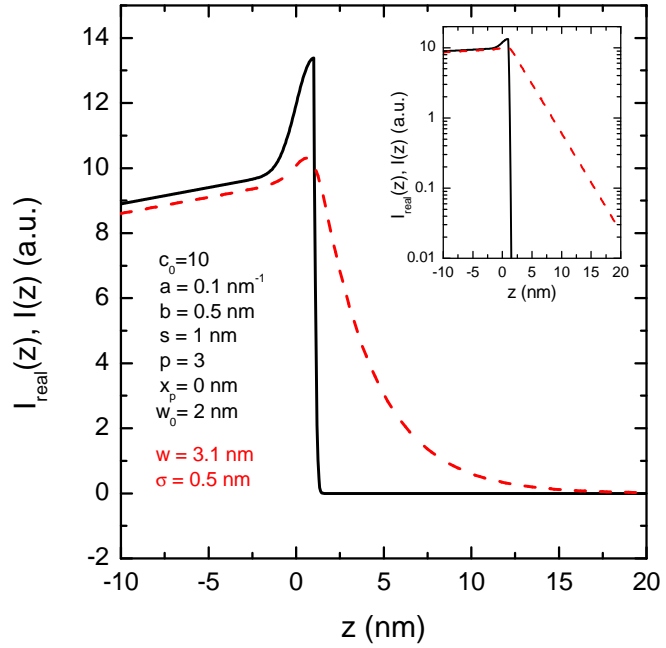
$$g_{\sigma}(z - z') = \frac{1}{\sqrt{2\pi}\sigma} \exp\left(\frac{-(z - z')^2}{2\sigma^2}\right) \quad (6.5)$$

Here, g_w is the DRF due to atomic mixing, g_{λ} is the DRF due to finite information depth⁷, and g_{σ} the DRF resulting from surface roughness of the sputtering crater. The successive application of the convolution integral to the real-space distribution I_{real} yields the expected measured distribution I_{meas} . The functional form of I_{real} has to be chosen according to the expected distribution in the sample. In the case of the (i)a-Si:D

⁶Note that this procedure is corresponding closely to the method used for the analysis of NUVPEs data, where an instrument transfer function is convoluted with an expected model DOS.

⁷Note that only within this section, λ stands for the information depth. In all other parts of this thesis, λ denotes a wavelength.

Figure 6.16: Assumed model deuterium distribution (black) and resulting expected SIMS signal (red), as calculated with the mixing-roughness-information depth (MRI) model. The used parameters of the depth resolution function are realistic (red in the list in the figure), illustrating that severe distortion of the real-space distribution is present. The inset shows the results in the logarithmic domain illustrating that the exponential decay is resulting from experimental broadening and not from deuterium in-diffusion into c-Si.



layers analyzed here, a piecewise-defined trial function was employed:

$$I_{\text{real}}(z) = \begin{cases} c_0 + a(z - s) + \frac{2p}{\sqrt{\pi}} \exp\left(-\frac{(z+x_p-s)^2}{w_0^2}\right), & z \leq s \\ c_0 + \frac{2p}{\sqrt{\pi}} \exp\left(-\frac{(x_p)^2}{w_0^2}\right) \text{erf}\left(\frac{z-s}{b}\right), & z > s \end{cases} \quad (6.6)$$

It essentially assumes a linear deuterium profile in the a-Si:H bulk (with parameters c_0 , being the concentration at the heterointerface, and the slope a) and a superimposed Gaussian 'pileup' (parameters p for the height, w_0 for the width and x_p for the position). In the c-Si, an error-function decay was assumed to account for deuterium in-diffusion into the c-Si, starting from the concentration on the a-Si:H side of the interface to ensure continuity. The characteristic decay length is b . Finally, a shift of the interface position away from zero was allowed by a global shift parameter s . Together with the three characteristic parameters from the MRI model (w, λ, σ), the total number of parameters is 10. Figure 6.16 shows a prototypical real-space distribution trial function (black line) and the expected measured signal assuming reasonable parameters for the DRFs (see below). The expected signal qualitatively resembles the actually measured spectra, and it becomes obvious that the experimental distortion of the real-space distribution is significant. Thus, in order to quantitatively analyze the SIMS spectra, obtaining a reasonable real-space distribution by the means of fitting the MRI model is crucial.

Estimating the SIMS depth-resolution function

Using physical reasoning, the number of free parameters can be reduced before the fitting: First of all, based on literature data for the deuterium diffusion coefficient in c-Si upon diffusion from a plasma [204], and taking into account the correct temperatures and deposition times it can be calculated that the maximum expected in-diffusion length is

0...0.4 nm. Therefore, b was set to the 'mean' value of 0.2 nm. With b being fixed to this order, it is clear that the exponential decay visible in the measured SIMS spectra must stem from one or both of the exponential DRFs (g_λ or g_w). For SIMS, the information depth is close to zero, as the detected atoms stem from the first monolayer(s). Typical values in the literature are in the range of ≈ 0.5 nm [101, 102]. Thus it is clear that the relevant DRF is the one describing the atomic mixing, and g_λ was therefore omitted for the sake of simplicity⁸. To further narrow down the value of w , the mixing length, information about the sputtering process is useful. In this case, Ar ions were employed for sputtering with a kinetic energy of 6.5 keV impinging on the sample at an angle of $55^\circ \dots 65^\circ$ versus the normal [161]. Based on textbook data, a mean ion impact depth can be calculated by the numerical value equation [280]

$$d_i = 1.622E^{0.84} \cos(\theta) = 3.3 \dots 4.5 \text{ nm} \quad (6.7)$$

The mean ion impact depth represents a reasonable estimate for w . It is found that the entirety of measured data can be fitted well assuming a single mixing length of $w = 3.1$ nm, which is close to the estimated value.

The roughness parameter σ is hardest to anticipate as it involves the interaction between the a-Si:H surface and the sputtering process, and temporal variations are possible due to the transient nature of the sputtering process [100, 280]. It seems reasonable to consider both a 'best guess' and an extreme value for comparison. A typical literature value (assuming a well-behaved sputtering process) would be $\sigma = 0.5$ nm, and the maximum possible value in this particular case is given by a simple argument: The sharpest features visible in the SIMS profiles as e.g. the peak near the interface in the ^1H spectra must be reproducible, and the maximum allowed Gaussian roughness broadening produces those features from a delta function. By this procedure, the maximum roughness broadening parameter is estimated to be $\sigma = 1.2$ nm. Thus, the number of free parameters is reduced to six, and c_0 , a , s , p , w_0 and x_p remain to be fitted to each data set.

Fitting results

During the fitting it became obvious that the best results (i.e. the lowest R squared values) are always obtained with $\sigma = 0.5$ nm, as all the sharp features of the spectra are hard to reproduce with larger roughness values. Therefore the discussion in the following is restricted to the best fits, which were obtained assuming $\sigma = 0.5$ nm. Figs. 6.17, 6.18 & 6.19 show the SIMS data, the respective MRI fits and the underlying assumed real-space deuterium distribution obtained by the fitting for the LP, HP and MP samples. First of all it has to be noted that the MRI model provides excellent fits to most SIMS spectra based on the model function given in Eq. 6.6 and with the g_w and g_σ functions as motivated above. The interface position as deduced from the ^{29}Si matrix peak was confirmed for all samples: The mean deviation of the shift parameter s from zero was -0.027 ± 0.222 nm. In terms of layer homogeneity, pronounced differences become apparent. These can best be observed plotting only the real-space

⁸Note that the information depth is a much more important parameter for Auger electron spectroscopy (AES) or sputter-assisted layer-by-layer XPS, where the escape depth of the Auger-/photoelectrons is reflected in g_λ .

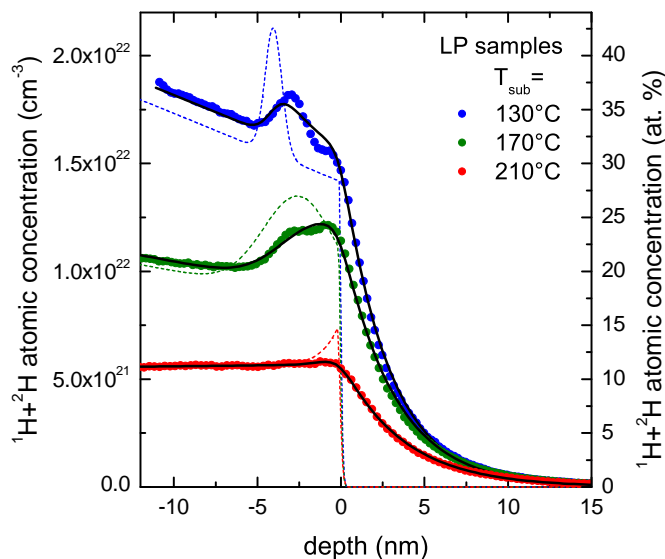


Figure 6.17: MRI fits to the (i)a-Si:D samples deposited with the LP PECVD parameters. The full line is the assumed real-space deuterium distribution convoluted with the depth-resolution-function (DRF) resulting from the MRI model, and was fitted to the measured SIMS data. The dashed line shows the underlying real-space deuterium distribution.

D+H distribution as obtained from the MRI fits, which is done in Fig. 6.20. It can be seen that the inhomogeneity is most pronounced for the layers with the highest overall deuterium concentration⁹. Interestingly, the SIMS spectra are inconsistent with a deuterium pileup right at the heterointerface. Instead, for four layers — representing the poorest structural properties from the previous analyses — a pronounced peak in the D+H concentration is seen at about 5 nm depth. A general trend seems to be that layers with lower overall D+H content display less inhomogeneity, however also the layers with lowest D+H concentration show some slowly varying features in the deuterium concentration. Apart from the pileup at 5 nm, which has a magnitude of up to 10 at. %, the variation in the D+H concentration stays within a ± 5 at. % range. Note that in contrast to the 'H pileup' picture generally invoked there are four layers — notably those that are compact layers with minimum D content and Urbach energy — that show a *minimum* of the D+H concentration at the heterointerface. In summary, the range of possible hydrogen/deuterium profiles is wide, clearly dependent on the deposition conditions and the presence of inhomogeneities seems to correlate well with poor overall bulk properties (low mass density, high Urbach slope). Next, the consistency of the obtained MRI fitting results shall be briefly assessed before the bulk properties of the a-Si:H layers are discussed.

6.5.5. Intermediate discussion of SIMS results

A simple consistency test of the MRI fitting procedure is to compare the deuterium concentration as obtained by integrating over the first 10 nm of the fitted real-space distribution with the D concentration as deduced from FTIRS spectra taken on 10 nm thick a-Si:D layers (cf. Figs. 6.12 & 6.13). This is done in Fig. 6.21 showing a reasonable agreement between the two methods. Given the challenge of accurately measuring

⁹Note that these are the layers deposited at the suboptimal PECVD conditions such as the lowest substrate temperatures, as also reflected e.g. in a high void density or Urbach slope.

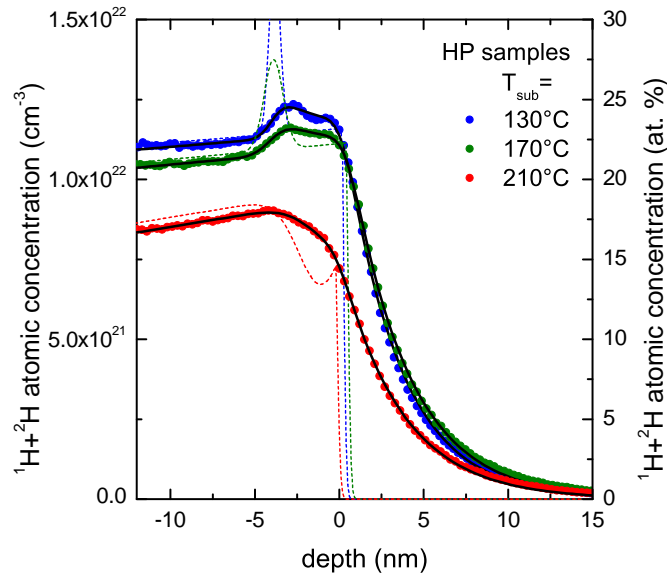


Figure 6.18: MRI fits to the (i)a-Si:D samples deposited with HP parameters. Symbols have the same meaning as above.

FTIRS on 10 nm thick samples, the uncertainty in the Si-D wagging mode proportionality factors and the subtleties of the SIMS analysis as discussed in this chapter, the moderate discrepancy of < 5 at. % is a satisfactory result and underlines the significance of the SIMS analysis.

The results of the MRI fitting to the SIMS spectra suggest a large impact of the a-Si:H deposition conditions on the homogeneity of the hydrogen distribution in the layers. The quality of the fits is surprisingly high, although the functional form of the chosen trial function for the real-space distribution is rather arbitrary. However, it provides the freedom to reproduce the essential features with a limited number of parameters¹⁰. The linear slope (controlled by the parameter a) is not pronounced, apart from the LP150 sample showing a 5 at. % variation from the linear slope alone. For all other samples, the major contribution to the inhomogeneity stems from a more or less extended feature in the first 10 nm of a-Si:H film which can be reasonably well approximated by a Gaussian. Beyond 10 nm thickness the H profile is almost flat (again excluding the LP150 sample which displays a considerable slope).

This prototypical form for the inhomogeneity points towards transient plasma conditions after ignition to be responsible for the observed H profiles. In a PECVD deposition system, the chemistry of the gas phase is not immediately stable after ignition of the glow discharge. Particularly for comparably small 'lab-type' reactors it was found that the transient plasma regime, being characterized by non-equilibrium conditions concerning concentrations of different molecular species and the plasma potential, can last for several tens or even hundreds of seconds [69, 170, 267]. One of the main causes for this effect is the unfavorable ratio of dead-volume to the actual plasma volume between the electrode plates which is typical for lab-type reactors. This leads to a disturbance of

¹⁰Note for example that the Gaussian initially incorporated to model a 'pileup' at the interface was turned into a broad dip by the fitting routine to accurately reproduce the spectra particularly of the MP samples.

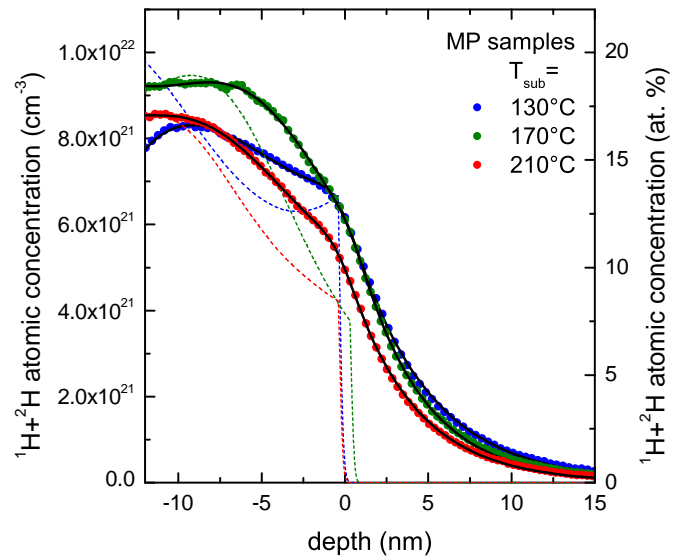


Figure 6.19: MRI fits to the (i)a-Si:D samples deposited with MP parameters. Symbols have the same meaning as above.

the plasma chemistry in the initial stage by diffusion of species from the dead volume into the plasma region and thus a prolonged transient phase¹¹. In the case of the cluster tool at HZB, a transient behavior of the DC plasma potential is observed which lasts for about 10...40 s depending on the deposition regime, corresponding to up to 7 nm of film thickness being grown during this transient phase. Although no time-resolved plasma diagnostics were available to analyze the plasma behavior, this can be taken as evidence for a transient initial growth phase, consistent with previous studies. Thus, the slowly varying inhomogeneities found by SIMS are tentatively explained by the transient plasma physics.

For the very sharp features, most notably the peaks around 5 nm depth, this explanation is not sufficient. It is not conceivable (and not consistent with the observed behavior of the DC potential) that transient effects of such sudden and pronounced nature are present. It must be considered that these features are to some extent of artifactual nature. One possible origin is the ¹H concentration which comes into play due to the HF dip prior to deposition. Although the original idea was to refrain from using ¹H spectra for quantitative analysis to avoid the problems with calibration mentioned above, these spectra had finally to be taken into account as considerable amounts of the hydrogen introduced by the HF dip remain in the layer. Omitting this contribution would have definitely produced artifacts as H and D compete for the same atomic sites. Including it on the other hand introduces the mentioned problems with ¹H calibration. Thus, in the region where ¹H contributes significantly to the total D+H content (i.e. the first 3...5 nm as obvious from Fig. 6.15), the spectrum may be affected by calibration problems. It is instructive to observe the spectra taken on the LP samples (Fig. 6.17): For LP200 and LP250, the ¹H and ²H combine to a smooth D+H spectrum which leads to broad features in the assumed real-space distribution. For LP150 however, there seems

¹¹An additional contribution could stem from the feedback loop steering the RF line (which consists of the RF source, the matching network and the plasma itself representing the impedance) which has time constants in the order of seconds.

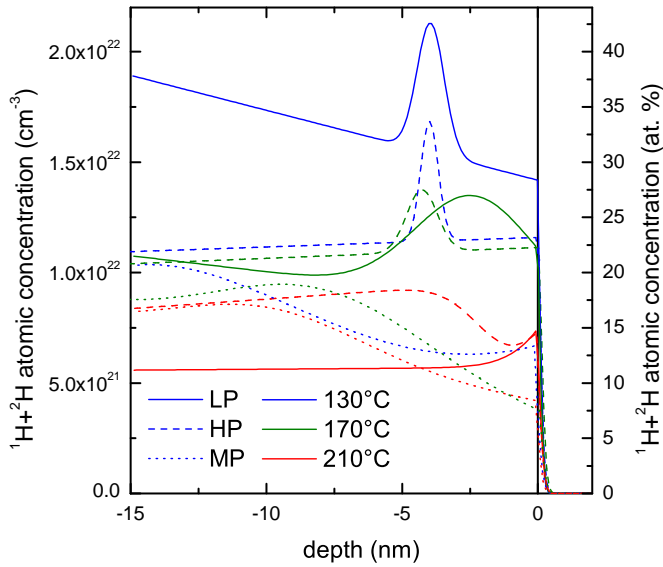
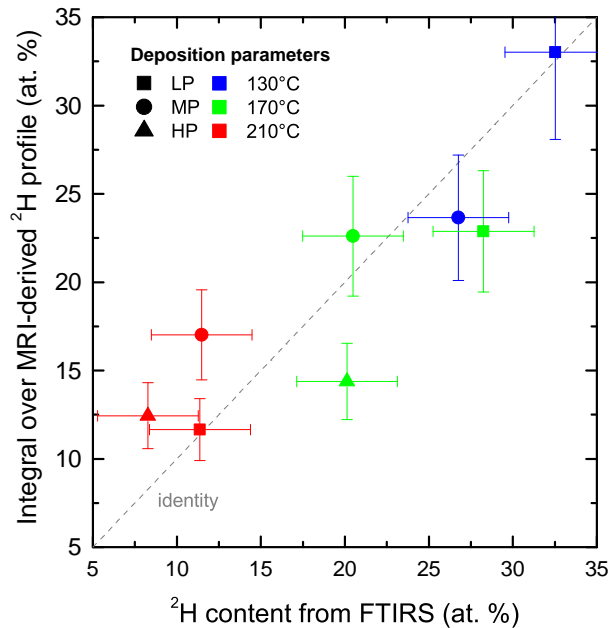


Figure 6.20: Real-space distribution of deuterium/hydrogen for the nine different (i)a-Si:D layers as derived from the MRI analysis described above. It is obvious that depending on both substrate temperature and PECVD parameter set, there are inhomogeneities in the deuterium/hydrogen distribution. However, the picture of a 'hydrogen pileup' at the heterointerface, as often invoked in literature, is not supported by the data. Possible reasons for that are discussed in the text.

to be part of the spectrum missing near the interface, leading to a sharp bump in the SIMS spectrum and an even sharper feature in the assumed real-space function, which only poorly reproduces the measured bump. If the ^1H contribution was only slightly higher in this case, the D+H spectrum and in effect the real-space distribution would be considerably smoother. The same argumentation applies to the HP150 spectrum as well. Thus, similar to classical deconvolution of a (usually Gaussian) point-spread-function for image reconstruction, sharp features in the blurred image are amplified. Here, the assumed uncertainty in the ^1H spectra can lead to sharp artifacts in the D+H sum spectrum which are amplified in the assumed real-space distribution. This may provide a tentative explanation for the pronounced features at 5 nm depth appearing in some samples.

Although the somewhat questionable calibration of the ^1H spectra causes problems for the quantitative analysis, the ^1H signal might become handy in a different context as it allows to assess the efficiency of H elimination during the growth process. As argued in section 2.1.4, this efficiency codetermines the quality of a-Si:H growth. Starting from a fully hydrogen-terminated c-Si surface after the HF dip [33], the hydrogen atoms are successively replaced by silicon atoms during the initial growth phase. In the case of poor growth conditions, this elimination process might be less efficient, leading to a higher concentration of hydrogen remaining at or in the vicinity of the heterointerface. An additional (indirect) indicator for the structural quality of the amorphous network is the matrix peak in the ^{29}Si spectra, which indicates a structural discontinuity as argued above. Indeed, as shown in Fig. 6.22, the amount of hydrogen remaining in the film in the vicinity of the heterointerface, expressed as a projected surface density to allow comparison to the expected initial surface coverage, clearly scales with the peak area of the ^{29}Si matrix peak, indicating the deviation from an undisturbed crystalline-amorphous matrix transition. Thus, additional qualitative evidence is presented for a locally poor network structure in the vicinity of the heterointerface, which is predominantly appearing in the layers deposited at lower temperatures.

Figure 6.21: Consistency check for the obtained real-space deuterium/hydrogen distributions: Integration over the first 10 nm of the MRI-derived distributions starting from the heterointerface yields D/H contents which are in good agreement with the bulk deuterium contents as measured with FTIRS on 10 nm thick a-Si:D layers.



6.6. Discussion of a-Si:H bulk properties

In this chapter, properties of thin (i)a-Si:H layers were determined. At some points the similarity or difference to pertinent data (mostly measured on thicker layers) was already highlighted, e.g. concerning the hydrogen microstructure. At this stage, the results obtained so far shall be discussed in entirety and compared to previously published data on thick films, taking into account the inhomogeneities present in some layers and their implication for the interpretation of data taken with bulk-integrating methods.

6.6.1. Structural properties

The structure of amorphous silicon strongly depends on the chosen deposition technique and -conditions. Layers of 'device-grade' quality can be made e.g. with H-diluted RF-sputtering, several different PECVD techniques (RF, VHF, remote ECR, etc.), hot-wire CVD (HWCVD), the expanding thermal plasma technique (ETP), among others. Each technique will in general have its own set of optimal parameters, which — if analyzed in detail — even depends on the particular setup. This makes comparison of a-Si:H layers in terms of deposition conditions a difficult task. However, the range of resulting microscopic structures of the amorphous network have been proven to be similar irrespective of the growth conditions, with some techniques allowing a wider range of layers to be made than others. Particularly, ETP seems to be able to produce a-Si:H of very different structure, whereas classical RF-PECVD is more limited. While many papers have been dedicated to optimizing a-Si:H growth for a given device application, there are much fewer studies where the microscopic aspects of the layers are elucidated and linked to each other, contributing to a canonical picture of a-Si:H properties and their interdependence. A small set set of those shall be listed here as the basis for the

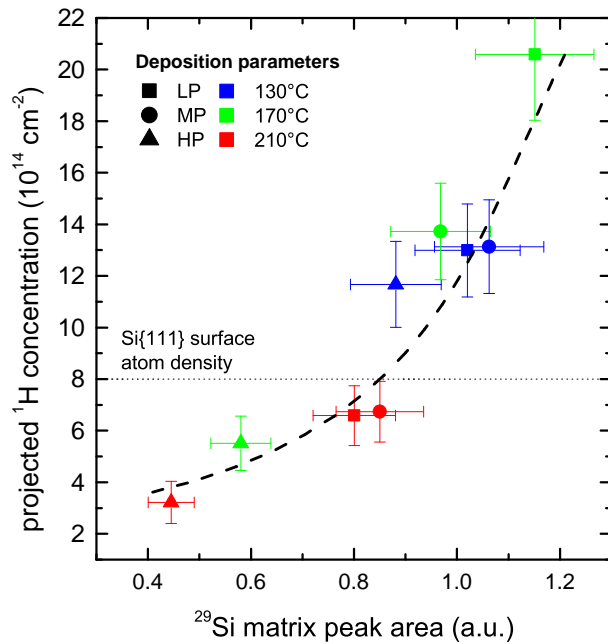


Figure 6.22: Indication for inferior amorphous network structure at the heterointerface accompanying suboptimal PECVD growth conditions: The amount of hydrogen from the HF dip still remaining in the a-Si:D layer can be taken as a monitor for the efficiency of H elimination during growth, and thus for the efficiency of sub-surface relaxation processes during a-Si:H growth. For high remaining ^1H concentrations, the structural discontinuity at the heterointerface probed by the ^{29}Si matrix peak is significantly enhanced as implied by the figure. Although this connection is tentative, it may provide a useful hint towards a correlation of a-Si:H growth conditions and structural properties of the heterointerface.

comparison with the data obtained in this chapter on thin PECVD (i)a-Si:H layer. To mention are the works of Smets *et al.* on ETP a-Si:H [228, 230], a paper of Tourir *et al.* on sputtered a-Si:H [263], and several papers on PECVD-deposited a-Si:H, namely from Lucovsky *et al.* [147], Langford *et al.* [139] and Manfredotti *et al.* [149], all of which make use of infrared spectroscopy to capture the hydrogen microstructure in the a-Si:H films. Important additional information comes from Raman spectroscopy [263], neutron scattering [279] and nuclear magnetic resonance measurements targeting the nuclear spin of the hydrogen atoms [86, 191]. There are some features which appear to be generic for a-Si:H as they are observed in all studies, which are:

- An approximately constant contribution of the LSM signal of about 5-10 at. %, indicative of isolated/distributed monohydrides. These distributed hydrogen atoms are also seen as a narrow-linewidth contribution in the NMR spectra. Some studies observe a slight decrease of the distributed H content with overall H content.
- A HSM contribution indicating clustered hydrides (or higher hydrides as claimed by some authors) which strongly depends on the deposition conditions and increases when suboptimal growth conditions are chosen, as e.g. low substrate temperatures. The contribution of this signal can vary between close to zero and more than 25 at. %. The clustered H signal is seen as a broad feature in the NMR spectra.
- A decreasing density of the films with increasing HSM contribution. While the most compact films display mass densities close to the c-Si value of 2.33 g/cm^{-3} , particularly films deposited at low temperatures have significantly lower densities down to $< 1.9\text{ g/cm}^{-3}$.

- An increasing indication for structural inhomogeneity as seen e.g. in small-angle neutron scattering [279], and network strain as seen e.g. in Raman spectroscopy [263] with increasing HSM contribution.

On the basis of the data presented so far, these four aspects can also be clearly identified in ultrathin (i)a-Si:H. Quantitatively, the layers in this work are very consistent with pertinent data in terms of H content and microstructure variation (cf. Fig. 6.4), indicating them to be typical despite their small thickness. The data of this thesis also reflect the fact that PECVD a-Si:H generally has a lower limit in terms of H content around 10 at. % for deposition temperatures below 250°C.

The variation of the mass density is smaller than observed in most studies, suggesting that the void contribution in the layers analyzed here is moderate. There might be some systematic error in the mass density data stemming from the extrapolation procedure of the SE-derived optical functions down to the static limit ($\lambda \rightarrow \infty$). However, the relative differences between the layers — and therefore the slope versus the H content — should be unaffected from such effect. Thus, the conclusion that the slope of ρ versus the H content is high enough to preclude compact H-decorated vacancies like mono- or di-vacancies to be the origin of the mass loss is valid in any case (cf. Ref. [228]).

The indications for a heterogeneous structure accompanying large HSM contributions are underscored by the scaling of the mass deficiency with the HSM to the power of 2/3, indicating the presence of microvoids which host the HSM phase. Additionally, the photoelectron data yield some clear indication for enhanced network strain with increasing HSM, which will be discussed in detail in the next chapter. Further, structural inhomogeneities on the macroscopic scale were revealed by the analysis of the SIMS spectra. These most probably result from transient growth behavior, and are characterized by two different contributions manifesting in the dependence on two separate parameters: Small-scale inhomogeneities are systematically increased when the deposition temperature is lowered, while additionally a slowly varying deviation from a flat SIMS spectrum is observed depending on the choice of the pressure/H dilution regime. While the latter most probably results from a long transient phase of the plasma chemistry for certain pressure regimes, leading to a gradual shift in the deposition conditions, the former is presumably caused by the details of the processes on the c-Si surface: The substrate temperature crucially determines the mobility of the growth precursors on the c-Si surface and thus the initial stages of a-Si:H growth, being island formation and coalescence. Although obscured by uncertainties in the ^1H spectra, an interface-near increase of D/H concentration is observed with decreasing deposition temperature, which indicates a deteriorating structure in the vicinity of the heterointerface. This observation is further corroborated by the increase of the cumulated hydrogen left over from the Si-H coverage of the c-Si surface prior to growth and the concordantly increasing ^{29}Si matrix peak evidencing a discontinuous network structure at the heterointerface.

6.6.2. Electronic properties

Some aspects of the a-Si:H electronic properties have been identified in the studies mentioned above. In addition, many works solely dedicated to elucidating the electronic properties of a-Si:H have been published. Useful in the context of this work are the

insight concerning band gap and Urbach slope which is provided from optical absorption studies (see e.g. Ref. [39] and references therein). Further, the magnetic resonance of the paramagnetic spins on the dangling bond defects has been used to elucidate on the defect densities in many papers¹² (see e.g. Refs. [28, 223]). Lastly, photoelectron spectroscopy data was used to monitor the reaction of the band edges upon tuning the deposition conditions [272, 274]. The prototypical picture emerging from the mentioned works in terms of the electronic properties of (i)a-Si:H as far as they are relevant in the present context can be summarized as follows:

- An increasing optical band gap with increased H content.
- An increase in the valence band tail width with increased H content.
- A *decrease* of the defect density with the density of distributed H for low H concentrations (< 5%), and an *increase* of the defect density as the deposition temperature is lowered, i.e. with increasing contribution of the HSM mode in IR spectra or the clustered hydrogen NMR signal.
- A retreat of the valence band edge upon increasing the H content.

These aspects are also confirmed from the data taken on thin (i)a-Si:H layers, with the exception of the behavior of the DB defect density which is hard to measure on ultrathin (i)a-Si:H layers as discussed above. Thus it can be concluded that thin (i)a-Si:H layers behave according to the picture which has emerged in the last three decades for thick a-Si:H layers. It is obvious that the H microstructure is an important parameter controlling the changes in the electronic structure if no doping is employed. While the retreat of the valence band is usually explained by the replacement of weak Si-Si bonds forming the top of the valence band by Si-H bonds, there is no obvious connection between H content and the valence band tail slope. From a naïve point of view, one would expect the defect density to decrease with the H content as hydrogen is expected to passivate dangling bonds. However, to saturate all the 10^{20} cm^{-3} defects found in unhydrogenated a-Si, only 2 at. % of hydrogen would be necessary. Thus it is obvious that the role of the *excess* hydrogen incorporated by the usual deposition techniques concerning the defect density is subtle. It is tempting to assume a collateral impact of the clustered hydrogen phase on both Urbach slope and defect density, e.g. by the deterioration of the amorphous network seen also in the void fraction which is increasing with the H content.

While these connections between hydrogen microstructure and the defect density have been studied in detail [223], the exact interplay between H microstructure and the absolute energetic positions of the a-Si:H band edges has not been the focus of many scientific works. However, this aspect is most important in the context of the a-Si:H/c-Si heterostructure as the band offsets are altered by the H content, which in turn will affect the transport properties. In the next chapter, these connections will be worked out in

¹²Furhter, the nuclear magnetic double resonance, i.e. the interaction between the electron spin residing on the DBs and the nuclear spin of the H atoms, helped to understand the interaction between H content and defect density [287].

detail, and the role of H content as a control parameter acting on both band lineup and a-Si:H electronic quality will be discussed in the context of theoretical models.

6.7. Chapter conclusion

The key question for this chapter was:

What is the relation between PECVD deposition conditions and the resulting structural and electronic properties of the (i)a-Si:H layers?

In comparing the properties of thin (i)a-Si:H with pertinent data on thick films it was found in this chapter that there is no pronounced difference between thick a-Si:H layers and the ultrathin layers employed in a-Si:H/c-Si heterojunction solar cells: 10 nm thick (i)a-Si:H layers behave essentially as was found for layers of >100 times the thickness. Further, there is a clear correlation between the PECVD deposition conditions and the resulting microscopic structure of the layers: Upon choosing suboptimal deposition conditions such as low substrate temperatures, a high growth rate or no H dilution, the bulk structural quality of the a-Si:H deteriorates. This is reflected in a higher void density and a shallower valence band tail. In consequence, the overall hydrogen content increases due to the dominant contribution of the clustered hydrogen in the inner surfaces of voids, and the mass density is reduced markedly. Although the band tails get shallower, the higher Si-H bond density leads to an overall widening of the a-Si:H band gap by a linear retreat of the valence band with respect to the Fermi level.

While these conclusions implicitly assumed a homogeneous structure, the hydrogen profiles found in layers of 50 nm thickness suggest the presence of inhomogeneities in the structural properties, which are also connected to the PECVD growth regime: The transient behavior of the initial stages of growth seems to impose a slowly varying contribution to the bulk H concentration depending on the deposition regime, while particularly suboptimal growth conditions lead to a disturbed structure in the vicinity of the heterointerface.

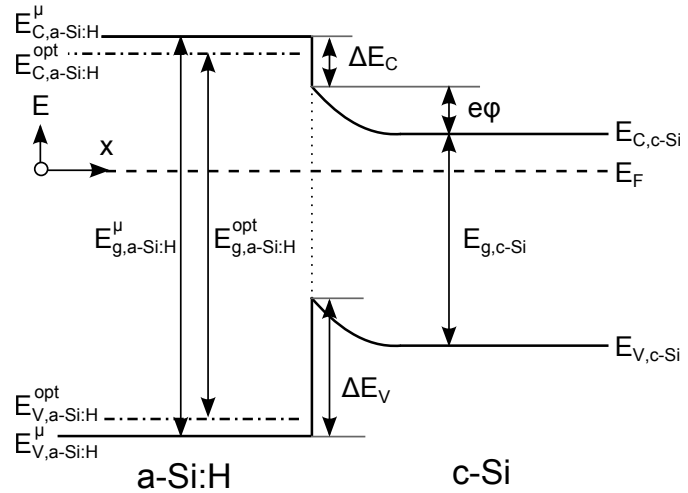
7. The a-Si:H/c-Si band lineup in device-relevant structures

In this chapter, the interplay between amorphous silicon microscopic properties and the band lineup at the a-Si:H/c-Si heterojunction is elucidated. Having characterized the (i)a-Si:H layers in detail, the missing quantity to quantify the band offsets is the equilibrium band bending on the c-Si side of the junction. In the following, surface photovoltage measurements determining the latter quantity are combined with photoelectron spectroscopy data to obtain the valence band offset. Taking into account the band gap as derived from spectroscopic ellipsometry allows to quantify the conduction band offset. This newly applied technique allows to consistently determine the band offsets in structures with a-Si:H layers of device-relevant thickness, thus avoiding problems associated with PES measurements on ultrathin (<3 nm) layers as were used before [219].

It is observed that only the valence band offset is changing upon increasing the a-Si:H bulk hydrogen content, while the conduction band offset stays essentially constant. This result is in qualitative accordance with theoretical studies on the reaction of the a-Si:H/c-Si band offsets upon tuning the a-Si:H hydrogen content. However, there is a discrepancy concerning the slope of the valence band retreat versus H content, which is discussed in the context of the microscopic information on the (i)a-Si:H layers. In conclusion it is found that the topological disorder associated with the clustered-H phase is counteracting the band gap widening as surmised from the H content alone. Thus, the H microstructure and not just the mere atomic concentration is highlighted to be important when interpreting the (i)a-Si:H electronic structure and the band lineup at the a-Si:H/c-Si heterojunction.

This chapter is based on the publication [E] from the list in the appendix.

Figure 7.1: Schematic of the band lineup in an (i)a-Si:H/(n)c-Si heterojunction in equilibrium. The bands on the a-Si:H part of the junction are assumed to be flat due to the high density of rechargeable states shielding the electric field built up by the immobile dopant ions in the c-Si. Thus, the valence band offset can be calculated with $\Delta E_V = -E_{V,a-Si:H}^\mu + E_{V,c-Si} + e\phi$. Note that in a-Si:H, the optical band gap $E_{g,a-Si:H}^{\text{opt}}$ (measured with optical methods) has to be distinguished from the mobility band gap $E_{g,a-Si:H}^\mu$ (determined with electrical techniques), as discussed in the text.



7.1. Introduction

The band offsets in a semiconductor heterojunction are a fundamental quantity, determining the distribution of band bending in the structure and affecting the electronic transport across the junction. They appear due to the difference in band gap between the two materials forming the heterostructure. Fundamentally, the exact alignment is defined by the energetic positions of the branch points of the semiconductors' virtual gap states (the so-called 'charge-neutrality levels') [167, 257, 258]. If present, interface dipoles or -defect states eventually alter the band structure-derived lineup.

Tuning the band gap of one of the materials offers a unique way to control the behavior of a heterojunction device (i.e. the optical or electrical transport properties) but naturally leads to changes in the band offsets. Depending on the nature of states that are removed or created when altering the band gap, a change in either one or both of the band offsets can occur. Thus, the exact reaction of the band lineup upon tuning the band gap is not trivially anticipated, on the other hand it can heavily affect the electronic behavior of a heterojunction device [35]. Despite the importance of HJ-derived devices such as lasers, transistors, photo-detectors and solar cells, there is only limited data on the connection between tunable material parameters of particularly amorphous materials and the resulting HJ band lineups, and the underlying principles are not thoroughly understood.

In this chapter, the a-Si:H/c-Si{111} heterojunction is analyzed, being a prototypical example for an amorphous/crystalline heterojunction. Due to the structural freedom provided by the adaptability of the amorphous network, a-Si:H allows to tune the band gap by altering its hydrogen content without severely deteriorating its electronic properties, as seen in the previous chapters. Besides its application in a-Si:H/c-Si HJ solar cells, this structure is also found in bipolar transistors [83]. In microcrystalline silicon, the a-Si:H/c-Si interface is present on a microscopic scale as the boundary between micro-sized silicon crystallites and the surrounding amorphous matrix, thus affecting the electronic transport in pertinent devices, as e.g. thin-film solar cells [271].

Controlling the hydrogen content of nominally undoped amorphous silicon layers by the choice of conditions during plasma-enhanced chemical vapor deposition, the (i)a-Si:H band gap can be varied within a range of 150 meV, as was confirmed by the analysis of spectroscopic ellipsometry data in the previous chapter. This band gap widening must lead to changes in the heterojunction band lineup. Observing the schematic band lineup in Fig. 7.1, it is obvious that the quantities needed to determine the band offsets in the a-Si:H/c-Si structure are the distance of the c-Si and a-Si:H valence band edges from the Fermi energy ($E_{V,c-Si}$ and $E_{V,a-Si:H}^\mu$), the equilibrium band bending $e\varphi$ and the a-Si:H band gap. Care has to be taken in distinguishing the a-Si:H optical band gap $E_{g,a-Si:H}^{\text{opt}}$ (as measured with optical methods) from the mobility band gap $E_{g,a-Si:H}^\mu$ (as determined with electrical techniques), as well as the respective band edges (cf. Fig. 7.1), as was discussed in the previous chapter. For the remainder of this chapter, the band offsets are defined as the energetic distances between c-Si band edges and a-Si:H *mobility* edges, as this procedure yields the quantities relevant for electronic transport. The c-Si band edge $E_{V,c-Si}$ can be readily determined from the conductivity of the crystalline substrate, thus only the a-Si:H valence mobility edge $E_{V,a-Si:H}^\mu$ and $e\varphi$ remain to be measured in order to obtain ΔE_V . With the additional knowledge of the a-Si:H mobility band gap $E_{g,a-Si:H}^\mu$, ΔE_C can be calculated.

In the following, the VB mobility edge as probed with photoelectron spectroscopy will be combined with data on the c-Si equilibrium band bending which is measured employing the surface photovoltage technique. Thus it is possible to monitor the changes in a-Si:H/c-Si band offsets upon tuning the a-Si:H band gap in a device-relevant structure.

7.2. Methods for the determination of band offsets

From an experimental point of view, the band offsets in a heterojunction are not trivially accessed. For the a-Si:H/c-Si system under study in this work, two different approaches have been pursued so far:

Firstly, electrical techniques such as capacitance or conductance measurements [67, 90, 125, 265], or internal photoemission (IPE) [45, 143] were used. The electrical methods to determine HJ band offsets are relatively indirect and often rely on either auxiliary data (affected by uncertainties) or numerical simulations in order to interpret the results. IPE is in principle a direct method and was successfully applied to crystalline heterojunctions (e.g. in III-V systems) or semiconductor-isolator junctions before [1]. For HJs comprising a-Si:H however, the significant contribution of the gap states to the photoelectric yield leads to difficulties in the interpretation of the data. Consequently, the values obtained by the different authors for ΔE_V with the methods mentioned above differ by a large amount, namely between $\Delta E_V \approx 0$ and $\Delta E_V \approx 0.7\text{ eV}$ (cf. the compilation of data in Ref. [20]). Additionally, most of the studies suffer from incomplete characterization of the a-Si:H layers in terms of composition and structure, which — in the light of the variations imposed by H content, network strain etc. seen in the previous chapter — results in an additional degree of uncertainty.

A second approach employs photoelectron spectroscopy on ultrathin a-Si:H layers which allows to detect the signal of the underlying c-Si substrate along with the a-Si:H pho-

toelectrons [29, 133, 219]. By either extrapolating the band edges of c-Si substrate and a-Si:H film visible in the spectrum to zero or, more sophisticated, fitting a combined a-Si:H and c-Si valence band edge DOS displaced by the band offset energy sought for, this method directly yields the valence band offset. However, it requires a-Si:H layers with thicknesses of only 0.5...3 nm. Unfortunately, the growth of such thin layers is not representative in terms of hydrogen content and amorphous silicon network equilibration [78], and the remaining density of a-Si:H/c-Si interface defects under ultrathin a-Si:H is large. Thus, the significance of the obtained results for heterojunction devices usually comprising a-Si:H thicknesses of the order of 10 nm is not guaranteed. Consistently, in a recent work based on the PES method, a variation of the a-Si:H/c-Si valence band offset with the thickness of the a-Si:H top layer was observed for the thickness range accessible with this method [133]. Thus, in the light of the shortcomings of the previously applied methods, it is important to revisit the a-Si:H/c-Si band offsets in a system with device-relevant a-Si:H thickness.

Additionally, to the author's knowledge, none of the two mentioned techniques has been used to study the variation in band offsets upon systematically changing the a-Si:H hydrogen content in order to tune its band gap. To fill this gap a systematic study on state-of-the-art a-Si:H layers with 10 nm thickness and $C_{\text{H,bulk}}$ varying between 12% and 24% is presented here. A new and straightforward method for the determination of HJ band offsets on device-relevant structures is developed and employed, combining photoelectron spectroscopy and surface photovoltage measurements performed on the same samples.

7.3. Revisiting a-Si:H valence band edge and band gap

It was found in photoelectron spectroscopy data that the a-Si:H valence band edge moves down in energy upon increasing the hydrogen content [272]. These early data on sputtered a-Si:H are corroborated by the CFSYS measurements on state-of-the-art PECVD films, which were presented in section 6.4.2. There, the valence band edge was extracted from CFSYS spectra by either extrapolation of a square-root function to the abscissa or by the definition of the mobility edge at a distance of 40 meV from the transition energy between valence band and exponentially decaying band tail. As the CFSYS samples were deposited under the same conditions as the FTIRS/SE samples, i.e. with the H content varying from 12...24%, the H content extracted from the FTIRS measurements was taken as the ordering parameter for the CFSYS-derived band edges. By this procedure it was shown in Fig. 6.8 that for both VB edge definitions, a slope of $\approx 12 \text{ meV/at. \%}$ is found for the valence band retreat upon increased H incorporation. The electrical methods previously used to determine ΔE_V involve carriers at the mobility edges, thus it is useful to relate the data taken here to the mobility edge for comparability with other approaches. On the other hand, one has to be aware that the band gap defined by the mobility edges ('mobility gap') was found to be systematically wider than the optical band gap (measured e.g. with absorption spectroscopy) by approximately 160 meV, which of course has to be taken into account when comparing optical and mobility data [285].

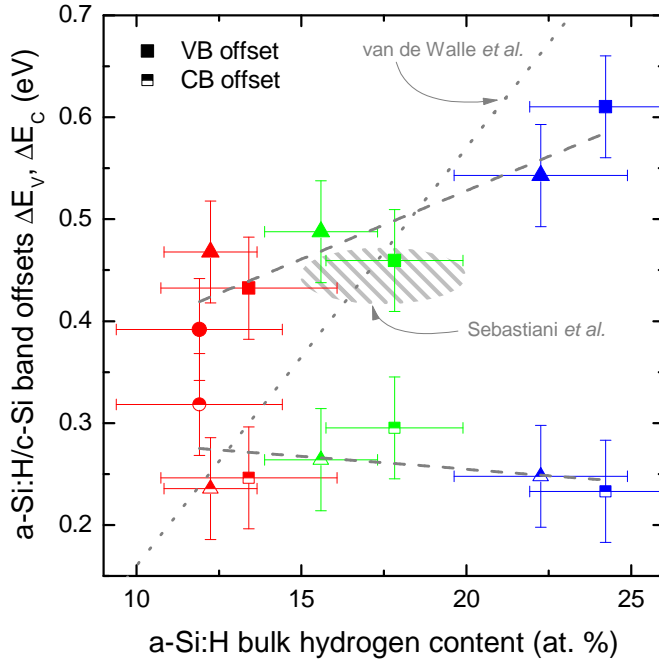


Figure 7.2: Valence band offset of (i)a-Si:H/(n)c-Si heterostructures as derived from the combination of PES and SPV data measured on the same samples (full symbols). When taking into account the band gap as obtained from SE fits, the conduction band offset can be calculated as well (half-open symbols). Note that the offsets were obtained based on the a-Si:H mobility edges and dashed lines are linear fits. Within experimental errors, only the valence band offset reacts on changes in the bulk H content. The gray hatched area marks the data point of Sebastiani *et al.* [219], while the gray dotted line is the prediction for the valence band offset by van de Walle *et al.* [53], as discussed in the text.

Notwithstanding the slight scatter in the data presented in Fig. 6.8, the increase in $E_{V,a-Si:H}^{\mu/ext}$ with the hydrogen content is pronounced, identical for both band edge definitions and consistent with the data on sputtered a-Si:H [272]. The discrepancy of ≈ 90 meV between the mobility edge and the band extrapolation-derived edge can be readily explained from the different band edge definitions, and is consistent with the observed difference between the mobility and Tauc gap [285]. Interestingly, the increase in $E_{V,a-Si:H}^{\mu/ext}$ is of the same magnitude as the widening of the band gap within experimental errors (cf. Fig. 6.5). If the gap widening was entirely due to a retreat of the valence band relative to E_F , this would lead to the expectation that predominantly the valence band offset is changing upon varying the H content as can be seen from Fig. 7.1. This speculation shall be verified in the following, making use of surface photovoltage measurements which probe the band bending in the c-Si towards the heterointerface, the quantity missing to calculate the band offsets from the band edge positions.

7.4. The a-Si:H/c-Si band offsets

It is obvious from Fig. 7.1 that based upon a known distance of c-Si VB edge from E_F (defined by the c-Si substrate doping concentration) and a measured valence band edge in the a-Si:H bulk, the band offsets can be precisely obtained by the equation

$$\Delta E_V = -E_{V,a-Si:H}^{\mu} + E_{V,c-Si} + e\varphi, \quad (7.1)$$

when the amount and distribution of equilibrium band bending $e\varphi$ in the structure is known. Due to the large density of rechargeable states in a-Si:H found in the band tails and the dangling bond defects in the band gap (a gap DOS of the order of $10^{17} \text{ cm}^{-3} \text{ eV}^{-1}$

being present), the electric field stemming from the immobile dopant ions in the c-Si is shielded in the a-Si:H already close to the heterointerface. The a-Si:H part of the junction will therefore only support a negligible fraction of the overall band bending [202]. Thus, the Dember-corrected SPV signal, identical to the equilibrium band bending in the c-Si, $e\varphi$, is assumed to be equal to the *total* band bending in the structure (as sketched in Fig. 7.1). This is a generally accepted assumption which is backed by both numerical simulations, showing only marginal band bending on the a-Si:H side of the junction (cf. section 7.6.2 and Ref. [202]), and the fact that deposition of nominally identical (i)a-Si:H layers on c-Si substrates of opposite doping type usually leads to SPV voltages whose sum equals the c-Si band gap within ± 50 meV [190]. The latter restricts the systematic error introduced by this assumption to < 50 meV. SPV was measured on the PES samples to quantify $e\varphi$ in the samples with known VB edge in the a-Si:H bulk. Doing so, a consistent set of data is obtained from which the valence band offset can be calculated and analyzed in terms of its variation with the H content. Fig. 7.2 shows the obtained offset of the a-Si:H VB mobility edge from the c-Si VB (ΔE_V) versus the (i)a-Si:H bulk hydrogen content $C_{\text{H,bulk}}$, again assuming that the H content measured on the FTIR/SE samples is representative for the nominally identical PES samples. The valence band offset increases pronouncedly with $C_{\text{H,bulk}}$, the linear fit of the data (red dashed line) yielding a slope of 13.4 ± 2.8 eV per at. % H, which is compatible with the slope observed in both band gap widening and VB retreat in the previous chapter. Then, the PES and SPV data are combined with the optical band gap obtained from SE, adding 160 meV to account for the difference between mobility- and optical gap [285], to calculate the offset between a-Si:H conduction band (CB) mobility edge and c-Si CB (blue data points and linear fit). The slope of the fit is -2.5 ± 2.7 meV per at. % H, i.e. compatible with zero.

Thus the data supports a variation in predominantly the valence band offset upon widening of the a-Si:H band gap by increased hydrogen incorporation. For comparison, the value for the VB offset obtained by Sebastiani *et al.* [219] on PECVD-deposited a-Si:H with 15...20% H content is shown (grey hatched area), agreeing reasonably well with the present samples of similar H content. The grey dotted line is a calculation of ΔE_V versus $C_{\text{H,bulk}}$ by van de Walle *et al.* [53], which will be discussed below.

7.5. Discussion I: The fundamental origin of the band lineup variations

7.5.1. Comparison to previous works

Experimental works

The variation of the a-Si:H optical band gap with $C_{\text{H,bulk}}$ measured on the 10 nm samples is consistent with previous results on thick layers. Cody *et al.* [41] found a slope of 14.8 meV per at. % of hydrogen, while Kaniadakis reports 12.7 meV per at. % [119], which is compatible to the value obtained here within experimental errors. Freeman *et al.* [72] found a slightly higher slope (≈ 20 meV per at. % H), however their samples were sputtered and due to the large range of deposition conditions covered in their study

displayed even differing values for the band gap for identical H content. In consequence, the error bar on this value is certainly large.

Additional support for the data presented here comes from the extrapolation to zero H content, which is suggested by the linearity of the data: A value of 1.52 ± 0.02 eV would result for pure a-Si, which is reasonably close to the reported ≈ 1.4 eV for annealed a-Si samples [43].

Early UV photoelectron spectroscopy experiments showed a retreat of the valence band edge by ≈ 0.8 eV for sputtered a-Si:H with a H content of 50% as compared to sputtered a-Si, while the position of the Fermi level relative to the core level peaks remained essentially constant, thus consistent with a removal of states at the top of the valence band [272]. PES measurements on a-Si:H layers prepared by PECVD showed a similar recession as compared to a-Si, the H content of these a-Si:H layers was however not exactly stated [274]. A rule-of-thumb calculation based on the sputtered a-Si:H data [272] assuming a linear retreat of the VB with the H content (although no intermediate H concentrations were explicitly analyzed in the pertinent study) would yield a slope of 11...12 meV per at. % H, which is surprisingly close to the value of 11.1 ± 2.8 meV measured here (cf. Fig. 6.8).

To the author's knowledge, there is only one experimental study where the band offsets of silicon-based heterojunctions were systematically varied. It was carried out on hydrogenated amorphous silicon carbide/crystalline silicon heterojunctions with NUVPEs on ultrathin layers [29]. The authors observed an increase of the a-Si_{1-x}C_x:H/c-Si valence band offset from 0.44 ± 0.02 eV found for pure a-Si:H with 15...20% hydrogen content to 0.95 eV for a-Si_{0.5}C_{0.5}:H/c-Si. The H content of the alloyed samples was not specifically analyzed in this study, although a competing incorporation of H and C during growth was previously observed which, in turn, affects the band gap widening [13, 15]. Further, there are no theoretical studies on which an analysis of the a-Si_{1-x}C_x:H/c-Si heterojunction could be based. The most simple system to study the effect of compositional variation on the band gap and -offsets is surely the unalloyed a-Si:H/c-Si heterojunction, for which some recent theoretical studies are available for comparison. In the next section the data obtained here will be discussed in the light of simulation results on the a-Si:H band edges and a-Si:H/c-Si band offsets.

Comparison to theory

Theoretical studies on the band structure of a-Si:H qualitatively agree on the band gap widening being caused by a retreat of the valence band edge upon increased hydrogen content, while the conduction band edge stays essentially constant [2, 177, 270]. In a simplified picture, this can be explained by the replacement of weak Si-Si bonds forming the top of the valence band by inclusion of hydrogen to form more stable (thus energetically deeper Si-H bonds). The more subtle aspects of the problem such as the chemical nature of the Si-H bonds or topological statistics render this matter more complicated from a theoretical point of view but are beyond the scope of this discussion.

Across the different studies and their theoretical approaches, the calculated slopes of the VB retreat differ. The reported values range from ≈ 15 meV per at. % hydrogen (close to the value reported here) to 40 meV, with the newer works yielding higher slopes. Ad-

ditionally, it must be noted that the calculated a-Si:H band gaps are mostly too small, as is often the case for calculated band structures.

For the theoretical treatment of the a-Si:H/c-Si heterojunction, there exist two different approaches: While the older studies comprise of separate computational treatment of the two phases forming the heterojunction [3, 53], the most recent publications attempt a microscopic simulation of the heterointerface itself with the goal to gain insight in both structural and electrical properties of the junction [178, 262]. Although promising from the conceptional point of view, the latter approach seems, at the time being, to suffer from stability problems (amorphization of the c-Si phase or recrystallization of the a-Si:H) and does not fully reproduce the essential electronic features of the a-Si:H/c-Si system (such as a low DOS in the band gap). Therefore the former studies still seem to represent a safer ground for comparison to experimental data.

The work of Allan *et al.* [3] is based on 'hydrogenation' of the Wooten-Winer-Weaire model for a-Si [284]. It features essential properties of a-Si:H such as a gap widening as compared to a-Si and exponentially decaying band tails with realistic slopes. The slope of the band gap versus H concentration is steep for the lowest H contents (as also observed experimentally [72]) and converges to a quasi-linear increase for $C_H > 3\%$, however with a slope as high as 34 meV per at. %. The authors attributed this discrepancy to the experimentally observed slope to the fact that at the low H contents featured in the model ($C_H < 8\%$), the hydrogenation still mainly affects the localized states in the band tails which would lead to increased widening of the gap as compared to more delocalized states. Based on the similar bond angles for their a-Si:H model as compared to c-Si and the resulting similar hybrid orbital energies, the authors argue in favor of a vanishing dipole contribution at the heterointerface and calculate the valence band offset by simply combining the energetic positions of the band edges, yielding $\Delta E_V = 0.36$ eV at $\approx 8\%$ hydrogen content. This value is reasonably close to the present results extrapolated to lower H content, however it is not stated how the VB offset evolves upon band gap increase.

The most comprehensive theoretical study on the band offsets in a-Si:H/c-Si was conducted by van de Walle and Yang [53]. They combined their own 'model solid theory' [266] with an *ab initio* pseudopotential calculation (density-functional theory in local-density approximation) to derive the a-Si:H properties [288] and also assumed the absence of interface-specific dipoles. This approach yields a VB offset of 0.2 eV for 11 % H content and a slope of ΔE_V with $C_{H,bulk}$ of 40 meV per at. % hydrogen. This prediction clearly contradicts the present data, as is obvious in Fig. 7.2 when comparing the grey dotted line with the data for the VB offset.

In an attempt to explain the discrepancy between calculations and the data presented here, the possible impact of interface dipoles which was neglected in the theoretical approaches discussed above will be discussed first. In modern theories of semiconductor HJ band alignment, the influences on the band offsets are separated into intrinsic contributions stemming from the complex band structure of the two materials forming the HJ, and extrinsic dipoles resulting from a difference in electronegativity or interface-bound defect states [167, 258]. There is agreement that the Si-Si bonds spanning the actual heterointerface are non-polar, however there is a possible shift in the band offsets due to a dipole contribution from polar Si-H bonds at the interface (Δ_{Si-H}) and from Si

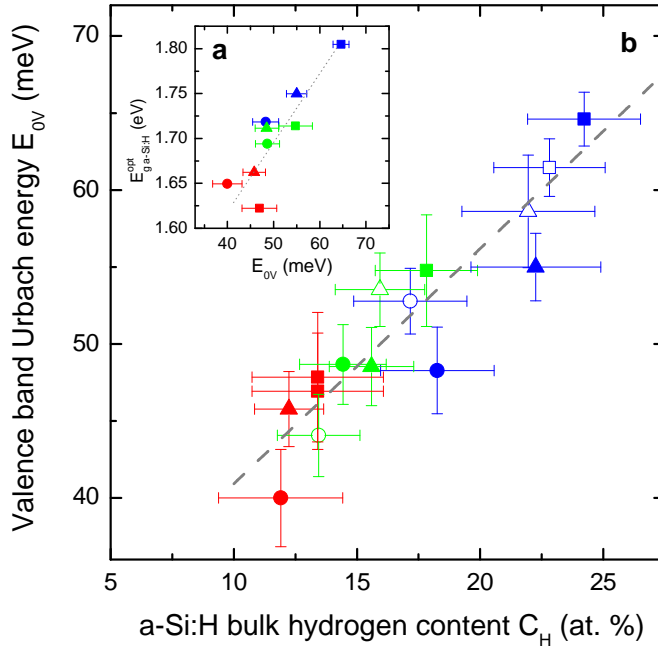


Figure 7.3: (a) Variation of the a-Si:H optical band gap when plotted against the valence band tail slope (Urbach energy) E_{0V} as derived from photoelectron spectra. The dotted line is a guide to the eye. (b) Increase of the Urbach energy E_{0V} , reflecting topological disorder and strain in the amorphous network, upon increased H incorporation, and linear fit to the data (dashed line).

dangling bonds carrying charges (Δ_{db}). A recent estimation of the magnitude of both effects yielded a possible $\Delta_{Si-H,max} = 90$ meV and $\Delta_{db,max} = 1.1$ eV in the geometrical limits, i.e. for a 100% coverage of the c-Si surface with Si-H bonds or a fully unsaturated c-Si surface (7×10^{14} eV $^{-1}$ cm $^{-2}$ surface defect states) [133]. For the samples analyzed here it is known that the difference in H content across the variety of samples is 15 at. %, which should be the range in which the Si-H bond density at the heterointerface varies, thus the impact of Δ_{Si-H} is marginal (< 15 meV). With photoconductance decay measurements, the dangling bond density at the a-Si:H/c-Si interface was found to be below $\approx 10^{13}$ eV $^{-1}$ cm $^{-2}$ for the layers under study here (cf. chapter 8 and Refs. [215, 216]), depending on the deposition conditions and consistent with older results from SPV measurements [210]. These data will be extensively discussed in the next chapter but shall be treated as given for the sake of this discussion. Thus, Δ_{db} across the range of samples could amount to only ≈ 13 meV in this case. Hence it can be concluded that a possible contribution of interface dipoles cannot not significantly affect the behavior of the band offsets in the present samples and therefore does not explain the observed difference between calculations and the data.

In the following it will be argued in favor of a different explanation: The data suggests that a competing influence on the band gap of both increased Si-H bond density and enhanced a-Si:H network disorder resulting from the details of H incorporation, not accounted for in the calculations, is responsible for the reduced measured slope of the valence band retreat.

7.5.2. Impact of disorder and hydrogen microstructure

Topological disorder

In a classic paper on optical absorption in a-Si:H, Cody *et al.* argued that the principal origin for the varying band gap of a-Si:H was not the hydrogen replacing Si-Si by Si-H bonds but the effect of topological disorder [40]. This argument was based on a universal connection between Urbach energy E_{0V} and band gap $E_{g,a-Si:H}^{\text{opt}}$ which they observed in a sample series where initially incorporated H was driven out by successive heating. They observed $E_{g,a-Si:H}^{\text{opt}}$ to collapse from about 1.7 eV to 1.5 eV due to the creation of localized states in the band tail upon H evolution, while E_{0V} increased from about 60 meV to 90 meV. Interestingly, the band tail retained its exponential shape across the whole range of data. The fact that the same $E_{g,a-Si:H}^{\text{opt}}$ vs. E_{0V} trend also held for the temperature dependence $E_g(T_{\text{meas}})$ versus $E_{0V}(T_{\text{meas}})$ for all analyzed samples was taken as evidence that the increased disorder (either of thermal nature from raising the temperature or of compositional nature from driving out the hydrogen) is the unifying origin for the variations in the band gap.

Plotting the optical band gap data from SE versus the Urbach energy E_{0V} as measured with CFSYS in Fig. 7.3a, a pronounced *increase* of the gap with the Urbach slope is observed. At first glance this result is contradicting the data shown by Cody, and points towards more subtle aspects governing the interplay between E_{0V} , $C_{H,\text{bulk}}$ and E_g . However, it must be noted that while Cody was driving out the H of an amorphous network already fixed in the moment of deposition, here the H content is controlled *a priori* by changing the deposition conditions. Thus, the Si network is able to accommodate a lower H content by changing its topology, without creating the same amount of localized states contributing to a broader band tail and smaller gap as was observed by Cody. The present data now suggests on the other hand that H incorporation itself is a source of disorder, as the Urbach energy systematically increases with $C_{H,\text{bulk}}$ (data from the previous chapter shown again in Fig. 7.3b). Thus, to reconcile Cody's observation of a band gap reduction with E_{0V} and the opposite result seen in Fig. 7.3a, one must assume at least *two* contributions of separate physical origin to the variation of the band gap: H content *and* topological disorder, which are—as obvious from Fig. 7.3—however practically connected by the enhanced disorder following from increasing H incorporation (for the H contents under study here). This means that the retreat of the valence band by increased Si-H bond density is partly compensated by the broadened and shifted valence band tail due to increased disorder resulting from the incorporation of hydrogen during PECVD growth.

Interplay of voids, disorder and electronic structure

In the previous chapter, the details of hydrogen incorporation and the resulting structural changes were analyzed in detail. Here the data shall be revisited in order to identify the possible *structural* origin of the disorder increasing with the H content.

First it shall be noted that it was found in simulations that the a-Si:H density has a considerable impact on the energetic position of the valence band, moving it up in en-

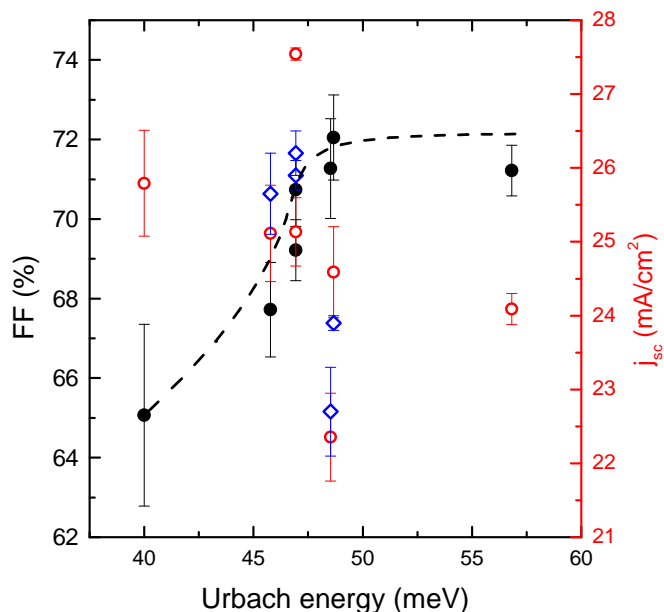
ergy with decreasing density [53]. The effect was quantified as $\Delta E = 2.46 \times f_m$ [eV]. In this case this would mean that the predicted slope of the VB retreat (≈ 40 meV per at. %) would be reduced by approximately ≈ 12 meV per at. % due to the loss in density accompanying the increased $C_{H,bulk}$. However, it is known that the density loss is caused by the increasing presence of voids and therefore does *not* denote a density loss in the bulk of the amorphous network. However, relevant for the band offsets is *only* the local bulk density at the interface in void-free regions [53]. Thus, the density effect does *not* account for the discrepancy between calculated and observed band lineup, as must be pointed out.

In terms of hydrogen microstructure, the results from the previous chapter (Figs. 6.3 & 6.4) can be summarized as follows: The samples are characterized by an approximately constant contribution from distributed monohydrides and a strongly increasing phase of clustered-monohydride-decorated voids. Therefore, the clear trends of the different a-Si:H properties versus the bulk H content (band gap, VB retreat) must be associated with the clustered-H phase. Most importantly in the context of this discussion, also the pronounced increase of the valence band tail slope with the H content must be associated with the clustered-H phase (visible as HSM in the IR spectra), based on this analysis. The possible cause for this important connection shall be elucidated in the following.

The connection between topological disorder and the band tail states in amorphous silicon was established on a fundamental level: A distribution of bond angles or -lengths differing from the c-Si equilibrium value suffices to create exponentially decaying band tails [234, 270]. More recently, the valence band tail was identified as being composed of short Si-Si bonds [61, 68], that form filamentary structures in the amorphous network [175]. A recent theoretical work on void-containing a-Si:H revealed the same filamentary structures starting predominantly from the inner surfaces of voids, which were identified to introduce additional strain or disorder in the a-Si:H network [36]. In the light of these results, the observed increase of E_{0V} with the HSM hydrogen content can be consistently explained: Quite counterintuitive at first glance, the appearance of voids does not lead to a relief of strain in the amorphous network (as could be anticipated due to the additional degrees of freedom offered by an empty volume), but creates additional strain, again manifesting in filamentary structures of short bonds that constitute the valence band edge in compact a-Si:H. As a consequence, the less pronounced retreat of the valence band edge upon H incorporation with respect to calculations taking into account *only* the replacement of Si-Si bonds by Si-H (without accompanying increase of strain or disorder due to the topological consequences of increased H incorporation) can be understood through the compensating effect of increased topological disorder associated with filaments of strained bonds attached to the inner surfaces of H-decorated voids.

Having analyzed the interplay of H incorporation, strain/disorder and the consequences for the a-Si:H band structure and a-Si:H/c-Si band lineup it is obvious that future theoretical treatments of the a-Si:H/c-Si interface should explicitly include the subtleties of the H microstructure and its variation across the a-Si:H compositional phase diagram.

Figure 7.4: Illuminated I/V parameters (fill factor FF and short-circuit current density j_{sc}) of solar cells processed on DSP (n)c-Si{111} substrates, plotted against the Urbach energy of the 5 nm thick undoped a-Si:H buffer layers. Red circles are j_{sc} values measured in the sun simulator while blue diamonds represent j_{sc} as deduced from EQE measurements. It is obvious that the fill factor systematically increases with E_{0V} while there is no pronounced correlation between j_{sc} and E_{0V} .



7.6. Discussion II: Impact of band offsets on carrier transport

7.6.1. Phenomenology in solar cell I/V curves

In section 4.2.4, the V_{oc} values of a solar cell series on DSP (n)c-Si{111} were presented and discussed. This series comprised different undoped a-Si:H buffer layers at a thickness of 5 nm. Here, the influence of the (i)a-Si:H buffer layer properties on the charge carrier transport across the heterojunction shall be explored in the light of the insight on the IBL properties gained in the previous chapter and on the band offsets obtained in this chapter. To this end, the fill factor FF and the short-circuit current density j_{sc} will be analyzed¹.

In the analysis of dark I/V curves in chapter 5, an impact of microscopic a-Si:H properties was suggested in the low-forward bias region where tunneling processes play a role. Thus, the presence of *localized states* at varying concentration in the band tails may influence the tunneling rate. Additionally, the *band offsets* may impact the charge carrier transport as they hinder the crossing of charge carriers from c-Si into the a-Si:H emitter. In the light of ΔE_V being about 2...3 times larger than ΔE_C for 'standard' (i)a-Si:H and thus possibly dominating the transport properties, the approximately 150 meV variation in ΔE_V mean a change by 30%, which is significant and suggests an impact on the hole transport.

Figures 7.4 & 7.5 show the fill factor and short circuit current density of the DSP (n)c-Si based cell series, plotted against the Urbach energy or the optical band gap of the undoped buffer layer, respectively. In order to exclude a possible drift in the lamp characteristics (as surmised in chapter 4), EQE-measured j_{sc} values are included in the figures for a subset of samples (blue data points). Observing Fig. 7.4 it is obvious that

¹While the latter reflects the efficiency of charge carrier extraction under short-circuit conditions, the former includes information about the transport under forward bias conditions.

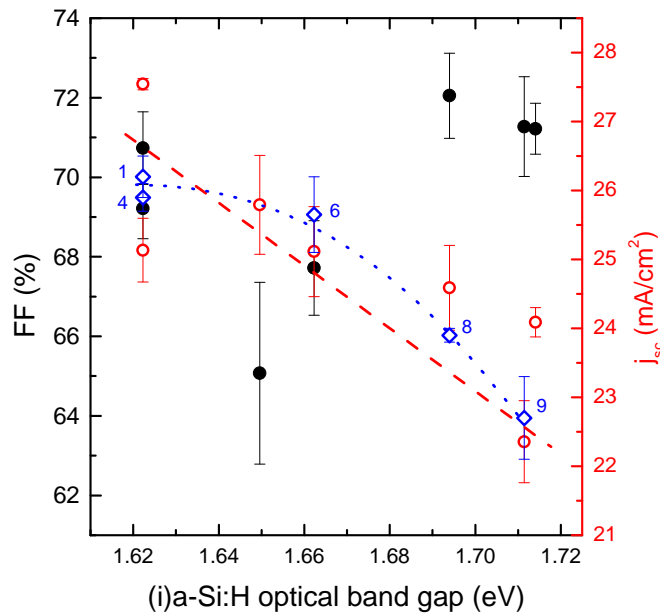


Figure 7.5: Illuminated I/V parameters (fill factor FF and short-circuit current density j_{sc}) of solar cells processed on DSP (n)c-Si substrates, plotted against the optical band gap of the 5 nm thick undoped a-Si:H buffer layers. Again, red circles are j_{sc} values measured in the sun simulator while blue diamonds represent j_{sc} as deduced from EQE measurements (numbers identify the wafers on which EQE/IQE was measured). It is suggested that j_{sc} decreases systematically with E_g while there is no pronounced correlation between FF and E_g .

while j_{sc} is scattered rather arbitrarily, the fill factor seems to systematically increase with the Urbach energy of the undoped a-Si:H buffer layer: After a steep increase between $E_{0V} = 40 \dots 50$ meV, FF saturates at about 72% for $E_{0V} > 50$ meV. The level of the FF saturation value is consistent with the values found previously for IBL thicknesses of 5 nm (cf. Fig. 4.14). In Fig. 7.5, a complementary trend is found: While the fill factor scatters when plotted against the band gap, a systematic and almost linear dependence of the short-circuit current on the (i)a-Si:H band gap — which is a measure for the valence band offset as shown above — is found.

7.6.2. Interpretation

Possible impacts on the fill factor

The observed trends in FF and j_{sc} are as surprising as they are interesting. The variations in the fill factor shall be discussed first: In Fig. 4.14, a pronounced difference in the FF loss accompanying the inclusion of IBLs was observed between the two substrate doping types. Starting from the 79% fill factor for *both* n- and p-type record cells without IBLs, the deterioration of FF upon inclusion of IBLs is very small for (p)c-Si based cells, while a FF loss of $>15\%$ absolute is observed for 10 nm thick IBLs on (n)c-Si. There are two straightforward explanations for a general FF loss upon inclusion of IBLs: First, the undoped layers represent a resistive element in the cell structure due to their small conductivity, which leads to an increased series resistance and a thus reduced fill factor. Second, a thick IBL with low defect density may not entirely shield the electric field from the c-Si dopant ions and thus support some fraction $\phi_{a-Si:H}$ of the overall band bending. For a thicker IBL, the band bending in the c-Si could therefore be successively reduced which may lead to a loss in V_{oc} and the fill factor. However, these two mechanisms would have the same magnitude for the doping-inversed structures and could not explain the

Table 7.1.: AFORS-HET solar cell simulation results for (n)c-Si and (p)c-Si based heterojunction solar cells, under variation of (a) valence band offset for a (n)c-Si based cell (first block), (b) the (i)a-Si:H buffer layer thickness for a (n)c-Si based cell (second block), and (c) the (i)a-Si:H buffer layer thickness for a (p)c-Si based cell (third block).

| Parameter variation | Structure | ΔE_{minor} eV | V_{oc} mV | j_{sc} mA/cm ² | FF % | η % | $\phi_{\text{a-Si:H}}$ meV |
|---------------------------|-----------|---------------------------------|-----------------------|---------------------------------------|-----------|-------------|-------------------------------|
| ΔE_{minor} | pi5Nn | 0.39 | 733 | 39.3 | 76.6 | 22.0 | 44 |
| | pi5Nn | 0.44 | 722 | 39.3 | 63.1 | 17.9 | 44 |
| | pi5Nn | 0.49 | 689 | 39.3 | 35.5 | 10.0 | 44 |
| IBL thickness on (n)c-Si | pi2.5Nn | 0.39 | 732 | 39.3 | 77.4 | 22.3 | 24 |
| | pi5Nn | 0.39 | 733 | 39.3 | 76.6 | 22.0 | 44 |
| | pi10Nn | 0.39 | 729 | 39.2 | 67.0 | 19.2 | 75 |
| IBL thickness on (p)c-Si | ni2.5Pp | 0.25 | 699 | 37.0 | 83.0 | 21.5 | 31 |
| | ni5Pp | 0.25 | 696 | 36.9 | 83.1 | 21.3 | 31 |
| | ni10Pp | 0.25 | 689 | 36.7 | 83.1 | 21.0 | 60 |

difference observed in Fig. 4.14². Based on the information contained in Fig. 7.4 it will be argued in the following that the difference is due to the asymmetry in the band offsets acting as a barrier for the extraction of minority carriers from the c-Si.

Numerical simulations

To complement the measured solar cell parameters, numerical simulations with the device simulator AFORS-HET were employed [241, 242]: The layers constituting the solar cells were parametrized employing the microscopic parameters where these were known (band gap E_g , Urbach energy E_{0V} etc.), and the structures did not comprise a back-side IBL for simplicity. The two most important 'tuning parameters' which are used to adjust the model to the measured solar cell parameters are the defect density at the heterointerface (which is modeled as a 5 nm thick c-Si layer with increased bulk defect density) and the a-Si:H emitter doping level. Tuning the first is necessary when a realistic interface defect density is desired as to date no interaction between a-Si:H dangling bonds and c-Si recombination parameters is present in AFORS-HET³. The emitter doping is used as a free parameter as the Fermi level position measured with CFSYS on doped layers is usually inconsistent with the E_F as implied from other techniques (e.g. SPV), which may result from a partial pinning of E_F at the defect-rich a-Si:H/vacuum interface of particularly the (p)a-Si:H layers. Thus, an emitter doping is chosen which leads to realistic solar cell behavior and kept constant throughout the simulations. It is important to note that AFORS-HET does not account for tunneling processes but assumes only thermionic emission for the charge carrier transport across

²Indeed, it will be shown below that the band bending distribution in the structure does *not* change markedly upon varying the IBL thickness.

³However, as will be shown in the next chapter, it is important to consider this aspect to correctly capture the passivation properties of a-Si:H/c-Si structures.

the band offsets.

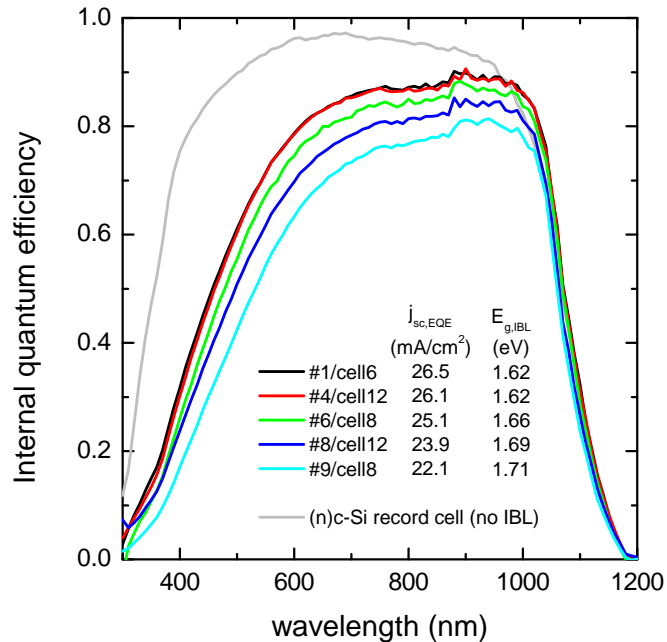
While in (n/i)a-Si:H/(p)c-Si solar cells, the c-Si minority carriers, which have to be extracted on the emitter side of the cell, have to surpass the comparably small conduction band offset of ≈ 0.25 eV, there is a barrier of $\approx 0.45 \dots 0.6$ eV for the minority carriers in (p/i)a-Si:H/(n)c-Si solar cells (cf. Fig. 7.2). Observing the first three simulation results in Table 7.1 it is obvious that thermionic emission alone is not sufficient to overcome the large barrier on the valence band side: When ΔE_V is increased even on a moderate level, the fill factor strongly degrades and reaches very low values even before the measured ΔE_V values are reached. Obviously, additional tunneling-mediated transport paths not taken into account in the AFORS-HET simulations exist in reality.

The tunneling signature observed in the dark I/V transport analysis (cf. chapter 5) suggests that tunneling into the localized states of the (i)a-Si:H valence band tail may be a realistic scenario. Such tunnel hopping transport was also directly observed in electrically detected magnetic resonance (EDMR) measurements on a-Si:H/c-Si solar cells [22]. If the valence band tail states facilitate tunnel-hopping processes which contribute to charge carrier transport, the trend in Fig. 7.4 can be understood: By increasing the slope of the valence band tail with decreasing E_{0V} , the density of available final states for tunneling processes is reduced, which will suppress the additional transport path through the large valence band offset. This may explain why the fill factor *increases* when the electronic quality of the undoped buffer layer is decreased, as shown in Fig. 7.4. Important to note, the simulations rule out a possible impact of a voltage drop in the IBL⁴: The second and third block of data in Table 7.1 show simulation results for a thickness variation of the IBL under a doped emitter layer for both (n)c-Si and (p)c-Si substrates. For the (n)c-Si substrates, a lower ΔE_V was assumed (corresponding to an 'effectively lowered barrier' due to the presence of tunneling processes, similar to the treatment of thermionic emission over a spike in the presence of tunneling) to yield realistic FF values. The last column shows the voltage drop across the IBL under equilibrium conditions. As expected, the voltage drop is indeed small also in the presence of a doped top layer ($\phi_{\text{a-Si:H}} < 80$ meV). Therefore, the FF loss cannot be due to a decrease of c-Si band bending, which is underpinned by an approximately constant V_{oc} . It is interesting to note that FF is indeed deteriorating much more pronouncedly for cells on (n)c-Si substrates as for the doping-inversed structures. The loss of 10% when going from 2.5 nm thick IBLs to 10 nm is comparable to the data in Fig. 4.14. Obviously, AFORS-HET correctly captures the trends when an effectively lowered barrier for the minority carrier transport is assumed.

The trend in j_{sc} in Figure 7.5 on the other hand cannot be understood from the simulations: As seen in the first block of results in Table 7.1, j_{sc} does not vary with the valence band offset. Indeed, in a naïve approach to the problem one would assume that the short-circuit current *increases* with the band gap, as the parasitic absorption

⁴In the SPV measurements on single undoped a-Si:H layers used in this chapter to calculate the band offsets, very similar values for the c-Si band bending were detected irrespective of a-Si:H growth conditions. Together with the constant $E_F - E_C$ in the (i)a-Si:H as observed in PES, this signifies that the (i)a-Si:H band bending must be constant. Comparison of SPV measurements of identical (i)a-Si:H layers deposited on both (n)c-Si and (p)c-Si substrates showed that $\phi_{\text{a-Si:H}} < 50$ meV for single (i)a-Si:H layers. However, this picture may change when a doped top layer is employed.

Figure 7.6: Internal quantum efficiency of solar cells processed on DSP (n)c-Si substrates, and reference IQE of (n)c-Si record cell. The global loss of output current with increasing IBL band gap implies that the valence band offset acts as an efficient barrier for hole extraction under j_{sc} conditions. The wafer numbers (#x) can be compared with the numbers shown in Fig. 7.5.



in the highly recombination-active a-Si:H bulk should decrease with increasing band gap. However, it seems that this effect — which may be present at a much lower level than the variation of 4 mA/cm² observed in the plots — is superimposed by a much more prominent effect. To shed light on this interesting trend visible in Figure 7.5, IQE measurements were performed.

IQE analysis

Fig. 7.6 shows the IQE curves of selected solar cells from five different wafers. First of all, it has to be noted that the low-wavelength response is very poor as compared to the cells analyzed in chapter 4 (the gray line marks the IQE of the (n)c-Si reference cell). This is attributed to increased parasitic absorption in the ECR-CVD-deposited (p)a-Si:H emitter layers, which is implied by significantly higher Urbach energies as compared to the PECVD-deposited (p)a-Si:H⁵. This explains the rather low j_{sc} values even taking into account the flat substrate. Secondly, there is a *global* loss of collection efficiency associated with the (i)a-Si:H band gap increase: Upon increasing the IBL band gap by roughly 100 meV, the IQE is globally reduced by about 15%, corresponding to the observed loss in j_{sc} . As there is no correlation to V_{oc} and the IBL was the only parameter changed within this series, this observation is most consistently explained as a transport barrier under j_{sc} conditions. Obviously, the blocking characteristics of the valence band offset depend on the bias regime: While under forward bias (and in consequence with currents $< j_{sc}$) the tunneling-mediated penetration of the band offset seems to allow for efficient carrier extraction if the density of localized states in reach of

⁵PES measurements revealed > 10 meV difference in E_{0V} for the same *nominal* doping concentration, although the effective doping level in ECR-deposited (p)a-Si:H is much lower as seen in Fig. 4.5.

the c-Si valence band is large enough, under j_{sc} conditions the offset seems to unfold a blocking character which depends on the absolute height of the band offset. A possible scenario for the transition between the regimes would be a saturation of the tunneling rate, which would depend on the density of final states for tunneling events and the height of the barrier represented by the band offset. At this point, this conclusion has a tentative character. It is obvious that detailed simulations with an approach including tunneling mechanisms are necessary to confirm the explanation offered here.

In conclusion it is suggested that the barriers for minority carrier extraction imposed by the band offsets heavily impact the transport properties. The observed differences between the substrate doping types can be linked to the fundamental asymmetry in the a-Si:H/c-Si band lineup. The subtleties in the transport seen in FF and j_{sc} depending on different microscopic parameters point towards a bias-dependent saturation of tunneling currents, while numerical simulations incorporating tunneling will be needed to work out the involved mechanisms in detail.

7.7. Chapter conclusion

The key question for this chapter was:

How is the exact heterojunction band lineup in dependence on a-Si:H deposition conditions and how does it impact charge carrier transport?

It was shown that upon increasing the a-Si:H bulk hydrogen content, a systematic retreat of the a-Si:H valence band edge leads to a widening of the band gap and an increase of the VB offset at the heterojunction with a slope of $\approx 13 \text{ meV/atom-\% H}$. While the general trend of $E_{V,a-Si:H}^\mu$ versus $C_{H,bulk}$ is consistent with previous experimental and theoretical works, a discrepancy is noted between the calculations and the experimental data in terms of the slope of the VB retreat. Based on the known interface defect- and bulk hydrogen densities of the a-Si:H layers, a dominant contribution from interface dipoles can be ruled out as an explanation. The hydrogen microstructure as analyzed in chapter 6 however suggests that the increasing contribution of voids, which leads to enhanced topological disorder as reflected in a broadened VB tail, counteracts the widening of the gap caused by the increased density of Si-H bonds, thus reducing the slope of the VB retreat. This effect seems to be a generic feature of the higher H content range of a-Si:H samples ($C_H > 10 \text{ atom-\%}$), based on the compatibility of the measured slope with pertinent data. This highlights the necessity to explicitly incorporate the changes in H microstructure and resulting Si network topology when modeling the a-Si:H/c-Si interface properties.

As a consequence of the variations in the VB offset, the transport signature of solar cells is dependent on the deposition conditions of the IBLs: The carrier extraction under j_{sc} conditions seems to be significantly hindered by a large VB offset as the output current decreases markedly with increasing ΔE_V . Under moderate forward bias however the tunneling of holes into the a-Si:H valence band tail seems to be able to take over a significant part of the transport, as also indicated by the dark I/V analysis in chapter 5. This results in the fill factor being dependent on the density of accessible final states

for the tunneling process, reflected in the Urbach energy of the IBL. Device simulations incorporating tunneling transport across the heterojunction are needed to confirm the dependence of illuminated I/V parameters on IBL microscopic properties.

8. The interplay of a-Si:H properties with a-Si:H/c-Si interface passivation

In this chapter, the passivation mechanism of (i)a-Si:H and (p/n)a-Si:H/(i)a-Si:H stacks on crystalline silicon surfaces is analyzed. Linking the detailed microscopic information about the thin (i)a-Si:H layers obtained in chapter 6 with the analytical description of recombination at the a-Si:H/c-Si heterointerface (cf. section 2.2.4), the phenomenology of passivation seen in chapter 4 can be understood.

It is found that in the annealed state, the heterointerface possesses no specific properties but merely serves as a window between the c-Si hosting the photo-generated charge carriers and the a-Si:H bulk with its dangling bond defects acting as dominant recombination centers. Annealing can be performed not only with the 'classical' hot plate method, but also using pulsed microwave radiation which yields an accelerated defect removal, supposedly resulting from the details of microwave absorption in a-Si:H. In the as-deposited state of the heterointerface, the measured interface defect densities are significantly higher than those expected from the (i)a-Si:H bulk quality, highlighting the impact of locally inferior network structures resulting from poor growth conditions.

Based on the finding that c-Si passivation properties are governed the a-Si:H bulk, the complex phenomenology of passivation seen in chapter 4 can be linked to bulk processes in the a-Si:H passivation layer. A model is set up which links these a-Si:H bulk processes to the recombination properties of the c-Si absorber. In the framework of this 'equilibrated interface model', the deterioration of c-Si surface passivation upon deposition of doped a-Si:H top layers can be understood by the defect equilibration in a-Si:H, occurring upon shifting the Fermi level at the heterointerface. The asymmetry in the behavior between doping-inversed doped/undoped a-Si:H stacks is thus explained by the inherent properties of the a-Si:H dangling bond defects.

This chapter is based on the publications [A], [D], [G], [H] and [I] from the list in the appendix.

8.1. Introduction

Of the fundamental questions raised at the end of chapter 4, three remain to be answered:

- How do the a-Si:H microscopic properties relate to the passivation potential of a given undoped a-Si:H buffer layer (IBL)?
- What is the microscopic effect of thermal post-treatment?
- What causes the degradation of passivation by IBLs upon deposition of doped a-Si:H top layers and how can it be diminished?

These questions shall provide a guideline through the last chapter of this thesis, where the phenomenology concerning the passivation by (i)a-Si:H and doped/undoped stacks as outlined in chapter 4 is explained by means of the results from the previous chapters, most notably making use of the a-Si:H properties determined in chapter 6. As explicitly stated in section 2.2.5 and confirmed in the solar cell series, the passivation of the c-Si substrate is the crucial parameter determining the solar cell V_{oc} . Thus, besides the goal of identifying well-suited PECVD parameter sets to best passivate a given technologically relevant c-Si surface, the aim of a *physical* approach to the problem must be to understand the interplay between a-Si:H and c-Si passivation on a fundamental level.

In the following, the first step will be to correlate the passivation quality obtained with different (i)a-Si:H layers with the microscopic parameters in the as-deposited state. Then, low-temperature annealing will be employed and the resulting transient behavior of the passivation is monitored. Two different methods based on hotplate- and pulsed microwave annealing are presented, and the superiority of microwave annealing in terms of required annealing time for a given passivation improvement is demonstrated. Next, the properties of the annealed heterointerface are discussed and again compared to a-Si:H bulk properties, resulting in a model which traces the density of defects at the annealed interface back to the a-Si:H bulk properties. This concept allows to estimate the equilibrated interface defect density for a given IBL based on its microscopic structure. Finally, the issue of a deteriorating passivation upon deposition of a doped top layer is discussed in the framework of an 'equilibrated interface model', which helps to understand the passivation behavior of a-Si:H stacks seen in chapter 4.

8.2. Correlation of a-Si:H bulk properties with a-Si:H/c-Si interface defects

The effective lifetime τ_{eff} as used throughout chapter 4 can be readily determined with photoconductance decay and therefore represents a convenient parameter for a technological optimization. However, as was shown in section 2.2.4, it is only loosely connected to the interface defect density. In order to analyze in more detail the dependence of the physical parameter D_{it} on a-Si:H layer properties and post-treatment, it has to be extracted from the PCD data. To this end, the semi-analytical model for a-Si:H/c-Si interface recombination developed by C. Leendertz [142] was employed to fit the PCD data. Doing so, an estimate for the product of interface defect density D_{it} and the

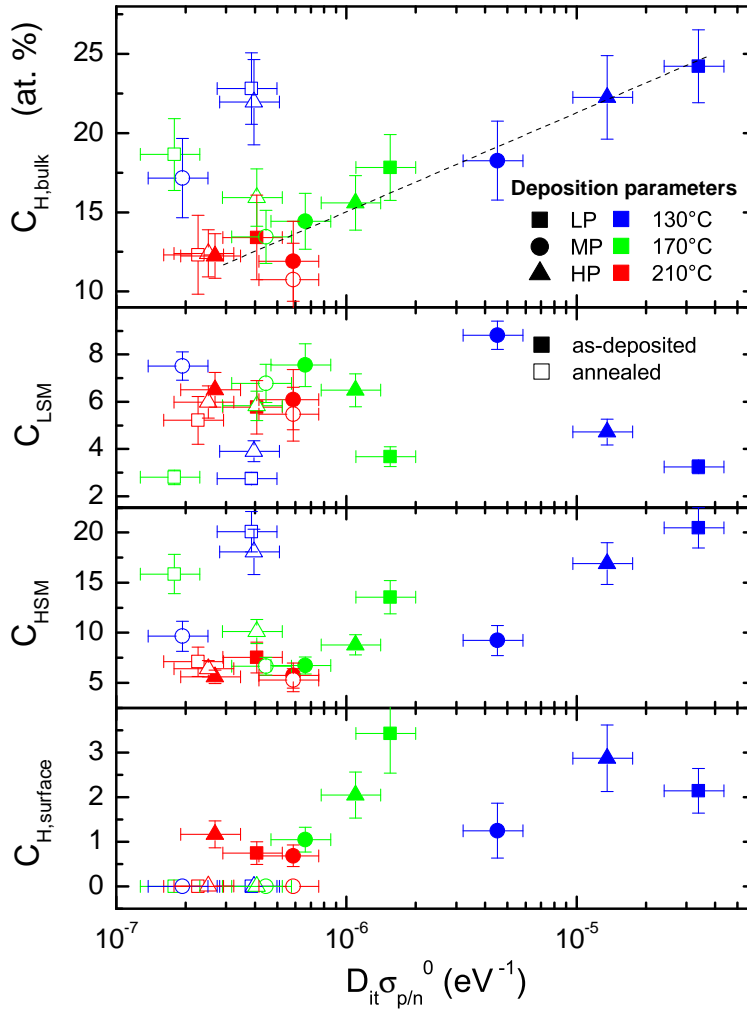


Figure 8.1: Correlation of FTIRS-derived hydrogen content in 10 nm thick (i)a-Si:H found in LSM, HSM, surface SiH₂ and LSM + HSM ('bulk H content') with the interface defect density expressed as the product $D_{it}\sigma_{p/n}^0$, in the as-deposited state (full symbols) and after annealing for 5' at 200°C (open symbols). $D_{it}\sigma_{p/n}^0$ was obtained by fitting τ_{eff} vs. Δn data obtained by PCD lifetime spectroscopy, as explained in section 2.2.4.

capture cross section of the neutral interface defects $\sigma_{p/n}^0$ can be determined¹. Taking a literature value for $\sigma_{p/n}^0$ (to be discussed later) allows to extract D_{it} which can then be compared to the a-Si:H layer properties.

The most straightforward comparison involves the hydrogen content and microstructure, as these properties can be measured on the same samples as used for the determination of D_{it} from PCD measurements. The results are shown in Fig. 8.1, where $D_{it}\sigma_{p/n}^0$ in both as-deposited (filled symbols) and annealed state (open symbols) is compared to the hydrogen concentration found in the LSM, HSM and surface SiH₂ modes, as well as the sum of LSM and HSM (bulk hydrogen content $C_{H,bulk}$). It is obvious that there is a pronounced correlation of the as-deposited interface defect density, quantified by

¹Note that within this thesis, identical cross sections for electrons and holes are assumed, thus $\sigma_p^0 = \sigma_n^0 \equiv \sigma_{p/n}^0$ as common in the literature (see e.g. Ref. [158] and references therein).

$D_{\text{it}}\sigma_{p/n}^0$, with the bulk H concentration, while the annealed samples show only marginal differences in $D_{\text{it}}\sigma_{p/n}^0$, consistent with Fig. 4.3. While there is also a fairly pronounced correlation between $D_{\text{it}}\sigma_{p/n}^0$ and C_{HSM} , resulting from the fact that C_{HSM} represents the dominant contribution to $C_{\text{H,bulk}}$, no connection seems to exist with C_{LSM} or $C_{\text{H,surface}}$. Based on the fact that the a-Si:H bulk H content was found to be a rather universal ordering parameter and clear correlations of other a-Si:H microscopic parameters to $C_{\text{H,bulk}}$ were observed, e.g. concerning the band gap/valence band retreat (Figs. 6.5 & 6.8), mass density (Fig. 6.6), and valence band tail slope (Fig. 6.9), a correlation of as-deposited D_{it} to those parameters is to be expected as well. However, before the implications of such apparent connections can be discussed it has to be tested whether the correlation of the *local* interface parameter D_{it} to the *bulk* parameter $C_{\text{H,bulk}}$ is real or merely a coincidence. Although the straight line in Fig. 8.1 linking the as-deposited $D_{\text{it}}\sigma_{p/n}^0(C_{\text{H,bulk}})$ values implies such a connection, the behavior of the annealed samples raises some doubts: While $D_{\text{it}}\sigma_{p/n}^0$ changes drastically upon annealing (only 5' at 200°C were employed in this case), the FTIRS-detected bulk hydrogen modes are only marginally affected as will be discussed in detail below². It is difficult to imagine a mechanism where a physical relation between bulk H configuration and interface defects in the as-deposited state is abrogated by a short low-temperature annealing step. Thus, the question of the fundamental origin of the passivation behavior cannot be answered at this stage. In order to tackle it further, the process of annealing is elucidated in the following, exploring both the transient dynamics in D_{it} upon annealing and the subtle microscopic changes which are imposed in the thin a-Si:H layer.

8.3. Low-temperature annealing

8.3.1. Microscopic reaction of the a-Si:H bulk

The first step towards monitoring the microscopic effects of annealing in the a-Si:H layers was to employ FTIRS. PCD samples symmetrically coated with 10 nm (i)a-Si:H were measured in the IR spectrometer, then annealed for 5' at 200°C and immediately measured again. As the same calibration of the IR spectrometer was used for both measurements, an analysis of difference spectra is possible. The results are shown in Fig. 8.2, again showing the as-deposited data from Fig. 6.2 in the upper panel, complemented by the FTIR spectra of the annealed samples and the difference spectra. The dramatic differences in terms of intensity and ratio of the bulk Si-H signals depending on the deposition conditions have been discussed in chapter 6. These differences in H bonding come along with distinctly different as-deposited D_{it} values as was shown in Fig. 8.1. Interestingly, upon annealing there are only marginal variations in the bulk Si-H signals while a drastic loss in the surface-related SiH₂ peak and the appearance of oxygen-related peaks at higher wave numbers are observed. The reduction of the surface

²The latter is obvious in Fig. 8.1 as for the bulk-related modes only a horizontal shift of the data points (within experimental error of the FTIRS analysis) is observed, i.e. the passivation is changing drastically without any marked reaction of the bulk H modes. The surface-SiH₂ mode on the other hand is eradicated upon annealing.

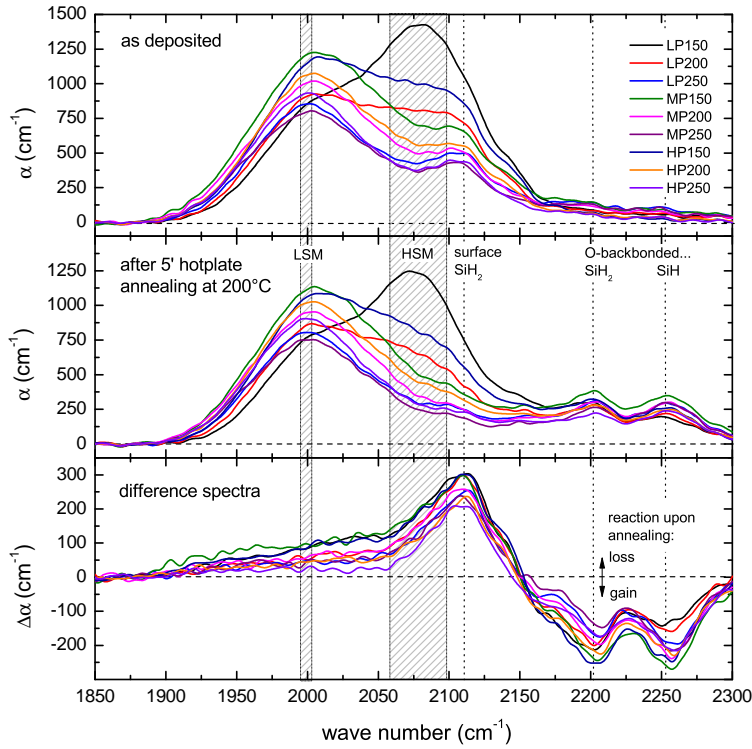
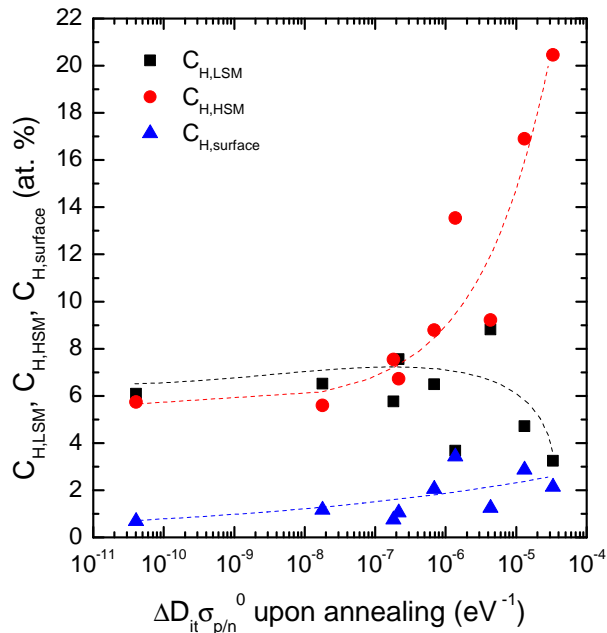


Figure 8.2: FTIR spectra for (i)a-Si:H layers of 10 nm thickness deposited at the nine standard deposition parameters listed in Table 4.2, in the as-deposited state as well as after annealing for 5' at 200°C. The lowest panel shows the difference spectra before and after annealing. Fitting of these spectra yielded the hydrogen contents displayed in Fig. 8.1.

SiH₂-signal and the appearance of oxygen-back-bonded Si-H is consistent with oxidation of the free a-Si:H surface during annealing. This finding is surprising as the annealing experiments were performed under nitrogen flow. However, the setup was simple and no cleaning purge prior to annealing was possible, so some oxygen may have remained in the annealing box, causing this effect. Additional support for this explanation comes from the fact that although the bulk-related modes are very distinctly dependent on the deposition conditions of the layers, the surface-related SiH₂ mode and the changes upon annealing are very similar for all the samples as seen in the lower panel of Fig. 8.2, consistent with a common origin of this effect which most probably is oxidation. Thus, the changes observed for wave numbers $> 2100 \text{ cm}^{-1}$ are purely surface-related, identical for all samples and therefore irrelevant for the understanding of the sample-dependent changes at the heterointerface upon annealing.

If there was an interplay between a-Si:H hydrogen bonding and interface defect removal during annealing, it would have to involve the bulk H modes in a-Si:H. A possible scenario which was invoked in previous publications would be thermal mobilization of hydrogen in the a-Si:H bulk and successive migration to the interface where dangling bond defects can be passivated [31, 32]. In such case, a correlation between D_{it} removal and changes in a-Si:H hydrogen bulk modes would be expected. Figures 8.3 shows the hydrogen content found in LSM, HSM and the surface SiH₂ mode versus the difference in $D_{it}\sigma_{p/n}^0$ after and before annealing. The picture from Fig. 8.1 is reflected here again in more clarity: The samples with the largest contribution of the HSM show the largest

Figure 8.3: Correlation between H configuration as determined by FTIRS and passivation improvement upon annealing, expressed as the difference in $D_{it}\sigma_{p/n}^0$ before and after annealing ($\Delta D_{it}\sigma_{p/n}^0$): The samples with the largest contribution of the HSM show the largest improvement in D_{it} upon annealing.



improvement in D_{it} upon annealing. Consistently, the amount of SiH_2 decorating the open a-Si:H surface increases along with the HSM when deposition conditions are sub-optimal³.

It is instructive to plot the difference in the IR modes before and after annealing versus the change in interface defect density upon annealing ($\Delta D_{it}\sigma_{p/n}^0$), which is done in Fig. 8.4. If the annealing effect was related to bulk hydrogen reconfiguration, a clear signature would be expected in this graph. There is a constant loss of 0.5...1 at. % seen in ΔC_{LSM} (black squares), while the values for ΔC_{HSM} and $\Delta C_{H,surface}$ are significantly scattered (open symbols). A closer inspection reveals that for each data set, ΔC_{HSM} and $\Delta C_{H,surface}$ are anticorrelated, which is due to the close proximity of the HSM and surface SiH_2 mode and resulting overlaps affecting the fitting procedure: While the surface SiH_2 mode is significant in the as-deposited state, this is not the case after annealing. In all the fits of annealed data, values for $C_{H,surface}$ compatible with zero were found by the fitting routine. However, it appears that this mode is not exactly zero in all cases but just small enough to allow a reasonable fit with a (slightly broadened) single HSM. Therefore, the HSM partly compensates for the missing surface SiH_2 mode after annealing, leading to a net *gain* in the HSM which is more pronounced if a larger $C_{H,surface}$ was present before annealing. However, this effect can be eliminated from the ΔC_{HSM} by inspecting the *sum* of ΔC_{HSM} and $\Delta C_{H,surface}$ (orange triangles), which thus represents the net loss of hydrogen from the combined HSM and surface SiH_2 mode. The scatter is removed by this procedure and one observes a much clearer trend now. Just as the ΔC_{LSM} data, the summed data are flat at around -1 at. % H loss upon annealing for most of the $\Delta D_{it}\sigma_{p/n}^0$ range, and only for the two samples showing the

³As stated before, suboptimal growth conditions are a low substrate temperature T_{sub} , and/or no H dilution.

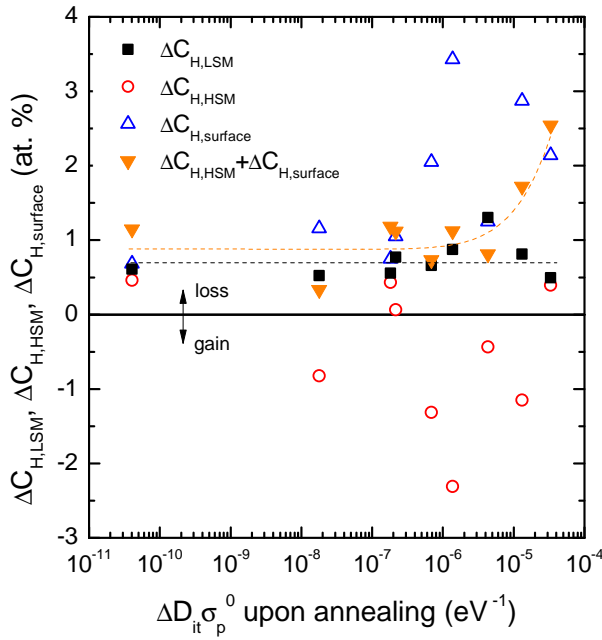


Figure 8.4: Correlation between the variation in H configuration seen in the FTIRS difference spectra and the passivation improvement $\Delta D_{it}\sigma_{p/n}^0$ upon annealing: There is a constant loss of 0.5...1 at.% seen in ΔC_{LSM} , while ΔC_{HSM} and $\Delta C_{H,surface}$ are anticorrelated as a result of the close proximity of the respective modes and the resulting 'cannibalism' in the fitting. Observing the sum of ΔC_{HSM} and $\Delta C_{H,surface}$ (orange triangles) yields a consistent picture: Apart from an increasing loss from the combined HSM+surface SiH₂ mode for the samples with the largest passivation increase, there is no correlation between the changes in the H configuration and the passivation development.

largest D_{it} removal, the H loss is increased.

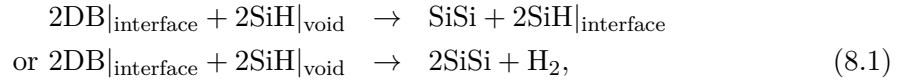
Thus, there is clearly no direct correspondence between changes in the bulk H configuration and the annealing effect seen in the interface defect density. It has to be noted that this result is in direct opposition to the conclusion drawn in Refs. [31, 32]. However, this result does *not* exclude local rearrangements of hydrogen near the interface as only marginal amounts of H would have to be relocated as will be shown in the following section.

8.3.2. Sensitivity of FTIRS

It is interesting to estimate the size of the IR signal which would be caused by a local H relocation involving only the amount of hydrogen actually needed for interface passivation. Until now, the product of D_{it} with the capture cross section for neutral defects $\sigma_{p/n}^0$ was analyzed. To estimate the amount of relocated hydrogen, a specific choice for $\sigma_{p/n}^0$ is necessary. In the literature, the values for $\sigma_{p/n}^0$ range from 10^{-15} cm² [183] or 10^{-16} cm² [173] to as low as 10^{-18} cm² [92]. In order to estimate an upper boundary for the H relocation, $\sigma_{p/n}^0 = 10^{-18}$ cm² will be used here. Then, for the LP150 sample displaying the largest improvement, $\Delta D_{it} = 3.3 \times 10^{13}$ eV⁻¹cm⁻² is found. D_{it} is the prefactor of the Gaussian defect density distribution⁴ assumed in the lifetime fit model [142], which has to be converted into an area density by integrating the Gaussian over the c-Si band gap. This procedure yields a dangling bond removal of $\Delta N_{db} = 1.07 \times 10^{13}$ cm⁻². If

⁴Its functional form is similar to Eq. 3.2 with D_{it} replacing N_d in the respective equation.

one assumes an effective reconstruction/relocation mechanism of the form



the latter equation representing a reconstruction of two Si-Si bonds releasing hydrogen, then the number of removed dangling bonds equals the number of removed a-Si:H HSM-monohydrides. In the FTIRS analysis the hydrogen content N_H^i in a given mode i is connected with its intensity I_i by

$$N_H^i = A_i I_i \quad \text{with } I_i = \int \frac{\alpha_i(\omega)}{\omega} d\omega. \quad (8.2)$$

Here, ω is the frequency in wave numbers, A_i a conversion factor which is proportional to the inverse of the oscillator strength of the mode, and $\alpha_i(\omega)$ the absorption coefficient of the given mode at frequency ω . The integral is performed over a reasonable region hosting the mode [139]. As reconstruction most likely occurs in voids and the respective clustered monohydrides are released with much lower activation energy (cf. the discussion of H effusion in appendix B), only the HSM shall be considered here. The change in the density of clustered SiH can be connected to the respective measured absorption by

$$\Delta I_{\text{HSM}} = \frac{\Delta N_{\text{HSM}}}{A_{2100}}, \quad (8.3)$$

with $A_{2100} = (2.1 \pm 0.2) \times 10^{20} \text{ cm}^{-2}$ [139]. Now ΔN_{HSM} is a volume density, thus

$$\Delta N_{\text{HSM}} = \frac{\Delta \# \text{SiH}}{V}, \quad (8.4)$$

with $\Delta \# \text{SiH}$ being the change in the number of clustered monohydrides. In analogy, for the area density of dangling bonds $\Delta \# \text{DB}$ one finds

$$\Delta N_{\text{db}} = \frac{\Delta \# \text{DB}}{A} \quad \text{with the area } A. \quad (8.5)$$

Thus one expects for the change in the integrated absorption ΔI_{HSM} in the given case:

$$\Delta I_{\text{HSM}} = \frac{\Delta N_{\text{db}}}{A_{2100}} \frac{A}{V} = \frac{\Delta N_{\text{db}}}{A_{2100}} \frac{1}{d} = 2.55 \times 10^{-2} \text{ cm}^{-1}, \quad (8.6)$$

taking into account a total a-Si:H layer thickness of $d \approx 20 \text{ nm}$. The measured HSM signal for the LP150 sample was $I_{\text{HSM}} \approx 63 \text{ cm}^{-1}$, thus the expected change in the LP150 HSM intensity upon annealing is about 4×10^{-4} , or more than three orders of magnitude smaller than the signal, even assuming the smallest capture cross section which corresponds to the maximum number of H atoms to be relocated. It must be noted that the detection of $\Delta I_{\text{HSM}} = 2.55 \times 10^{-2} \text{ cm}^{-1}$ or even considerably less for the samples with smaller D_{it} improvement upon annealing would be beyond the capability of the IR spectrometer, even though the setups used in this thesis provide state-of-the-art resolution. However, there *is* a measurable difference between as-deposited and

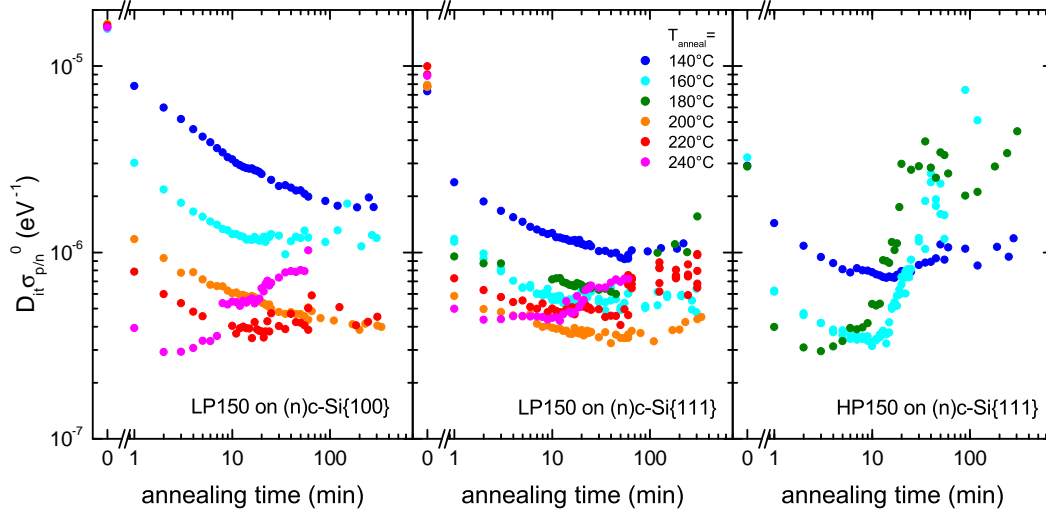


Figure 8.5.: Annealing dynamics of (i)a-Si:H on c-Si with {111} and {100} surface orientation, for different annealing temperatures. While the stretched-exponential behavior often invoked to describe a-Si:H/c-Si annealing transients is observed for the lower annealing temperatures, the higher T_{anneal} lead to a second regime where the passivation deteriorates after reaching a minimum D_{it} value. Generally, the transients are dependent on both (i)a-Si:H and c-Si surface parameters, thus suggesting a complex mechanism.

annealed state (cf. Fig. 8.2) which is about 6% relative for the HSM for LP150, or 150 times larger than the difference needed to explain the annealing effect. From Fig. 8.2 it is indicated that all the samples display a loss in the integrated HSM of about that order of magnitude, thus being significantly larger than the expected relocation signal. Obviously, the small net hydrogen loss upon annealing due to the onset of H effusion mobilizes enough H atoms to easily explain any observed difference in interface defect states. Thus it must be concluded that a detailed analysis by FTIRS of the direct interplay of hydrogen (re)distribution and interface defects is impossible due to the extremely small amount of H actually needed to passivate the interface. In order to learn more about the physical nature of the annealing effect, the dynamics of annealing shall be analyzed in the next section.

8.3.3. Annealing dynamics

The dynamics of interface defect annealing have been studied in several previous works [54, 58, 166, 189]. Most of the studies analyzed only a small number of samples, and none of them incorporated a microscopic analysis of the involved layers. Further, only indirect empirical parameters such as the effective lifetime τ_{eff} or even the open-circuit voltage of solar cell devices V_{oc} were monitored during the annealing. Thus it is worthwhile to revisit the analysis of annealing dynamics making use of the physical parameter $\Delta D_{\text{it}} \sigma_{p/n}^0$ as extracted from PCD fits and to complement the picture with the microscopic information about a-Si:H layers and a-Si:H/c-Si heterojunction obtained in the previous chapters.

Figure 8.5 shows annealing results of 10 nm thick (i)a-Si:H layers deposited at two differ-

ent parameter sets⁵ on both sides of DSP-(n)c-Si substrates with different crystal orientation. Annealing was done on a hotplate under nitrogen flow at different temperatures. It is obvious that the annealing dynamics depend on the (i)a-Si:H deposition conditions, the annealing temperature and the substrate orientation, rendering the behavior rather complex. Additionally, while the low- T_{anneal} transients can be well described with a stretched exponential as was often invoked in previous studies [58, 189] and linked to dispersive hydrogen motion in a-Si:H [115], the transients taken at higher T_{anneal} show a minimum in D_{it} followed by an *increase* instead of a gradual saturation towards a fixed value. The appearance of this second 'degradation' regime in the annealing dynamics seems to proceed smoothly with increasing T_{anneal} , but is dependent on at least the (i)a-Si:H deposition conditions. A possible dependence on the crystal orientation is hard to derive from the limited amount of data presented here.

This observation is pointing towards a competition of two effects: The first of those leads to a decrease in D_{it} and perceptibly takes place already at low T_{anneal} , however with a 'time constant' which decreases with T_{anneal} . The second leads to an increase of D_{it} and seems to yield notable effects only for higher T_{anneal} , with the onset- T_{anneal} depending markedly on the (i)a-Si:H deposition conditions. Possible candidates for the first effect would be firstly hydrogen release from a-Si:H, e.g. originating from the microscopic voids, and adsorption at unpassivated c-Si surface dangling bonds, and secondly thermally activated silicon network reconstruction e.g. at voids touching the heterointerface. The deterioration effect could further stem from thermal desorption of hydrogen from Si-H bonds at the heterointerface.

Indeed there were attempts in the literature aiming at a description of a-Si:H/c-Si heterojunction annealing similar to hydrogen adsorption and diffusion processes on c-Si surfaces [165]. In the light of the rather feature-less annealing curves and the high number of free parameters which would have to be invoked to describe both the D_{it} removal and deterioration upon annealing, it is restrained from attempting to fit the annealing dynamics here. Further it is obvious that the fit parameters would depend on both a-Si:H film (deposition conditions) and surface properties (orientation), which would prevent identifying a simple and unifying origin of the trends visible in Fig. 8.5 from the analysis of the dynamics alone.

Indeed, the issue is even more complicated, as it will be shown next that not only the parameters of the heterostructure (a-Si:H deposition, c-Si orientation) determine the annealing transient at a given annealing temperature, but also the annealing method.

8.3.4. Hotplate- versus microwave annealing

Experimental approach

From a technological point of view, annealing on a hotplate is disadvantageous: Direct and full area contact of the sample with a hot surface may introduce contamination, which is particularly negative when successive deposition processes have to be performed afterwards, which is the case when low- T_{sub} (i)a-Si:H layers need annealing before doped

⁵Here, the parameter sets LP150 and HP150 were chosen as they show the most pronounced D_{it} decrease upon annealing.

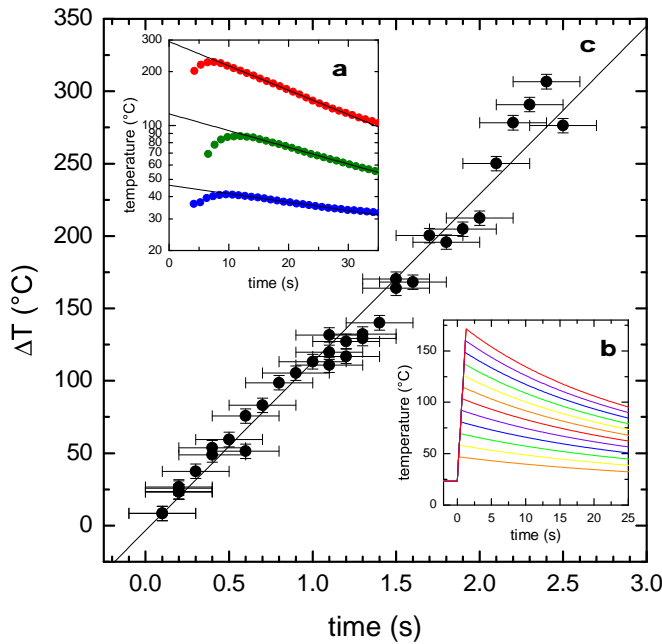


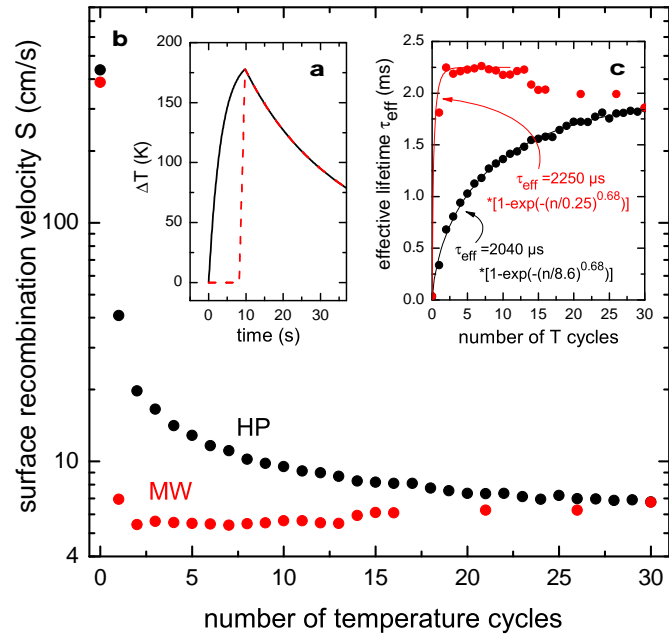
Figure 8.6: Determination of microwave heating characteristics for an (i)a-Si:H/(n)c-Si prototype sample. (a) Temperature decay curves after MW heating are fitted with a mono-exponential decay law. (b) The manifold of fitted decays for several heating times are then used to estimate the temperatures at the end of the heating process, which are shown over MW exposure time in panel (c).

a-Si:H deposition. Additionally, picking up the c-Si sample while it is in full contact with the hotplate would be a challenge in an automated handling system. Thus it is highly desirable to implement a contactless annealing method.

In industrial annealing, inductive heating is very common for the annealing of cast iron or other conductive solids, but also microwave (MW) exposure is widely applied. Due to the flat nature of the c-Si samples, the geometrical conditions for generating eddy currents by induction are not optimal and a specially tailored coil would be necessary. Microwave cavities on the other hand are widespread in the form of microwave ovens for cooking, therefore MW annealing can be easily explored.

To this end, the samples were exposed to microwaves in a conventional MW oven with a nominal output power of 700 W of 2.45 GHz magnetron-generated MW radiation. The microwave was operated at 700 W and the power absorbed in the sample was controlled by inserting a defined quantity of water (200 ml) as additional absorber inside the cavity. A general problem of employing a MW cavity for heating is the determination and control of the sample temperature. As any kind of cable introduced into the MW cavity acts as an antenna producing hazardous MW leaks, other methods for temperature measurements had to be explored. Pyrometers based on the detection of IR radiation are not accurate enough in the temperature range of interest. Thus, an indirect method had to be employed: A standard annealing recipe was defined at the beginning, which was temperature-calibrated once. All parameters influencing the microwave absorbance (quantity and position of water in the microwave; size, position and nature of the sample, thickness of the a-Si:H layer) were kept constant. Using a dummy sample, a heating curve was determined by exposing the sample to MW radiation for defined periods of time and measuring the temperature decay of the sample immediately after turning off

Figure 8.7: Passivation transients of nominally identical samples being pulse-annealed in the microwave and on the hotplate with similar temperature profiles. (a) T profiles for a 10 s contact with the hotplate at 210 °C (black line) and for a 1.6 s MW exposure (red dashed line). (b) Comparison of S upon successive pulse annealing steps with T profiles shown in (a) on the HP (black) and in the MW (red). (c) Linear plot of τ_{eff} with stretched-exponential fits, indicating a much reduced time constant for MW annealing.



the radiation by contact of the sample with a thermocouple⁶. Then, an exponential decay law was fitted to every $T(t)$ curve to estimate the maximum temperature reached at the moment of MW switch-off (Fig. 8.6a). From the manifold of fitted exponential decays (Fig. 8.6b) it is now possible to deduce the dependence of temperature increase on microwave exposure time (Fig. 8.6c), which showed to be linear to a good approximation in the T range of interest. For the particular setup and sample type the heating coefficient was 114.0 ± 1.6 K/s, which demonstrates the efficiency of MW-heating as compared to hotplate annealing.

Comparison of hotplate and microwave

In the following, hotplate and microwave heating shall be compared with respect to annealing efficiency. The extremely high heating coefficient of the MW precludes a static annealing regime. Instead, the sample must be subjected to short pulses which correspond to a certain peak temperature as determined with the method sketched above. Thus, an annealing cycle consists of a short heating period ($t_{\text{heat}} = 1 \dots 2.5$ s) followed by a much longer relaxation period ($t_{\text{relax}} = 1 \dots 2$ min) to allow for the sample to reach room temperature again.

For the comparison, DSP (n)c-Si{111} samples with 10 nm symmetrical (i)a-Si:H passivation layers were again used, employing the (i)a-Si:H parameter set which shows the most pronounced annealing effect (LP150). In Fig. 8.5 it was found that hotplate annealing of LP150 layers on this substrate type leads to the best results for $T_{\text{anneal}} = 200^\circ\text{C}$. To enable a direct comparison between the microwave and the hotplate, two nominally identical samples have to be subjected to temperature profiles being as closely similar

⁶To this end, a miniature PT-100 thermocouple was used, possessing a minimum heat capacity itself.

as possible. A sample put on the hotplate (kept at $T = 210^\circ\text{C}$) for 10s and then removed is heated and cooled according to the profile depicted in Fig. 8.7a, reaching a peak temperature of $T_{\text{anneal}} = 200^\circ\text{C}$. The microwave exposure time needed to yield the *same* peak temperature was 1.6 s (T profile shown in Fig. 8.7b). Note that the time during which the sample resides near the peak temperature is still considerably longer on the hotplate due to less efficient heating.

Fig. 8.7c shows the resulting evolution of the surface recombination velocity S as calculated by eq. 2.34 assuming an infinite τ_{SRH} for the two samples after being exposed to an increasing number of temperature cycles on the hotplate (HP, black data points) and in the microwave (MW, red data points). It is obvious that the development upon MW annealing is much faster: After only 2 cycles, the saturation value of surface passivation is reached, while on the hotplate more than 20 cycles are needed to reach similar S . Note that both annealing transients can be fitted with a stretched exponential in the τ_{eff} domain, as invoked before [58, 189], with a much smaller time constant for the MW anneal⁷. Thus it is demonstrated that MW annealing proceeds with enhanced efficiency as compared to HP annealing. In the following, possible reasons shall be briefly discussed.

Tentative explanation

It is instructive to review the mechanism of microwave absorption in a-Si:H. Generally, MW absorption in a material can be due to 'conduction loss' and 'polarization loss'. The first mechanism is caused by acceleration of free charge carriers which are subject to electrical resistance leading to dissipation of heat in the material. The second mechanism is due to the inability of the electrical polarization in the material imposed by the electric field vector of the incident MW to follow the rapid \vec{E} field reversal. The significance of this mechanism depends on the polarizability of the material and the abundance of polar bonds. Thus, the absolute value of absorption and the proportion of the two mechanisms are dependent on MW frequency and material parameters [160]. It is to be expected that in a-Si:H the high density of polar Si-H bonds contributes significantly to microwave absorption as compared to c-Si. Consistently, a MW heating coefficient reduced by 10...20% is measured for the 'naked' c-Si substrate as compared to the a-Si:H/c-Si samples. In the light of the extremely small layer thickness added by the a-Si:H (a relative change of 6×10^{-5} in thickness) this signifies a strongly enhanced MW absorption in the thin a-Si:H layer⁸. A common explanation of the annealing effect is the saturation of c-Si surface DBs by mobile hydrogen [32], as mentioned above. In this context it must be highlighted that MW absorption mechanism in a-Si:H involves exactly the type of bonds that need to be broken in order to mobilize bound hydrogen. Although there can be no *resonant* absorption process involved — with the lowest-energy Si-H vibrational modes having 3...4 orders of magnitude higher frequencies than the MW excitation — it is conceivable that a non-thermal contribution to the vibrational energy

⁷Note in addition that it appears that the deterioration of the passivation seen as a second regime in Fig. 8.5 is also present here, setting in for the MW annealing for >10 annealing pulses.

⁸Note that the enhanced absorption coefficient may also partly be due to the much higher resistivity of (i)a-Si:H as compared to the (n)c-Si substrate. However, the polar Si-H bonds are certainly involved in the absorption process.

of the Si-H bond is imposed by the intense electric field, effectively lowering the barrier for bond breaking.

In conclusion, the results on MW annealing are consistent with the prevalent picture of H mobilization to explain the annealing effect.

8.3.5. Microscopic preconditions for the annealing effect

As mentioned, the involvement of hydrogen motion is commonly accepted in the literature concerning the annealing effect at the a-Si:H/c-Si heterojunction [32, 54, 165, 189]. In this section it was shown that in contrast to the results obtained by other groups, which mainly investigated annealing at high temperatures and over longer times, no systematic connection between the passivation improvement upon annealing and changes in the H content or -microstructure as determined by bulk-integrating methods were found. It was shown however, that the baseline bulk H relocation occurring around 200°C in all samples due to the onset of H effusion suffices to explain the observed lifetime improvement. Note that the passivation phenomenology would also be compatible with a (partial) impact of local network reconstruction, as e.g. the collapse of voids touching the heterointerface. Also in this case, H relocation is involved as the voids are decorated with H as seen above.

Analysis of SIMS difference spectra

To explore possible local structural changes upon annealing and obtain complementary information about the H relocation, SIMS difference spectra were taken for the three different (i)a-Si:H layers which showed the largest D_{it} improvement upon annealing (deposition temperature 150°C). The samples were pieces of the same a-Si:D-coated wafers which were analyzed in the as-deposited state (cf. section 6.5), and had been annealed for 20' at 200°C. All of those samples showed a slight loss in bulk H content. For LP150 the loss fraction amounted to 7...8%, being comparable to the number calculated above from FTIRS data after 5' annealing, while the other two samples showed a slightly larger loss, consistent with the longer annealing time. No special features were found at or near the heterointerface in the ^1H , ^2H or combined spectra.

Indeed, this observation can be readily understood from an estimation of the sensitivity: Mobilizing 10^{13} cm^{-2} H atoms within a layer with roughly 10^{22} cm^{-3} hydrogen concentration from an assumed 'action zone' of 1 nm adjacent to the interface (being about the lateral minimum resolution of the SIMS measurement) would reduce the H concentration in that zone by a factor of only 0.01 which is clearly beyond the resolution on the concentration axis if occurring as a change superimposed on a 10^{22} cm^{-3} signal. Thus, the only measurable differences upon annealing concern the baseline H loss, which was also observed with FTIRS.

One alternative explanation for the annealing effect concerned structural changes, such as network reconstruction at voids. If such effects were taking place at the heterointerface, a variation in the ^{29}Si matrix peak could be expected, which however was absent as well. Thus, no indication for a structural change (either concerning the H content or the Si network) upon annealing was found in the analysis of the SIMS spectra, again

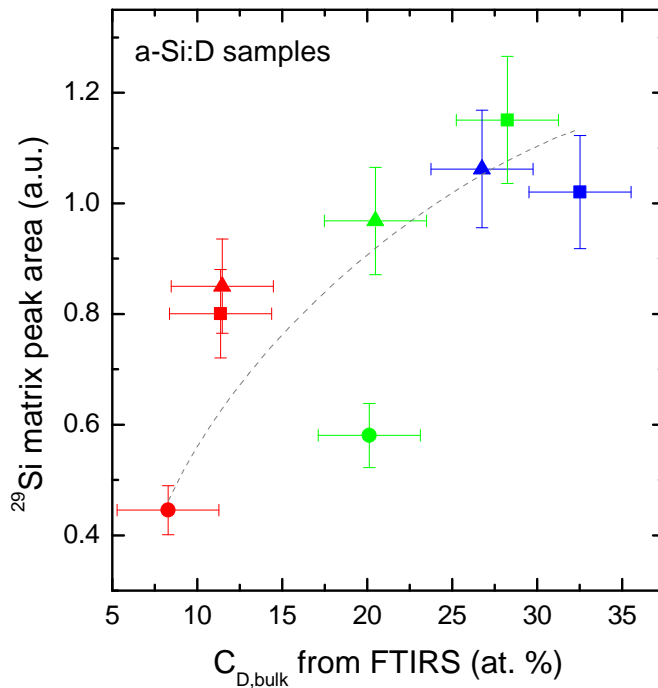


Figure 8.8: Correlation of the integrated area under the ^{29}Si matrix peak from the SIMS spectra of a-Si:D samples (being a measure for the structural discontinuity at the heterointerface) with the bulk hydrogen content of a-Si:D samples as measured with FTIRS. The correlation, even though not very pronounced, suggests the coexistence of high bulk hydrogen quantities and poor structural properties at the interface. This may explain the apparent correlation between as-deposited passivation and bulk H content as a collateral effect of suboptimal a-Si:H growth conditions, which is the underlying cause for *both* effects: Void- and thus hydrogen-rich a-Si:H bulk and poor interfacial structure resulting in a high as-deposited D_{it} .

highlighting that the effects leading to the pronounced D_{it} decrease upon annealing are extremely subtle from a structural point of view and evade detection by the available methods.

Summary of annealing phenomenology

Thus, the results on the annealing effect can be summarized as follows: While the a-Si:H bulk properties and H distribution stay approximately constant upon annealing within detection limits for *all* the samples apart from a slight net loss of H which involves about the same number of H atoms for *all* the samples, the interface defect density is reduced dramatically only for *some* samples — depending on the (i)a-Si:H deposition conditions — leading to similar annealed D_{it} for *all* the samples. Thus, there cannot be a direct connection between as-deposited D_{it} and the *bulk* properties. Presumably there are only local structural conditions determining the as-deposited D_{it} whose changes upon annealing cannot be detected with the methods at hand. This would mean that the puzzling and clear correlation between the annealing potential and the bulk hydrogen content as seen in Fig. 8.1 is a coincidence. This puzzle can be solved based on the SIMS analysis, as will be shown next.

8.4. The as-deposited state of the heterointerface

In section 6.5.5 it was argued that the PECVD growth conditions analyzed here lead to large differences in the quality of the initial growth: Fig. 6.21 revealed that of the

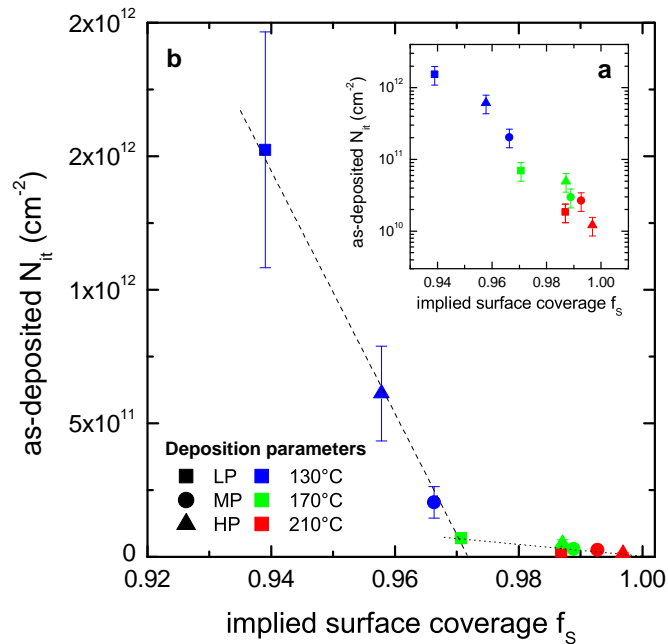


Figure 8.9: As-deposited interface defect density N_{it} vs. implied surface coverage f_s of c-Si surface by a-Si:H, in a semilogarithmic (a) and linear plot (b). f_s results if one assumes that the voids in (i)a-Si:H causing the loss in mass density are touching the heterointerface, thus leaving c-Si surface fractions uncovered. The linear regime visible for the low- T_{sub} samples indeed implies a c-Si surface fraction not covered by a-Si:H, as discussed in the text.

initial Si-H surface coverage prior to deposition, very different fractions of hydrogen persist in the a-Si:H layers⁹, with the layers of higher structural quality — deposited mostly at higher temperatures — having lower remaining ^1H fractions. There was a correlation between the integrated residual ^1H content and the ^{29}Si matrix peak, linking the efficiency of ^1H elimination during growth to the resulting structural quality of the interface region. Fig. 8.8 indicates that there is as well a correlation between the bulk ^2H concentration measured by FTIRS and the structural discontinuity at the heterointerface as seen in the ^{29}Si matrix peak. Note that this plot could be redrawn with any measure for the bulk hydrogen or deuterium content on the ordinate (either measured by SIMS or FTIRS): The correlation is universal because the different measures for the D/H content are exchangeable as was shown above. Thus it is suggested that a high bulk hydrogen content and a poor interfacial structure have the same origin: Non-ideal PECVD growth conditions. Obviously, this is the underlying cause for the correlation between as-deposited D_{it} , being ruled by the local interfacial structure, and the bulk H content. Thus, this correlation therefore does not imply a causality between these two observations but merely a common origin.

8.4.1. Limits of the as-deposited interface defect density

Having identified locally poor structural conditions as the most probable cause for the high D_{it} of the samples deposited at low temperatures, one can take further steps towards identifying structural features possibly causing the high D_{it} . The low- T_{sub} samples were found to possess a reduced mass density, implying the presence of voids in the material. In a simple attempt to relate the increasing void fraction with D_{it} one could tentatively

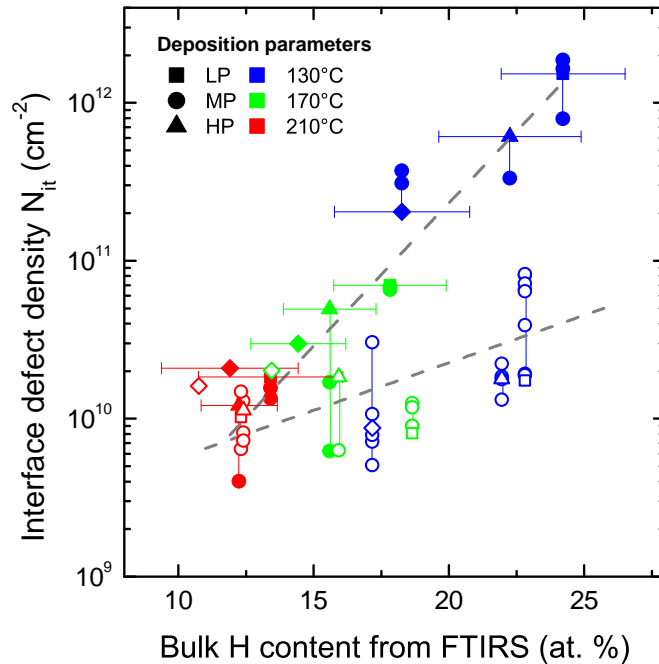
⁹Note that the difference amounted to more than a factor of 10.

assume a homogeneous structure of the a-Si:H layer, thus neglecting the details of the initial growth process: If the voids in a-Si:H are touching the a-Si:H/c-Si heterointerface this will necessarily result in an 'unpassivated' c-Si surface fraction in that sense that the Si-Si network is interrupted at these area fractions. Then, a void fraction would correspond to an 'implied uncovered c-Si surface fraction', thought to result from the contact area between a void and the c-Si surface. Note however that there may be Si-H bonds which take over the passivating effect, so not all the c-Si surface bonds which are not attached to another Si-atom during deposition are necessarily carrying defects. If such a picture was true, there would result a linear relationship between the interface defect density and the 'implied surface coverage' as calculated from the mass density. At the surface or interface of a phase-mixed medium, the bulk volume fractions of the medium's constituents are transferred to identical area fractions at this interface. Thus, to calculate the implied surface coverage in the case of void-containing a-Si:H is straightforward as it directly results from the mass deficiency as $1 - f_m = \rho / \rho_{\text{a-Si:H}}$. The density of interface defects N_{it} can readily be determined from fits of PCD measurements which have yielded $D_{\text{it}} \sigma_{p/n}^0$: By choosing a capture cross section $\sigma_{p/n}^0$, D_{it} is obtained. D_{it} now defines the Gaussian distribution of interface defects, which is integrated across the c-Si band gap to yield N_{it} . Out of the large range of $\sigma_{p/n}^0$ featured in the literature, the newer values tend to be of order $1 \dots 5 \times 10^{-17} \text{ cm}^2$ [158]. Here and in the following, the value of $\sigma_{p/n}^0 = 1 \times 10^{-17} \text{ cm}^2$ will be used. This particular choice will be underpinned later.

It is instructive to plot the density of interface defects N_{it} versus the c-Si surface fraction covered by a-Si:H which is implied by the mass density (Fig. 8.9). Panel (a) shows a semilogarithmic picture of the correlation, showing no particular features besides the expected trend of N_{it} versus $1 - f_S$. More interesting is the plot in the linear domain (Fig. 8.9b), where two regimes become apparent: For the more compact films ($f_m < 0.02$), N_{it} increases only slowly with the void fraction, which negates the applicability of the simple 'surface coverage' picture for those films. For the less dense films ($f_m > 0.02$) however, N_{it} linearly increases with f_S as would be expected for a growing unpassivated surface fraction.

The surface atom density on c-Si{111}, representing the geometrical limit for the c-Si{111} surface defect density assuming one DB per Si atom, amounts to $7.8 \times 10^{14} \text{ cm}^{-2}$, which allows to calculate the efficiency of the passivation by Si-H for the uncovered surface fractions. The dashed line corresponds to every 20th surface atom in the area fractions uncovered by a-Si:H carrying a dangling bond. Thus it is shown that for the less dense films, the trend in Fig. 8.9a can be explained with small parts of the c-Si surface being uncovered by the (i)a-Si:H layer due to an increasing void fraction, resulting from suboptimal growth conditions. The differences in N_{it} for the films with higher quality are very subtle (Fig. 8.9a) and possibly result from the local Si-Si network structure at the interface, or differences in the local H distribution [78]. Due to the differences in the N_{it} values being about the order of the error bars, no analysis shall be attempted here. Instead, in the next section, the properties of the annealed heterointerface shall be elucidated with the goal to identify a fundamental parameter determining the final state of the annealing process. Thereby, the best passivation which is possible to be

Figure 8.10: Correlation of interface defect density N_{it} with (i)a-Si:H bulk hydrogen content in the as-deposited state of layers with 10 nm thickness and after annealing for 5' at 200°C. The data shown already in Fig. 8.1 is complemented by additional lifetime samples (circles), which were assumed to have the same H content as the FTIRS samples deposited under identical conditions. Error bars for the H content are shown only once for each layer type for clarity, while the reproducibility of lifetime results can be assessed from the vertical scatter of the PCD results.



achieved with a given a-Si:H layer can be estimated.

8.5. Properties of the equilibrated heterointerface

8.5.1. The annealed interface defect density

The comparison of H bonding configuration and $D_{it}\sigma_{p/n}^0$ in Fig. 8.1 showed almost vanishing differences in the passivation quality after annealing between the different (i)a-Si:H layers (within experimental errors). This result could be anticipated from Fig. 4.3 where the τ_{eff} values of the respective annealed samples were shown to be very similar. In the light of the subtle differences in annealed N_{it} it is important to obtain better statistics, thus the lifetime data is complemented with PCD measurements on additional nominally identical samples of each type for the following analysis. Taking these data into account and redrawing the correlation between total bulk H content and N_{it} yields figure 8.10, corresponding to the first panel from Fig. 8.1 with exchanged axes. It is obvious that indeed there is a remaining slope of N_{it} versus the a-Si:H hydrogen content *after* annealing when taking statistics over several samples. The dashed lines are separate exponential fits to the as-deposited and annealed data.

In the previous sections it was reasoned that the as-deposited N_{it} is most likely being governed by *local* properties of the heterointerface which must significantly differ from the a-Si:H bulk properties in the as-deposited state. This is the only logical explanation for the large variation in N_{it} upon annealing, which is *not* accompanied by measurable changes in the a-Si:H bulk properties, implying that only the particular local state of the interface is altered. Thermodynamics would suggest a final state of the interface which is at least closer to the state of the adjacent bulk than the initial state, due to equi-

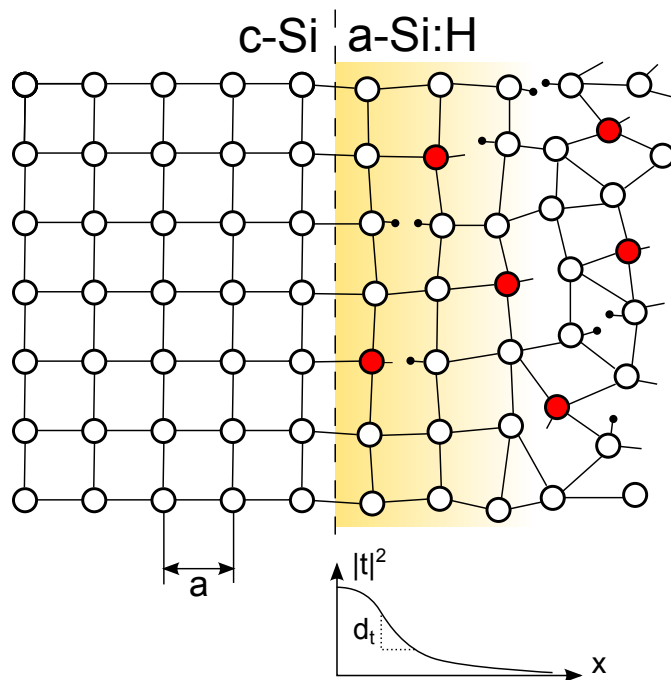


Figure 8.11: Schematic of the a-Si:H/c-Si heterointerface illustrating the gradual loss of long-range order within the first three monolayers when crossing from c-Si into the a-Si:H. Through tunneling processes with exponentially decaying probability, thus accessing a finite range (yellow area), charge carriers from the c-Si can reach defect states in the a-Si:H (red) resulting in recombination. Thus, the a-Si:H bulk defect density is coupled to the c-Si hosting the photogenerated charge carrier through those tunneling processes, which determines the a-Si:H/c-Si interface recombination properties as will be argued in the text.

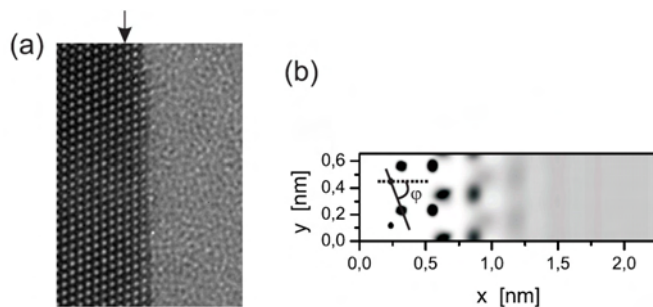


Figure 8.12: HR-TEM picture of the a-Si:H/c-Si heterointerface underlining the schematic picture from Fig. 8.11. (a) TEM picture of an a-Si:H/c-Si sample from HZB, the arrow marks the position of the last row of c-Si atoms as obtained by an iterative image simulation process [259]. (b) Two-dimensional atomic distribution function of the a-Si:H adjacent to the interface as obtained by the image simulation.

bration processes. Starting from this assumption it is instructive to ask which interface defect densities could be expected in the case of an 'ideal' interface in that sense that it does not possess local properties but merely represents a window between the a-Si:H bulk and the c-Si absorber hosting the excess charge carriers. This would correspond to either a perfect as-deposited state — possibly being realized with optimal deposition conditions —, or the state after a complete anneal when all the deviations of the interfacial properties from the bulk state were lifted by thermally activated equilibration processes with the adjacent bulk. This picture shall be explored in the following.

It is intuitive to assume that in the case of an 'ideal' interface without special attributes, the defect density seen by the excess charge carriers in the c-Si will be connected to the bulk defect density in the amorphous silicon. There are two mechanisms through which an interaction between a-Si:H defects and c-Si excess carriers is possible. Firstly, there will be some defects located right at the interface between crystalline and amorphous silicon, which can be directly accessed from the c-Si. Secondly, defects in the vicinity of

the heterointerface may be reached from the c-Si through tunneling processes within a tunneling length. The fact that even in an amorphous network the defects are not freely distributed but located at 'lattice' sites has to be taken into account as the c-Si lattice is extended into the a-Si:H at least approximately for a few monolayers as the short-range order of c-Si is preserved in a-Si:H. This can indeed be directly confirmed from high-resolution transmission electron microscopy (HR-TEM) images. An a-Si:H/c-Si sample from the same deposition setup as used throughout this thesis has been measured and analyzed in detail by Thiel [259]. The results of the image simulation are shown in Fig. 8.12 confirming the schematic from Fig. 8.11.

Thus, in the immediate vicinity of the heterointerface the defects will be located on lattice planes before the structural information is lost deeper inside the a-Si:H. A schematic picture of the interface region illustrating these aspects is shown in Fig. 8.11. A crucial question in the context of a-Si:H/c-Si heterojunctions now concerns the way of mapping a given a-Si:H bulk defect density, which is strictly constant over the depth axis in this picture of an 'ideal' interface, onto the two-dimensional interface. The best choice concerning the parametrization of this connection depends on the relative values of the four parameters lattice constant a , tunneling length d_t , width of a-Si:H/c-Si transition zone and a-Si:H bulk defect density N_d .

First, the tunneling length shall be estimated. In the framework of one-dimensional quantum mechanics and using a transfer matrix formalism, the tunneling probability $|t|^2$ of an electron with effective mass m^* and energy E through a square potential with height $V > E$ is found to be [21]

$$|t|^2 = \frac{1}{1 + \frac{V^2 \sinh^2 \alpha x}{4E(V-E)}} \quad \text{with } \alpha = \frac{1}{\hbar} \sqrt{2m^*(V-E)}. \quad (8.7)$$

Here, in order to get a rough estimate for the effective tunneling length, the energy of the electron is taken to be the kinetic energy from its thermal velocity in the c-Si at 300 K $v_{\text{th}} = 2.3 \times 10^5$ m/s. As both electrons and holes have to reach the amorphous bulk in order to recombine at a-Si:H defects, the smaller of both tunneling ranges will dominate the recombination process. As the valence band offset is larger than the conduction band offset by a factor of 2...3, this barrier and thus the hole tunneling process will be the limiting one, and therefore V is chosen such that the energy barrier $V - E$ is equal to the valence band offset (≈ 0.45 eV). For amorphous silicon, the effective tunneling masses of electrons and holes are usually assumed to be identical [8, 79], and range between $0.075 \dots 0.25m_e$. Here the measured value of $0.09m_e$ reported by Shannon *et al.* [221] will be used. In this picture, the effective interface defect density N_{it} can be calculated from the a-Si:H bulk defect density N_d as follows:

$$N_{\text{it}} = \int_{x=0}^{\infty} N_d |t(x)|^2 dx = N_d \int_{x=0}^{\infty} |t(x)|^2 = N_d d_t, \quad (8.8)$$

where d_t is found to be 2.7 nm from integration over Eq. 8.7. As the lattice constant a is 0.356 nm and thus smaller than d_t by a factor of 5, the first 2...3 monolayers where the lattice information is still approximately preserved make up only a small part of the sampled volume, thus the defects can be treated as arbitrarily distributed in space

and the simple integration approach reflected in equation 8.8 is justified. Additionally, the typical defect densities in a-Si:H are of order 10^{16} cm^{-3} and therefore only every 5×10^6 th lattice site is occupied by a defect, which further reduces the significance of a (pseudo)lattice extending into the a-Si:H. Thus it seems reasonable to assume the tunneling length as the significant length scale in the problem and to treat the defects as randomly distributed in a-Si:H, leading to $N_{\text{it}} = N_d d_t$ with $d_t = 2.7 \text{ nm}$.

N_{it} is obtained from fits of PCD data as described above. The bulk defect density N_d in the ultrathin layers on the other hand cannot be directly measured (cf. section 6.4.2), therefore other parameters must be found which allow to extract a reasonable estimate of N_d to be compared to the interface defect density N_{it} governing the effective lifetime. There is no straightforward connection between the a-Si:H hydrogen content and the defect density¹⁰. A much better indicator for N_d is the Urbach energy, or valence band tail slope, which is connected to N_d through the defect equilibration processes inherent to a-Si:H (cf. section 2.1.3). Thus, E_{0V} — which can be accurately measured with CFSYS at an information depth comparable to the layer thickness, thus being representative of the 'bulk' of the thin layer — can be taken as a direct measure for N_d in the annealed (i)a-Si:H layers as was shown in extensive studies on thick a-Si:H layers [249]. Consistent with intuition, the Urbach energy does not change within experimental errors upon annealing for short times at 200°C , which was verified by annealing a few selected samples *in-situ* for 20' in the PES setup (data shown in Fig. 6.9). Therefore, E_{0V} is assumed to be constant upon annealing for all the samples. In Fig. 8.13, the interface defect density N_{it} is shown over the E_{0V} values measured in the as-deposited state. There is a weak correlation of the as-deposited N_{it} with the Urbach energy, which is consistent as both E_{0V} and the as-deposited N_{it} are correlated with the hydrogen content (trends shown in Figs. 6.9 & 8.1). After annealing, N_{it} is reduced and a slight slope versus E_{0V} again remains — similar to the picture of N_{it} versus C_H as discussed above — while E_{0V} stays constant.

In the literature, there is extensive data on the correlation between the a-Si:H bulk defect density and the Urbach energy [249]. In Fig. 8.13, a representative set of bulk defect density data $N_d(E_{0V})$ from Ref. [249] is included, plotted against the right ordinate. Using the model for the probing of bulk defects via tunneling as sketched above, one can then compare the as-deposited and annealed interface N_{it} of the (i)a-Si:H/(n)c-Si samples with equilibrium bulk defect densities of thick a-Si:H films, by scaling the right axis relative to the left axis such that $N_{\text{it}} = N_d d_t$ is fulfilled. Doing so in Fig. 8.13, a good agreement with the bulk defect data is found for the samples deposited at 210°C , i.e. for the samples which show only small changes in N_{it} upon annealing. The samples deposited at 170°C and more clearly 130°C strongly deviate from the bulk a-Si:H data in the as-deposited state while *all* annealed samples are consistent with the bulk a-Si:H data trend, including the slight increase of N_{it} with the Urbach energy. The dashed lines in the figure denote exponential fits of as-deposited and annealed N_{it} values.

¹⁰As discussed in chapter 2, the hydrogen in its dispersed phase is in fact responsible for saturating dangling bonds at very low C_H but tends to increase the defect density again when being integrated in its clustered form for higher C_H . Thus, the interplay of defects and hydrogen is subtle in the range of C_H covered in the present samples.

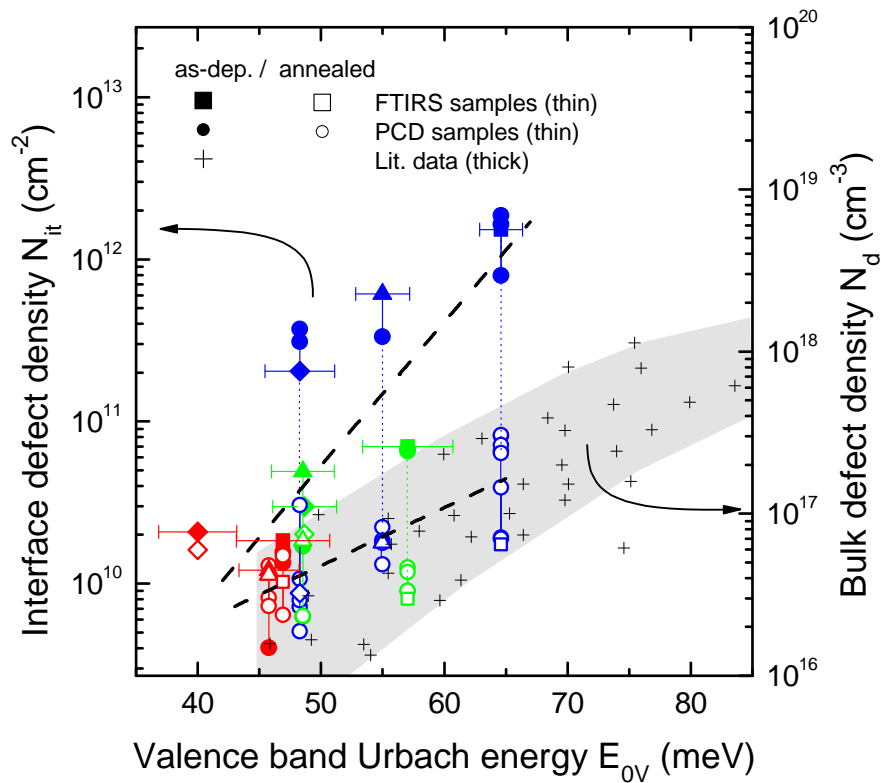


Figure 8.13.: Interface defect density N_{it} in the as-deposited and annealed state versus Urbach energy E_{0V} of the (i)a-Si:H passivation layer. The right axis is scaled such that $N_{it} = N_d d_t$ with $d_t = 2.7$ nm, which allows to map bulk defect densities onto the interface, i.e. to compare a quasi- N_{it} from bulk defect data of thick a-Si:H films [249] with the PCD data of the thin (i)a-Si:H layers. Large symbols: FTIRS samples, small circles: additional PCD samples nominally identical to FTIRS samples. The correspondence of the annealed N_{it} values with the effective interface defect densities expected from the a-Si:H bulk suggests that tunneling and successive recombination leads to the heterointerface being ruled by the properties of the a-Si:H bulk.

8.5.2. Intermediate discussion

The behavior seen in Fig. 8.13 can be interpreted as an equilibration of the defect density at the heterointerface with that of the a-Si:H bulk upon annealing. Obviously, the low- T_{sub} samples are far away from the equilibrium N_{it} in the as-deposited state, supposedly due to microvoids leaving part of the c-Si surface unpassivated and/or locally poor structural conditions leading to increased defect densities. Upon the short low- T annealing step, no bulk a-Si:H reconfiguration takes place — neither E_{0V} nor the H bonding change significantly —, but the heterointerface equilibrates with the a-Si:H bulk, presumably by short-range H diffusion and/or local network reconstruction. For the low- T_{sub} samples that have a specifically poor interface region as probed by SIMS and an as-deposited N_{it} rising linearly with the void volume, thus suggesting parts of the c-Si surface being touched by macroscopic voids as shown above, a partial reconstruction of the network at the interface is likely to happen: From the analysis in chapter 7 it

follows that such a silicon network is highly strained, particularly around the large voids, rendering reconstruction processes energetically favorable. Consistently it was found in previous studies that such reconstruction effects even start around 200 °C [16] if the network quality is poor. Thus, equilibration of the Si network and local H redistribution during annealing lead to a final state compatible with the a-Si:H bulk defect densities. The lower boundary for the annealed interface defect density is therefore given by the a-Si:H bulk quality, for which the Urbach energy is an important and fundamental parameter.

The conclusion drawn here is logical, consistent with a large amount of previous data and allows to explain the annealing behavior from fundamental properties of a-Si:H. Thus it is compelling, but it has to be noted that it is not *compulsory* as shall be outlined in the following. There are two parameters which are to a large extent indefinite and thus allow to tune the picture drawn above. The first is the effective tunneling mass and the second and more important quantity is the capture cross section of neutral defects $\sigma_{p/n}^0$. As mentioned above, its value ranges from $10^{-15} \dots 10^{-18} \text{ cm}^2$ in the literature and reliable measurements are difficult. While for *relative* comparisons of D_{it} or N_{it} values from different samples its value is not important, an *absolute* determination of N_{it} is necessary here. Obviously, the value of $\sigma_{p/n}^0 = 10^{-17} \text{ cm}^2$ chosen here allows to draw this conclusion, but other values are still possible. Of course, this argument could also be turned around and the analysis presented above could be taken as a basis to fix the value of $\sigma_{p/n}^0$. The effective tunneling mass m^* is only insecure within a factor of 3, which has less considerable impact than $\sigma_{p/n}^0$.

The appealing aspect of the interpretation presented here is its simplicity. Still, the as-deposited N_{it} of the low- T_{sub} samples are not explained and invoking a local non-equilibrium state of the interface surely is somewhat arbitrary, but it is supported at least by the increasing inhomogeneity seen in the SIMS spectra. The strength of the model lies its direct derivation of the N_{it} values for the high- T_{sub} layers and the annealed samples, without having to invoke more than the a-Si:H bulk properties. There is plenty of indications for charge carriers from the c-Si tunneling into the a-Si:H, be it from transport (chapter 5) or SPV measurements [138]. Thus it seems consistent to invoke this mechanism for the recombination properties as well, and doing so it is logical that the a-Si:H bulk defects are limiting N_{it} in the ideal case.

In the following section, the consequences of the microscopic picture of the a-Si:H/c-Si heterointerface developed here shall be explored. Particularly, it shall be attempted to answer the last remaining leitmotif question — asking for the cause of the passivation degradation upon deposition of doped a-Si:H top layers — based on the model presented above.

8.6. Impact of a-Si:H chemical potential on the passivation

8.6.1. Phenomenology and possible origins

An inherent feature of c-Si surface passivation by (i)a-Si:H seems to be the deterioration of passivation upon deposition of a doped top layer, most pronouncedly for (p/i)a-Si:H stacks. Based on H effusion experiments showing a more pronounced effusion peak for

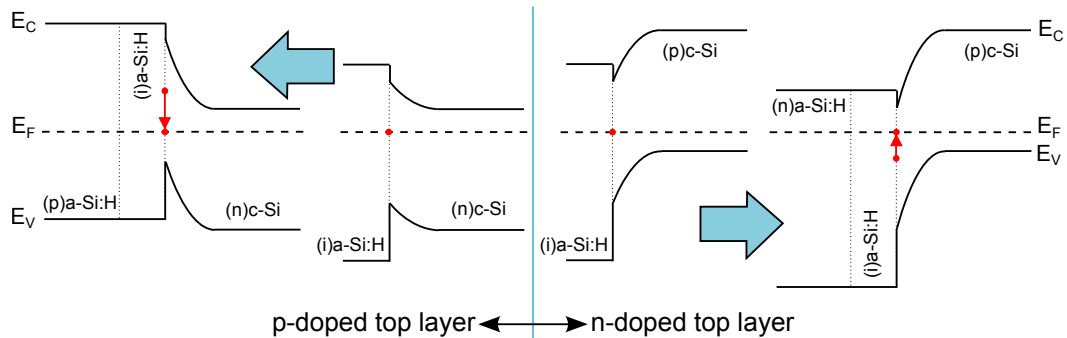


Figure 8.14.: Shift of the Fermi energy at the heterointerface ($E_{F,S}$) by deposition of a doped a-Si:H top layer. In the following it will be argued that such a shift leads to an increase of interface defect density by E_F -dependent equilibration of the a-Si:H bulk defect density.

(p/i)a-Si:H stacks than for the sum of single (p)a-Si:H and (i)a-Si:H layer effusion spectra while the effect was absent for the n/i combination, de Wolf *et al.* argued recently that an increased Si-H bond rupture rate due to the shift of the Fermi level in the (i)a-Si:H layer upon deposition of doped top layers is responsible for the deterioration of the passivation [56, 57]. The absence of the effect for (n/i)a-Si:H stacks was explained by the fundamental asymmetry of the H diffusion activation energy which is significantly lower when E_F is in the lower part of the a-Si:H band gap due to the amphoteric nature of the dangling bonds and the correlation energy separating its two charge states.

This general asymmetry in the passivation deterioration is found again in this work, visible in the comparison of doping-inversed structures in Figs. 4.8 & 4.10. While for (p/i)a-Si:H stacks, where E_F is in the lower half of the a-Si:H band gap, the passivation deteriorates significantly even for low doping concentrations of the top layer, the (n/i)a-Si:H stacks with E_F being in the upper half even show an increase in the passivation for the low doping levels before it begins to slowly deteriorate at higher (n)a-Si:H doping concentration. Thus, the position of the Fermi level could be invoked as the principle origin of the degradation effect also in the framework of the data presented here.

However, in the light of the picture developed above for the interplay of a-Si:H/c-Si interface defect density as probed by the minority carriers in the c-Si and the a-Si:H bulk properties, a different origin than Si-H bond rupture is possible: As mentioned in section 2.1.3, the position of the Fermi level is the most important parameter determining the a-Si:H bulk defect density through defect equilibration processes converting weak Si-Si bonds into dangling bonds, being an inherent property of a-Si:H. Thus, it could be possible to understand the passivation phenomenology upon shifting the Fermi level by defect equilibration processes happening in the a-Si:H bulk. Additional support comes from the fact that an involvement of the density of weak Si-Si bonds in the passivation was already demonstrated — in the form of a correlation between annealed N_{it} and Urbach energy E_{0V} as seen above in Fig. 8.13.

To substantiate this hypothesis, the following steps would have to be taken: First, to determine whether Si-H bond rupture and successive H effusion are involved in the degradation process as surmised by de Wolf *et al.*. Secondly, to take combined data of the a-Si:H Fermi level position and of the resulting interface defect density, and to

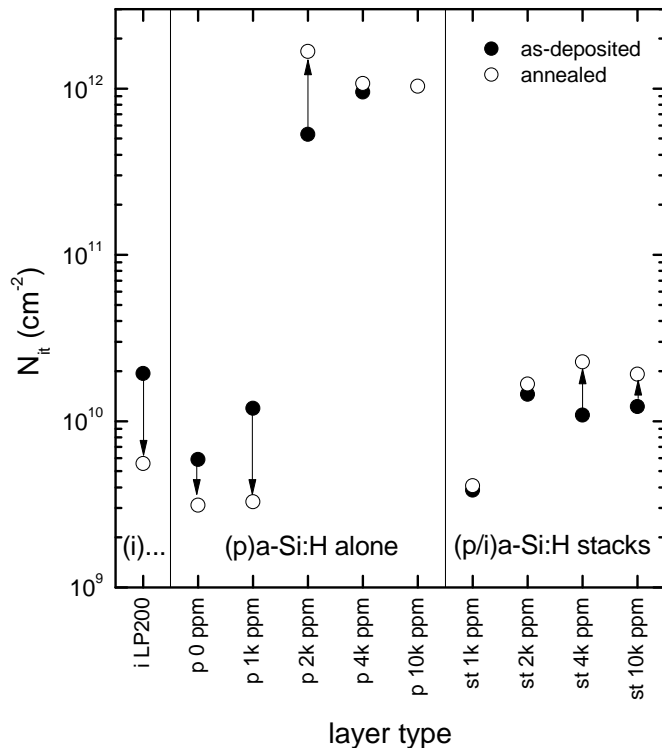


Figure 8.15: Interface defect density N_{it} of single (i)a-Si:H and (p)a-Si:H layers as well as for (p/i)a-Si:H stacks, with varying (p)a-Si:H doping concentration. 'i LP200' is the single (i)a-Si:H layer, 'p x ppm' denotes single (p)a-Si:H with x ppm gas phase doping, 'st x ppm' are (p)a-Si:H/(i)a-Si:H stacks with the respective p-layer doping. Thicknesses were 10 nm for both layer types. It is obvious that for high (p)a-Si:H doping, the as-deposited passivation is very poor while the initially excellent passivation by (i)a-Si:H is deteriorated by deposition of a highly doped (p)a-Si:H top layer, as seen also in Fig. 4.6.

analyze their correlation to decide if the defect equilibration process yields a consistent quantitative description of the processes which are observed. These two steps will be taken in the following sections.

8.6.2. Looking for E_F -dependent Si-H bond breaking

As depicted schematically in Fig. 8.14, a Fermi level shift is expected to be present in the *bulk* of the intrinsic layer upon deposition of a doped top layer of either doping type as the band bending in a-Si:H is usually small due to the large number of rechargeable states. To test the hypothesis of E_F -dependent Si-H bond breaking proposed by de Wolf *et al.*, FTIR spectra of single (i)a-Si:H, (p)a-Si:H and (p/i)a-Si:H stack layers are analyzed in the following, looking for indications of H loss associated with the depassivation. If the mechanism invoked by de Wolf *et al.* was indeed at work it would have to involve the whole of the (i)a-Si:H bulk as there is only negligible a-Si:H band bending (cf. Table 7.1), thus the FTIRS technique would be able to resolve it. The largest impact on the effective lifetime was observed for (p/i)a-Si:H stacks in this work and in the literature [57], therefore this system was chosen for the test. The experiment was conducted as follows: (i)a-Si:H layers of 10 nm thickness were deposited on both sides of DSP (n)c-Si{111} substrates. Quarters of 4" wafers were used as substrates, therefore 4 samples could be prepared in the same PECVD run ensuring comparability between the samples. τ_{eff} was again measured with PCD to verify the passivating property of the (i)a-Si:H layers. In a next step, 10 nm thick (p)a-Si:H layers with varying doping concentration were deposited on top of the (i)a-Si:H layers on both sides of the wafer.

In each (p)a-Si:H PECVD run, nominally identical substrate quarters were also coated solely with (p)a-Si:H to serve as reference samples. Again, PCD was measured on both types of samples. Then, FTIRS was measured on one of the (i)a-Si:H samples left uncoated by (p)a-Si:H, on the single (p)a-Si:H layers with different doping levels and on the (p/i)a-Si:H stacks comprising layers from the same PECVD runs as used to deposit the single layers.

First, the lifetime data which is shown in Fig. 8.15 shall be briefly analyzed: The general trends are known from the analyses presented above. The (i)a-Si:H layer provides good passivation, as does the (p)a-Si:H when it has no or only few B_2H_6 added during deposition, i.e. being nominally undoped. For doping concentrations of 2000 ppm or more, the N_{it} values of the (p)a-Si:H layers are strongly enhanced. While the passivation of layers providing reasonable N_{it} in the as-deposited state can be further increased by annealing (arrows in Fig. 8.15), initially poor passivation further decreases upon annealing. As compared to the single (i)a-Si:H layers (leftmost data point), the passivation is deteriorated if (p)a-Si:H layers with significant doping (≥ 2000 ppm) are deposited on top of the (i)a-Si:H, consistent with the trends shown in Fig. 4.8. Note that the thickness of the (i)a-Si:H layer had to be 10 nm (thus lowering the potential deterioration effect as compared to the data from Fig. 4.8) as this is the minimum thickness which still allows a quantitative FTIRS analysis. However, the deterioration is obvious in Fig. 8.15. Thus a response in the IR spectra is expected if Si-H bond rupture in the bulk was the cause for the loss in passivation.

In Fig. 8.16, the FTIR spectra are shown for the single (i)a-Si:H layer (black), the single (p)a-Si:H layers with varying gas phase doping concentration (red), as well as for the stacks consisting of (p)a-Si:H/(i)a-Si:H layers (blue) deposited in the same PECVD runs as the respective single layers. For comparison with the layer stacks, the sum of the single layer signals is shown as well (green). Note that the spectra are shown in the absorbance domain, i.e. before calculation of the absorption coefficient. This is most intuitive as the signal for the layer stack then consists of the simple sum of the single layer signals. Additionally, the impact of the error in the estimation of the layer thickness which yields the largest contribution to the overall error when performing quantitative analysis of FTIRS data — e.g. to extract the number of atoms contributing to a mode, as needed to compile the data in Fig. 8.1 — is excluded.

If there was a loss in Si-H bond density depending on the a-Si:H Fermi level causing the passivation deterioration, one would expect a difference between sum signal and layer stack signal. However, there is only a very slight visible difference, corresponding to a gain in the range of the isolated monohydrides ($\approx 2000 \text{ cm}^{-1}$) for the stacks as compared to the sum signal, which seems to be very similar for all the stacks irrespective of the (p)a-Si:H doping. This becomes even more obvious when directly observing the difference spectra between sums of the single layers and the stack spectra, as are shown in Fig. 8.17: The difference spectrum is almost identical for all the layer stacks, independent of the (p)a-Si:H top layer doping. The high-frequency features most likely are interference fringes due to multiple internal reflections of the infrared light in the c-Si wafer due to angular mismatch in the sample mounting leading to violations of the desired Brewster-angle conditions. The large-frequency features may be interpreted as a 'reorganization' of hydrogen bonding in the stacks as compared to the sum of the

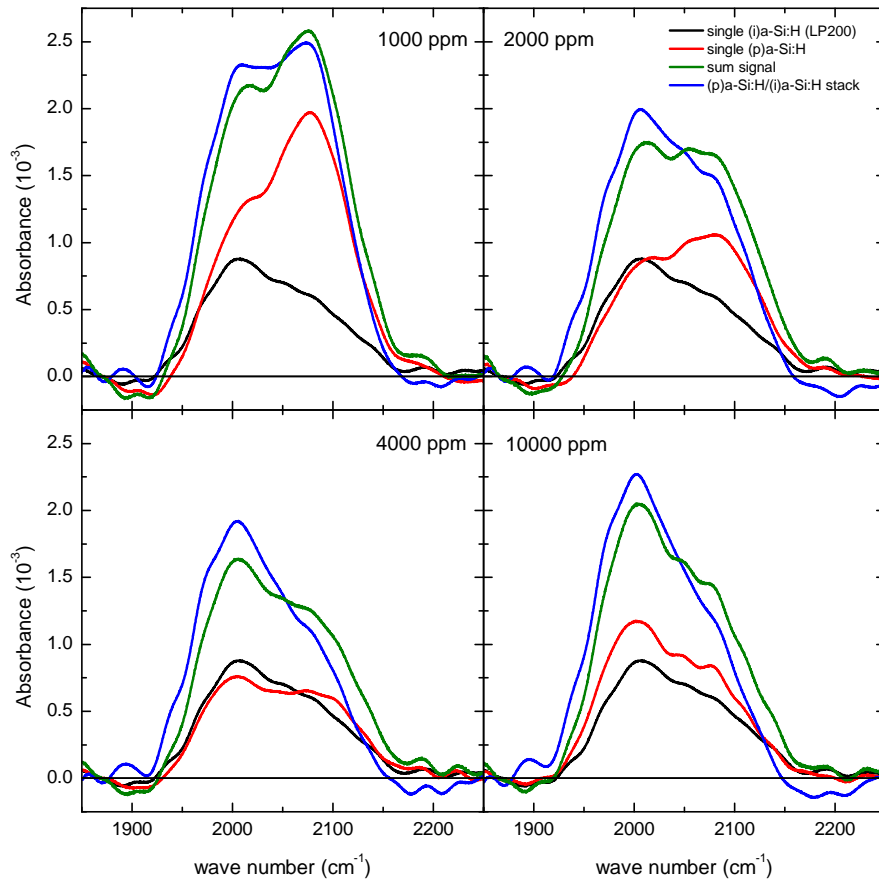
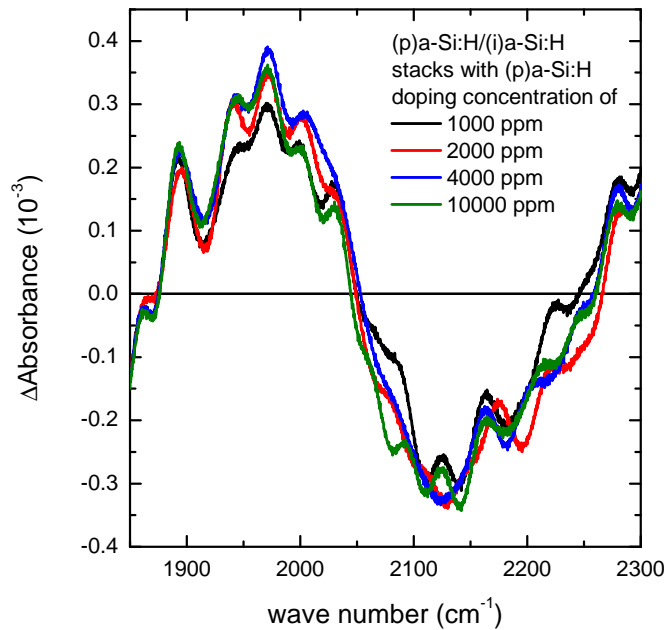


Figure 8.16.: FTIR spectra of single (i)a-Si:H and (p)a-Si:H layers as well as for (p/i)a-Si:H stacks, and the sum spectrum of single (i)a-Si:H and (p)a-Si:H layers. Other than in previous plots of FTIR spectra, the absorbance is plotted instead of the absorption coefficient as like this the stack spectrum is expected to be simply the sum of the single layer spectra, which is indeed observed to a good approximation.

single layers: In the previous FTIRS analysis (section 6.2.1) it was shown that a noticeable fraction of the hydrogen probed in the ultrathin a-Si:H is related to the open surface. This concerns a relative fraction of about 10% as obvious when comparing the surface- and bulk-related H content in Fig. 8.1. This surface layer is dihydride-rich [78] as the subsurface relaxation processes during PECVD growth have not yet affected this zone. Summing up two signals from single layers yields a doubled weight of this surface layer in the spectrum. In a stack however, the imperfect surface region of the (i)a-Si:H layer is likely to be restructured during the overgrowth of the doped layer, which should result in a loss in surface-related SiH_2 and a gain in monohydrides. Consequently, a stack should display a gain in the LSM and a loss in the $2100 \dots 2200 \text{ cm}^{-1}$ range when compared to the sum of the single layer spectra, resulting from the restructuring of the (i)a-Si:H surface layer. This effect should be independent of the top layer doping and involve about 5% of the sum or stack signal.

The difference spectra shown in Fig. 8.17 are consistent with this expectation, apart

Figure 8.17: Difference spectra of (p/i)a-Si:H stacks and the sum spectra of single (i)a-Si:H and (p)a-Si:H layers: The difference spectra are almost identical and do *not* depend on the top layer doping. The difference spectra can be tentatively explained by the presence of two SiH₂-rich surfaces in the case of the sum spectrum, while the H reconfiguration upon top layer deposition leads to a gain in LSM ($\approx 2000 \text{ cm}^{-1}$) and a loss in HSM and surface-related modes ($2100 \dots 2200 \text{ cm}^{-1}$). The data clearly contradict the presence of a E_F -dependent H loss which was previously invoked to explain the deterioration of passivation upon doped top layer deposition [57].



from the fact that the size of the difference signal amounts to about 10% of the sum or stack signal. Care has to be taken however to give a quantitative judgement as the absorption coefficient spectra would be required for doing so. Most importantly, the fact that no change is observed in the difference spectra whatsoever the top layer doping illustrates clearly that there is no H loss depending on the Fermi level shift. An alternative explanation for the passivation deterioration, which does not depend on invoking Si-H bond rupture, will be given in the next section.

8.6.3. Modeling E_F -dependent interface defect equilibration

As outlined already in section 2.1.3, the equilibrium defect density in a-Si:H depends on the position of the Fermi level as it influences the energy balance of the conversion reaction between weak Si-Si bonds and dangling bond defects. While E_F acts as a 'lever' deciding how many defects are created from weak bonds, there is obviously a second important parameter for this mechanism, which is the amount of weak bonds available as initial state of the conversion process. The macroscopic parameter reflecting this potential 'pool' of defects, i.e. the density of strained bonds, is the Urbach energy which directly measures the density of electronic states associated with those bonds. In consequence, the pronounced correlation between E_{0V} and N_d in previous data [249] shown in Fig. 8.13 can be seen as evidence for the presence of a weak-bond – dangling bond conversion mechanism (cf. section 2.1.3).

If the model relating interface defects and a-Si:H bulk defects presented above was true, the Fermi-level dependent equilibrium bulk defect density in a-Si:H could provide an elegant explanation for the deterioration effects upon deposition of doped top layers: When the Fermi level in the (i)a-Si:H layer is shifted by the influence of the doped layer (Fig. 8.14), the temperature provided during PECVD deposition of the (p)a-Si:H is high

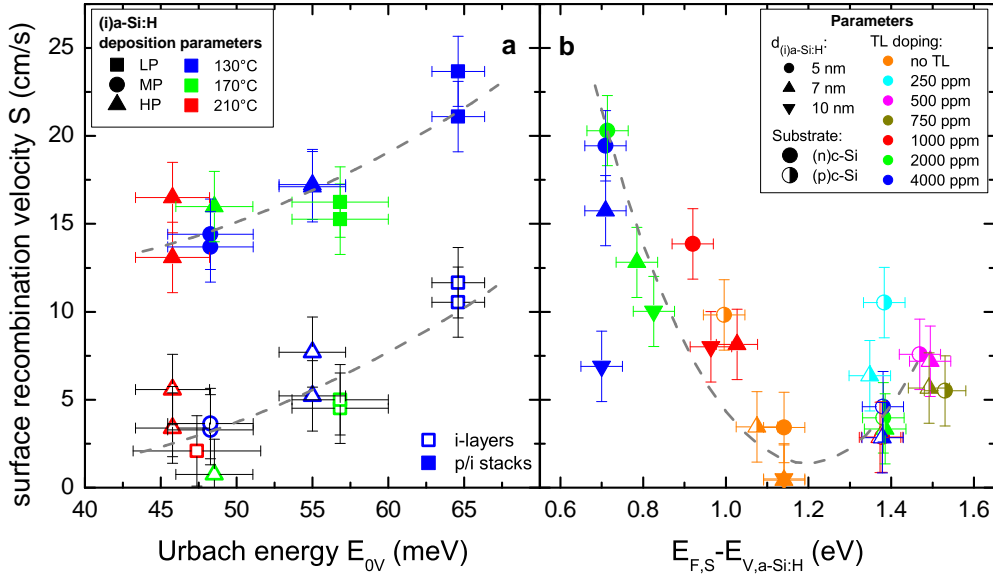


Figure 8.18.: (a) Surface recombination velocity S for (i)a-Si:H layers and (p/i)a-Si:H stacks (4000 ppm (p)a-Si:H doping) in dependence on the (i)a-Si:H Urbach energy E_{0V} . (b) S for (p/i)a-Si:H/(n)c-Si stacks and (n/i)a-Si:H/(p)c-Si stacks with varying top layer doping concentration. The abscissa displays the Fermi level position at the heterointerface $E_{F,S}$ as implied by measurements of the c-Si equilibrium band bending using SPV. The trends observed here suggest E_F - and E_{0V} -dependent defect equilibration in the a-Si:H bulk to be the cause of the interface recombination phenomenology, as will be explained in the text. The dashed lines are guides to the eye.

enough and the deposition time long enough to allow for equilibration, additional dangling bond defects in the a-Si:H would be created from weak Si-Si bonds according to the defect equilibration concept, which in consequence would manifest in increased recombination. In the following, the available data will be reviewed to compile a consistent picture of the deterioration effect, and a quantitative comparison to the prediction of accepted models describing the weak-bond – dangling bond conversion shall be attempted.

Signature for E_F -dependent passivation in lifetime data

The two main parameters for a-Si:H defect equilibration are the Fermi level position E_F and the Urbach energy E_{0V} . It is instructive to revisit the c-Si minority carrier lifetime data presented so far in this thesis in terms of these two fundamental parameters. As both doping types have to be explored for the substrates to cover the maximum range of E_F position in the IBLs (cf. Fig. 8.14), it is reasonable to analyze the surface recombination velocity instead of τ_{eff} . Thus, the impact of different substrate thicknesses and Auger-limited bulk lifetimes can be ruled out from the data. In the following, the absence of extrinsic bulk defects was assumed ($\tau_{\text{SRH}} = \infty$), the Auger lifetime was parametrized as in Eq. 2.9 [122] and the surface recombination velocity S is calculated from Eq. 2.34.

Two different trends are expected: First, for a fixed Fermi level position at the heteroin-

interface one would expect a variation of passivation with the Urbach energy of the layer adjacent to the interface. Indeed this is observed when plotting the surface recombination velocity of c-Si samples comprising different 5 nm thick (i)a-Si:H passivation layers (Fermi level fixed to approximately 1.3 eV as all layers are undoped), and for (p/i)a-Si:H stacks with the same top layer doping for every (i)a-Si:H passivation layer (Fermi level fixed by the top layer doping). Fig. 8.18a shows the respective data for single (i)a-Si:H layers (open symbols) and stacks with 4000 ppm top layer doping (full symbols).

A second trend should emerge when the Urbach energy is kept fixed (e.g. by employing a single (i)a-Si:H passivation layer deposition parameter set) while varying the Fermi level position. This can be achieved by changing the doping concentration of the a-Si:H top layer, and, to a lesser extent, by changing the (i)a-Si:H thickness and thus the band bending supported by the (i)a-Si:H (cf. Table 7.1). The limits of the Fermi level shift are given by the substrate doping type (only one half of the band gap is accessible for a given doping type) and the controllability of a-Si:H doping¹¹. Further, the Fermi level position at the heterointerface under an a-Si:H stack is not easily accessed due to the small band bending present in the (i)a-Si:H layer depending on its thickness, therefore taking the bulk E_F position of the doped layer as measured by CFSYS may lead to errors. As outlined above (chapter 7), the SPV technique offers a convenient way of measuring E_F at the heterointerface, termed $E_{F,S}$. This parameter was considered in the following as E_F at the heterointerface is the crucial parameter for the definition of the defect density probed by the c-Si minority carriers¹². Fig. 8.18b shows the interface recombination velocity of (p/i)a-Si:H/(n)c-Si stacks and their doping-inversed counterparts versus the Fermi level position at the heterointerface as measured with SPV. It is obvious that for the (p/i)a-Si:H stacks $E_{F,S}$ can be controlled in a much wider range than for the (n/i)a-Si:H stacks. This is due to the fact that even with the minimum PH_3 flow rates in the PECVD reactor, corresponding to 250 ppm gas phase doping, the resulting $E_{F,S}$ is already significantly shifted away from mid-gap. For the (p/i)a-Si:H stacks a relatively clear trend emerges: Starting from the usual low S values for purely intrinsic layers, the recombination is increased systematically when the Fermi level at the heterointerface is shifted towards the valence band edge. On the (n/i)a-Si:H side the trend is much less clear, but it appears that up to $E_{F,S} > 1.4$ eV there is only a slight deterioration of the passivation.

Description of the model

In a next step it shall be attempted to model the behavior observed in the two previous figures based on the Fermi level-dependent defect equilibration in a-Si:H. As outlined in section 2.1.3 there are several models in the literature which aim at describing the mechanism of E_F -dependent conversion of strained bonds into dangling bonds in bulk

¹¹Note that the latter has principal limits as e.g. the minimum distance between the band edges and E_F where the Fermi level gets pinned in the band tail states, and practical limits which are given by the ability of the deposition system to define the gas phase doping in a suitable range. In practice, a well-defined Fermi level position is much harder to achieve in (n)a-Si:H layers due to the much higher doping efficiency of those layers.

¹²Note that due to the small voltage drop across the (i)a-Si:H buffer layer, $E_{F,S}$ is expected to be closely similar to E_F in the bulk of the doped layer.

Table 8.1.: Parameters of the defect pool model. The third column shows the literature values employed by Powell and Deane [184], while the fourth column lists the parameters used here in the framework of the EIDR model, as discussed in the text.

| Function | Name | Value in Ref. [184] | Value here | Unit |
|---------------------------|----------|---------------------|---------------------------------|------------------|
| Measurement temperature | T | 300 | 300 | K |
| Equilibration temperature | T^* | 500 | 400/460 ¹ | K |
| DOS at VB edge | N_{V0} | 2×10^{21} | 2×10^{21} | cm ⁻³ |
| Hydrogen concentration | C_H | 5×10^{21} | 1×10^{22} ² | cm ⁻³ |
| Intrinsic E_F | E_i | 1.05 | 1.05 | eV |
| Correlation energy | U | 0.2 | 0.2 | eV |
| Width of defect pool | σ | 0.178 | 0.178 | eV |
| Energy of defect pool | E_p | $E_i + 0.44/2$ | $E_i + 0.44/2$ | eV |
| Urbach energy at 300 K | E_{0V} | 45 | variable | meV |
| Fermi energy at 300 K | E_F | variable | variable | eV |

¹ Depending on the doped a-Si:H deposition temperature.

² Corresponding to the mean H content measured with FTIRS.

a-Si:H. One of the most prominent and widely accepted models is the so-called 'defect-pool-model' by Powell and Deane [184–186]. It allows to calculate the equilibrium defect distribution of the dangling bond defects in a-Si:H, i.e. the concentration, energetic distribution in the a-Si:H band gap and the charge state of the defects, depending on a set of material and extrinsic parameters (listed in Table 8.1). Of these, the most prominent are the Urbach energy E_{0V} , quantifying the 'pool' of potential defects found in strained Si-Si bonds, and the Fermi energy E_F serving as a lever for the conversion of strained bonds into dangling bonds. The procedure for the estimation of interface defect density from the defect pool model now is the following: For each Urbach energy (being fixed by the choice of (i)a-Si:H deposition parameters) and each Fermi energy at the heterointerface (which is measured by the SPV technique) an (i)a-Si:H bulk defect density can be calculated employing the defect pool model. Here, the equations from Ref. [184] were used. The one-particle defect distribution consists of six contributions with pairwise similar magnitude and pairwise separation by U . If E_F is not exactly in the intrinsic position at E_i , two of the six contributions dominate the other four and their sum can well be approximated by a Gaussian (cf. Figures 4 and 5 in Ref. [184]). Therefore, a Gaussian fit was employed to map the a-Si:H defect distribution as calculated from the defect-pool-model onto a single Gaussian distribution which approximates the dominant contribution to the defect distribution. This approximation to the a-Si:H bulk defect density is then converted into an effective interface defect density using Eq. 8.8, i.e. assuming the interaction between c-Si excess charge carriers and a-Si:H defects through tunneling as outlined above. The resulting interface defect distribution, characterized by its position E_d , width σ_d and amplitude D_{it} , is fed into the analytical lifetime calculation model described in section 2.2.4. The other parameters of the lifetime model are the known substrate data (thickness, doping type and -concentration) and the capture cross sections ($\sigma_{p/n}^0$ for neutral donors, and the conversion factors for charged defects and be-

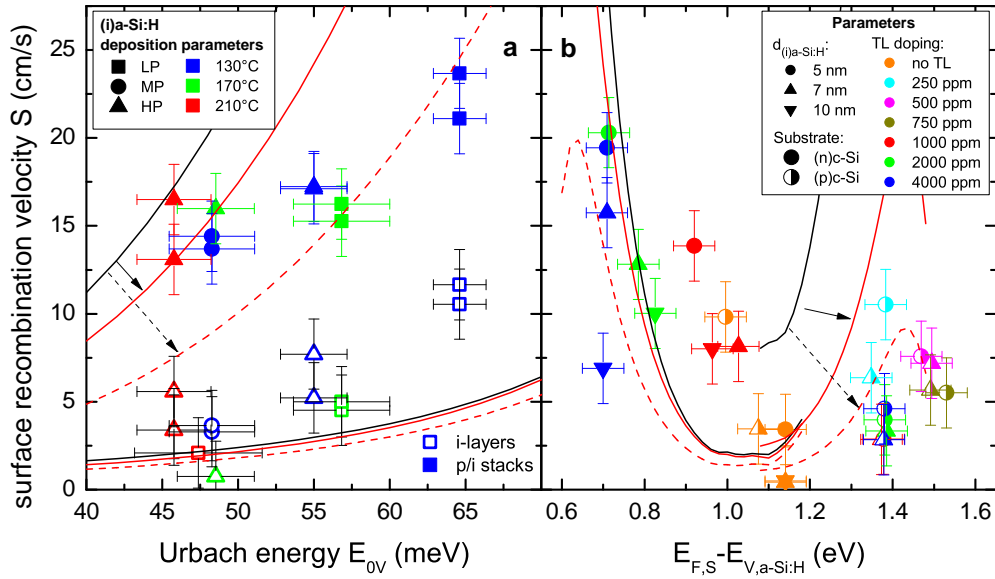


Figure 8.19.: Data sets from Fig. 8.18 with the prediction of the EIDR model. Black line: Without any incorporation of c-Si band bending. Red line: EIDR with a rudimentary implementation of c-Si band bending by incorporation of a fixed charge Q_f , however without correct injection-dependence. Dashed red line: Q_f enhanced by 50% as compared to the value corresponding to the correct dark band bending. Details are discussed in the text.

tween donors and acceptors, cf. section 2.2.4). No fixed charge Q_f at the heterointerface was assumed at this stage. By this procedure, starting from the parameters in Table 8.1, measuring $E_{F,S}$ and E_{0V} and assuming an equilibrated a-Si:H defect distribution and the tunneling connection between c-Si minority carriers and a-Si:H bulk, the effective lifetime or interface recombination velocity S can be calculated. In the following, this approach will be referenced as the 'equilibrated interface defect recombination model' (EIDR model).

Results

The results of this procedure for S in dependence on E_{0V} and $E_{F,S}$ as measured on the samples shown in the previous two figures are displayed in Fig. 8.19. The black lines were calculated with the procedure outlined above. It is obvious that the general trends in the data are indeed reproduced. For some aspects such as the $E_{F,S}$ position corresponding to the maximum lifetime or the $S(E_{0V})$ trend for the single (i)a-Si:H layers a quantitative agreement is found. For the doped/undoped a-Si:H layer stacks however, the correspondence is poor.

If comparing the model as outlined above in its present form with the conditions in the structures for which the deviation is most pronounced, the cause for this deficiency is obvious: The lifetime calculation does not take into account any c-Si band bending. Thus, the undoped layers on an (n)c-Si substrate — imposing only negligible band bending in the c-Si — are described well, but the contribution of the c-Si band bending to the passivating effect in a corresponding heterostructure is ignored: With increasing band

bending, one carrier type is progressively repelled from the heterointerface which limits the recombination rate as described in section 2.2.6. This 'field-effect passivation' is exploited by passivating layers such as Al_2O_3 or SiN_x carrying a significant fixed charge. Although the field effect is much smaller for doped a-Si:H than in these prominent examples, a contribution is to be expected which would lower the recombination velocities for the doped/undoped stacks in Fig. 8.19 and for extreme $E_{F,S}$ positions in Fig. 8.19. To correctly incorporate band bending into a-Si:H/c-Si interface recombination is a highly non-trivial task, which goes beyond the simple variant of the lifetime model employed here as it assumes a fixed charge outside the c-Si to impose a c-Si band bending. However, the assumption of an injection-independent charge is not realistic for the given system as will be discussed later.

To prove that the general concept of the bulk defect mapping has indeed the potential to *quantitatively* describe the passivation in a-Si:H/c-Si it will be attempted to rudimentary incorporate c-Si band bending into the modeling making use of the fixed charge Q_f . What can be practically exploited to this end is the fact that the Fermi level at the heterointerface *defines* the c-Si band bending¹³. Thus, the following strategy is suggested: For each $E_{F,S}$ the corresponding band bending is calculated with the help of Eq. 7.1¹⁴. Then the analytical equations of the lifetime model are inverted to yield the fixed charge Q_f which produces the correct band bending at the absence of excess charge carriers, with the correct amount and distribution of dangling bond defects from the defect pool calculation already taken into account. The next step is the same as before: To calculate the surface recombination velocity with the defect pool parameters as input and, in this case, the fixed charge yielding the correct band bending in the dark. The results for this approach are shown as full red lines in Fig. 8.19. It is obvious that while the passivation for purely undoped layers is not affected, an additional passivating effect is present for the doped/undoped stacks which is more prominent the more $E_{F,S}$ is shifted away from the intrinsic position, i.e. the more c-Si band bending is present in the structure. This effect is more pronounced for the (n)a-Si:H/(i)a-Si:H samples, i.e. for $E_{F,S}$ in the upper half of the band gap.

In conclusion, the general trends in the data are correctly reproduced: The undoped layers are described well also quantitatively, and the rudimentary inclusion of band bending yielding field-effect passivation is shifting the simulated curves even closer to the measured data. When assessing the quality of correspondence it has to be kept in mind that no fitting is involved. However, there are some remaining issues which shall be discussed in the following.

8.6.4. Possible issues and consequences

The most important issue concerns the c-Si band bending: Note that while it is quantitatively correct for the dark case with the present assumption of a fixed charge, this is not necessarily true for the charge carrier density at which the recombination velocity

¹³Indeed, the band bending is the quantity measured with SPV, which is then transformed into E_F at the heterointerface with known c-Si doping and a-Si:H/c-Si band offsets.

¹⁴Note that the zero point is suitably chosen to be the a-Si:H valence band mobility edge here, thus $E_F = -E_{V,a-Si:H}^\mu$ in equation 7.1.

is actually evaluated in Fig. 8.19, being of order $5 \times 10^{15} \text{ cm}^{-3}$. In a-Si:H, the charges are located at the dangling bonds which are electrically connected to the c-Si bulk and are indeed recharged depending on the splitting of the quasi-Fermi levels. Thus, the assumption of an injection-independent charge is a significant simplification in the present system. While the description of (i)a-Si:H layers which impose only small band bending is acceptable with the simple model, increasing discrepancies are to be expected when applied to doped/undoped stacks. In addition, the model is quite sensitive towards the charge distribution as can be seen from the dashed red lines in Fig. 8.19: Here Q_f was increased by 50% as compared to the value needed to reproduce the SPV-measured band bending in the dark¹⁵. With this choice of Q_f , the model reproduces the whole of the data well.

Therefore, to yield a quantitative picture, the calculation still has to be considerably refined in the future to incorporate injection level-dependent recharging of dangling bonds. While the missing injection-dependence of the band bending may account for most of the observed flaws, there are some other aspects which are not reflected in the model output and shall be briefly listed in the following for completeness.

First of all, the model does not yet include the variations in the less important microscopic parameters: The hydrogen atom density changes with the deposition conditions of the undoped a-Si:H layers, while the model assumes a constant concentration of $1 \times 10^{22} \text{ cm}^{-3}$. The measured trend could be easily integrated into the model by parametrizing the H density vs. the Urbach energy, however the impact is marginal. The same is true for the change in band gap and in consequence in the valence band offset¹⁶.

While these aspects can be seen as 'fine tuning' of the model, there is one larger practical doubt: It is not given *a priori* that the short time (around 15 min) at elevated temperatures during PECVD deposition of the doped top layer is sufficient to ensure an equilibrated a-Si:H bulk defect density. Particularly, the $T_{\text{sub}}=130^\circ\text{C}$ during (p)a-Si:H deposition (the (n)a-Si:H is deposited at 190°C) are slightly less than the commonly assumed 500 K glass temperature: While equilibration processes also take place below T^* , they proceed at much lower rates. The fact that (p/i)a-Si:H stacks usually show an additional loss of passivation when being annealed post-deposition (cf. Fig. 8.15) may be taken as evidence that the equilibrium defect density is not yet reached in the as-deposited state. This may contribute to the measured S values still being smaller than estimated from the model in Fig. 8.19a.

Lastly, several of the defect pool parameters were only estimated by Powell and Deane

¹⁵Note that this is a rather modest increase given the fact that Q_f varies over orders of magnitude within the band bending range to be covered.

¹⁶Note that it was found in CFSYS measurements that both the work function and the Fermi energy stay constant in their position relative to the conduction band edge, consistent with a removal of states at the top of the valence band. As historically the defect pool model is formulated with the energy zero point at the valence band edge, incorporating a changing band gap would yield a change of the dangling bond defect density from the band gap widening *alone*. As this does not seem realistic, the change in band gap was ignored in this case. In the future, the conduction band edge could serve as reference energy for the defect pool model and the correct implementation of the changing valence band offset may slightly vary the characteristics of the recombination part in the model.

by adjusting the model to data available at that time, and could be chosen differently without invoking too much of discrepancy with existing data. This includes the correlation energy U , the energetic position of the defect pool E_p and its width σ . By tuning only one of these parameters, the model can be achieved to reproduce the measured data more precisely particularly for E_F in the upper half of the band gap¹⁷. However, in the light of the flaws still existent in the model, it does not seem appropriate to vary the fundamental a-Si:H parameters in order to obtain a better fit. At this stage, the model has to be seen as a 'proof-of-concept' for the approach to link a-Si:H bulk defects and interface recombination. In the future, it would be desirable to test a refined model against a larger set of data which may help to shed further light on the recombination behavior of the a-Si:H/c-Si heterointerface.

8.7. Discussion

In this chapter, the phenomena connected to interface recombination in the a-Si:H/c-Si system were linked to microscopic properties of the involved a-Si:H layers and the compositional details of the heterostructure. First it was shown by detailed analyses of FTIRS and SIMS data that the as-deposited passivation is ruled by local properties of the heterointerface, which are subtle and hard to resolve experimentally. While SIMS yielded some evidence for increasing inhomogeneity and a pathological interfacial structure in those layers showing the highest interface recombination in the as-deposited state, there was no indication for structural reconfiguration, either involving hydrogen or the Si network, accompanying the pronounced decrease of recombination in these layers upon annealing. Only a global H loss affecting all (i)a-Si:H layers upon annealing irrespective of the gain in passivation was found, while the other bulk parameters did not change markedly. Thus, the explanation given here — poor local interface properties resulting from suboptimal growth conditions leading to inferior passivation properties — is the only logical explanation reconciling the entirety of experimental data, but it still remains tentative without the evidence of structural equilibration of the interface region with the bulk of the a-Si:H layers. FTIRS experiments in attenuated-total-internal-reflection mode may help to gather the missing bit of information.

In the following, the annealed interface properties were linked to the a-Si:H bulk in terms of recombination-active defect densities. It was shown that the defect density under undoped a-Si:H passivation layers is compatible with expectation if tunneling of charge carriers into the a-Si:H and successive recombination at dangling bond states is assumed. While the underlying idea is simple and the calculations are straightforward, the most critical aspect of this picture is certainly the uncertainty of the capture cross sections¹⁸. At this stage the description has the character of a proof-of-concept and disregards some subtleties of the given system.

Due to the appealing simplicity and the quantitative correspondence to the measured

¹⁷Better correspondence can e.g. be obtained by assuming $U = 0.3$ eV.

¹⁸Further doubts concern the validity of the Shockley-Read-Hall formalism in combination with the occupation statistics for amphoteric dangling bonds if recombination actually takes place involving tunneling processes. Also, the details of tunneling into localized states should be considered.

data, the concept was further extended to the description of doped/undoped a-Si:H stack structures. Once having connected a-Si:H bulk and the recombination properties of the heterointerface, it is straightforward to revisit the metastable effects in a-Si:H for their potential relevance to interface recombination. As the Fermi-level dependence of a-Si:H/c-Si interface recombination was already established on by other studies [57], connecting E_F -dependent a-Si:H bulk defect equilibration with the heterointerface is consequent. In addition, it is particularly suggested by the absence of E_F -dependent bulk hydrogen effusion, which was surmised to be the origin of depassivation in previous studies but could not be experimentally confirmed here. Although the unresolved issues of the tunneling approach apply here as well, the results obtained already with a rather simple model — naïvely connecting the defect-pool-description of dangling bonds [184] and fixed-charge interface recombination [142] — are promising: The potential of the approach is clearly demonstrated in Fig. 8.19 and a surprising degree of correspondence between measured data and analytical modeling was reached given the fact that no fitting is involved. The model is based on the combination of two well-established analytical descriptions, taking as input only literature data, measured quantities and the thoroughly motivated assumption of a bulk-defect-dominated interface recombination through tunneling.

It may be hoped that incorporating the interplay between chemical (de)passivation by E_F -dependent dangling bond creation and c-Si band bending through injection-dependent recharging of amphoteric defects will help to reach a consistent description of a-Si:H/c-Si interface recombination with the true potential of a quantitative prediction. In the framework of the EIDR model, some of the peculiarities of a-Si:H/c-Si interface recombination can be explained elegantly from fundamental properties of amorphous silicon: The deterioration of the passivation provided by undoped a-Si:H is explained by the Fermi level shift imposed by the doped top layers. Additionally, the asymmetry in the passivation properties between doping-inversed doped/undoped a-Si:H stacks results from the asymmetry in the a-Si:H dangling bond defect density between (p)a-Si:H and (n)a-Si:H which in turn reflects the amphoteric nature of these defect states.

Towards application of doped/undoped a-Si:H layer stacks as emitters in a-Si:H/c-Si heterojunction solar cells, the analysis presented above highlights the Urbach energy as a crucial device parameter: The minimum distance of $E_{F,S}$ from the intrinsic position is more or less fixed by the necessity of a significant c-Si band bending for charge carrier transport, thus requiring a minimum doping to minimize losses in the fill factor. The (i)a-Si:H Urbach energy, being the second controllable parameter of the interface defect equilibration, is therefore even more important. By minimizing E_{0V} adjacent to the interface, the amount of recombination-active a-Si:H bulk defects created by depositing a doped top layer can be controlled. This fundamental property of a-Si:H/c-Si heterojunctions comprising undoped passivation layers has not been identified so far. To break these rather fundamental considerations down to the device level again, the implied V_{oc} resulting from the EIDR-model-derived surface recombination velocities¹⁹ was calculated using the simple model from section 2.2.5. Note that no band bending is

¹⁹Here, the model with Q_f chosen to yield the SPV-measured dark band bending was employed. Thus the results correspond to the full red lines in Fig. 8.19.

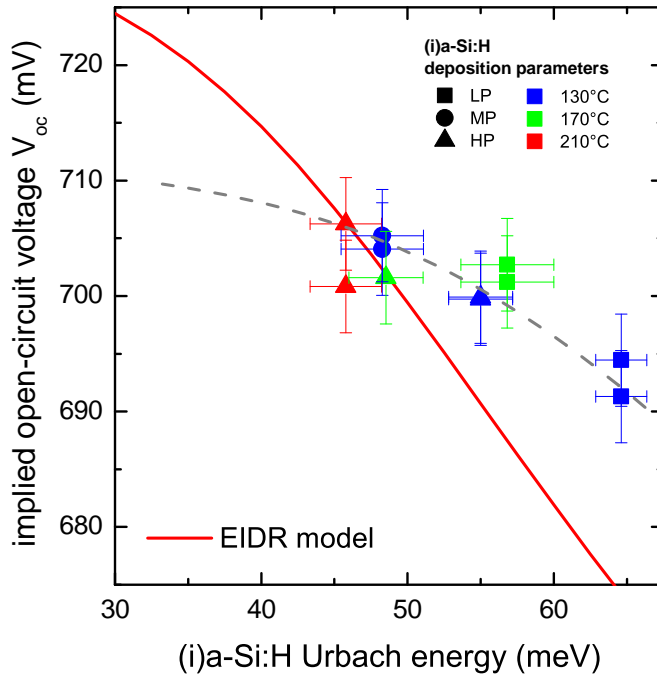


Figure 8.20: Implied V_{oc} for (p/i)a-Si:H/(n)c-Si stacks with 4000 ppm top layer doping, depending on the Urbach energy E_{0V} of the IBL. The data points represent the measured $\{S, E_{0V}\}$ values as also shown in Fig. 8.19a (dashed line is a guide to the eye). The red line is the prediction of the EIDR model including c-Si band bending as also shown in Fig. 8.19a. Note however that the calculation of V_{oc} from S following section 2.2.5 is assuming flat bands, thus the V_{oc} values represent a lower limit due to the absence of field-effect passivation.

included in the calculation of V_{oc} from S , thus the resulting V_{oc} values represent a lower limit. Fig. 8.20 shows that in order to reach V_{oc} values above ≈ 710 mV, the Urbach energy of the (i)a-Si:H passivation layer should be around 40 meV, which represents a challenge for the PECVD growth of ultrathin a-Si:H layers.

Note however that as shown in the previous chapter, minimizing the Urbach energy may lead to fill factor losses in (n)c-Si based solar cells for thicker IBLs, which poses additional constraints on the optimum choice of (i)a-Si:H buffer layers for solar cell device application.

8.8. Chapter conclusion

The key questions for this chapter were:

- How do the a-Si:H microscopic properties relate to the passivation potential of a given (i)a-Si:H buffer layer?
- What is the microscopic effect of thermal post-treatment?
- What causes the degradation of passivation by IBLs upon deposition of doped a-Si:H top layers and how can it be diminished?

In the present chapter it was shown that the (i)a-Si:H hydrogen content and Urbach energy serve as ordering parameters for the passivation potential in both the as-deposited and annealed state of the IBLs. However, it was suggested that in the case of the *as-deposited* passivation, this correlation is a coincidence: The local state of the heterointerface, which however could not be resolved experimentally on a microscopic scale, seems to rule the passivation properties in the as-deposited state. It was shown —

in accordance with previous works — that low-temperature annealing can significantly improve these local interfacial properties, while pulsed microwave annealing was demonstrated to yield the annealed state of the heterointerface faster than hotplate annealing, supposedly due to the preferential absorption of MW radiation at the Si-H bonds. During the annealing process, the a-Si:H bulk properties do not change markedly — apart from a slight global hydrogen loss due to the onset of effusion —, which suggests the structural changes accompanying the annealing process to be of local nature, happening in the vicinity of the heterointerface.

The resulting *annealed* state of the a-Si:H/c-Si interface was shown to possess no particular properties but to merely serve as a window between the c-Si hosting the excess charge carriers and the defect-rich a-Si:H bulk. In consequence it was found that the a-Si:H bulk defect density is governing the passivation properties of the annealed a-Si:H/c-Si system and thus the limit of reachable interface passivation by a tunneling recombination process involving the a-Si:H dangling bonds.

Based on this finding, a self-evident explanation of the passivation phenomenology of doped a-Si:H/(i)a-Si:H stacks can be given: As it is found that the Fermi level position at the heterointerface *and* the IBL Urbach energy are co-determining the passivation potential of a-Si:H stacks, the well-known defect equilibration in amorphous silicon is suggested to govern the passivation potential. The shift of E_F at the heterointerface as imposed by the deposition of a doped top layer in conjunction with the E_F -dependent conversion of strained bonds into dangling bonds leads to the observed increased recombination. A simple model, which combines the defect-pool model to describe the E_F -dependent defect creation with a description of a-Si:H/c-Si interface recombination, can provide an explanation of the observed passivation behavior. As the defect creation is assumed to result from the breaking of Si-Si bonds, the model is able to reconcile the experimentally observed absence of Si-H bond rupture during passivation deterioration, which was invoked by previous models. With a yet to achieve incorporation of injection-dependent recharging of defects, a quantitative description with the proposed model seems feasible. Further, the Urbach energy — quantifying the amount of potential defects — is identified as a crucial material parameter for undoped a-Si:H to be used as passivating buffer layer.

9. Conclusions and Outlook

9.1. Main conclusions of this thesis

The objective of this thesis was to examine the properties of a-Si:H/c-Si heterojunctions comprising thin undoped amorphous silicon buffer layers. Both the fundamental aspects of the (i)a-Si:H/(p/n)c-Si heterojunction as well as the performance and behavior of solar cell devices comprising this type of junction have been explored. In this section, the main results shall be summarized.

Analysis of (i)a-Si:H bulk properties

The insight gained by infrared- and photoelectron spectroscopy, hydrogen effusion, SIMS and spectroscopic ellipsometry has yielded a consistent picture of the 'bulk' of 10 nm thick (i)a-Si:H layers and have proven useful in understanding the properties of the heterojunction. In comparing thin (i)a-Si:H films with pertinent data on thick layers it was found that there is no pronounced difference: 10 nm thick (i)a-Si:H films behave essentially as layers of >100 times the thickness. Further, there is a clear correlation between the PECVD deposition conditions and the resulting microscopic structure of the layers: Upon choosing suboptimal deposition conditions (low substrate temperature, high growth rate, no H dilution), the structural quality of the a-Si:H bulk deteriorates. This is reflected in a higher void density and a shallower valence band tail. In consequence, the overall hydrogen content increases due to the dominant contribution of the clustered H on the inner surfaces of the voids, and the mass density of the film is reduced.

Fundamental aspects of the a-Si:H/c-Si heterojunction

In a next step, the microscopic information on the a-Si:H layers was used to explore the fundamental aspects of the a-Si:H/c-Si heterojunction, namely the band lineup and the passivation properties. It was found that the hydrogen content and the Urbach energy — quantifying the density of strained Si-Si bonds — are important ordering parameters: The Si-H bond density and the density of strained Si-Si bonds were found to codetermine the widening of the a-Si:H band gap and thus the heterojunction band offsets. As both conduction band edge and Fermi level in (i)a-Si:H stay constant when varying the hydrogen content, only the valence band offset is changing upon varying the a-Si:H band gap by a retreat of the a-Si:H valence band edge, as was demonstrated here for the first time.

In terms of passivation of c-Si surface dangling bonds, the observed behavior is more subtle due to the additional degree of freedom offered by thermal post-treatment, but hydrogen content and Urbach energy again serve as useful ordering parameters: While

the as-deposited passivation seems to be ruled by the local (non-equilibrium) state of the interface, the annealed heterointerface has no particular properties but serves as a window between the c-Si hosting the photogenerated charge carriers and the defect-rich a-Si:H. It was found that the passivation properties of the annealed a-Si:H/c-Si system are compatible with a tunneling recombination process involving the a-Si:H bulk defect density.

Taking this finding as a basic principle yields an elegant way of understanding the properties of doped a-Si:H/(i)a-Si:H stacks and their passivation potential. The puzzling phenomenology of top layer- *and* substrate-doping-dependent lifetime deterioration of a-Si:H stacks as compared to single (i)a-Si:H layers can be resolved when taking into account the position of the Fermi level at the heterointerface and the well-known defect equilibration concept in amorphous silicon: The shift of E_F at the heterointerface, as imposed by the deposition of a doped top layer, in conjunction with the E_F -dependent conversion of strained bonds into dangling bonds leads to the observed increased recombination. On the one hand, the proposed model reconciles the absence of H reconfiguration during lifetime deterioration as invoked by previous models, on the other hand the Urbach energy — reflecting the amount of potential defects — is identified as a crucial material parameter for undoped a-Si:H to be used as buffer layer. Thus, the ideal (i)a-Si:H in terms of passivation potential has the lowest Urbach energy.

Transport across the a-Si:H/c-Si heterojunction

More aspects come into play when considering the *electronic transport* across the heterojunction. In a first step, the transport mechanisms were elucidated based on dark I/V curves and lock-in thermography measurements, revealing two different regimes: The transport properties in the bias range defining the V_{oc} point in the I/V curve (high forward bias) are compatible with diffusion in the neutral bulk and thus ruled by the classical Shockley diode equation. Although a systematic trend in the ideality factor depending on the absorber passivation suggests an impact of the band structure which significantly deviates from the assumptions underlying the Shockley theory, the correspondence is robustly established for a large range of different samples. This allows to use the measured value of the high-forward-bias saturation current density to monitor the absorber passivation which proves useful for the analysis of passivation in contacted structures.

Under low bias, the picture is subtle: In the ideal case, tunneling processes seem to dominate the I/V characteristics under low forward bias particularly for (p)c-Si based cells, with the multi-tunneling-capture/emission model providing a promising explanation for the signature observed experimentally. This result reflects the impact of the large valence band offset on the transport which represents a significant barrier for holes crossing from the c-Si into the a-Si:H. Thus, alternative transport paths are highlighted to be important, such as tunneling of holes into the localized states of the valence band tail. Further, a large fraction of a-Si:H/c-Si solar cells seems to be affected by the presence of point- or stripe-like defective regions which leads to a high level of the low-forward-bias current and a recombination signature in the transport.

While the ideal (i)a-Si:H buffer layer for passivation purposes has the best structural

properties, the choice would depend on the substrate if transport is concerned: While on (p)c-Si wafers, the small conduction band offset does not pose a hindrance on minority carrier transport, the opposite substrate doping type is more delicate: The large valence band offset — increasing further with (i)a-Si:H hydrogen content — is a severe barrier to the holes, and in consequence tunneling processes have to take over part of the carrier transport. This fundamentally different situation on (n)c-Si renders the solar cell fill factor much more sensitive to the thickness of the undoped buffer layers. Furthermore, the density of localized states energetically close to the c-Si valence band, i.e. the slope of the a-Si:H valence band tail, affects the efficiency of hole tunneling transport, impacting the fill factor. There is further indication that even under j_{sc} conditions the band offsets play a role as the short-circuit current is reduced with increasing valence band offset. These effects render the choice of undoped buffer layers more difficult, as increasing density of tail states and further increase of valence band offset counteract each other concerning the effect on hole transport. A buffer layer with an intermediate band gap and valence band tail slope is suggested to be optimal for charge carrier transport.

Technological issues — transfer to solar cell technology

So far, the conclusions were restricted to the mirror-polished Si{111} surface. Although the findings concerning passivation and transport should be valid for other surface orientations and -morphologies as well, the growth of purely amorphous silicon without epitaxial phases is restricted to subsets of the deposition parameter space depending on the nature of the c-Si surface. Particularly, the c-Si{100} surface is prone to promote epitaxial growth for high H dilution and/or substrate temperature. Further, the technologically relevant textured c-Si{100} surface and the KOH-etched c-Si{100} surface, being interesting for back-junction heterojunction solar cells, are less well-defined concerning crystal orientation and thus may lead to suboptimal growth for some parameter sets. Generally, it can be stated that the deposition regimes leading to the best layers in terms of structural properties are most critical on suboptimal or epitaxy-affected surfaces. Thus, choosing an (i)a-Si:H recipe for passivation layers in technological applications will always require a trade-off¹.

Low-temperature annealing offers the possibility of using suboptimal PECVD conditions to avoid epitaxy on critical surfaces while maintaining a good passivation. Pulsed microwave annealing was demonstrated here to be a contact-less annealing method which achieves a given passivation improvement faster than the classical hotplate, thus having potential for industrial application.

In the analysis of solar cell transport, a visible impact of local recombination-active regions on the I/V characteristics was found. Although this finding is not uncommon for silicon solar cells, a careful revision of the processing scheme is suggested in order to minimize the damaging effects. The same is advised even more urgently by the monitoring

¹In this work, the LP200 parameter set has proven useful on both textured and KOH-etched surfaces, but it is probable that other optimum conditions exist for other surface morphologies. Particularly the textured surface was found to be critical as the distribution of pyramid sizes, the sharpness of the edges and valleys etc. are not always reproducible which renders the choice of a suited a-Si:H passivation layer even harder.

of passivation properties through the process chain with the help of transport measurements revealing a significant detrimental impact of the electron-beam-evaporation step for metal deposition.

This latter effect is the probable cause for the disappointing fact that the V_{oc} potential of the developed doped/undoped a-Si:H emitter stacks, which significantly exceeded 700 mV, could not yet be realized in a solar cell. In terms of efficiencies, a partial success can be reported: Incorporating the (i)a-Si:H buffer layers developed here, a back-contacted back-junction a-Si:H/c-Si heterojunction solar cell with a V_{oc} of 673 mV and a fill factor of 76% was recently demonstrated by a joint effort of HZB and ISFH [164]. Although the maximum V_{oc} still leaves room for improvement, the IBLs contributed 40 mV of V_{oc} improvement and the cell reached $20.2 \pm 0.4\%$ conversion efficiency, beating the current world record efficiency for this cell type by almost 5% absolute. This result demonstrates that by entirely controlling the processing technology, excellent cell results can be reached with the (i)a-Si:H layers developed here.

9.2. Outlook

Although the results on (i)a-Si:H/c-Si heterostructures presented in this thesis represent a self-contained piece of work, some further activities on both fundamental- and device level are implied.

Technology

In terms of solar cell processing, the next steps are quite obvious: A thermal evaporation setup for solar cell metalization allowing the presence of photolithography masks is ordered and will be installed at HZB within the next months. Excluding a detrimental impact of x-rays during metalization should enable to preserve the implied V_{oc} values well in excess of 700 mV through the entire processing chain and demonstrate such passivation on the device level. Further, the wet-chemical steps for texturization should be carefully reviewed and it should be worked towards reproducible texturization results. A possibly important aspect which was highlighted in literature [118] but not touched in the present thesis is the impact of the TCO work function on the hetero-emitter: A high work function — which Al-doped ZnO certainly has as compared to the classically employed ITO — could lead to a penetration of the band bending imposed at the ZnO/a-Si:H junction through the entire emitter stack and diminish the c-Si band bending. Further, the band lineup at the TCO/a-Si:H heterojunction was found to influence charge carrier transport. In this context it is suggested to assess the impact of the TCO layer on c-Si band bending and carrier transport with simulation and experimental means. Microcrystalline contact layers could provide a useful additional degree of freedom in the design of front contacts for a-Si:H/c-Si heterojunction solar cells. Concerning the back-junction solar cell, further optimization of the (i)a-Si:H layers could be targeted. To this end, a careful exploration of the deposition parameter space around the working recipes on c-Si{100} surfaces would be needed.

Device simulation

The presence and significance of tunneling processes in the a-Si:H/c-Si charge carrier transport as highlighted in this thesis has an obvious impact on device simulations. While the presence of tunneling effects in the low-forward-bias region of dark I/V curves is of rather academic interest due to the missing connection to illuminated I/V performance, the inability to simulate (n)c-Si based solar cells with AFORS-HET in the presence of large valence band offsets should draw attention to this topic.

Fundamental aspects

Two fundamental issues concerning the passivation topic still persist:

First, the microscopic conditions in the as-deposited state of the heterojunction and the processes taking place upon annealing which provide the significant passivation improvement could not be resolved due to the finite resolution of the techniques employed here. The structural changes upon annealing — although certainly present — are elusive enough to avoid detection by SIMS also in the shallow profiling mode, and involve a too small number of H atoms to stick out of the background H reconfiguration, which is caused by the onset of hydrogen effusion, in FTIRS measurements. Thus it is suggested to tackle the problem with specific interface-sensitive methods. A first step could involve high-resolution FTIR spectroscopy in the attenuated total-internal-reflection mode (ATR-FTIR), where the IR beam is coupled into the c-Si substrate and undergoes multiple internal reflections, probing the interface and adjacent a-Si:H by its evanescent modes during reflection [84]. This method may provide the necessary insight concerning hydrogen bonding at the a-Si:H/c-Si interface.

Secondly, the modeling of the recombination properties in a-Si:H/c-Si heterojunctions based on the concept of a tunneling-mediated interaction between a-Si:H defects and c-Si excess charge carriers as employed here is rudimentary at the present stage. Some important aspects are still missing or should be described in more detail: Examples are the injection-dependent recharging of a-Si:H defects and the resulting redistribution of band bending in the structure, as well as the detailed description of the tunneling process taking into account the occupation statistics of the final states. Some of these aspects will be treated in the PhD thesis of Caspar Leendertz, which is being worked on in parallel to this thesis.

A. Experimental details

A.1. Fourier-transform infrared spectroscopy

Measurement details

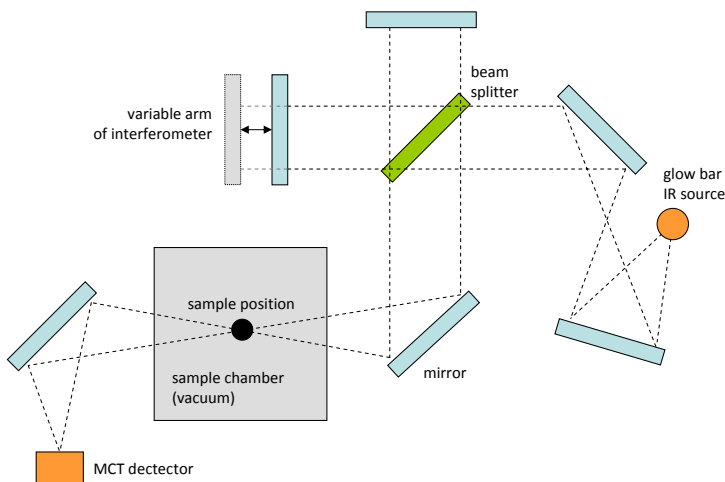


Figure A.1.: Schematic of the FTIR setup. The main part of the setup is a Michelson interferometer, which operates with polychromatic IR radiation from a glow bar IR source and where the resulting interferogram is shone through the sample whose absorption is to be measured. To perform a measurement, the variable arm of the interferometer is displaced and the change in intensity is recorded. Fourier transforming the recorded spectrum (which is in the length domain) yields the absorption spectrum in the wave number domain.

The FTIR spectra were measured on a Bruker IFS 66v/S and a Bruker IFS 125HR, which both can provide a vacuum in both the beam path and the sample chamber to minimize the impact of atmospheric conditions. Without evacuation of the sample space, transient contributions from carbon dioxide and water vapor render a quantitative analysis almost impossible¹, as the ratio of two measured signals is analyzed (see below). For the measurements analyzed here, a nitrogen-cooled mercury-cadmium-telluride (MCT) detector with nominal sensitivity range $12000 \dots 500 \text{ cm}^{-1}$ was used in combination with a potassium bromide (KBr) beam splitter with a spectral range of $7500 \dots 370 \text{ cm}^{-1}$ and the built-in glow bar IR source. The strongly decaying signal intensity below 700 cm^{-1} prevented to analyze the SiH wagging modes at 640 cm^{-1} ,

¹One then even detects the changing concentration of carbon dioxide in the room stemming from the breathing operator.

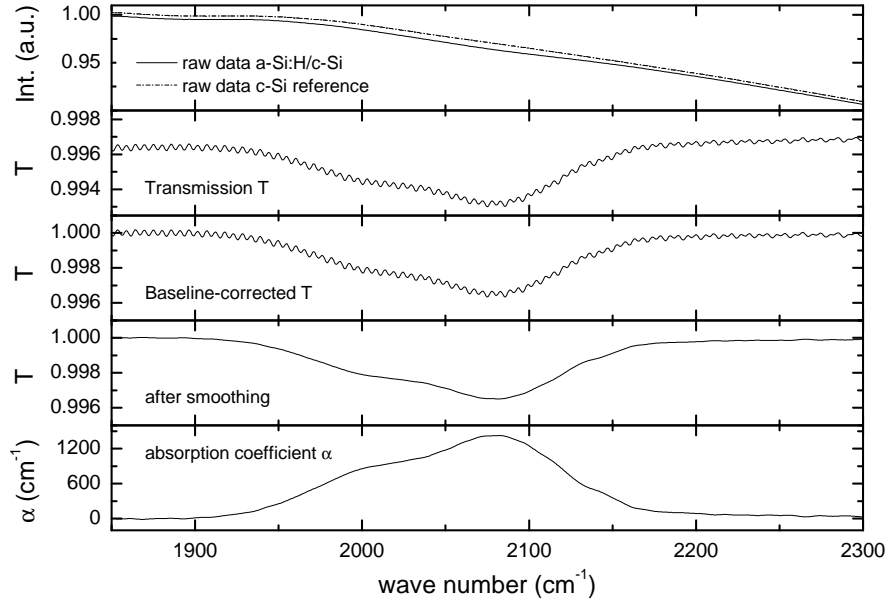


Figure A.2.: FTIRS data processing, as described in the text, applied to an example spectrum in the SiH stretching mode region.

therefore the stretching modes around $2100 \dots 2000 \text{ cm}^{-1}$ were targeted. A schematic of the spectrometer is depicted in Fig. A.1.

For each sample, 480 single measurements were averaged in one measurement run in the wavenumber range $8000 \dots 200 \text{ cm}^{-1}$ at a resolution of 4 cm^{-1} and with an aperture of 1.5 mm to focus the IR beam. The sample chamber was evacuated for exactly 20 minutes down to a pressure of about 2 mbar before every measurement run, which was found to be sufficient by test runs. To avoid multiple reflections of the beam in the c-Si wafer, the beam was polarized parallel to the plane of incidence by a polarizer inside the sample chamber and the sample was mounted such that Brewster angle conditions are fulfilled with the incident beam. Based on literature values for the refractive indices, the expected Brewster angles θ_B were

$$\theta_{B,\text{a-Si:H}}(1000 \dots 3000 \text{ cm}^{-1}) = 70, 99^\circ - 71, 91^\circ \quad (\text{A.1})$$

$$\theta_{B,\text{c-Si}} = 73, 99^\circ, \quad (\text{A.2})$$

while the optimum angle was found to be 74° versus the normal in test runs. Burrows *et al.* had found an optimum angle of 73° in similar experiments [32].

Data processing

A measured IR spectrum is usually expressed as an absorbance A versus wave number, which is defined as

$$A = -\log_{10} T = -\log_{10} \frac{I}{I_0}, \quad (\text{A.3})$$

where T is the transmission and I the measured intensity of the beam after passing through the a-Si:H/c-Si sample. I_0 is a reference beam intensity after passing through

an identical c-Si substrate without a-Si:H film.

Here, the raw intensity spectra were exported, and the following analysis scheme was applied: The transmission T was calculated from the intensity data of the sample I and the reference intensity I_0 by

$$T = I/I_0. \quad (\text{A.4})$$

A baseline correction was made by subtracting a line passing through the T data at 1851 cm^{-1} and 2350 cm^{-1} , which are points outside the stretching mode region. To eliminate a possible impact of noise in the T data, the average of 50 data points around the fixing points at 1851 cm^{-1} and 2350 cm^{-1} was taken to define the baseline.

Next, the data was smoothed employing an algorithm by Kauppinen *et al.* [120] to eliminate residual interference fringes. Smoothing is obtained by convoluting the data with a symmetrical smoothing function, which is mathematically equivalent to the multiplication of the Fourier transform of the data with an apodization function. Note that as the FTIRS method actually measures the Fourier transform of the IR spectrum, this smoothing algorithm is commonly implemented in FTIRS measurement software. Here, the discrete-Fourier-transformed data was multiplied with a boxcar function

$$A_0(t) = \begin{cases} 1, & |x| \leq X_0, \\ 0, & |x| > X_0, \end{cases} \quad (\text{A.5})$$

which is usually employed in FTIRS data processing. The smoothed data is then obtained by inverse discrete Fourier transformation. The best results were obtained with $X_0 = 0.086 \text{ cm}$, which was used for all the spectra.

The absorption coefficient α is then obtained from the smoothed T data by the Lambert-Beer law

$$T = e^{-\alpha d} \Rightarrow \alpha = -\frac{\ln(T)}{d}, \quad (\text{A.6})$$

with d being the cumulated a-Si:H thickness. The successive application of these data processing steps to an example spectrum is shown in Fig. A.2. Note that the error in α is dominated by the uncertainty concerning the layer thickness d . The determination of d with SE yields an error of about 0.15 nm as indicated by the SE fitting routine (see below). For the total error of the summed a-Si:H thickness, 0.5 nm was assumed for the FTIRS analysis, thus slightly overestimating the uncertainty.

Fitting of FTIRS data

The α data of the stretching-mode region was fitted by five Gaussian functions, corresponding to the modes A–E listed in Table 6.1. The allowed range and starting values for the different fit values are listed in Table A.1 and were chosen according to Burrows *et al.* [31, 32]. The as-deposited and annealed data sets were fitted at once, with independent values for amplitude and width of the modes, and a coupled value for the position. At the same time, the difference of the modeled modes between as-deposited and annealed state was fitted to the difference spectra. Thus, three partial fits (to as-deposited, annealed and difference spectra) were done for two sets of fit parameters, ensuring the consistency of as-deposited and annealed fit parameters and the reproduction of the difference spectra.

Table A.1.: Parameters of modeled silicon-hydrogen stretching modes for the fitting of FTIRS data.

| Name | Hydride type | Position | | FWHM | | Amplitude cm^{-1} |
|------|------------------------------------|--------------------|--------------------|--------------------|-------------------------------|------------------------|
| | | range cm^{-1} | start cm^{-1} | range cm^{-1} | start cm^{-1} | |
| A | SiH | 1980-2020 | 2005 | 5-150 | 80 | free |
| B | SiH clustered/SiH ₂ | 2060-2110 | 2088 | 5-150 | 80 | free |
| C | SiH ₂ surface | — | 2112 | 0-40 | 1 ^y 0 ² | free |
| D | SiH ₂ (O ₂) | 2190-2210 | 2205 | 0-50 | 25 | free |
| E | SiH(O ₃) | — | 2253 | 0-50 | 25 | free |

¹ This value was used for the as-deposited state.

² This value was used for the annealed state.

Calculation of the hydrogen content

For the calculation of the hydrogen content found in the different modes, the method of Langford *et al.* [139] was employed. The hydrogen content N_H^i in a given mode i is connected with its intensity I_i by

$$N_H^i = A_i I_i \quad \text{with } I_i = \int \frac{\alpha_i(\omega)}{\omega} d\omega. \quad (\text{A.7})$$

Here, ω is the frequency in wave numbers, A_i a conversion factor which is proportional to the inverse of the oscillator strength of the mode, and $\alpha_i(\omega)$ the absorption coefficient of the given mode at frequency ω . The integral is performed over a reasonable region hosting the mode. By comparison of FTIRS measurements with nuclear-reaction analysis of the respective layers, Langford *et al.* obtained the following conversion factors:

$$A_{2000} = (9.0 \pm 0.1) \times 10^{19} \text{ cm}^{-2} \quad (\text{A.8})$$

$$A_{2100} = (2.1 \pm 0.2) \times 10^{20} \text{ cm}^{-2}, \quad (\text{A.9})$$

which were used in the present study. Note that these conversion factors do not depend on the association of the HSM to a particular hydrogen configuration (dihydrides or clustered monohydrides) [139]. For the surface-SiH₂ mode, the A_{2100} conversion factor was used. For the analysis of deuterated amorphous silicon, the conversion factors can be estimated by multiplication with $\sqrt{2}$ to account for the different mass of the deuterium atom [26].

For convenience, the hydrogen content of a given mode measured in at. % is often quoted in the present work, which was calculated by

$$C_H = 100 \times \frac{N_H}{N_H + N_{Si}} \quad \text{with } N_{Si} = 5 \times 10^{22} \text{ cm}^{-3}. \quad (\text{A.10})$$

Note that the silicon atom density was assumed to be constant, i.e. the observed variations in the mass density were not taken into account. Thus, the quoted C_H values have to be seen as 'effective atomic percent'.

FTIRS fit results - HP samples

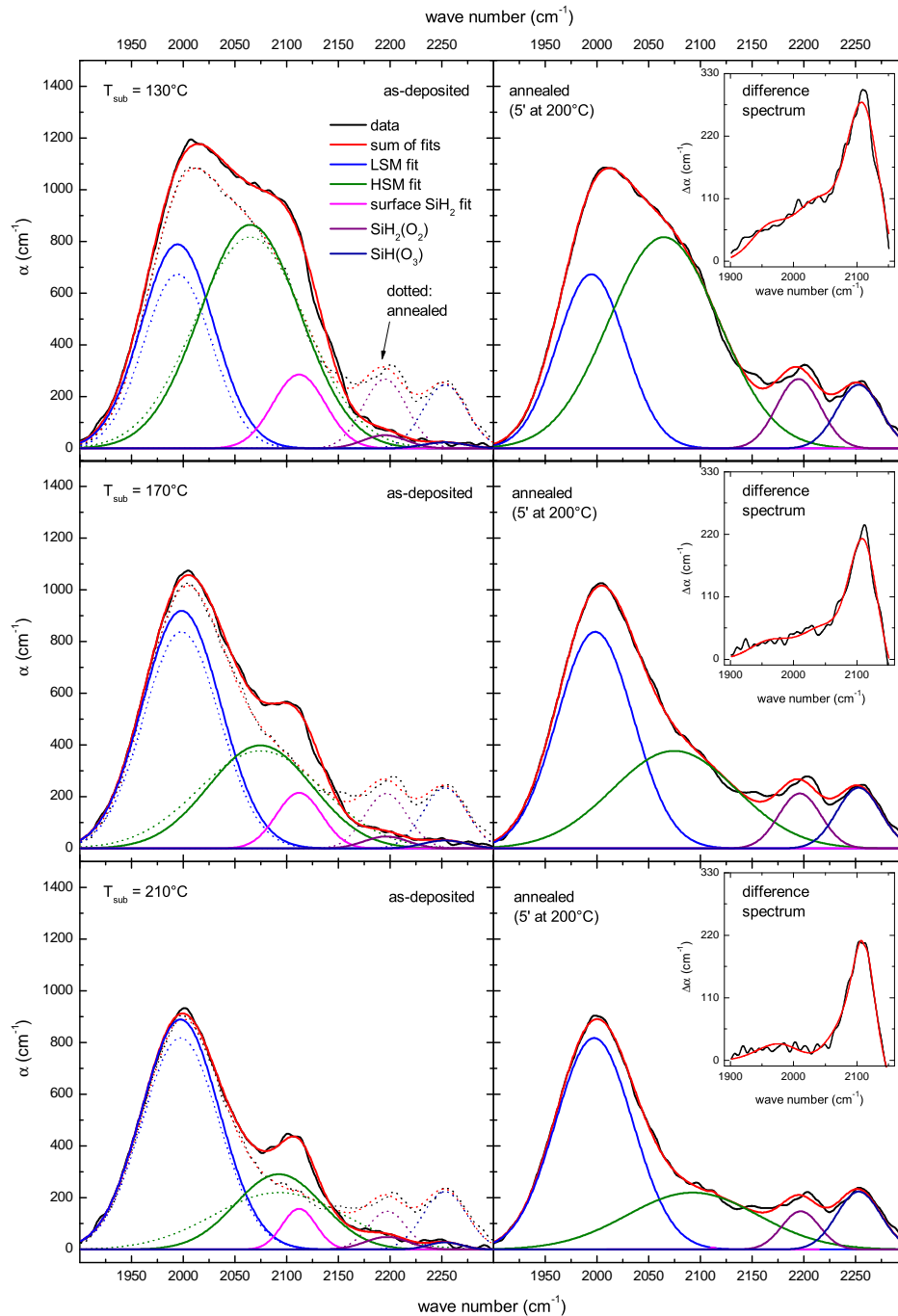


Figure A.3.: Example of fitting results for the FTIR spectra of 10 nm thick (i)a-Si:H layers deposited at the HP parameter sets.

A.2. Photoelectron spectroscopy

Description of photoemission at low excitation energies

Photoemission is based on the photoelectrical effect, which was first observed by Hertz [99] and explained by Einstein [66]. Classically, it is described as a three-step process consisting of photo-excitation of electrons, their transport towards the surface and escape over the work function barrier ϕ_{wf} [237]. Electrons which did not undergo inelastic scattering between excitation and escape carry information about the distribution of kinetic energies in the initial state which can be analyzed. To this end, monochromatic radiation is used for the excitation to define the amount of energy transferred to the electrons, and energy-selective detection is usually employed.

There are different variants of photoelectron spectroscopy with specific assets and drawbacks. The most common techniques (UPS, XPS) employ a fixed excitation energy and detect the energetic distribution of escaping electrons. In total yield spectroscopy, all the emerging photoelectrons are detected while the excitation energy is swept. Finally, in constant-final-state-yield spectroscopy (CFSYS), the count rate of emerging electrons is detected at a fixed final state energy while the excitation energy is varied. In order to understand the specifics of the different methods, it is instructive to review the photoemission process in more detail².

Using the three-step model and assuming the independence of the three steps of the photoemission, the current of primary photoelectrons, which have not undergone inelastic scattering, can be written as

$$I_P(e, \hbar\omega) = J(E, \hbar\omega) \cdot T_{PES}(E) \cdot D(E), \quad (\text{A.11})$$

with the photoionization current J , the transfer function T_{PES} and the escape probability D . The transfer function takes into account the loss of *primary* photoelectrons by inelastic scattering, which may however contribute to the total measured current of photoelectrons as secondary electrons, thus $I_{tot}(E, \hbar\omega) = I_P(E, \hbar\omega) + I_S(E, \hbar\omega)$.

Photoionization

Photoionization is closely related to the optical absorption which is described by the imaginary part of the dielectric function ϵ_2 :

$$\begin{aligned} J(E, \hbar\omega) &\propto \hbar\omega \epsilon_2(\hbar\omega) \propto \frac{1}{\hbar\omega} \sum_{i,f} \langle i | \vec{e}_\nu \cdot \vec{p} | f \rangle \underbrace{\delta(E_i - E_f - \hbar\omega)}_{\text{absorption process}} \underbrace{\delta(E - E_f)}_{\text{en. analyzer}} \\ &\propto \frac{1}{\hbar\omega} P^2(\hbar\omega) N_i(E - \hbar\omega) N_f(E) \\ &\propto \hbar\omega R^2(\hbar\omega) N_i(E - \hbar\omega) N_f(E). \end{aligned} \quad (\text{A.12})$$

Here, the absorption process is described in random-phase approximation (valid for amorphous semiconductors), and $\langle i | \vec{e}_\nu \cdot \vec{p} | f \rangle$ is the matrix element of the ν -th component of the momentum operator between the initial state i and final state f . For

²The following paragraph is based on Ref. [132]

unpolarized light one finds $\langle i | \vec{e}_\nu \cdot \vec{p} | f \rangle \propto P^2$ with the momentum matrix element P^2 , and it is usually assumed that an averaged $P^2(\hbar\omega)$ can be used which only depends on the excitation energy and not on the specific initial and final states [256]. The momentum matrix element $P^2(\hbar\omega)$ is further fundamentally connected to the dipole matrix element $R^2(\hbar\omega)$ by $P^2(\hbar\omega) = m_e^2 \omega^2 \hbar^{-2} R^2(\hbar\omega)$ due to commutator relations. Thus, the last line in equation A.12 is found with the density of initial- and final states N_i and N_f , respectively.

Jackson *et al.* found that $R^2(\hbar\omega)$ peaks at about $\hbar\omega = 3.4$ eV and decays as $R^2(\hbar\omega) \propto (\hbar\omega)^{-5}$ for $\hbar\omega > 3.4$ eV in amorphous silicon [110]. Thus, the current of primary photoelectrons is given by

$$\begin{aligned} I_P(E, \hbar\omega) &\propto \hbar\omega R^2(\hbar\omega) N_i(E - \hbar\omega) N_f(E) \cdot T_{PES}(E) \cdot D(E) \\ &\propto (\hbar\omega)^{-4} N_i(E - \hbar\omega) N_f(E) \cdot T_{PES}(E) \cdot D(E), \end{aligned} \quad (\text{A.13})$$

Mean free path and escape probability $T_{PES}(E)D(E)$

The mean free path λ_{mfp} of excited electrons in silicon due to scattering has a broad minimum at $E_{\text{kin}} = 10 \dots 100$ eV due to electron-phonon and electron-electron interactions [116, 117] as well as plasmon excitation for $E_{\text{kin}} > 16.7$ eV, with $\lambda_{mfp} < 0.5$ nm in this energy region [145]. Thus, to probe more than the mere surface of the sample either high kinetic energies of the photoelectrons are desirable (as realized in XPS) or very low energies that barely suffice to overcome the work function barrier. As for amorphous silicon the work function amounts to about 4 eV, the photoelectrons need to have at least this energy. In the case of $E_{\text{kin}} = 4$ eV, a mean free path of $\lambda_{mfp} \leq 4 \dots 10$ nm results.

It was shown that the product of transfer function and escape probability has a non-trivial but not strongly varying form for photoelectrons with energies in the vicinity of the work function barrier [132]. Taking into account both the limited penetration depth of the exciting UV light and the elastic and inelastic scattering processes, analytical descriptions of $T_{PES}(E) \cdot D(E)$ can be obtained [11]. It is important to note that scattering has a strong impact on the total current of photoelectrons: Only 1-2% of the excited electrons actually escape. At low excitation- and thus low photoelectron energies, the majority of scattering events produces an energy loss which is sufficiently high to impede the escape of the respective electron. Thus, no secondary electrons contribute to the count rate and therefore $I_{\text{tot}}(E, \hbar\omega) \approx I_P(E, \hbar\omega)$.

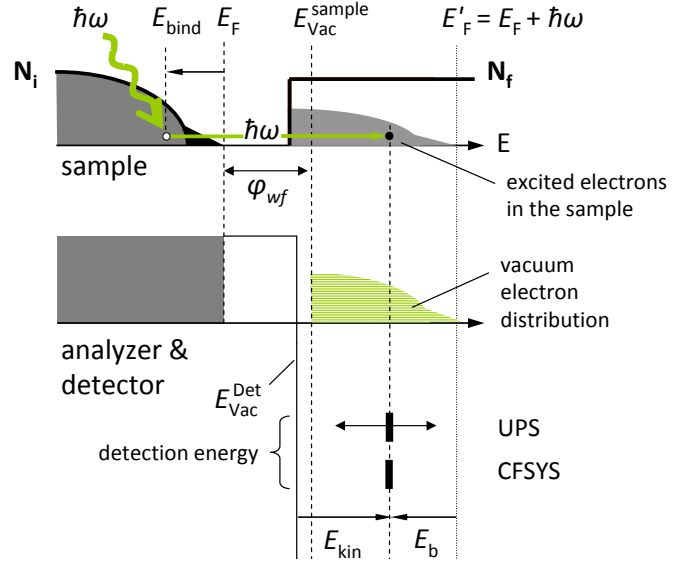
Variants of photoelectron spectroscopy

In the following, the two variants of PES employed in this thesis shall be briefly discussed.

Near-UV UPS: As the matrix element $R^2(\hbar\omega)$ is constant due to a fixed excitation energy $\hbar\omega_f$, it follows from equation A.13 that

$$I_P(E, \hbar\omega_f) \propto N_i(E - \hbar\omega_f) N_f(E) \cdot T_{PES}(E) \cdot D(E). \quad (\text{A.14})$$

Figure A.4: Schematic of the photoemission process and the PES analysis modes. The electrons are excited from the initial state density N_i into the density of final states N_f by monochromatic radiation with energy $\hbar\omega$. After escape into the vacuum (assuming the absence of inelastic scattering), the resulting distribution of excited electrons can be measured by two PES modes. The reference energy is the detector vacuum level E_{Vac}^{Det} , relative to which the kinetic energy of photoelectrons E_{kin} is detected. Sample and detector are electrically connected, thus the Fermi levels align (and not the vacuum levels). The binding energy E_{bind} is measured relative to E_F . The measured spectrum is limited by the E_F on one side and by $E_{bind} = \hbar\omega - e\phi_{wf}$ on the other side.



On the one hand, obviously no assumptions concerning R^2 have to be taken. On the other hand $\hbar\omega$ has to be chosen high enough to provide also the electrons with highest binding energy (i.e. the valence band electrons) with enough kinetic energy to overcome ϕ_{wf} . As the maximum of R^2 is reached at $\hbar\omega = 3.4\text{ eV}$, the sensitivity of the method is *globally* reduced, which is particularly important for the analysis of small concentrations of electronic states in the band gap. Additionally, the dependence of $T_{PES}(E) \cdot D(E)$ on the kinetic energy has to be taken into account, which leads to the excitation depth varying with the binding energy of the electronic states to be quantified, which complicates the analysis. Further, assumptions concerning the density of states in the conduction band have to be taken. In a-Si:H, the conduction band DOS is usually assumed to be energy-independent [272, 274, 283].

CFSYS: As mentioned above, the (final state) kinetic energy of the photoelectrons is fixed at $E_{kin} = E_{an}$ and $\hbar\omega$ is swept in CFSYS. This results in

$$I_P(E_{an}, \hbar\omega) \propto \hbar\omega R^2(\hbar\omega) N_i(E_f - \hbar\omega_f), \quad (\text{A.15})$$

assuming a constant photon flux impinging on the sample. It is obvious from Eq. A.15 that no assumptions concerning the conduction band DOS have to be taken and that E_{an} can be chosen as to yield the maximum photoelectron escape fraction, which allows to maximize both excitation depth and sensitivity of the method. On the other hand, the dependence of the matrix element on the excitation energy has to be taken into account. Here, the dependence $R^2(\hbar\omega) \propto (\hbar\omega)^{-5}$ as found by Jackson [110] is used to analyze the data.

It is important to consider that the reflectivity of the sample and the photon flux provided by the lamp may change with the excitation energy. To take this into account,

the reflectivity R is measured by monitoring both the incident photon flux Φ_{ph} and the reflected flux Φ_R . Then, similar to the internal quantum efficiency introduced in section 3.4, the internal photoelectron yield $Y_{\text{int}}(E_{\text{kin}}, \hbar\omega)$ is calculated via

$$Y_{\text{int}}(E_{an}, \hbar\omega) = \frac{I_{\text{tot}}^{\text{CFSYS}}(E_{an}, \hbar\omega)}{e\Phi_{ph}(1-R)}. \quad (\text{A.16})$$

Thus, in a practical CFSYS experiment,

$$Y_{\text{int}}(E_{an}, \hbar\omega) \propto (\hbar\omega)^{-4} N_i(E_{an} - \hbar\omega_f). \quad (\text{A.17})$$

When the final state energy E_{an} is chosen to yield the maximum flux of photoelectrons, the sensitivity of CFSYS is greatly superior to that of UPS, as can be readily seen from the comparison of spectra in Fig. 3.2.

Data analysis

When analyzing PES data, one has to take into account the energy resolution of the setup which is dependent on the excitation energy due to the impact of the monochromator. This dependence on $\hbar\omega$ does not have an effect on UPS measurements where only the fixed energy resolution of the analyzer has to be taken into account. For CFSYS however, the changing spectral broadening introduced by the monochromator is convoluted with the analyzer function. In both cases however, the 'instrument transfer function' B_{PES} is known. As mentioned above, a forward calculation based on a model DOS $N_{\text{mod}}(E)$ and the transfer function B_{PES} is used to fit the measured data.

In the case of CFSYS, the $(\hbar\omega)^4 Y_{\text{int}}(E, \hbar\omega)$ data are directly proportional to the initial state DOS, thus a fitting of $N_{\text{mod}}(E) * B_{\text{CFSYS}}(E, \hbar\omega)$ to $(\hbar\omega)^4 Y_{\text{int}}(E, \hbar\omega)$ is done. The fitted $N_{\text{mod}}(E)$ can then be normalized to a true DOS as explained in section 3.2.2. For some quantities, such as the energetic position of the valence band edge relative to the Fermi level or the Urbach energy, no normalization is necessary.

For UPS measurements, the usual assumption of a constant a-Si:H conduction band DOS is made, thus $N_{\text{mod}}(E) * B_{\text{UPS}}(E)$ is fitted to $I_{\text{tot}}^{\text{CFSYS}}$, where $B_{\text{UPS}}(E)$ now also contains an assumption concerning the electron-energy-dependence of the transfer- and escape function $T_{PES}(E) \cdot D(E)$, while no photon-energy-dependence of the instrumental broadening has to be incorporated. Again, the resulting fitted $N_{\text{mod}}(E)$ is normalized if required.

A.3. Spectroscopic ellipsometry

General principle of SE

Spectroscopic ellipsometry measures the change in polarization of a light beam upon reflection at the sample surface for varying excitation wavelengths. It exploits the fact that the Fresnel coefficients describing the reflection properties of a surface depend on the angle between the polarization vector of the beam and the plane of incidence. The measured quantity is ρ , the ratio of the complex-valued reflection coefficients:

$$\rho = \frac{r_{\text{par}}}{r_{\text{perp}}} \equiv \tan \Psi \exp(i\Delta). \quad (\text{A.18})$$

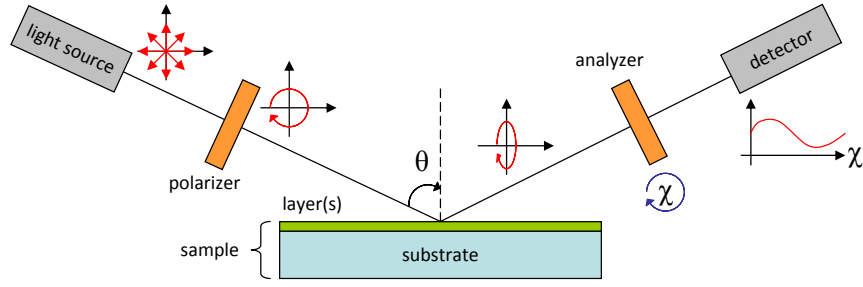


Figure A.5.: Schematic of the spectroscopic ellipsometry setup. The monochromatic light from a suited source (e.g. lamp and monochromator) is circularly polarized and hits the sample. Due to the usually different complex reflection coefficients for the parallel and perpendicular polarization contributions, the reflected light is elliptically polarized. The reflected beam passes a rotatable linear polarizer ('analyzer') which slices the contribution to the polarization in the analyzer plane out of the reflected beam, which is then quantified by the detector. By rotating the analyzer and sweeping the excitation energy, the ratio of the complex reflection coefficients is obtained for each photon energy.

This fundamental equation of ellipsometry defines the quantities Ψ and Δ , where Δ measures the change in phase difference between the two principal polarizations through reflection, and $\tan \Psi$ is the ratio of the amplitudes. The biggest assets of the method are that one measurement yields two quantities and only ratios of measured quantities are analyzed, which avoids reference measurements.

Fig. A.5 shows a schematic of a typical setup: A monochromatic light source (either a laser or a combination of lamp, monochromator and optics) shines light at frequency ω through a circular polarizer onto the sample. Upon incidence on the sample the light wave E_i can be described by

$$\vec{E}_i = E_0 e^{i\omega t} \vec{e}_{\text{par}} + E_0 e^{i\omega t + \delta_0} \vec{e}_{\text{perp}}, \quad (\text{A.19})$$

with the amplitude E_0 and the polarization unit vectors \vec{e}_{par} and \vec{e}_{perp} . The reflection at the sample is described by the complex reflection coefficients $\tilde{r}_{\text{par}} = |r_{\text{par}}| e^{i\delta_{\text{par}}}$ and $\tilde{r}_{\text{perp}} = |r_{\text{perp}}| e^{i\delta_{\text{perp}}}$. Both a change in the amplitude by $|r_{\text{par/perp}}|$ and in the phase by $\delta_{\text{par/perp}}$ can occur. The reflected wave E_r has the form

$$\begin{aligned} \vec{E}_r &= E_0 \tilde{r}_{\text{par}} e^{i\omega t} \vec{e}_{\text{par}} + E_0 \tilde{r}_{\text{perp}} e^{i\omega t + \delta_0} \vec{e}_{\text{perp}} \\ &= E_0 |r_{\text{par}}| e^{i\omega t + \delta_{\text{par}}} \vec{e}_{\text{par}} + E_0 |r_{\text{perp}}| e^{i\omega t + \delta_0 + \delta_{\text{perp}}} \vec{e}_{\text{perp}}. \end{aligned} \quad (\text{A.20})$$

It is quantified by measuring the light intensity after passing through a linear polarizer ('analyzer') with adjustable polarization plane (defined by the angle χ) which samples the contribution to \vec{E}_r in the plane defined by \vec{e}_χ . For the analyzer at angle χ , the light wave after passing the analyzer is described by the projection of the parallel and perpendicular polarization components onto the sampling plane:

$$\vec{E}_{\text{an}} = \left(E_0 |r_{\text{par}}| e^{i\omega t + \delta_{\text{par}}} \cos \chi + E_0 |r_{\text{perp}}| e^{i\omega t + \delta_0 + \delta_{\text{perp}}} \sin \chi \right) \vec{e}_\chi. \quad (\text{A.21})$$

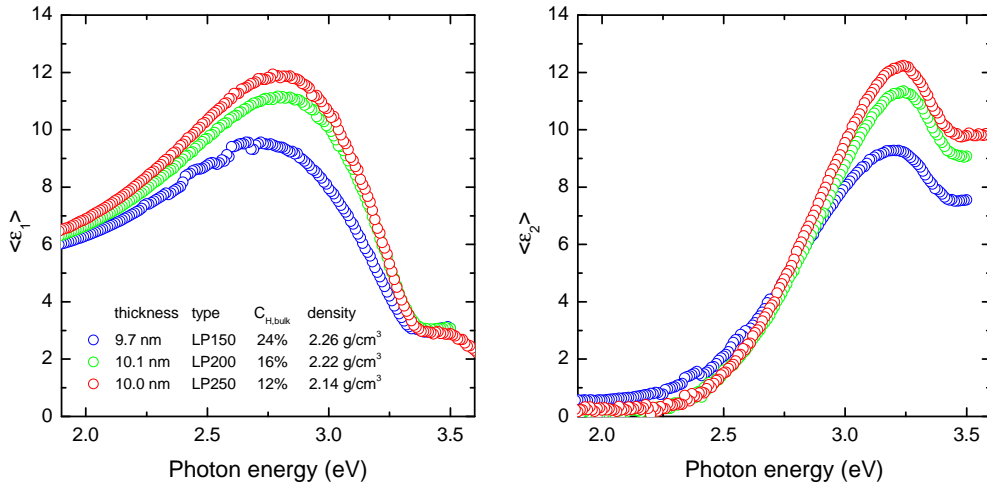


Figure A.6.: Examples of pseudo-dielectric functions for typical (i)a-Si:H layers (LP150, LP200 and LP250). The left panel shows the real part and the right panel the imaginary part of $\langle \epsilon \rangle$. Note that due to the violation of the assumptions underlying the pseudo-dielectric function (a flat semi-infinite medium), the spectra show sharp features at about the photon energy where the a-Si:H films gets transparent.

The detector measures the intensity $I = |\vec{E}|^2$, thus

$$\begin{aligned}
 I(\chi) &= |\vec{E}_{\text{an}}|^2 \\
 &= \frac{1}{2} E_0^2 (|r_{\text{par}}|^2 + |r_{\text{perp}}|^2) [1 - \cos(2\Psi) \cos(2\chi) + \cos \Delta \sin(2\Psi) \sin(2\chi)] \\
 &\equiv S_0 [1 + S_1 \cos(2\chi) + S_2 \sin(2\chi)], \tag{A.22}
 \end{aligned}$$

with Δ and Ψ as defined above. It is obvious that there is a global factor S_0 which depends on the light intensity, and two factors S_1 and S_2 which vary with the analyzer angle χ . By measuring the intensity variation upon turning the analyzer, the so-called Fourier coefficients S_1 and S_2 can be obtained by Fourier analysis. The connection to the ellipsometric angles Ψ and Δ is given by

$$\begin{aligned}
 S_1 &= -\cos(2\Psi) \\
 S_2 &= \sin(2\Psi) \cos \Delta. \tag{A.23}
 \end{aligned}$$

Now, either the set $\{S_1, S_2\}$ or the set $\{\Psi, \Delta\}$ can be analyzed further.

The pseudo-dielectric function

Spectroscopic ellipsometry aims at quantifying the dielectric function of a material. In most cases the material is not present in an isolated form but integrated into a structure as e.g. into a layer stack. It can be shown that in the case of the sample being an ideally flat semi-infinite medium with dielectric function $\epsilon = \epsilon_1 + i\epsilon_2$, the connection between ϵ and ellipsometric parameters is given by [4]

$$\epsilon = \epsilon_1 + i\epsilon_2 = \sin^2 \theta \left[1 + \left(\frac{1 - \rho}{1 + \rho} \right)^2 \tan^2 \theta \right], \tag{A.24}$$

with the angle of incidence θ between the polarized beam and the sample normal. A common first approach to SE data analysis is the calculation of a so-called 'pseudo-dielectric function', which is then termed $\langle\epsilon\rangle$, from equation A.24. This means *assuming* a flat semi-infinite medium for the analysis which is rarely the case in reality. While this approach yields satisfactory results for flat, compact and thick layers, the deviation from the simple assumed structure increases when inhomogeneities such as surface- or interface layers are present, the sample has a rough surface, or only a thin film on a foreign substrate is analyzed. In these cases, model-based fitting of the SE data is compulsory to yield detailed insight and avoid artifacts.

In the present case of 10 nm thick a-Si:H layers, it is obvious that the assumption of a semi-infinite medium is not very promising. For photon energies $\hbar\omega < 3.3$ eV, the penetration depth is more than 10 nm in typical a-Si:H as calculated from the absorption coefficient. Therefore, a significant contribution of the c-Si substrate to the overall optical properties is to be expected. In addition, a surface roughness layer is present in all cases which may distort the results [4]. Nonetheless, the $\langle\epsilon\rangle$ data of exemplary samples shall be given here for comparison. Fig. A.6 shows the $\langle\epsilon_1\rangle$ and $\langle\epsilon_2\rangle$ as derived from SE raw data taken at an angle $\theta = 74^\circ$ for three samples covering the range of a-Si:H deposition conditions. The bulk hydrogen content and the mass density are given in the figure. There are some sharp features in the dielectric functions at about the photon energy where the penetration depth approaches the film thickness which may stem from the varying contribution of the substrate. Apart from these features the general trends are in accordance with the data shown e.g. by Fontcuberta i Morral *et al.* [71] for polymorphous silicon with varying hydrogen content and void density. A closer inspection of the $\langle\epsilon\rangle$ data is not suggested due to the obvious violation of the assumptions underlying the pseudo- ϵ approach. Therefore, the data were analyzed with model-based fitting.

Model-based fitting

As mentioned in section 3.2.3, the data taken at two angles was fitted at once with a single set of parameters. The fits were done in the $\{S_1, S_2\}$ domain with the program *rig-vm*³ [181]. The fit model consisted of a crystalline wafer with known thickness and optical functions from literature [9], the a-Si:H layer parametrized either by the Tauc-Lorentz approach following Jellison *et al.* [114], or with the modified Tauc-Lorentz model of Ferlauto *et al.* [70], and a surface roughness layer with a-Si:H host matrix in the framework of the Bruggeman effective medium approach [30]. The three layers (substrate, a-Si:H bulk and surface roughness) are combined using a coherent transfer matrix formalism which calculates the optical properties of the layer stack based on the dielectric functions of the constituents. Thus, $\{S_1, S_2\}$ values are calculated based on the parametrized optical functions of the single layers, which are then fitted to the measured $\{S_1, S_2\}$ data. The data taken at two angles of incidence θ is fitted with a single set of model parameters. Fig. A.7 displays a typical result of such fitting for the LP200 sample shown in Fig. A.6 as well. Note that the fitted optical model provides excellent agreement with the measured data across the whole range photon energies.

³Fraunhofer Institute for Surface Engineering and Thin Films, Germany

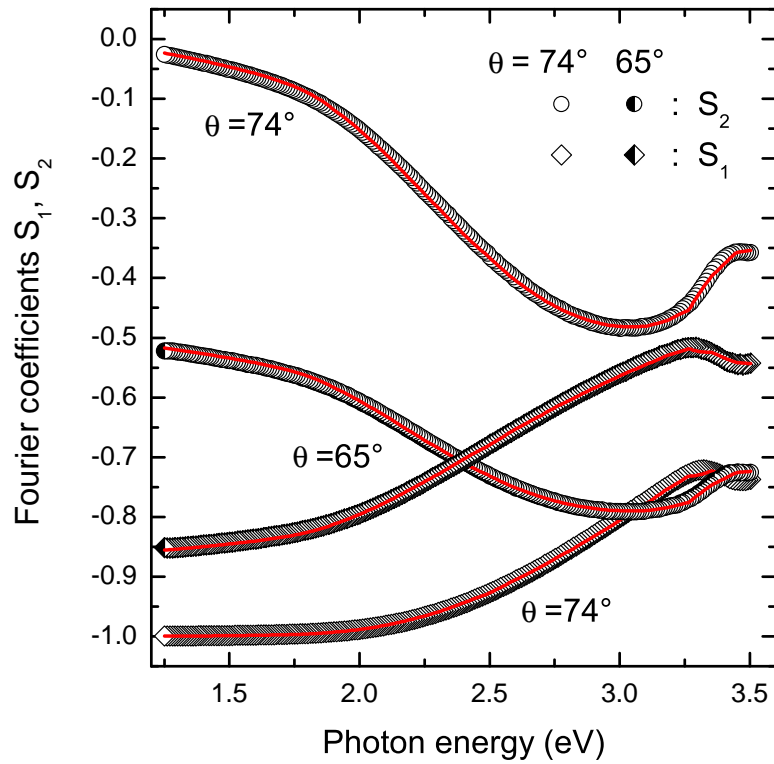


Figure A.7.: Model-based fit of a single set of SE data taken on a LP200 sample. The fits are performed in the $\{S_1, S_2\}$ domain employing the Jellison model to parametrize the a-Si:H layer [114], and both angles of incidence θ are fitted with a single set of parameters.

B. Hydrogen effusion experiments

B.1. Hydrogenated a-Si:H samples

To complement the FTIRS experiments and gain further insight about the H bonding in thin (i)a-Si:H, hydrogen effusion was measured. In a first step, one-sided samples co-deposited with the FTIRS samples were measured, i.e. (i)a-Si:H layers of 10 nm thickness. The samples had identical substrates and the same PECVD runs as the front side a-Si:H layers of the FTIRS samples, while the thickness was checked with SE on the FTIRS samples. It has to be noted that a calibrated measurement of hydrogen desorbing from a film of only 10 nm thickness is extremely challenging, as the signal is in the order of magnitude of the background noise from the hydrogen abundant in the setup and from the substrate. To realize the best conditions for a quantitative measurement, a steep heating ramp was chosen to maximize the desorption rate. This is only possible at the expense of the total number of data points, as the quadrupole spectrometer has a fixed scanning speed. Thus, one data point per 25 K is the resulting thermal resolution of the measurement, which is certainly a trade-off but still permits comparison of the spectra.

Raw data processing

Fig. B.1 shows the calibrated signals for the nine different (i)a-Si:H layers from 200 °C to 1000 °C. It is quite obvious that the H background contributes significantly to the signal which prevents a quantitative analysis without further data processing. In the light of the setup not permitting other measurement options with the given film thickness¹, the only way seems to be a baseline correction 'by eye'. This of course hosts a certain degree of arbitrariness, however by comparison with pertinent effusion data on (i)a-Si:H and auxiliary measurements on deuterated a-Si:D layer it will be attempted to underpin the choice of baseline *a posteriori*. A naïve attempt would be to subtract a line spanning from the first data point at 200 °C to the last one at 1050 °C. However, this leads to an overall form of the spectra which differs greatly from the usual (i)a-Si:H signals, displaying a prominent shoulder at about 900 °C. Additionally, integration of the calibrated spectra then yields total H contents of up to 36 at. % which is in strong opposition to the FTIRS results and does not seem to be realistic, even for thin layers.

Comparison with previously published data on (i)a-Si:H (mostly thicker layers) suggests that the shoulder seen at 900 °C in the raw data is an artifact [56, 57, 64], which may stem from a nonlinearity of the background signal (e.g. the onset of a cutoff in the H background due to exhaust of the H adsorbed on the walls of the setup). Thus

¹Note that a further increase in the heating ramp slope would reduce the resolution on the T axis even further.

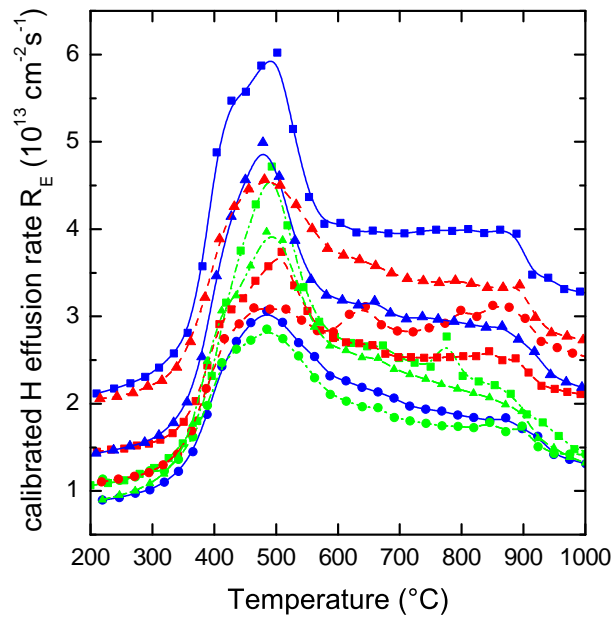


Figure B.1: Raw data of hydrogen effusion measurements performed by F. Einsele at the Forschungszentrum Jülich on 10 nm thick (i)a-Si:H layers. It is obvious that there is a baseline shift resulting from parasitic H signals.

it was chosen to fix the baseline at the top of the 900 °C shoulder, which means at 870...910 °C. Using this value and a second fixed point at the minimum of the signal prior to the onset between 200...280 °C yields the baseline-corrected spectra shown in Fig. B.2a. For comparison, the inset Fig. B.2b displays an (i)a-Si:H effusion spectrum from the literature [56], together with the signal of a hydrogen-terminated c-Si{100} surface. It is obvious that the overall form of the spectra is in good agreement with the literature spectrum. One further notes a dominant change in the amplitude of the peak around 500 °C, depending on the deposition conditions. There are also some slight differences in the high-temperature tail, which are however less pronounced.

Interpretation of effusion data

To interpret this qualitative result, a brief review shall be given of the standard picture used to interpret H effusion results on a-Si:H: It is commonly accepted nowadays that there are two prominent contributions to the H effusion signal in a-Si:H [14, 17–19]: Firstly, the evolution of molecular hydrogen from the inner surfaces of (interconnected) voids, formed by the simultaneous breaking of two Si-H bonds in close proximity, accompanied by the emission of H₂ and the reconstruction of a Si-Si bond. This effect is of course related to the existence of voids in the material and leads to a low-temperature peak in H evolution around 350...400 °C which does not shift in temperature with film thickness. Secondly, the diffusion of atomic hydrogen through compact parts of the film with a final release from the surface, leading to a high-temperature H evolution peak whose exact position on the T axis depends on the film thickness as the process is diffusion-limited. In films of $> 1 \mu\text{m}$ thickness this peak is located around 700 °C, with its position shifting downwards on the T axis to about 500 °C when the film thickness approaches zero. In the light of the typical half width of the peaks of $> 50 \text{ }^\circ\text{C}$, it is thus not to be expected that films of the nm range will display a two-peak structure in

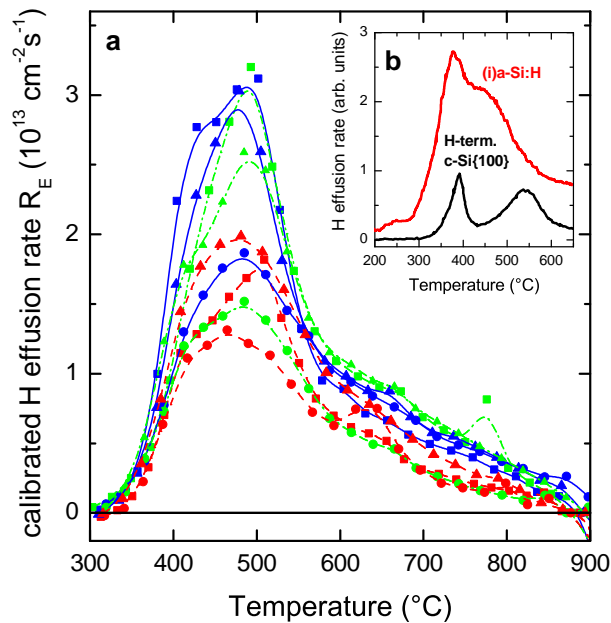


Figure B.2: (a) Baseline-corrected data of hydrogen effusion measurements on 10 nm thick (i)a-Si:H layers. (b) Effusion spectra on (i)a-Si:H and hydrogen-terminated c-Si{100} for comparison (data taken from Ref. [56]).

the given setup. Thus, the one-peak signature of the (i)a-Si:H film analyzed here can be explained from the small thickness of the layers in combination with limited experimental resolution. The superposition of the void- and the bulk-signal leads to a broad peak around 450 $^{\circ}\text{C}$. Due to the insufficient resolution on the T axis, deconvoluting the two contributions is impossible in this case, thus the microstructure as deduced from FTIRS cannot be tested based on the *hydrogen* effusion measurements.

There is however, the possibility to crosscheck the total H content as seen in FTIRS by integrating the calibrated H effusion spectra. It must be noted however, that due to the arbitrariness introduced by the baseline procedure and the poor resolution, the data does not lend itself to a quantitative analysis. Thus, the following must be seen as a zeroth order test of the FTIRS results. After integrating the calibrated signals and calculating the atomic percentage from the a-Si:H atom density, the H content as deduced from H effusion can be compared to the total H content from FTIRS (LSM, HSM and surface SiH_2). The results in Fig. B.3 show a surprisingly clear correlation and even an approximate accordance of the values yielded by the two methods. The slope of the correlation is not 1 but 0.61 ± 0.12 as obtained from a linear fit (dashed red line), which may be caused by a nonlinear background signal. The main conclusion that can be drawn from the H effusion analysis is a confirmation of the general trend in total H content as deduced from FTIRS.

B.2. Deuterated a-Si:D samples

Exchanging the hydrogen for deuterium in the amorphous silicon layers allows to perform D effusion measurement with a much enhanced resolution as the background signal is lower by orders of magnitude and thus a much slower heating ramp can be chosen. To this end, deuterium effusion measurements were performed on two exemplary sam-

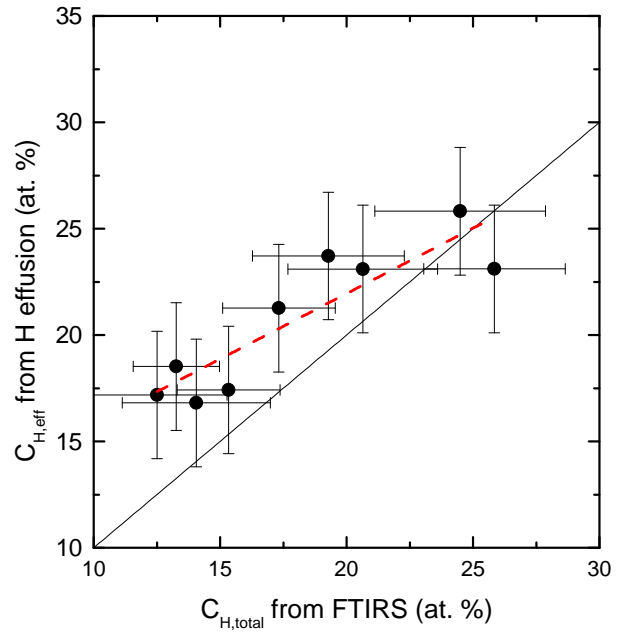


Figure B.3: Comparison of (i)a-Si:H hydrogen content as measured with FTIRS to the integrated H effusion signals. There is a reasonable agreement between the two independently measured data sets, despite the challenges in H effusion on 10 nm thick a-Si:H layers.

ples out of the a-Si:D layers processed for the SIMS analysis. The limited availability of the setup did not allow to measure D effusion for the whole range of (i)a-Si:D deposition conditions, therefore two extreme cases of the spectrum were chosen (LP150 and LP250). The fundamental difference in the resolution can immediately be seen in Fig. B.4: The D effusion spectra indeed show the expected two-peak structure with the peak maxima at approximately 360°C and 460°C, consistent with literature [14, 17, 18]. It is interesting to compare the general form of the spectra to the FTIR spectra shown in Fig. 6.2. As noted above, the low-temperature peak in effusion is related to reconstruction of voids in the material while the high-temperature peak stems from molecular hydrogen originating from broken Si-H bonds which is diffusing in the a-Si:H bulk. Thus, it is tempting to assume a relation between the low-temperature effusion peak and the HSM signal in IR spectroscopy and the high-temperature effusion peak with the LSM. Indeed, this qualitative correlation holds for the two layers analyzed here, as can be seen from the comparison of Fig. B.4 with Fig. 6.2.

Although it must be noted that the relation between H/D effusion and IR spectroscopy is complex [19], the assignment of the HSM to void-related hydrogen helped to reconcile the experimental findings from IR spectroscopy and H effusion [17, 275]. Thus, the qualitative correspondence between the D effusion spectra and the FTIR spectra of the respective layers can be seen as a confirmation of the conclusions drawn in chapter 6 concerning the void density and the two bulk hydrogen phases.

Further deuterium effusion measurements in calibrated mode are currently underway in order to quantitatively support the FTIRS data taken on the deuterated layers.

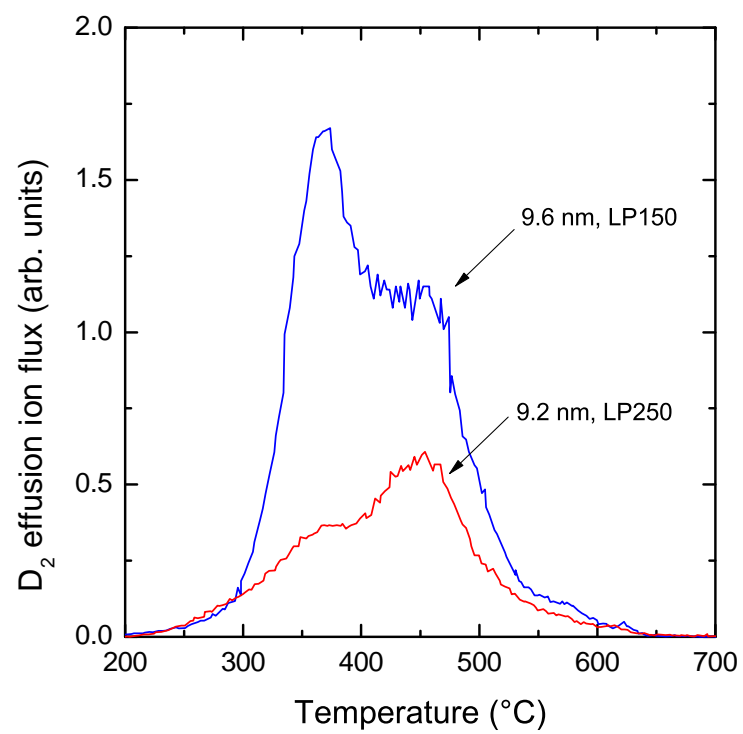


Figure B.4.: Deuterium effusion results on two (i)a-Si:D layers (LP150 and LP250) of 10 nm thickness. The D₂ spectra (full lines) display the expected two-peak structure due to the enhanced resolution when analyzing deuterium effusion.

List of Figures

| | |
|---|----|
| 1.1. Annual output of worldwide solar cell production and share of different technologies | 2 |
| 2.1. Radial atomic distribution function $G(r)$ of a-Si as obtained by x-ray diffraction | 6 |
| 2.2. Molecular orbitals and resulting DOS of a-Si:H | 8 |
| 2.3. Distributed and clustered H in a-Si:H as seen by NMR | 12 |
| 2.4. Dependence of paramagnetic defect density on distributed H in a-Si:H | 13 |
| 2.5. Schematic of hydrogen transport in a-Si:H | 14 |
| 2.6. Generic picture of glass-like behavior and evidence from DC conductivity in a-Si:H | 15 |
| 2.7. Preconditions for metastable behavior | 16 |
| 2.8. Two common types of RF-PECVD reactors | 18 |
| 2.9. Balance of species at the a-Si:H growth front | 19 |
| 2.10. Auger recombination process in indirect semiconductors | 23 |
| 2.11. Injection dependence of the excess carrier lifetime resulting from different bulk recombination mechanisms | 25 |
| 2.12. Numerical solution of semiconductor equations under illumination | 31 |
| 2.13. Band structure of an a-Si:H/c-Si heterojunction solar cell | 37 |
| 3.1. Schematic of the photoelectron spectroscopy (PES) setup | 43 |
| 3.2. Comparison of UPS and CFSYS spectra taken on the same (i)a-Si:H sample | 44 |
| 3.3. Example of CFSYS data analysis and different valence band edge definitions | 48 |
| 3.4. Schematic of the surface photovoltage (SPV) measurement setup | 51 |
| 3.5. Example of forward current dark I-V data | 54 |
| 4.1. a-Si:H/c-Si solar cell efficiencies reached by different institutions | 56 |
| 4.2. Record a-Si:H/c-Si solar cells made at HZB | 57 |
| 4.3. Effective lifetime for different (i)a-Si:H parameters | 60 |
| 4.4. Implied open-circuit voltage for (i)a-Si:H on different c-Si surfaces | 61 |
| 4.5. Doping efficiency for a-Si:H made by PECVD | 63 |
| 4.6. Effective lifetime of (i)a-Si:H and (p/i)a-Si:H stacks with varying (i)a-Si:H thickness | 65 |
| 4.7. Implied V_{oc} of (i)a-Si:H and (p/i)a-Si:H stacks with varying (i)a-Si:H deposition conditions | 66 |
| 4.8. Minority carrier lifetime of (p/i)a-Si:H stacks with varying (i)a-Si:H thickness and (p)a-Si:H doping on DSP (n)c-Si | 67 |

| | |
|---|-----|
| 4.9. Minority carrier lifetime of (p/i)a-Si:H stacks with varying (p)a-Si:H doping on (n)c-Si with different substrate surface morphology | 68 |
| 4.10. Minority carrier lifetime of (n/i)a-Si:H stacks with varying (i)a-Si:H thickness and (n)a-Si:H doping on DSP (p)c-Si | 69 |
| 4.11. Illuminated I/V data for solar cells on (n)c-Si and (p)c-Si comprising undoped buffer layers | 70 |
| 4.12. Reflectance data for selected solar cells on (p)c-Si and (n)c-Si | 72 |
| 4.13. IQE data measured on selected solar cells on (n)c-Si and (p)c-Si and comparison to record cells | 73 |
| 4.14. Variation of FF and j_{sc} with the (i)a-Si:H buffer layer thickness on (n)c-Si and (p)c-Si | 75 |
| 4.15. Solar cell V_{oc} values versus (i)a-Si:H buffer layer deposition conditions | 76 |
| 4.16. Monitoring of implied V_{oc} throughout the processing chain | 78 |
| 5.1. Possible charge carrier transport paths through a-Si:H/c-Si heterojunctions | 85 |
| 5.2. Activation energy of diffusion current density $E_{a,j01}$ for different solar cells | 87 |
| 5.3. Averaged high-forward-bias diode ideality factor $n_{1,avg.}$ for different solar cells | 88 |
| 5.4. Band lineup of a (p)a-Si:H/(n)c-Si solar cell structure and distribution of built-in and applied voltage | 89 |
| 5.5. V_{oc} as implied from the HFB saturation current density $j_{0,1}$ compared to device V_{oc} as measured under illumination | 91 |
| 5.6. Activation energy $E_{a,j02}$ of the low-forward-bias current $j_{0,2}$ vs. the slope of the exponential factor A | 92 |
| 5.7. Photoelectron spectrum of (n)a-Si:H as used in emitters for heterojunction solar cells | 93 |
| 5.8. Results of lock-in thermography measurements on a-Si:H/c-Si solar cells | 96 |
| 5.9. Correlation of the LFB saturation current density $j_{0,2}$ with the value of the effective second diode ideality factor $n_2 = e/(AKT)$ | 97 |
| 6.1. Exemplary FTIR spectrum of a 10 nm thick a-Si:H layer measured in Brewster-angle transmission mode | 104 |
| 6.2. FTIR spectra of (i)a-Si:H layers deposited at different PECVD conditions | 106 |
| 6.3. Hydrogen content found in the three dominant Si-H stretching modes, depending on deposition conditions | 107 |
| 6.4. Contributions of LSM and HSM to total H content, and respective peak positions | 108 |
| 6.5. Optical band gap of (i)a-Si:H layers as derived from modeling of SE data | 109 |
| 6.6. Mass density of (i)a-Si:H films versus bulk hydrogen content | 110 |
| 6.7. He-I UPS valence band spectra of two different (i)a-Si:H layers | 111 |
| 6.8. Correlation between energetic distance of valence band edge and E_F and the bulk hydrogen content in (i)a-Si:H | 113 |
| 6.9. Correlation between valence band Urbach energy E_{0V} and bulk hydrogen content in (i)a-Si:H | 114 |

| | |
|---|-----|
| 6.10. Energetic position of the Gaussian dangling bond distribution versus bulk hydrogen content in (i)a-Si:H | 115 |
| 6.11. (i)a-Si:H bulk defect density N_d plotted against valence band Urbach energy E_{0V} | 116 |
| 6.12. Comparison of H content in a-Si:H and a-Si:D | 119 |
| 6.13. Comparison of H microstructure in a-Si:H and a-Si:D | 120 |
| 6.14. Typical SIMS raw data taken on a 50 nm thick (i)a-Si:D layer | 121 |
| 6.15. SIMS spectra of three different (i)a-Si:D layers in the logarithmic and linear domain | 122 |
| 6.16. Assumed model deuterium distribution and resulting measured SIMS spectrum as calculated with the MRI model | 124 |
| 6.17. MRI fits to the (i)a-Si:D samples deposited with LP parameters. | 126 |
| 6.18. MRI fits to the (i)a-Si:D samples deposited with HP parameters | 127 |
| 6.19. MRI fits to the (i)a-Si:D samples deposited with HP parameters | 128 |
| 6.20. Real-space distribution of deuterium/hydrogen as implied by the MRI analysis | 129 |
| 6.21. Consistency check of the real-space deuterium/hydrogen distributions obtained by the MRI analysis | 130 |
| 6.22. Indication for a structurally poor heterointerface accompanying suboptimal PECVD growth conditions | 131 |
| 7.1. Schematic of the band lineup in an (i)a-Si:H/(n)c-Si heterojunction in equilibrium | 136 |
| 7.2. Valence- and conduction band offsets of (i)a-Si:H/(n)c-Si heterostructures as derived from the combination of PES and SPV data | 139 |
| 7.3. Cross-correlation of a-Si:H optical band gap, valence band tail slope and hydrogen content | 143 |
| 7.4. Correlation of FF and j_{sc} with the Urbach energy E_{0V} of (i)a-Si:H buffer layers | 146 |
| 7.5. Correlation of FF and j_{sc} with the band gap E_g of (i)a-Si:H buffer layers | 147 |
| 7.6. IQE of (n)c-Si solar cells on DSP substrates | 150 |
| 8.1. Correlation of FTIRS-derived hydrogen content with interface defect density | 155 |
| 8.2. FTIR spectra of as-deposited and annealed (i)a-Si:H of different type, and the difference spectra | 157 |
| 8.3. Correlation between H configuration and passivation improvement upon annealing | 158 |
| 8.4. Correlation between the variation in H configuration and the passivation improvement upon annealing | 159 |
| 8.5. Annealing dynamics of (i)a-Si:H on c-Si with {111} and {100} surface orientation | 161 |
| 8.6. Determination of microwave heating characteristics for a (i)a-Si:H/c-Si prototype sample | 163 |

| | |
|--|-----|
| 8.7. Comparison of annealing efficiency of hotplate and microwave in the pulsed annealing regime | 164 |
| 8.8. Correlation of SIMS ^{29}Si matrix peak and bulk deuterium content in (i)a-Si:D | 167 |
| 8.9. As-deposited interface defect density N_{it} plotted against implied surface coverage f_S of c-Si by (i)a-Si:H | 168 |
| 8.10. Correlation of interface defect density N_{it} with (i)a-Si:H bulk hydrogen content in the as-deposited state and after annealing | 170 |
| 8.11. Schematic picture of the a-Si:H/c-Si heterointerface | 171 |
| 8.12. HR-TEM picture of the a-Si:H/c-Si heterointerface | 171 |
| 8.13. Interface defect density N_{it} in the as-deposited and annealed state versus Urbach energy E_{0V} | 174 |
| 8.14. Shift of the Fermi energy at the heterointerface ($E_{F,S}$) by deposition of a doped top layer | 176 |
| 8.15. Interface defect density of single (i)a-Si:H and (p)a-Si:H layers as well as for (p/i)a-Si:H stacks | 177 |
| 8.16. FTIR spectra of single (i)a-Si:H and (p)a-Si:H layers as well as for (p/i)a-Si:H stacks, and the sum spectrum of single (i)a-Si:H and (p)a-Si:H layers | 179 |
| 8.17. Difference spectra of (p/i)a-Si:H stacks and the sum spectra of single (i)a-Si:H and (p)a-Si:H layers | 180 |
| 8.18. Surface recombination velocity S for (i)a-Si:H layers and (p/i)a-Si:H stacks in dependence on the (i)a-Si:H Urbach energy E_{0V} and interface Fermi level $E_{F,S}$ | 181 |
| 8.19. S versus E_{0V} and S versus $E_{F,S}$ data with predictions of the EIDR model | 184 |
| 8.20. Implied V_{oc} for (p/i)a-Si:H/(n)c-Si stacks depending on Urbach energy of the IBL | 189 |
| | |
| A.1. Schematic of the FTIRS setup | 197 |
| A.2. Illustration of FTIRS data processing | 198 |
| A.3. Example of FTIR spectra fit results | 201 |
| A.4. Schematic of the variants of photoelectron spectroscopy | 204 |
| A.5. Schematic of the spectroscopic ellipsometry setup | 206 |
| A.6. Examples of pseudo-dielectric functions for typical (i)a-Si:H layers . . . | 207 |
| A.7. Example of model-based fits of SE data | 209 |
| | |
| B.1. Raw data of hydrogen effusion measurements on 10 nm thick (i)a-Si:H layers | 212 |
| B.2. Baseline-corrected data of hydrogen effusion measurements on 10 nm thick (i)a-Si:H layers | 213 |
| B.3. Comparison of (i)a-Si:H H content as measured with FTIRS to integrated H effusion signals | 214 |
| B.4. Deuterium effusion data on 10 nm thick (i)a-Si:D layers | 215 |

List of Tables

| | |
|---|-----|
| 3.1. Parameters of the lifetime fit model | 50 |
| 4.1. Passivation by different a-Si:H layer combinations on (n)c-Si with polished {111} or textured {100} surface | 58 |
| 4.2. PECVD deposition parameters of the (i)a-Si:H layers analyzed in this thesis | 60 |
| 4.3. j_{sc} values for (n)c-Si and (p)c-Si based solar cells obtained by different methods | 72 |
| 4.4. Development of implied V_{oc} upon successive deposition steps during heterojunction solar cell processing | 77 |
| 5.1. List of transport models applicable to a-Si:H/c-Si heterojunctions | 86 |
| 6.1. Peak assignment of Si-H stretching modes in a-Si:H | 105 |
| 7.1. AFORS-HET solar cell simulation results for (n)c-Si and (p)c-Si based heterojunction solar cells | 148 |
| 8.1. Parameters of the defect pool model | 183 |
| A.1. Modes used for fitting of FTIRS data | 200 |

List of Symbols and Abbreviations

| | |
|-------------------------------------|--|
| α | Absorption coefficient |
| α_i | Absorption coefficient in i -th IR mode |
| β | Precursor loss probability in the description of a-Si:H growth |
| χ | Analyzer angle in spectral ellipsometry |
| ΔD_{it} | Change in interface defect density |
| $\Delta n, \Delta p$ | Excess concentration of electrons and holes under non-equilibrium conditions |
| Δ | Shift in phase difference (spectral ellipsometry analysis parameter) |
| Δ_{db} | Change in dangling bond density |
| $\delta_{par}, \delta_{perp}$ | Phase shifts for two polarizations (spectral ellipsometry analysis parameter) |
| Δ_{Si-H} | Change in Si-H bond density |
| ϵ | Dielectric function |
| ϵ_1 | Real part of dielectric function |
| ϵ_2 | Imaginary part of dielectric function |
| η | Solar cell conversion efficiency |
| η_{IQE} | Internal quantum efficiency |
| γ | Recombination/desorption coefficient of a-Si:H growth precursors |
| λ | Wave length |
| λ_{mfp} | Mean free path |
| $\langle \epsilon \rangle$ | Pseudo-dielectric function |
| $\langle \epsilon_1 \rangle$ | Real part of pseudo-dielectric function |
| $\langle \epsilon_2 \rangle$ | Imaginary part of pseudo-dielectric function |
| ω | Angular frequency |
| ω | Frequency |
| Φ_0 | Incident photon flux |
| $\phi_{a-Si:H}$ | a-Si:H band bending in equilibrium |
| Φ_R | Reflected photon flux |
| ϕ_{wf} | Work function |
| Ψ | Ratio of amplitudes for the two polarizations (spectral ellipsometry analysis parameter) |
| Ψ_{bi} | Built-in potential in p/n junction |
| ρ | Mass density |
| σ | Width of the a-Si:H defect pool |
| σ_n, σ_p | Capture cross section for electrons and holes in Shockley-Read-Hall recombination |
| σ_0 | Prefactor in a-Si:H conductance |
| σ_{DC} | DC conductivity |

| | |
|-------------------------------------|---|
| σ_d | Width of Gaussian defect distribution |
| $\sigma_{n/p}^0$ | Capture cross section for neutral dangling bonds (amphoteric recombination) |
| $\sigma_{n/p}^{+/-}$ | Capture cross section for positively/negatively charged dangling bonds (amphoteric recombination) |
| τ | General lifetime |
| τ_s | Lifetime of precursor molecule in a-Si:H growth |
| τ_{Auger} | Minority carrier lifetime due to Auger recombination |
| τ_{bulk} | Minority carrier lifetime due to general bulk recombination |
| τ_{eff} | Effective minority carrier lifetime |
| τ_{rad} | Minority carrier lifetime due to radiative recombination |
| τ_{SRH} | Minority carrier lifetime due to Shockley-Read-Hall recombination |
| θ | Angle of incidence |
| θ_B | Brewster angle |
| $\tilde{r}_{\text{par/perp}}$ | Complex reflectance parameters for parallel and perpendicular polarization |
| φ | c-Si band bending in equilibrium |
| \vec{e}_α | Unit vector defining the analyzer plane in spectral ellipsometry |
| \vec{e}_{par} | Unit vector defining the plane of parallel polarization |
| \vec{e}_{perp} | Unit vector defining the plane of perpendicular polarization |
| A | Exponential factor of low-forward-bias diode equation |
| a | Si-Si bond length |
| a_3 | Si-Si second-next nearest neighbor distance |
| A_{2000} | Si-H stretching mode conversion factor for 2000 cm^{-1} mode |
| A_{2100} | Si-H stretching mode conversion factor for 2100 cm^{-1} mode |
| A_i | Absorbance in i -th IR mode |
| B | Radiative recombination constant |
| b | Characteristic decay length of deuterium in-diffusion |
| B_{PES} | Broadening function due to finite energy resolution of PES apparatus |
| C | Atomic coordination number |
| c | Velocity of light in vacuum |
| c_0 | Deuterium concentration at the heterointerface |
| $C_{\text{H,bulk}}$ | Hydrogen concentration associated with the bulk IR modes |
| $C_{\text{H,surface}}$ | Hydrogen concentration associated with the surface |
| C_{HSM} | Hydrogen concentration associated with the HSM |
| C_{LSM} | Hydrogen concentration associated with the LSM |
| C_H | Total hydrogen concentration |
| D | Escape probability of photoelectrons |
| d | Layer thickness |
| $D(E)$ | Escape probability of photoelectrons in a-Si:H |
| D^+ | Positively charged dangling bond state |
| D^- | Negatively charged dangling bond state |
| D^0 | Neutral dangling bond state |
| D_0 | Prefactor of hydrogen diffusion coefficient in a-Si:H |

| | |
|--|--|
| D_s | Surface diffusion coefficient of precursor species during a-Si:H growth |
| d_t | Tunneling length |
| d_{depl} | Depletion region width |
| D_{eff} | Effective diffusion constant |
| d_{el} | Electrode distance |
| D_{min} | Minority carrier diffusion constant |
| D_{it} | Interface defect density |
| D_n, D_p | Diffusion constant of electrons and holes |
| E | Electric field |
| $E(k)$ | Energy band dispersion |
| $E^{+/0}$ | Dangling bond energy level for transitions from neutral to positive charge state |
| $E^{0/-}$ | Dangling bond energy level for transitions from neutral to negative charge state |
| E_0 | Amplitude of incident light wave |
| E_B | Energy barrier height |
| E_C | General conduction band energy |
| E_g | General band gap |
| E_i | Intrinsic Fermi energy |
| E_p | Energetic position of a-Si:H defect pool |
| E_r | Reflected light wave |
| E_T | Energy level of localized/trap state |
| E_V | General valence band energy |
| E_{04} | Band gap defined by $\alpha = 10^4 \text{ cm}^{-1}$ |
| E_{0V} | a-Si:H valence band tail slope, Urbach energy |
| $E_{\text{AM1.5}}$ | Spectral power density of AM1.5 solar spectrum |
| E_{center} | Center energy of interface defect distribution |
| E_{don} | Donor state energy |
| E_{pass} | Passing energy of photoelectron energy analyzer |
| E_{tr} | Transport energy in a-Si:H |
| $E_{a,j01}$ | Activation energy of saturation current density $j_{0,1}$ |
| $E_{a,j02}$ | Activation energy of saturation current density $j_{0,2}$ |
| E_{an} | Final state energy of photoelectrons (defined by analyzer settings) |
| E_d | Defect state energy |
| $E_{F,n}$ | Quasi-Fermi level of electrons |
| $E_{F,p}$ | Quasi-Fermi level of holes |
| E_F | Fermi energy |
| $E_{g,\text{a-Si:H}}^\mu$ | a-Si:H mobility band gap |
| $E_{g,\text{a-Si:H}}^{\text{opt}}$ | a-Si:H optical band gap |
| $E_{g,\text{c-Si}}$ | c-Si band gap |
| $E_{V,\text{a-Si:H}}^0$ | a-Si:H valence band edge as defined by linear extrapolation |
| $E_{V,\text{a-Si:H}}^\mu$ | a-Si:H valence band mobility edge |
| $E_{V,\text{a-Si:H}}^{\text{ext}}$ | a-Si:H valence band edge as defined by square-root extrapolation |
| $E_{V,\text{a-Si:H}}^t$ | Energy of transition from a-Si:H valence band tail to the valence band |

| | |
|-------------------------|--|
| $E_{V,c-Si}$ | c-Si valence band edge |
| E_{wb} | Energy of weak bond in a-Si:H valence band tail |
| eeh | Auger process involving two electrons and one hole |
| ehh | Auger process involving one electrons and two holes |
| F^0, F^+, F^- | Occupancy functions for the three charge states of dangling bonds |
| f_m | a-Si:H mass deficiency as compared to compact a-Si |
| f_S | Surface coverage fraction |
| FF | Fill factor of solar cell illuminated I/V curve |
| G | Generation rate |
| $G(r)$ | Radial atomic distribution function |
| g_λ | Depth resolution function due to finite information depth |
| g_σ | Depth resolution function due to surface roughness |
| g_w | Depth resolution function due to atomic mixing |
| I | Total intensity of light beam |
| I_0 | Reference intensity in IR spectroscopy |
| I_{meas} | Deuterium profile measured with SIMS |
| I_{real} | Real-space deuterium distribution |
| I_i | Intensity associated with i-th IR mode |
| I_{tot}^{CFSYS} | Measured photoelectron intensity in CFSYS mode |
| J | Photoionization current |
| j_0 | General saturation current density |
| $j_{0,1}$ | Saturation current density of high-forward bias diode |
| $j_{0,2}$ | Saturation current density of low-forward bias diode |
| j_{hole} | Hole current |
| j_{phot} | Photo-generated current |
| j_F | Forward current in solar cell structure |
| j_{mpp} | Current density at maximum power point |
| j_{sc} | Short-circuit current delivered by solar cell under illumination |
| k | Boltzmann's constant |
| l | Surface diffusion length of a-Si:H growth precursors |
| L_e, L_h | Diffusion length of electrons and holes |
| L_{bulk} | Bulk diffusion length of minority carriers |
| L_{eff} | Effective diffusion length of minority carriers |
| m^* | Electron effective mass |
| m_e | Electron mass |
| N | Number of valence electrons of an atom |
| n, p | Concentration of electrons and holes |
| n_0, p_0 | Equilibrium concentrations of electrons and holes |
| $N_0(U)$ | Distribution function of defect formation energies |
| n_1, p_1 | Reference electron- and hole concentrations for Shockley-Read-Hall recombination |
| n_2 | Low-forwards bias diode ideality factor |
| N_A, N_D | Density of acceptors or donators |
| N_C, N_V | Conduction- and valence band effective density of states |
| N_H^i | Hydrogen content associated with i-th IR mode |

| | |
|------------------------------|--|
| n_i | Intrinsic carrier concentration |
| N_i, N_f | Density of initial states and final states |
| n_S, p_S | Electron- and hole concentration at recombination-active surface |
| N_{0V}^{tail} | Valence band tail DOS prefactor |
| $n_{1,\text{avg.}}$ | High-forward bias diode ideality factor averaged over different temperatures |
| $n_{1,\text{SRH}}$ | Auxiliary quantity for the calculation of SRH recombination rate |
| n_1 | High-forward bias diode ideality factor |
| N_d | Bulk defect density |
| n_d | General diode ideality factor |
| N_{it} | Interface defect density |
| $N_{\text{mod}}(E)$ | a-Si:H model density of states used for fitting PES data |
| N_t | c-Si bulk defect density |
| N_{V0} | Density of states at the a-Si:H valence band edge |
| N_{wb} | Density of weak Si-Si bonds |
| P_3^0 | Neutral phosphorous atom (valence state three) |
| P_4^+ | Positively charged phosphorous atom (valence state four) |
| p_C | Chamber pressure in PECVD system |
| p_{in} | Incident power density (in the form of radiation) |
| R | Reflectance |
| r | General distance |
| R^2 | Dipole matrix element |
| r_g | a-Si:H growth rate |
| R_H | Hydrogen dilution factor in PECVD deposition |
| R_P | Parallel resistance in solar cell equivalent circuit |
| R_S | Series resistance in solar cell equivalent circuit |
| S | Surface recombination velocity |
| S_0, S_1, S_2 | Fourier coefficients (spectral ellipsometry analysis parameter) |
| S_{back} | Back-side surface recombination velocity |
| S_{front} | Front-side surface recombination velocity |
| Si_4^0 | Neutral silicon atom (valence state four) |
| T | General temperature |
| T^* | Equilibration temperature in defect pool model |
| T_G | Glass temperature |
| T_{anneal} | Annealing temperature |
| T_{depo} | Nominal deposition temperature |
| T_Q | Quench temperature |
| T_{sub} | Substrate temperature |
| T_{PES} | Transfer function of photoelectrons in a-Si:H |
| U | General Coulomb correlation energy |
| U_F | General formation energy |
| U_i | Recombination rate for i-th recombination process |
| $U_{\text{a-Si:H}}$ | Correlation energy for a-Si:H dangling bonds |
| U_{d0} | Formation energy for neutral defects |
| V | General (applied) voltage |

| | |
|------------------------|--|
| V_1, V_2 | Partition of external voltage in material 1 and 2 |
| v_{th} | Thermal velocity of charge carriers |
| V_{D1}, V_{D2} | Partition of built-in voltage in material 1 and 2 |
| V_{mpp} | Voltage at maximum power point |
| V_{oc} | Open circuit voltage of a solar cell under illumination |
| V_{SPV} | Surface photovoltage |
| W | Wafer thickness |
| w | Characteristic length of atomic mixing in SIMS analysis |
| w_0 | Width of Gaussian pileup in SIMS analysis |
| x | General spatial coordinate |
| X_e, X_h | Transmission factors for electrons and holes in Anderson model |
| x_p | Position of pile-up function in SIMS analysis |
| Z | Optimum number of covalent bonds of an atom |
| ' | minute |
| (i)a-Si:H | Undoped hydrogenated amorphous silicon |
| (n/p)a-Si:H | n-/p-doped hydrogenated amorphous silicon |
| (n/p)c-Si | n-/p-doped crystalline silicon |
| '' | inch |
| a-Si | Amorphous silicon |
| a-Si:H | Hydrogenated amorphous silicon |
| AFORS-HET ... | 'Automat for the simulation of heterostructures' (software) |
| AM1.5 | Air mass 1.5 (solar spectrum) |
| ATR | Attenuated total reflection |
| BC-SHJ | Back-contacted silicon heterojunction solar cell |
| BSF | Back-surface field |
| c-Si | Crystalline silicon |
| C/V | Capacitance/voltage |
| CB | Conduction band |
| CFSYS | Constant-final-state yield photoelectron spectroscopy |
| CRN | Continuous random network |
| CVD | Chemical vapor deposition |
| CZ | Czochralski-grown |
| D | Deuterium |
| DB | Dangling bond |
| DC | Direct current |
| DLIT | Dark lock-in thermography |
| DOS | Density of states |
| DRF | Depth resolution function |
| DSP | Double-side polished |
| ECR | Electron cyclotron resonance |
| EDMR | Electrically detected magnetic resonance |
| EIDR | Equilibrated interface defect recombination |
| EQE | External quantum efficiency |
| ESR | Electron spin resonance |
| ETP | Expanding thermal plasma |

| | |
|-----------------------|--|
| FTIRS | Fourier-transform infrared spectroscopy |
| FZ | Float-zone-grown |
| H | Hydrogen |
| HF | Hydrofluoric acid |
| HFB | High forward bias |
| HIT | 'Heterojunction with intrinsic thin layer' (Sanyo) |
| HJ | Heterojunction |
| HP, HP _{xxx} | 'High pressure' (a-Si:H deposition parameter set), xxx= <i>nominal</i> temperature |
| HR-TEM | High-resolution transmission electron microscopy |
| HSM | High-frequency stretching mode (in a-Si:H IR spectroscopy) |
| HV | High vacuum |
| HWCVD | Hot-wire chemical vapor deposition |
| I/V | Current-voltage |
| IBL | Undoped hydrogenated amorphous silicon buffer layer |
| IPA | Isopropyl alcohol |
| IPE | Internal photoemission |
| IQE | Internal quantum efficiency |
| IR | Infrared |
| ITO | Indium tin oxide |
| KOH | Potassium hydroxide |
| LFB | Low forward bias |
| LP, LP _{xxx} | 'Low pressure' (a-Si:H deposition parameter set), xxx= <i>nominal</i> temperature |
| LRO | Long-range order |
| LSM | Low-frequency stretching mode (in a-Si:H IR spectroscopy) |
| MCT | Mercury-cadmium-telluride |
| MIS | Metal-insulator-semiconductor |
| MP, MP _{xxx} | 'Medium pressure' (a-Si:H deposition parameter set), xxx= <i>nominal</i> temperature |
| MRI | Mixing-roughness-information depth model (in SIMS analysis) |
| MRO | Medium-range order |
| MTCE | Multi-tunneling capture/emission model |
| MW | Microwave |
| NMR | Nuclear magnetic resonance |
| NUVPES | Near-ultraviolet photoelectron spectroscopy |
| PCD | Photoconductance decay |
| PECVD | Plasma-enhanced chemical vapor deposition |
| PES | Photoelectron spectroscopy |
| PL | Photoluminescence |
| PV | Photovoltaics |
| QMS | Quadrupole mass spectrometer |
| RCA | 'Radio Company of America' (silicon cleaning procedure) |
| RDF | Radial distribution function |
| RF | Radio frequency |

| | |
|-----------------|--|
| rig-vm | Simulation system for optical properties of thin films |
| SC | Solar cell |
| SE | Spectral ellipsometry |
| SHJ | Silicon heterojunction |
| SIMS | Secondary-ion mass spectroscopy |
| SPV | Surface photovoltage |
| SR | Spectral response |
| SRH | Shockley-Read-Hall |
| SRO | Short-range order |
| TCO | Transparent conductive oxide |
| TE | Thermionic emission |
| UHV | Ultra-high vacuum |
| UPS | Ultraviolet excitation photoelectron spectroscopy |
| UV | Ultraviolet |
| VB | Valence band |
| VHF | Very high frequency |
| XPS | x-ray excitation photoelectron spectroscopy |
| ZnO, ZnO:Al ... | (Al-doped) Zinc oxide |

Bibliography

- [1] V. V. Afanas'ev. *Internal Photoemission Spectroscopy: Principles and Applications*. Elsevier, Oxford, UK, 1 edition, 2008.
- [2] D. C. Allan and J. D. Joannopoulos. Electronic Structure of Hydrogenated Amorphous Silicon. *Physical Review Letters*, 44(1):43–47, Jan 1980.
- [3] G. Allan, C. Delerue, and M. Lannoo. Electronic structure and localized states in a model amorphous silicon. *Physical Review B*, 57(12):6933–6936, Mar 1998.
- [4] I. An, H. Arwin, C. Chen, R. W. Collins, A. S. Ferlauto, J. N. Hilfiker, J. Humlicek, E. A. Irene, G. E. Jellison, J. Lee, F. A. Modine, A. Röseler, M. Schubert, H. G. Tompkins, and J. A. Zapien. *Handbook of Ellipsometry*. William Andrew Publishing/Springer, 2005.
- [5] P. W. Anderson. Absence of diffusion in certain random lattices. *Physical Review*, 109(5):1492–1505, Mar 1958.
- [6] R. L. Anderson. Experiments on Ge-GaAs Heterojunctions. *Solid State Electronics*, 5:341–51, 1962.
- [7] H. Angermann, T. F. Schulze, E. Conrad, J. Rappich, L. Korte, and M. Schmidt. Cleaning and passivation of structured n-type Si substrates: Preparation and interface properties of a-Si:H/c-Si hetero solar cells. In *Proc. of the 23rd Eur. PVSEC, 2008, Valencia, Spain*, pages 1422–6, 2008.
- [8] N. Archontas, N. Georgoulas, C. A. Dimitriadis, F. Templier, M. Oudwan, and G. Kamarinos. Two dimensional simulation and modeling of the electrical behavior in nanocrystalline silicon thin-film transistors. *Journal of Applied Physics*, 103(10):104507, 2008.
- [9] M. Auslender and S. Hava. Doped n-type Silicon (n-Si). In E. D. Palik, editor, *Handbook of Optical Constants of Solids*, pages 571–86. Academic Press, Inc., Orlando, 1985.
- [10] Misc. authors. Trends in Photovoltaic Applications. Technical report, International Energy Agency, 2010.
- [11] C. N. Berglund and W. E. Spicer. Photoemission Studies of Copper and Silver: Theory. *Physical Review*, 136:A1030–44, 1964.
- [12] Hannes Ner Beushausen. Charakterisierung und thermische Nachbehandlung von ultradünnen amorphen Silizium-Schichten. Master's thesis, Universität Bremen, 2010.

- [13] W. Beyer. Structural and electronic properties of silicon-based amorphous alloys. *Journal of Non-Crystalline Solids*, 97-8(2):1027–1034, 1987.
- [14] W. Beyer. Hydrogen effusion: A probe for surface desorption and diffusion. *Physica B: Condensed Matter*, 170(1-4):105 – 114, 1991.
- [15] W. Beyer, R. Hager, H. Schmidbaur, and G. Winterling. Improvement of the photoelectric properties of amorphous SiC_x:H by using disilylmethane as a feeding gas. *Applied Physics Letters*, 54(17):1666–1668, 1989.
- [16] W. Beyer, H. Mell, and H. Overhof. Electronic transport in hydrogenated amorphous silicon. *Journal de Physique (Paris)*, 42(C-4, pt.1):103–6, 1983.
- [17] W. Beyer and H. Wagner. The role of hydrogen in a-Si:H – results of evolution and annealing studies. *Journal of Non-Crystalline Solids*, 59-60(1):161 – 168, 1983. Proceedings of the Tenth International Conference on Amorphous and Liquid Semiconductors.
- [18] W. Beyer, H. Wagner, J. Chevallier, and K. Reichelt. Comparative study of hydrogen evolution from amorphous hydrogenated silicon films. *Thin Solid Films*, 90(2):145 – 152, 1982.
- [19] D. K. Biegelsen, R. A. Street, C. C. Tsai, and J. C. Knights. Hydrogen evolution and defect creation in amorphous Si:H alloys. *Physical Review B*, 20(12):4839–4846, Dec 1979.
- [20] C. Bittencourt and F. Alvarez. *Amorphous Silicon and its Alloys*, chapter 3.8, pages 174–179. INSPEC, edited by T. Searle, 1998.
- [21] G. Blatter. Quantum mechanics. Lecture Notes, ETH Zürich, 2006.
- [22] C. Boehme, J. Behrends, K. v. Maydell, M. Schmidt, and K. Lips. Investigation of hopping transport in n-a-Si:H/c-Si solar cells with pulsed electrically detected magnetic resonance. *Journal of Non-Crystalline Solids*, 352:1113–6, 2006. Proceedings of the 21st International Conference on Amorphous and Nanocrystalline Semiconductors (ICANS 21).
- [23] K. Bothe, R. Sinton, and J. Schmidt. Fundamental Boron-Oxygen-related carrier lifetime limit in mono- and multicrystalline Silicon. *Progress in Photovoltaics: Research and Applications*, 13(4):287–296, 2005.
- [24] O. Breitenstein, P. P. Altermatt, K. Ramspeck, M. A. Green, J. Zhao, and A. Schenk. Interpretation of the commonly observed I–V characteristics of c-Si cells having ideality factor larger than two. In S. G. Bailey, editor, *Proceedings IVth World Conference on Photovoltaic Energy Conversion*, pages 879–884, IEEE, Piscataway, New York, 2006.
- [25] O. Breitenstein, J. Bauer, A. Lotnyk, and J.-M. Wagner. Defect induced non-ideal dark I–V characteristics of solar cells. *Superlattices and Microstructures*, 45:182–189, 2009.

- [26] M. H. Brodsky, Manuel Cardona, and J. J. Cuomo. Infrared and Raman spectra of the silicon-hydrogen bonds in amorphous silicon prepared by glow discharge and sputtering. *Physical Review B*, 16(8):3556, October 1977.
- [27] M. H. Brodsky, G. H. Döhler, and P. J. Steinhardt. On the measurement of the conductivity density of states of evaporated amorphous silicon films. *physica status solidi b*, 72(2):761–770, 1975.
- [28] M. H. Brodsky and R. S. Title. Electron Spin Resonance in Amorphous Silicon, Germanium, and Silicon Carbide. *Physical Review Letters*, 23(11):581–585, Sep 1969.
- [29] T. M. Brown, C. Bittencourt, M. Sebastiani, and F. Evangelisti. Electronic States and Band Lineups in C-Si(100)/a-Si_{1-x}C_x:H Heterojunctions. *Physical Review B*, 55:9904–9, 1997.
- [30] D. A. G. Bruggemann. Dielektrizitätskonstanten und Leitfähigkeiten der Mischkörper aus isotropen und anisotropen Substanzen. *Annalen der Physik (Leipzig)*, 5(24):636, 1935.
- [31] M. Z. Burrows, U. K. Das, S. Bowden, S. S. Hegedus, R. L. Opila, and R. W. Birkmire. Improved Passivation of a-Si:H / c-Si Interfaces Through Film Restructuring. In *MRS Symp. Proc.*, volume 1066, pages 1066–A02–05, 2008.
- [32] M. Z. Burrows, U. K. Das, R. L. Opila, S. De Wolf, and R. W. Birkmire. Role of hydrogen bonding environment in a-Si:H films for c-Si surface passivation. *Journal of Vacuum Science and Technology A*, 26:683–687, July 2008.
- [33] V. A. Burrows, Y. J. Chabal, G. S. Higashi, K. Raghavachari, and S. B. Christman. Infrared spectroscopy of Si(111) surfaces after HF treatment: Hydrogen termination and surface morphology. *Applied Physics Letters*, 53(11):998–1000, 1988.
- [34] P. Rocai Cabarrocas, Y. Bouizem, and M. L. Theye. Defect density and hydrogen bonding in hydrogenated amorphous silicon as functions of substrate temperature and deposition rate. *Philosophical Magazine B*, 65(5):1025–1040, 1992.
- [35] F. Capasso and G. Margaritondo, editors. *Heterojunction Band Discontinuities - Physics and Device Applications*. North-Holland, Amsterdam, 1987.
- [36] S. Chakraborty and D. A. Drabold. Static and dynamic properties of hydrogenated amorphous silicon with voids. *Physical Review B*, 79(11):115214, Mar 2009.
- [37] W. Y. Ching, Daniel J. Lam, and Chun C. Lin. Theoretical studies of electronic states produced by hydrogenation of amorphous silicon. *Physical Review Letters*, 42(12):805–808, Mar 1979.
- [38] W. Y. Ching, Daniel J. Lam, and Chun C. Lin. Electronic states and bonding configurations in hydrogenated amorphous silicon. *Physical Review B*, 21(6):2378–2387, Mar 1980.

- [39] G. D. Cody. Urbach Edge, Disorder, and Absorption On-set in a-Si:H. In *Amorphous and Nanocrystalline Silicon Science and Technology*, volume 862 of *MRS Symposia Proceedings*, page A1.3.1, 2005.
- [40] G. D. Cody, T. Tiedje, B. Abeles, B. Brooks, and Y. Goldstein. Disorder and the Optical-Absorption Edge of Hydrogenated Amorphous Silicon. *Physical Review Letters*, 47(20):1480–1483, Nov 1981.
- [41] G. D. Cody, C. R. Wronski, B. Abeles, R. B. Stephens, and B. Brooks. Optical characterization of amorphous silicon hydride films. *Solar Cells*, 2:227–43, 1980.
- [42] P.G. Le Comber and W.E. Spear. Electronic Transport in Amorphous Silicon Films. *Physical Review Letters*, 25:509–11, 1970.
- [43] G.A.N. Connell and William Paul. Is there an intimate relation between amorphous and crystalline semiconductors? *Journal of Non-Crystalline Solids*, 8-10:215 – 222, 1972.
- [44] P.J. Cousins, D.D. Smith, H.C. Luan, J. Manning, T.D. Dennis, A. Waldhauer, K.E. Wilson, G. Harley, and G.P. Mulligan. Gen III: improved performance at lower cost. In *Conference Proceedings of the 35th IEEE PVSC*, 2010.
- [45] M. Cuniot and Y. Marfaing. Energy-Band Diagram of the a-Si:H/c-Si Interface as Determined by Internal Photoemission. *Philosophical Magazine B*, 57:291–300, 1988.
- [46] CEA-INES D. Munoz. Personal communication (2011).
- [47] J. Damon-Lacoste and P. Roca i Cabarrocas. Toward a better physical understanding of a-Si:H/c-Si heterojunction solar cells. *Journal of Applied Physics*, 105(6):063712–7, March 2009.
- [48] J. Damon-Lacoste, P. Roca i Cabarrocas, P. Chatterjee, Y. Veschetti, A.S. Gudovskikh, J.P. Kleider, and P.J. Ribeyron. About the efficiency limits of heterojunction solar cells. *Journal of Non-Crystalline Solids*, 352(9-20):1928 – 1932, 2006.
- [49] U. Das, S. Bowden, M. Burrows, S. Hegedus, and R. Birkmire. Effect of process parameter variation in deposited emitter and buffer layers on the performance of silicon heterojunction solar cells. In *Conference Record of the 2006 IEEE 4th World Conference on Photovoltaic Energy Conversion*, pages 1283–6, 2006.
- [50] U. Das, M. Lu, D. Xu, O. Jani, S. Bowden, S. Hegedus, and R. Birkmire. Designing Rear Surface for Carrier Transport in all back contact silicon heterojunction solar cells. In *Proceedings of 18th Photovoltaic Solar Energy Conference, Kolkata, India*, pages 1283–6, 2009.
- [51] U. K. Das, M. Z. Burrows, M. Lu, S. Bowden, and R. W. Birkmire. Surface passivation and heterojunction cells on Si (100) and (111) wafers using DC and RF plasma deposited Si:H thin films. *Applied Physics Letters*, 92:063504–3, 2008.

- [52] S. Dauwe, J. Schmidt, and R. Hezel. Very low surface recombination velocities on p- and n-type silicon wafers passivated with hydrogenated amorphous silicon films. In *Conf. Rec. 29th IEEE PV Spec. Conf.*, pages 1246–9, 2002.
- [53] C.G. Van de Walle and L. H. Yang. Band discontinuities at heterojunctions between crystalline and amorphous silicon. *Journal of Vacuum Science and Technology B*, 13:1635–8, 1995.
- [54] S. de Wolf, H. Fujiwara, and M. Kondo. Impact of annealing on passivation of a-Si:H / c-Si heterostructures. In *Proc. 33rd IEEE Photovoltaic Specialists Conference*, San Diego, CA, 2008. IEEE Operations Center.
- [55] S. de Wolf and M. Kondo. Abruptness of a-Si:H/c-Si interface revealed by carrier lifetime measurements. *Applied Physics Letters*, 90:042111, 2007.
- [56] S. de Wolf and M. Kondo. Boron-doped a-Si:H/c-Si interface passivation: Degradation mechanism. *Applied Physics Letters*, 91:112109, 2007.
- [57] S. de Wolf and M. Kondo. Nature of doped a-Si:H/c-Si interface recombination. *Journal of Applied Physics*, 105(10):103707, 2009.
- [58] S. de Wolf, S. Olibet, and C. Ballif. Stretched-exponential a-Si:H/c-Si interface recombination decay. *Applied Physics Letters*, 93:032101, 2008.
- [59] H. Dember. *Zeitschrift für Physik*, 32:554, 1932.
- [60] D. Diouf, J.P. Kleider, T. Desrues, and P.J. Ribeyron. 2D simulations of interdigitated back contact heterojunction solar cells based on n-type crystalline silicon. *physica status solidi (c)*, pages 1033–6, 2010.
- [61] J. Dong and D. A. Drabold. Atomistic Structure of Band-Tail States in Amorphous Silicon. *Physical Review Letters*, 80(9):1928–1931, Mar 1998.
- [62] B. Dunn and J. D. Mackenzie. Transport properties of glass-silicon heterojunctions. *Journal of Applied Physics*, 47(3):1010–1014, 1976.
- [63] J. Dziewior and W. Schmid. Auger coefficients for highly doped and highly excited silicon. *Applied Physics Letters*, 31(5):346–348, 1977.
- [64] F. Einsele. *Amorphe Siliziumoxidschichten zur Oberflächenpassivierung und Kontaktierung von Heterostruktur-Solarzellen aus amorphem und kristallinem Silizium*. Dissertation, RWTH Aachen, 2010.
- [65] F. Einsele, P. J. Rostan, M. B. Schubert, and U. Rau. Recombination and resistive losses at ZnO/a-Si:H/c-Si interfaces in heterojunction back contacts for Si solar cells. *Journal of Applied Physics*, 102:094507–6, November 2007.
- [66] A. Einstein. Über einen die Erzeugung und Verwandlung des Lichtes betreffenden heuristischen Gesichtspunkt. *Annalen der Physik (Leipzig)*, 17:134–48, 1905.

- [67] J. M. Essick and J. D. Cohen. Band offsets and deep defect distribution in hydrogenated amorphous silicon-crystalline silicon heterostructures. *Applied Physics Letters*, 55:1232–4, 1989.
- [68] P. A. Fedders, D. A. Drabold, and S. Nakhmanson. Theoretical study on the nature of band-tail states in amorphous Si. *Physical Review B*, 58(23):15624–15631, Dec 1998.
- [69] L. Feitknecht, J. Meier, P. Torres, J. Zürcher, and A. Shah. Plasma deposition of thin film silicon: kinetics monitored by optical emission spectroscopy. *Solar Energy Materials and Solar Cells*, 74(1-4):539 – 545, 2002.
- [70] A. S. Ferlauto, G. M. Ferreira, J. M. Pearce, C. R. Wronski, R. W. Collins, Xunming Deng, and Gautam Ganguly. Analytical model for the optical functions of amorphous semiconductors from the near-infrared to ultraviolet: Applications in thin film photovoltaics. *Journal of Applied Physics*, 92(5):2424–2436, 2002.
- [71] A. Fontcuberta i Morral, P. Roca i Cabarrocas, and C. Clerc. Structure and hydrogen content of polymorphous silicon thin films studied by spectroscopic ellipsometry and nuclear measurements. *Physical Review B*, 69(12):125307, Mar 2004.
- [72] E. C. Freeman and W. Paul. Optical constants of rf sputtered hydrogenated amorphous Si. *Physical Review B*, 20(2):716–728, Jul 1979.
- [73] W. Fuhs, G. Heder, K. Niemann, and J. Stuke. Properties of junctions between amorphous and crystalline silicon. In *Proceedings of the 6th International Conference on Amorphous and Liquid Semiconductors, Leningrad (USSR)*, pages 343–8. Soviet Academy of Sciences, A.F. Ioffe, 1975.
- [74] H. Fujiwara, T. Kaneko, and M. Kondo. Application of hydrogenated amorphous silicon oxide layers to c-Si heterojunction solar cells. *Applied Physics Letters*, 91:133508–3, 2007.
- [75] H. Fujiwara and M. Kondo. Real-time monitoring and process control in amorphous/crystalline silicon heterojunction solar cells by spectroscopic ellipsometry and infrared spectroscopy. *Applied Physics Letters*, 86:032112, 2005.
- [76] H. Fujiwara and M. Kondo. Effects of a-Si:H layer thicknesses on the performance of a-Si:H/c-Si heterojunction solar cells. *Journal of Applied Physics*, 101:054516–9, 2007.
- [77] H. Fujiwara, M. Kondo, and A. Matsuda. Real-time studies of amorphous and microcrystalline Si:H growth by spectroscopic ellipsometry and infrared spectroscopy. *Thin Solid Films*, 455-456:670–4, 2004.
- [78] H. Fujiwara, Y. Toyoshima, M. Kondo, and A. Matsuda. Interface-layer formation mechanism in a-Si:H thin-film growth studied by real-time spectroscopic ellipsometry and infrared spectroscopy. *Physical Review B*, 60:13598–604, 1999.

- [79] J. Furlan, Z. Gorup, A. Levstek, and S. Amon. Thermally assisted tunneling and the Poole–Frenkel effect in homogenous a-Si. *Journal of Applied Physics*, 94(12):7604–7610, December 2003.
- [80] A. Gallagher and J. Scott. Gas and surface processes leading to hydrogenated amorphous silicon films. *Solar Cells*, 21(1-4):147 – 152, 1987.
- [81] G. Ganguly and A. Matsuda. Defect formation during growth of hydrogenated amorphous silicon. *Physical Review B*, 47:3661–70, 1993.
- [82] G. Ganguly, S. Ray, and A. K. Barua. Photo-induced changes in the properties of undoped and boron-doped a-Si:H films. *Philosophical Magazine B*, 54(4):301–309, 1986.
- [83] M. Ghannam, J. Nijs, R. Mertens, and R. DeKeersmaecker. A silicon bipolar transistor with a hydrogenated amorphous emitter. In *International Electron Devices Meeting*, volume 30, pages 746 – 748, 1984.
- [84] J. J. H. Gielis, P. J. van den Oever, B. Hoex, M. C. M. van de Sanden, and W. M. M. Kessels. Real-time study of a-Si:H/c-Si heterointerface formation and epitaxial Si growth by spectroscopic ellipsometry, infrared spectroscopy, and second-harmonic generation. *Physical Review B*, 77:205329–16, 2008.
- [85] R. B. M. Girisch, R. P. Mertens, and R. F. De Keersmaecker. Determination of Si-SiO₂ interface recombination parameters using a gate-controlled point-junction diode under illumination. *IEEE Transactions on Electron Devices*, 35(2):203–222, 1988.
- [86] K. K. Gleason, M. A. Petrich, and J. A. Reimer. Hydrogen microstructure in amorphous hydrogenated silicon. *Physical Review B*, 36(6):3259–3267, Aug 1987.
- [87] M. A. Green. *Solar Cells -Operating Principles, Technology and System Application*. The University of New South Wales, 1992.
- [88] M. A. Green, A. W. Blakers, and C. R. Osterwald. Characterization of high-efficiency silicon solar cells. *Journal Of Applied Physics*, 58 (11):4402, 1985.
- [89] A. S. Grove and D. J. Fitzgerald. Surface effects on p-n junctions: Characteristics of surface space-charge regions under non-equilibrium conditions. *Solid-State Electronics*, 9:783–806, 1966.
- [90] A.S. Gudovskikh, S. Ibrahim, J.-P. Kleider, J. Damon-Lacoste, P. Roca i Cabarrocas, Y. Veschetti, and P.-J. Ribeyron. Determination of band offsets in a-Si:H/c-Si heterojunctions from capacitance-voltage measurements: Capabilities and limits. *Thin Solid Films*, 515(19):7481 – 7485, 2007.
- [91] S. Guha, K. L. Narasimhan, and S. M. Pietruszko. On light-induced effect in amorphous hydrogenated silicon. *Journal of Applied Physics*, 52(2):859–860, 1981.

- [92] M. Hack and M. Shur. Physics of amorphous silicon alloy p-i-n solar cells. *Journal Of Applied Physics*, 58(2):997–1020, 1985.
- [93] R. N. Hall. Electron-Hole Recombination in Germanium. *Physical Review*, 87:387, 1952.
- [94] M. Hamasaki. Radiation effects on thin-oxide MOS capacitors caused by electron beam evaporation of aluminum. *Solid-State Electronics*, 26(4):299 – 303, 1983.
- [95] M. Shahidul Haque, H. A. Naseem, and W. D. Brown. Interaction of aluminum with hydrogenated amorphous silicon at low temperatures. *Journal of Applied Physics*, 75(8):3928–3935, 1994.
- [96] N. Hata, S. Wagner, P. Roca i Cabarrocas, and M. Favre. Deposition-induced defect profiles in amorphous hydrogenated silicon. *Applied Physics Letters*, 56:2448–50, 1990.
- [97] K. Heilig. Determination of doping factor, mobility ratio and excess concentration using photovoltages at extreme band bendings. *Solid-State Electronics*, 21(7):975–80, July 1978.
- [98] G. Hering. Cell production survey 2010. Technical report, Photon International, 2010.
- [99] H. Hertz. Ueber einen Einfluss des ultravioletten Lichtes auf die elektrische Entladung. *Annalen der Physik (Leipzig)*, 31:983–1000, 1887.
- [100] S. Hofmann. Cascade mixing limitations in sputter profiling. *Journal of Vacuum Science and Technology B*, 10(1):316–323, 1992.
- [101] S. Hofmann. Atomix Mixing, Surface Roughness and Information Depth in High-resolution AES Depth Profiling of a GaAs/AlAs Superlattice Structure. *Surface and Interface Analysis*, 21:673–678, 1994.
- [102] S. Hofmann. Profile reconstruction in sputter depth profiling. *Thin Solid Films*, 398–399:336–342, 2001.
- [103] S. Hofmann. Sputter-depth profiling for thin-film analysis. *Philosophical Transactions of the Royal Society of London A*, 362:55–75, 2004.
- [104] J. Hubin, A. V. Shah, and E. Sauvain. Effects of dangling bonds on the recombination function in amorphous semiconductors. *Philosophical Magazine Letters*, 66(3):115, 1992.
- [105] G. Hurkx, H.C. Degraaff, W.J. Kloosterman, and M.P.G. Knuvers. A New Analytical Diode Model Including Tunneling And Avalanche Breakdown. *IEEE Transactions on Electron Devices*, 39(9):2090–2098, 1992.
- [106] G. A. M. Hurkx. On the modelling of tunnelling currents in reverse-biased p-n junctions. *Solid State Electronics*, 32(8):665–668, 1989.

- [107] P. Roca i Cabarrocas. Plasma enhanced chemical vapor deposition of amorphous, polymorphous and microcrystalline silicon films. *Journal of Non-Crystalline Solids*, 266-269(Part 1):31 – 37, 2000.
- [108] H. Ibach and H. Lüth. *Festkörperphysik*. Springer, 2002.
- [109] W. B. Jackson, D. K. Biegelsen, R. J. Nemanich, and J. C. Knights. Optical absorption spectra of surface or interface states in hydrogenated amorphous silicon. *Applied Physics Letters*, 42:105–7, 1983.
- [110] W. B. Jackson, S. M. Kelso, C. C. Tsai, J. W. Allen, and S.-J. Oh. Energy dependence of the optical matrix element in hydrogenated amorphous and crystalline silicon. *Physical Review B*, 31:5187–98, 1985.
- [111] B. Jagannathan and W.A. Anderson. Interface effects on the carrier transport and photovoltaic properties of hydrogenated amorphous silicon/crystalline silicon solar cells. *Solar Energy Materials and Solar Cells*, 44(2):165–176, November 1996.
- [112] N. Jensen, U. Rau, R. M. Hausner, S. Uppal, L. Oberbeck, R. B. Bergmann, and J. H. Werner. Recombination mechanisms in amorphous silicon/crystalline silicon heterojunction solar cells. *Journal of Applied Physics*, 87:2639–45, 2000.
- [113] P. John, I. M. Odeh, M. J. K. Thomas, M. J. Tricker, F. Riddoch, and J. I. B. Wilson. Studies of the mechanism of the decomposition of hydrogenated a-Si films. *Philosophical Magazine Part B*, 42:671, 1980.
- [114] G. E. Jellison Jr. and F. A. Modine. Parameterization of the optical functions of amorphous materials in the interband region. *Applied Physics Letters*, 69(3):371–373, 1996.
- [115] J. Kakalios, R. A. Street, and W. B. Jackson. Stretched-exponential relaxation arising from dispersive diffusion of hydrogen in amorphous silicon. *Physical Review Letters*, 59(9):1037–1040, Aug 1987.
- [116] E. O. Kane. Simple model for collision effects in photoemission. *Physical Review*, 147:335–9, 1966.
- [117] E. O. Kane. Electron scattering by pair production in silicon. *Physical Review*, 159:624–31, 1967.
- [118] A. Kanevce and W. K. Metzger. The role of amorphous silicon and tunneling in heterojunction with intrinsic thin layer (HIT) solar cells. *Journal of Applied Physics*, 105(9):094507–7, May 2009.
- [119] G. Kaniadakis. *Properties of Amorphous Silicon*. INSPEC, The Institution of Electrical Engineers, London, 1989.
- [120] J.K. Kauppinen, D.J. Moffatt, H.H. Mantis, and D.G. Cameron. Smoothing of spectral data in the fourier domain. *Applied Optics*, 21(10):1866–1872, 1982.

- [121] W. Kern. The Evolution Of Silicon Wafer Cleaning Technology. *Journal of the Electrochemical Society*, 137:1887–92, 1990.
- [122] M. J. Kerr and A. Cuevas. General parameterization of Auger recombination in crystalline silicon. *Journal of Applied Physics*, 91(4):2473, February 2002.
- [123] M. J. Kerr, A. Cuevas, and P. Campbell. Limiting Efficiency of Crystalline Silicon Solar Cells Due to Coulomb-Enhanced Auger Recombination. *Progress in Photovoltaics: Research and Applications*, 11:97–104, 2003.
- [124] W. M. M. Kessels, A. H. M. Smets, D. C. Marra, E. S. Aydil, D. C. Schram, and M. C. M. van de Sanden. On the growth mechanism of a-Si:H. *Thin Solid Films*, 383(1-2):154 – 160, 2001.
- [125] J. P. Kleider and A. S. Gudovskikh. Characterization of amorphous/crystalline silicon interfaces from electrical measurements. In *Amorphous And Polycrystalline Thin-Film Silicon Science And Technology*, volume 1066 of *MRS Symposia Proceedings*, pages 1066–A04–01, 2008.
- [126] J. P. Kleider, A. S. Gudovskikh, and P. Roca i Cabarrocas. Determination of the conduction band offset between hydrogenated amorphous silicon and crystalline silicon from surface inversion layer conductance measurements. *Applied Physics Letters*, 92(16):162101, 2008.
- [127] J. C. Knights. Unknown title. *Japanese Journal of Applied Physics*, 18:101, 1979.
- [128] M. Kondo, S. De Wolf, and H. Fujiwara. Understanding of passivation mechanism in heterojunction c-si solar cells. In A. Nathan, A. Flewitt, J. Hou, S. Miyazaki, and J. Yang, editors, *Amorphous And Polycrystalline Thin-Film Silicon Science And Technology – 2008*, volume 1066 of *Materials Research Society Symposium Proceedings*, pages 1066–A03–01, Warrendale, PA, 2008.
- [129] L. Korte. *Die elektronische Struktur des amorph-kristallinen Silizium-Heterostruktur-Kontakts*. Ph.d. thesis, ISSN 0936-0891, Philipps-Universität Marburg, Marburg/Lahn, 2006.
- [130] L. Korte, E. Conrad, H. Angermann, R. Stangl, and M. Schmidt. Advances in a-Si:H/c-Si Heterojunction Solar Cell Fabrication and Characterization. *Solar Energy Materials and Solar Cells*, 93:905–10, 2009.
- [131] L. Korte, A. Laades, K. Lauer, R. Stangl, D. Schaffarzik, and M. Schmidt. Surface photovoltage investigation of recombination at the a-Si/c-Si heterojunction. *Thin Solid Films*, 517:6396–400, 2009.
- [132] L. Korte and M. Schmidt. Investigation of gap states in phosphorous-doped ultra-thin a-Si:H by near-UV photoelectron spectroscopy. *Journal of Non-Crystalline Solids*, 354:2138–43, 2008.

- [133] L. Korte and M. Schmidt. Doping and thickness dependence of band offsets at the amorphous/crystalline silicon heterojunction. *Journal of Applied Physics*, 2010. accepted.
- [134] L. Korte and M. Schmidt. Doping type and thickness dependence of band offsets at the amorphous/crystalline silicon heterojunction. *Journal of Applied Physics*, 109:063714–1–6, 2011.
- [135] L. Korte, T. F. Schulze, C. Leendertz, M. Schmidt, and B. Rech. Band alignment at amorphous/crystalline silicon hetero-interfaces. In *Amorphous and Polycrystalline Thin-Film Silicon Science and Technology*, volume 1321 of *MRS Symposia Proceedings*, pages A15–03, 2011.
- [136] R. C. Kumar. Diffusion theory of current transport in anisotype heterojunctions. *Int. J. Electronics*, 27(2):185–188, 1969.
- [137] M. V. Kurik. Urbach rule. *physica status solidi (a)*, 8(1):9–45, 1971.
- [138] A. Laades. *Preparation and Characterization of a-Si:H/c-Si Heterojunctions*. PhD thesis, Technische Universität Berlin, 2005.
- [139] A. A. Langford, M. L. Fleet, B. P. Nelson, W. A. Lanford, and N. Maley. Infrared absorption strength and hydrogen content of hydrogenated amorphous silicon. *Physical Review B*, 45(23):13367, Jun 1992.
- [140] C. Leendertz, N. Mingirulli, T. F. Schulze, J. P. Kleider, B. Rech, and L. Korte. Physical Insight into Interface Passivation of a-Si:H/c-Si Heterostructures by Analysis of Injection-dependent Lifetime and Band Bending. In *Proceedings of the 25rd European Photovoltaic Solar Energy Conference, 6-10 September 2010, Valencia, Spain*, pages 1377–1381. WIP Munich, 2010.
- [141] C. Leendertz, N. Mingirulli, T. F. Schulze, J. P. Kleider, B. Rech, and L. Korte. Discerning passivation mechanisms at a Si:H/c Si interfaces by means of photoconductance measurements. *Applied Physics Letters*, in press, 2011.
- [142] C. Leendertz, R. Stangl, T. F. Schulze, M. Schmidt, and L. Korte. A recombination model for a-Si:H/c-Si heterostructures. *physica status solidi c*, 7:1005, 2010.
- [143] N. Lequeux and M. Cuniot. Internal photoemission measurements on a - Si_{1-x}Gex : H/c - si heterojunctions. *Journal of Non-Crystalline Solids*, 114(Part 2):555–557, December 1989.
- [144] K. Levenberg. A Method for the Solution of Certain Problems in Least Squares. *Quarterly of Applied Mathematics*, 2:164–168, 1944.
- [145] L. Ley. Photoemission and Optical Properties. In J. D. Joannopoulos and G. Lucovsky, editors, *The Physics of Hydrogenated Amorphous Silicon II - Electronic and Vibrational Properties*, volume 56 of *Topics in Applied Physics*, chapter 3, pages 61–168. Springer, Berlin, 1984.

- [146] SANYO Electric Co. Ltd. Sanyo develops hit solar cells with world's highest energy conversion efficiency of 23.0 Website, May 2009.
- [147] G. Lucovsky, R. J. Nemanich, and J. C. Knights. Structural interpretation of the vibrational spectra of a-Si:H alloys. *Physical Review B*, 19(4):2064–2073, Feb 1979.
- [148] D. Macdonald, J. Tan, and T. Trupke. Imaging interstitial iron concentrations in boron-doped crystalline silicon using photoluminescence. *Journal of Applied Physics*, 103(7):073710, 2008.
- [149] C. Manfredotti, F. Fizzotti, M. Boero, P. Pastorino, P. Polesello, and E. Vittone. Influence of hydrogen-bonding configurations on the physical properties of hydrogenated amorphous silicon. *Physical Review B*, 50(24):18046–18053, Dec 1994.
- [150] L. F. Marsal, I. Martin, J. Pallares, A. Orpella, and R. Alcubilla. Annealing effects on the conduction mechanisms of p⁺-amorphous- Si_{0.8}C_{0.2}H/n-crystalline-Si diodes. *Journal of Applied Physics*, 94(4):2622–2626, 2003.
- [151] L. F. Marsal, J. Pallares, X. Correig, J. Calderer, and R. Alcubilla. Electrical characterization of n-amorphous/p-crystalline silicon heterojunctions. *Journal of Applied Physics*, 79(11):8493–8497, June 1996.
- [152] A. Matsuda. Plasma and surface reactions for obtaining low defect density amorphous silicon at high growth rates. volume 16, pages 365–368. AVS, 1998.
- [153] A. Matsuda, K. Nomoto, Y. Takeuchi, A. Suzuki, A. Yuuki, and J. Perrin. Temperature dependence of the sticking and loss probabilities of silyl radicals on hydrogenated amorphous silicon. *Surface Science*, 227(1-2):50 – 56, 1990.
- [154] A. Matsuda and K. Tanaka. Investigation of the growth kinetics of glow-discharge hydrogenated amorphous silicon using a radical separation technique. *Journal Of Applied Physics*, 60(7):1351–56, 1986.
- [155] A. Matsuda and K. Tanaka. Guiding principle for preparing highly photosensitive si-based amorphous alloys. *Journal of Non-Crystalline Solids*, 97-98(Part 2):1367 – 1374, 1987. Amorphous and Liquid Semiconductors.
- [156] H. Matsuura, T. Okuno, H. Okushi, and K. Tanaka. Electrical properties of n-amorphous/p-crystalline silicon heterojunctions. *Journal of Applied Physics*, 55:1012–9, 1984.
- [157] K.R. McIntosh and R.A. Sinton. Uncertainty in photoconductance lifetime measurements that use an inductive-coil detector. In *Proceedings of the 23rd European Photovoltaic Solar Energy Conference, 1-5 September 2008, Valencia, Spain*, pages 77–82, 2008.
- [158] R. Meaudre and M. Meaudre. Method for the determination of the capture cross sections of electrons from space-charge-limited conduction in the dark and under

- illumination in amorphous semiconductors. *Applied Physics Letters*, 85(2):245–247, 2004.
- [159] J. Meier, S. Dubail, J. Cuperus, U. Kroll, R. Platz, P. Torres, J. A. Anna Selvan, P. Pernet, N. Beck, N. Pellaton Vaucher, Ch. Hof, D. Fischer, H. Keppner, and A. Shah. Recent progress in micromorph solar cells. *Journal of Non-Crystalline Solids*, 227-230(Part 2):1250 – 1256, 1998.
- [160] A. C. Metaxas and R. J. Meredith. *Industrial microwave heating*. IEE power engineering series, 1983.
- [161] M. Meuris, P. de Bisschop, J. F. Leclair, and W. Vandercorst. Determination of the Angle of Incidence in a Cameca IMS-4f SIMS Instrument. *Surf. Interface Anal.*, 14:739–743, 1989.
- [162] A. G. Milnes and D. L. Feucht. *Heterojunctions and Metal-Semiconductor Junctions*. Academic Press, 1972.
- [163] H. Mimura and Y. Hatanaka. Carrier transport mechanisms of p-type amorphous-n-type crystalline silicon heterojunctions. *Journal of Applied Physics*, 71(5):2315–2320, March 1992.
- [164] N. Mingirulli, J. Haschke, R. Gogolin, R. Ferré, T. F. Schulze, J. Düsterhöft, N.-P. Harder, L. Korte, R. Brendel, and B. Rech. Efficient interdigitated back-contacted silicon heterojunction solar cells. *physica status solidi (RRL) – Rapid Research Letters*, 5:159–161, 2011.
- [165] J. Mitchell. New insight into the hydrogen surface passivation mechanism at low temperatures. In *Proc. 24th European Photovoltaic Solar Energy Conference*, page 1AO.3.5, 2009.
- [166] J. Mitchell, D. Macdonald, and A. Cuevas. Thermal activation energy for the passivation of the n-type crystalline silicon surface by hydrogenated amorphous silicon. *Applied Physics Letters*, 94(16):162102–3, April 2009.
- [167] W. Mönch. *Semiconductor Surfaces and Interfaces*, volume 26 of *Springer Series in Surface Sciences*. Springer, Berlin, Heidelberg, New York, 2nd ed. edition, 1995.
- [168] A. N. Nazarov, Ya. N. Vovk, V. S. Lysenko, V. I. Turchanikov, V. A. Scryshevskii, and S. Ashok. Carrier transport in amorphous SiC/crystalline silicon heterojunctions. *Journal of Applied Physics*, 89(8):4422–4428, April 2001.
- [169] H. C. Neitzert, W. Hirsch, and M. Kunst. Structural changes of a-Si:H films on crystalline silicon substrates during deposition. *Physical Review B*, 47(7):4080–4083, Feb 1993.
- [170] V. S. Nguyen and P. H. Pan. Initial transient phenomena in the plasma enhanced chemical vapor deposition process. *Applied Physics Letters*, 45(2):134–136, 1984.

- [171] Tak H. Ning. Electron trapping in SiO₂ due to electron-beam deposition of aluminum. *Journal of Applied Physics*, 49(7):4077–4082, 1978.
- [172] S. Oguz, R. W. Collins, M. A. Paesler, and William Paul. Effects of partial evolution of H from a-Si:H on the infrared vibrational spectra and the photoluminescence. *Journal of Non-Crystalline Solids*, 35-36(Part 1):231 – 236, 1980.
- [173] S. Olibet, E. Vallat-Sauvain, and C. Ballif. Model for a-Si:H/c-Si interface recombination based on the amphoteric nature of silicon dangling bonds. *Physical Review B*, 76:35326, 2007.
- [174] S. Olibet, E. Vallat-Sauvain, L. Fesquet, C. Monachon, A. Hessler-Wyser, J. Damon-Lacoste, S. De Wolf, and C. Ballif. Properties of interfaces in amorphous/crystalline silicon heterojunctions. *physica status solidi (a)*, 207(3):651–656, 2010.
- [175] Y. Pan, F. Inam, M. Zhang, and D. A. Drabold. Atomistic Origin of Urbach Tails in Amorphous Silicon. *Physical Review Letters*, 100(20):206403, May 2008.
- [176] K. C. Pandey, T. Sakurai, and H. D. Hagstrum. Si(111): SiH₃—A Simple New Surface Phase. *Physical Review Letters*, 35(25):1728–1731, Dec 1975.
- [177] D. A. Papaconstantopoulos and E. N. Economou. Calculations of the electronic properties of hydrogenated silicon. *Physical Review B*, 24:7233, 1981.
- [178] M. Peressi, L. Colombo, and S. de Gironcoli. Role of defects in the electronic properties of amorphous/crystalline Si interface. *Physical Review B*, 64(19):193303, October 2001.
- [179] S. S. Perlman and D. L. Feucht. p-n heterojunctions. *Solid-State Electronics*, 7(12):911–923, 1964.
- [180] J. Perrin, Y. Takeda, N. Hirano, Y. Takeuchi, and A. Matsuda. Sticking and recombination of the SiH₃ radical on hydrogenated amorphous silicon: The catalytic effect of diborane. *Surface Science*, 210(1-2):114 – 128, 1989.
- [181] A. Pflug. RIG-VM simulation system, Fraunhofer IST. <http://www.simkopp.de/rvm/>.
- [182] J. C. Phillips. Topology of covalent non-crystalline solids I: Short-range order in chalcogenide alloys. *Journal of Non-Crystalline Solids*, 34(2):153 – 181, 1979.
- [183] H. Plagwitz. *Surface passivation of crystalline silicon solar cells by amorphous silicon films*. PhD thesis, Universität Hannover, 2007.
- [184] M. J. Powell and S. C. Deane. Improved Defect-Pool Model for Charged Defects in Amorphous Silicon. *Physical Review B*, 48:10815–27, 1993.
- [185] M. J. Powell and S. C. Deane. Defect-pool model and the hydrogen density of states in hydrogenated amorphous silicon. *Physical Review B*, 53:10121–32, 1996.

- [186] M. J. Powell, C. van Berkel, A. R. Franklin, S. C. Deane, and W. I. Milne. Defect pool in amorphous-silicon thin-film transistors. *Physical Review B*, 45(8):4160–4170, Feb 1992.
- [187] J.B. Prise. *Semiconductor Silicon*, chapter Anisotropic Etching of Silicon with KOH-H₂O-Isopropyl Alcohol, page 339. The Electrochemical Society Proceeding Series, Princeton NJ, USA, 1973.
- [188] D. Pysch, M. Bivour, M. Hermle, and S. W. Glunz. Amorphous silicon carbide heterojunction solar cells on p-type substrates. *Thin Solid Films*, Article in Press, Corrected Proof, 2011.
- [189] D. Pysch, J. Ziegler, J.-P. Becker, D. Suwito, S. Janz, S. W. Glunz, and M. Hermle. Stretched-exponential increase in the open-circuit voltage induced by thermal annealing of amorphous silicon-carbide heterojunction solar cells. *Applied Physics Letters*, page 093510, 2009.
- [190] HZB R. Rössler. Personal communication (2011).
- [191] J. A. Reimer, R. W. Vaughan, and J. C. Knights. Proton Magnetic Resonance Spectra of Plasma-Deposited Amorphous Si: H Films. *Physical Review Letters*, 44(3):193–196, Jan 1980.
- [192] S. Rein. *Lifetime Spectroscopy*. Springer Berlin Heidelberg New York, 2005.
- [193] Z. Remes, M. Vanecek, P. Torres, U. Kroll, A. H. Mahan, and R. S. Crandall. Optical determination of the mass density of amorphous and microcrystalline silicon layers with different hydrogen contents. *Journal of Non-Crystalline Solids*, 227-230(Part 2):876 – 879, 1998.
- [194] A. R. Riben and D. L. Feucht. Electrical transport in nGe-pGaAs Heterojunctions. *International Journal of Electronics*, 20(6):583–599, 1966.
- [195] J. Robertson. Deposition mechanism of hydrogenated amorphous silicon. *Journal of Applied Physics*, 87:2608–17, 2000.
- [196] R. Robertson and A. Gallagher. Reaction mechanism and kinetics of silane pyrolysis on a hydrogenated amorphous silicon surface. *The Journal of Chemical Physics*, 85(6):3623–3630, 1986.
- [197] A. Rose. Space-Charge-Limited Currents in Solids. *Physical Review*, 97:1538 – 1544, 1955.
- [198] M. Rosling, H. Bleichner, P. Jonsson, and E. Nordlander. The ambipolar diffusion coefficient in silicon: Dependence on excess-carrier concentration and temperature. *Journal of Applied Physics*, 76(5):2855–2859, 1994.
- [199] R. Rössler. Entwicklung von mikrokristallinen Silizium-Emitterschichten für waferbasierte Heterostruktursolarzellen. Diplomarbeit, Technische Universität Darmstadt, 2010.

- [200] D. Roy and D. Tremblay. Design of electron spectrometers. *Reports on Progress in Physics*, 53:1621–74, 1990.
- [201] R. Robertson and A. Gallagher. Mono- and disilicon radicals in silane and silane-argon DC discharges. *Journal of Applied Physics*, 59(10):3402–3411, 1986.
- [202] F.A. Rubinelli. Amorphous-crystalline silicon anisotype heterojunctions: Built-in potential, its distribution and depletion widths. *Solid-State Electronics*, 30(3):345–351, March 1987.
- [203] C. T. Sah, R. N. Noyce, and W. Shockley. Carrier generation and recombination in p-n junctions and p-n junction characteristics. In *Proc. of the IRE*, volume 45, pages 1228–1243, 1957.
- [204] P. V. Santos and W. B. Jackson. Trap-limited hydrogen diffusion in a-Si:H. *Physical Review B*, 46(8):4595–4606, Aug 1992.
- [205] Sanyo. HIT-N240SE10 technical manual, 2011.
- [206] A. Schenk and U. Krumbein. Coupled defect-level recombination: Theory and application to anomalous diode characteristics. *Journal of Applied Physics*, 78(5):3185–3192, 1995.
- [207] M. Scherff. personal communication, EU project HETSI, Jan. 2011.
- [208] J. Schmidt. *Untersuchungen zur Ladungsträgerrekombination an den Oberflächen und im Volumen von kristallinen Silicium-Solarzellen*. PhD thesis, Universität Hannover, 1998.
- [209] J. Schmidt. Measurement of differential and actual recombination parameters on crystalline silicon wafers. *IEEE Transactions on Electron Devices*, 46:2018–25, 1999.
- [210] M. Schmidt, L. Korte, A. Laades, R. Stangl, Ch. Schubert, H. Angermann, E. Conrad, and K.v. Maydell. Physical aspects of a-Si:H/c-Si hetero-junction solar cells. *Thin Solid Films*, 515:7475–80, 2007.
- [211] M. Schmidt, A. Schoepke, L. Korte, O. Milch, and W. Fuhs. Density distribution of gap states in extremely thin a-Si:H layers on crystalline silicon wafers. *Journal of Non-Crystalline Solids*, 338-340:211–4, 2004. Konferenz-Beitrag zur ICAMS-20, Campos de Jordao, Brasilien.
- [212] R. Schropp and M. Zeman. *Amorphous and Microcrystalline Silicon Solar Cells*. Kluwer Academic Publishers, 1998. chapter 6.
- [213] W. Schülke. Structural investigation of hydrogenated amorphous silicon by X-ray diffraction. *Philosophical Magazine Part B*, 43:451–468, 1980.

- [214] T. F. Schulze, H. N. Beushausen, T. Hansmann, L. Korte, and B. Rech. Accelerated interface defect removal in amorphous/crystalline silicon heterostructures using pulsed annealing and microwave heating. *Applied Physics Letters*, 95:182108, 2009.
- [215] T. F. Schulze, H. N. Beushausen, C. Leendertz, A. Dobrich, T. Hannappel, L. Korte, and B. Rech. Impact of a-Si:H structural properties on the annealing behavior of a-Si:H/c-Si heterostructures used as precursors for high-efficiency solar cells. In *Defects in Inorganic Photovoltaic Materials*, volume 1268 of *MRS Symposia Proceedings*, 2010.
- [216] T. F. Schulze, H. N. Beushausen, C. Leendertz, A. Dobrich, B. Rech, and L. Korte. Interplay of amorphous silicon disorder and hydrogen content with interface defects in amorphous/crystalline silicon heterojunctions. *Applied Physics Letters*, 96(25):252102, 2010.
- [217] T. F. Schulze, L. Korte, E. Conrad, M. Schmidt, and B. Rech. Electrical transport mechanisms in a-Si:H/c-Si heterojunction solar cells. *Journal of Applied Physics*, 107:023711, 2010.
- [218] J.-W. A. Schüttauf, K. H. M. van der Werf, I. M. Kielen, W. G. J. H. M. van Sark, J. K. Rath, and R. E. I. Schropp. Excellent crystalline silicon surface passivation by amorphous silicon irrespective of the technique used for chemical vapor deposition. *Applied Physics Letters*, 98(15):153514, 2011.
- [219] M. Sebastiani, L. Di Gaspare, G. Capellini, C. Bittencourt, and F. Evangelisti. Low-Energy Yield Spectroscopy as a Novel Technique for Determining Band Offsets: Application to the c-Si(100)/a-Si:H Heterostructure. *Physical Review Letters*, 75:3352–5, 1995.
- [220] K. D. Sevier. *Low Energy Electron Spectrometry*. Wiley-Interscience, New York, 1972.
- [221] J. M. Shannon and K. J. B. M. Nieuwesteeg. Tunneling effective mass in hydrogenated amorphous silicon. *Applied Physics Letters*, 62(15):1815–1817, 1993.
- [222] A. Shih, J.-L. Yeh, S.-C. Lee, and T. R. Yang. Structural and electronic differences between deuterated and hydrogenated amorphous silicon. *Journal Of Applied Physics*, 88(3):1684–1688, 2000.
- [223] T. Shimizu, K. Nakazawa, M. Kumeda, and S. Ueda. Incorporation scheme of h reducing defects in a-si studied by nmr and electron-spin-resonance. *Physica B & C*, 117:926–928, 1983.
- [224] W. Shockley. The Theory of p-n Junctions in Semiconductors and p-n Junction Transistors. *Bell System Technical Journal*, 28:435, 1949.
- [225] W. Shockley and W. T. Read. Statistics of the Recombinations of Holes and Electrons. *Physical Review*, 87(5):835, 1952.

- [226] F. Siebke, W. Beyer, J. Herion, and H. Wagner. Surface and bulk density of states of a-Si:H determined by CPM and total-yield photoelectron spectroscopy. *Journal of Non-Crystalline Solids*, 137-138:339–42, 1991.
- [227] R. A. Sinton and A. Cuevas. Contactless determination of current–voltage characteristics and minority-carrier lifetimes in semiconductors from quasi-steady-state photoconductance data. *Applied Physics Letters*, 69(17):2510–2512, October 1996.
- [228] A. H. M. Smets, W. M. M. Kessels, and M. C. M. van de Sanden. Temperature dependence of the surface roughness evolution during hydrogenated amorphous silicon film growth. *Applied Physics Letters*, 82(6):865–867, 2003.
- [229] A. H. M. Smets, W. M. M. Kessels, and M. C. M. van de Sanden. Vacancies and voids in hydrogenated amorphous silicon. *Applied Physics Letters*, 82:865–7, 2003.
- [230] A. H. M. Smets and M. C. M. van de Sanden. Relation of the Si-H stretching frequency to the nanostructural Si-H bulk environment. *Physical Review B*, 76(7):073202, Aug 2007.
- [231] R. J. Smith and Myron Strongin. Electronic-structure studies of hydrogenated amorphous silicon films. *Physical Review B*, 24(10):5863–5873, Nov 1981.
- [232] Z E. Smith and S. Wagner. Band tails, entropy, and equilibrium defects in hydrogenated amorphous silicon. *Physical Review Letters*, 59:688–91, 1987.
- [233] Y.J. Song, M.R. Park, E. Guliants, and W.A. Anderson. Influence of defects and band offsets on carrier transport mechanisms in amorphous silicon/crystalline silicon heterojunction solar cells. *Solar Energy Materials and Solar Cells*, 64(3):225–240, October 2000.
- [234] C. M. Soukoulis, M. H. Cohen, and E. N. Economou. Exponential band tails in random systems. *Physical Review Letters*, 53:616–9, 1984.
- [235] W. E. Spear, D. Allan, P. Le Comber, and A. Ghaith. A new approach to the interpretation of transport results in a-Si. *Philosophical Magazine B*, 41(4):419–438, 1980.
- [236] W. E. Spear and P. G. Le Comber. Substitutional Doping of Amorphous Silicon. *Solid State Communications*, 17:1193–1196, 1975.
- [237] W.E. Spicer. Photoemissive, photoconductive, and optical absorption studies of alkali-antimony compounds. *Physical Review*, 112:114–22, 1958.
- [238] J. Sritharathikhun, H. Yamamoto, S. Miyajima, A. Yamada, and M. Konagai. Optimization of amorphous silicon oxide buffer layer for High-Efficiency p-Type hydrogenated microcrystalline silicon Oxide/n-Type crystalline silicon heterojunction solar cells. *Japanese Journal of Applied Physics*, 47:8452–5, 2008.

- [239] R. Stangl, A. Froitzheim, L. Elstner, and W. Fuhs. Amorphous/crystalline silicon heterojunction solar cells, a simulation study. In *17th European Photovoltaic Solar Energy Conference*, page 1383, October 2001.
- [240] R. Stangl, A. Froitzheim, M. Schmidt, and W. Fuhs. Design criteria for amorphous/crystalline silicon heterojunction solar cells - a simulation study. In *Proceedings of the 3rd World Conference in Photovoltaic Energy Conversion*, pages 4P-A8-45, 2003.
- [241] R. Stangl, M. Kriegel, K. v. Maydell, L. Korte, M. Schmidt, and W. Fuhs. AFORS-HET, an open-source on demand numerical PC program for simulation of (thin film) heterojunction solar cells, version 1.2. In *Conference record of the Thirty-First IEEE Photovoltaic Specialists Conference*, pages 1556-9, Lake Buena Vista, FL, 2005. IEEE Operations Center.
- [242] R. Stangl, C. Leendertz, and J. Haschke. *Solar Energy*, chapter Numerical Simulation of Solar Cells and Solar Cell Characterization Methods: The Open-Source on Demand Program AFORS-HET, pages 319-352. InTech, 2010.
- [243] R. A. Street. Hydrogen chemical potential and structure of a-Si:H. *Physical Review B*, 43:2454-7, 1991.
- [244] R. A. Street. *Hydrogenated Amorphous Silicon*. Cambridge University Press, 1991.
- [245] R. A. Street, J. Kakalios, and M. Hack. Electron drift mobility in doped amorphous silicon. *Physical Review B*, 38:5603-9, 1988.
- [246] R. A. Street, J. Kakalios, C. C. Tsai, and T. M. Hayes. Thermal-equilibrium processes in amorphous silicon. *Physical Review B*, 35:1316-33, 1987.
- [247] R. A. Street and K. Winer. Defect equilibria in undoped a-Si:H. *Physical Review B*, 40:6236-49, 1989.
- [248] R.A. Street. Distribution of the density of states of bonded hydrogen in amorphous hydrogenated silicon. *Solar Cells*, 30(1-4):207 - 218, 1991.
- [249] M. Stutzmann. The defect density in amorphous silicon. *Philosophical Magazine B*, 60:531-46, 1989.
- [250] M. Stutzmann, D.K. Biegelsen, and R.A. Street. Detailed investigation of doping in hydrogenated amorphous silicon and germanium. *Physical Review B*, 35:5666-701, 1987.
- [251] S. M. Sze and K. Ng Kwok. *Physics of Semiconductor Devices*. John Wiley & Sons, Inc., Hoboken, New Jersey, 3rd edition, 2007.
- [252] M. Taguchi, E. Maruyama, and M. Tanaka. Temperature dependence of amorphous/crystalline silicon heterojunction solar cells. *Japanese Journal of Applied Physics*, 47:814-818, 2008.

- [253] K. Tanaka, E. Maruyama, T. Shimada, and H. Okamoto. *Amorphous Silicon*. John Wiley & Sons, 1999.
- [254] M. Tanaka, M. Taguchi, T. Matsuyama, T. Sawada, S. Tsuda, S. Nakano, H. Hanafusa, and Y. Kuwano. Development of new a-Si/c-Si heterojunction solar cells: ACJ-HIT (artificially constructed junction-heterojunction with intrinsic thin-layer). *Japanese Journal of Applied Physics*, 31:3518–22, 1992.
- [255] M. Tanielian. Adsorbate effects on the electrical conductance of a-Si: H. *Philosophical Magazine B*, 45(4):435–462, 1982.
- [256] J. Tauc, R. Grigorovici, and A. Vancu. Optical properties and electronic structure of amorphous germanium. *physica status solidi*, 15:627–37, 1966.
- [257] C. Tejedor and F. Flores. A simple approach to heterojunctions. *J. Phys. C*, 11:L19–23, 1978.
- [258] J. Tersoff. Theory of semiconductor heterojunctions: The role of quantum dipoles. *Physical Review B*, 30:4874–7, 1984.
- [259] K. Thiel. *Strukturelle Untersuchung der amorph/kristallinen Grenzfläche mittels quantitativer hochauflösender Transmissionselektronenmikroskopie an den Systemen a-Si/c-Si und a-Ge/c-Si*. PhD thesis, Georg-August-Universität zu Göttingen, 2006.
- [260] T. Tiedje, J. M. Cebulka, D. L. Morel, and B. Abeles. Evidence for exponential band tails in amorphous silicon hydride. *Physical Review Letters*, 46:1425–8, 1981.
- [261] V. Yu. Timoshenko, A. B. Petrenko, M. N. Stolyarov, Th. Dittrich, W. Fuessel, and J. Rappich. Quantitative analysis of room temperature photoluminescence of c-Si wafers excited by short laser pulses. *Journal of Applied Physics*, 85(8):4171–5, April 1999.
- [262] M. Tosolini, L. Colombo, and M. Peressi. Atomic-scale model of $c - Si/a-Si:H$ interfaces. *Physical Review B*, 69(7):075301, Feb 2004.
- [263] H. Tourir, K. Zellama, and J.-F. Morhange. Local Si-H bonding environment in hydrogenated amorphous silicon films in relation to structural inhomogeneities. *Physical Review B*, 59(15):10076–10083, Apr 1999.
- [264] Y. Tsunomura, Y. Yoshimine, M. Taguchi, T. Baba, T. Kinoshita, H. Kanno, H. Sakata, E. Maruyama, and M. Tanaka. Twenty-two percent efficiency HIT solar cell. *Solar Energy Materials and Solar Cells*, 93:670–673, 2009.
- [265] T. Unold, M. Rösch, and G. H. Bauer. Defects and transport in a-Si:H/c-Si heterojunctions. *Journal of Non-Crystalline Solids*, 266-269(Part 2):1033–1037, May 2000.
- [266] C. G. Van de Walle. Band lineups and deformation potentials in the model-solid theory. *Physical Review B*, 39(3):1871–1883, Jan 1989.

- [267] M N van den Donker, B Rech, W M M Kessels, and M C M van de Sanden. Transient depletion of source gases during materials processing: a case study on the plasma deposition of microcrystalline silicon. *New Journal of Physics*, 9(8):280, 2007.
- [268] W. Vandervorst, H. E. Maes, and R. F. De Keersmaecker. Secondary ion mass spectrometry: Depth profiling of shallow as implants in silicon and silicon dioxide. *Journal Of Applied Physics*, 56(5):1425–1433, 1984.
- [269] Y.P. Varshni. Band-to-Band Radiative Recombination in Groups IV, VI, and III-V Semiconductors (I). *physica status solidi (b)*, 19(2):459–514, 1967.
- [270] J. A. Vergés. Bethe lattices incorporating short-range disorder: Application to hydrogenated amorphous silicon. *Physical Review Letters*, 53(23):2270–2273, Dec 1984.
- [271] O. Vetterl, F. Finger, R. Carius, P. Hapke, L. Houben, O. Kluth, A. Lambertz, A. Mueck, B. Rech, and H. Wagner. Intrinsic microcrystalline silicon: A new material for photovoltaics. *Solar Energy Materials and Solar Cells*, 62(1-2):97 – 108, 2000.
- [272] B. von Roedern, L. Ley, and M. Cardona. Photoelectron Spectra of Hydrogenated Amorphous Silicon. *Physical Review Letters*, 39:1576, 1977.
- [273] B. von Roedern, L. Ley, and M. Cardona. Spectroscopic determination of the position of the fermi-level in doped amorphous hydrogenated silicon. *Solid State Communications*, 29(5):415–7, 1979.
- [274] B. von Roedern, L. Ley, M. Cardona, and F. W. Smith. Photoemission studies on in situ prepared hydrogenated amorphous silicon films. *Philosophical Magazine B*, 40:433–50, 1979.
- [275] H. Wagner and W. Beyer. Reinterpretation of the silicon-hydrogen stretch frequencies in amorphous-silicon. *Solid State Communications*, 48(7):585–587, 1983.
- [276] T.H. Wang, E. Iwaniczko, M.R. Page, D.H. Levi, Y. Yan, H.M. Branz, and Q. Wang. Effect of emitter deposition temperature on surface passivation in hot-wire chemical vapor deposited silicon heterojunction solar cells. *Thin Solid Films*, 501(1-2):284 – 287, 2006. Proceedings of the Third International Conference on Hot-Wire CVD (Cat-CVD) Process.
- [277] T.H. Wang, Q. Wang, E. Iwaniczko, M.R. Page, D.H. Levi, Y. Yan, C.W. Teplin, Y. Xu, X.Z. Wu, and H.M. Branz. Heterojunction silicon solar cells with high open-circuit voltages by interface optimization. In W. Hoffmann u. a., editor, *Nineteenth European Photovoltaic Solar Energy Conference : proceedings of the international conference held in Paris, France, 7 - 11 June 2004*, pages 1296–9, Munich, Florence, 2004. WIP, ETA.

- [278] D. Wesner and W. Eberhardt. Photoemission and photoyield of amorphous Si films. *Physical Review B*, 28(12):7087–7093, Dec 1983.
- [279] D. L. Williamson, D. W. M. Marr, J. Yang, B. Yan, and S. Guha. Nonuniform H distribution in thin-film hydrogenated amorphous Si by small-angle neutron scattering. *Physical Review B*, 67(7):075314, Feb 2003.
- [280] R. G. Wilson, F. A. Stevie, and C. W. Magie. *Secondary Ion Mass Spectrometry – A practical handbook for depth profiling and bulk impurity analysis*. John Wiley & Sons, 1989.
- [281] K. Winer. Chemical-equilibrium description of the gap-state distribution in a-Si:H. *Physical Review B*, 63:1487–90, 1989.
- [282] K. Winer, I. Hirabayashi, and L. Ley. Distribution of Occupied Near-Surface Band-Gap States in a-Si:H. *Physical Review B*, 38:7680–93, 1988.
- [283] K. Winer and L. Ley. Surface states and the exponential valence-band tail in a-Si:H. *Physical Review B*, 36:6072–8, 1987.
- [284] F. Wooten, K. Winer, and D. Weaire. Computer Generation of Structural Models of Amorphous Si and Ge. *Physical Review Letters*, 54:1392–5, 1985.
- [285] C. R. Wronski, S. Lee, M. Hicks, and S. Kumar. Internal photoemission of holes and the mobility gap of hydrogenated amorphous silicon. *Physical Review Letters*, 63:1420–3, 1989.
- [286] Y. Wu, J. T. Stephen, D. X. Han, J. M. Rutland, R. S. Crandall, and A. H. Mahan. New Hydrogen Distribution in a-Si:H: An NMR Study. *Physical Review Letters*, 77(10):2049–2052, Sep 1996.
- [287] S. Yamasaki, S. Kuroda, K. Tanaka, and S. Hayashi. Hyperfine interaction between hydrogens and dangling bonds in a-Si:H studied by endor. *Solid State Communications*, 50(1):9 – 11, 1984.
- [288] L. H. Yang, C. Y. Fong, and C. S. Nichols. Impurity-defect complexes and doping mechanism in a-Si:H. *Physical Review Letters*, 66(25):3273–3276, Jun 1991.
- [289] J. Zhao, A. Wang, and M. A. Green. 24.5Efficiency PERL Cells on FZ Substrates. *Progress in Photovoltaics: Research and Applications*, 7:471–474, 1999.

Publications

Publications in the framework of this thesis

Peer-reviewed journal publications

- [A] T. F. Schulze, H. N. Beushausen, T. Hansmann, L. Korte, and B. Rech: 'Accelerated interface defect removal in amorphous/crystalline silicon heterostructures using pulsed annealing and microwave heating', *Applied Physics Letters* **95**, 182108 (2009).
- [B] T. F. Schulze, L. Korte, E. Conrad, M. Schmidt, and B. Rech: 'Electrical transport mechanisms in a-Si:H/c-Si heterojunction solar cells', *Journal of Applied Physics* **107**, 023711 (2010).
- [C] T. F. Schulze, L. Korte, E. Conrad, M. Schmidt, and B. Rech: 'High-forward-bias transport mechanism in a-Si:H/c-Si heterojunction solar cells', *physica status solidi a* **207**, 657 (2010).
- [D] T. F. Schulze, H. N. Beushausen, C. Leendertz, A. Dobrich, B. Rech, and L. Korte: 'Interplay of amorphous silicon disorder and hydrogen content with interface defects in amorphous/crystalline silicon heterojunctions', *Applied Physics Letters* **96**, 252102 (2010).
- [E] T. F. Schulze, L. Korte, F. Ruske, and B. Rech: 'Band lineup in amorphous/crystalline silicon heterojunctions and the impact of hydrogen microstructure and topological disorder', *Physical Review B* **83**, 165314 (2011).

Conference proceedings

- [F] T. F. Schulze, L. Korte, K. von Maydell, M. Schmidt, and B. Rech: 'Insight into electronic transport and interface passivation in a-Si:H/c-Si heterojunction solar cells by temperature-dependent I-V characterization', *Proceedings of the 24th European Photovoltaic Solar Energy Conference and Exhibition*, Hamburg, pp. 2213-2217 (2009).
- [G] T. F. Schulze, H. N. Beushausen, C. Leendertz, A. Dobrich, T. Hannappel, L. Korte, and B. Rech: 'Impact of a-Si:H structural properties on the annealing behavior of a-Si:H/c-Si heterostructures used as precursors for high-efficiency solar cells', in *'Defects in Inorganic Materials'*, *Materials Research Society Symposium Proceedings* **Vol. 1268**, EE01-07 (2010).

- [H] T. F. Schulze, N. Mingirulli, C. Leendertz, H. N. Beushausen, B. Rech, and L. Korte: 'Impact of a-Si:H structural properties on annealing behavior and V_{oc} of a-Si:H/c-Si heterojunction solar cells', *Proceedings of the 25th European Photovoltaic Solar Energy Conference and Exhibition*, Valencia (Spain), pp. 1276-1281 (2010).
- [I] T. F. Schulze, C. Leendertz, N. Mingirulli, L. Korte, and B. Rech: 'Impact of Fermi-level dependent defect equilibration on V_{oc} of amorphous/crystalline silicon heterojunction solar cells', *Proceedings of the 1st International Conference on Silicon Photovoltaics (SiliconPV)*, Freiburg (Germany), to appear in *Energy Procedia* (2011).

Other publications by the author or involving the author

The most important publications are marked with an asterisk.

Peer-reviewed journal publications

- [J] M. Brühwiler, T. F. Schulze, S.M. Kazakov, Z. Bukowski, R. Puzniak, N.D. Zhigadlo, J. Karpinski, and B. Batlogg: 'Superconductivity in the β -pyrochlore Osmates', *Physica C* **460-462**, p. 62-65 (2007).
- [K] * T. F. Schulze, P. S. Häfliger, Ch. Niedermayer, K. Mattenberger, S. Bubenhofer, and B. Batlogg: 'Direct link between high temperature sodium order and low temperature magnetism in Na_xCoO_2 ', *Physical Review Letters* **100**, 026407 (2008).
- [L] * T. F. Schulze, M. Brühwiler, P. S. Häfliger, S. M. Kazakov, Ch. Niedermayer, K. Mattenberger, J. Karpinski, and B. Batlogg: 'Spin fluctuations, magnetic long-range order, and Fermi surface gapping in Na_xCoO_2 ', *Physical Review B* **78**, 205101 (2008).
- [M] H. Angermann, E. Conrad, L. Korte, J. Rappich, T. F. Schulze, and M. Schmidt: 'Passivation of textured substrates for a-Si:H/c-Si hetero-junction solar cells: Effect of wet-chemical smoothing and intrinsic a-Si:H interlayer', *Materials Science and Engineering B* **159-160**, 219-223 (2009).
- [N] C. Leendertz, R. Stangl, T. F. Schulze, M. Schmidt, and L. Korte: 'A recombination model for a-Si:H/c-Si heterostructures', *physica status solidi c* **7**, 1005 (2010).
- [O] * D. Amkreutz, J. Müller, M. Schmidt, T. Hänel, and T. F. Schulze: 'Electron-beam crystallized large grained silicon solar cell on glass substrate', *Progress in Photovoltaics: Research and Applications*, in press/online (2011).
- [P] * N. Mingirulli, J. Haschke, R. Gogolin, R. Ferré, T. F. Schulze, J. Düsterhöft, N.-P. Harder, L. Korte, R. Brendel, and B. Rech: 'Efficient interdigitated back-contacted silicon heterojunction solar cells'. *physica status solidi – Rapid Research Letters* **5**, 159-161 (2011).

- [Q] * C. Leendertz, N. Mingirulli, T. F. Schulze, J. P. Kleider, B. Rech, and L. Korte: 'Discerning passivation mechanisms at a Si:H/c Si interfaces by means of photoconductance measurements', *Applied Physics Letters*, in press (2011).

Conference proceedings

- [R] H. Angermann, T. F. Schulze, E. Conrad, J. Rappich, L. Korte, and M. Schmidt: 'Cleaning and Passivation of Structured n-Type Si Substrates: Preparation and Interface Properties of a-Si:H/c-Si Hetero Solar Cells', *Proceedings of the 23rd European Photovoltaic Solar Energy Conference and Exhibition*, Valencia (Spain), pp. 1422-1426 (2008).
- [S] D. Amkreutz, J. Müller, M. Schmidt, J. Haschke, T. Hänel, and T. F. Schulze: 'Optical and electrical properties of electron beam crystallized thin film silicon solar cells on glass substrates', *Proceedings of the 24th European Photovoltaic Solar Energy Conference and Exhibition*, Hamburg, pp. 2506-2509 (2009).
- [T] D. Amkreutz, J. Müller, M. Schmidt, T. F. Schulze, T. Hänel, and J. Haschke: 'Efficient Electron Beam Crystallised Large Grained Silicon Solar Cells on Glass Substrates', *Proceedings of the 25th European Photovoltaic Solar Energy Conference and Exhibition*, Valencia (Spain), pp. 2832 - 2836 (2010).
- [U] C. Leendertz, N. Mingirulli, T. F. Schulze, J. P. Kleider, B. Rech, and L. Korte: 'Physical insight into interface passivation of a-Si:H/c-Si heterostructures by analysis of injection-dependent lifetime and band bending ', *Proceedings of the 25th European Photovoltaic Solar Energy Conference and Exhibition*, Valencia (Spain), pp. 1377-1381 (2010).
- [V] L. Korte, T. F. Schulze, C. Leendertz, M. Schmidt, and B. Rech: 'Band alignment at amorphous/crystalline silicon hetero-interfaces', in '*Amorphous and Polycrystalline Thin-Film Silicon Science and Technology*', *Materials Research Society Symposium Proceedings* **Vol. 1321**, A15-03, submitted (2011).

Acknowledgment

The work presented in this thesis was carried out under the supervision of Prof. Dr. Bernd Rech and Dr. Lars Korte from Helmholtz-Zentrum Berlin, Institute Silicon Photovoltaics. I wish to express deepest gratitude to them for their competent guidance and support during the entire thesis, and for critical reading of the manuscript. Only through their invaluable expertise and countless stimulating discussions this pursuit became possible. I particularly enjoyed the pleasant atmosphere in the group and the practical freedom of research I experienced. I am also deeply grateful to Dr. habil. Manfred Schmidt for co-supervising my work at the early stages, for many fruitful discussions and for his enlightening view on the world.

I am obliged to Prof. Dr. Mario Dähne from TU Berlin for being first examiner and Prof. Dr. Pere Roca i Cabarrocas from École Polytechnique for being co-examiner in the doctoral examination procedure.

I am indebted to many people at the Institute Silicon Photovoltaics who contributed by preparing samples, performing measurements or providing assistance in analysis or simulations.

First of all I would like to thank my diploma students Hannes Ner Beushausen, Robert Rößler and Felix Käß, who helped with PECVD depositions, performed FTIRS and SE measurements and -data analysis, provided me with tricky questions, and finally delivered great diploma theses. They contributed a lot to the overall outcome of my thesis. My semester students from Ecole Polytechnique, Thomas Hannsmann and El Mahdi el Mhamdi, helped a lot despite their short stays, also by bringing in fresh ideas like microwave annealing or light-soaking.

Caspar Leendertz generously provided his lifetime fit tool and countless answers concerning semiconductor modeling, shared his view on device simulation and assisted with SPV measurements as well as in solving programming issues. Nicola Mingirulli contributed significantly by preparing many lifetime samples, by sharing his profound knowledge on solar cell device topics, and by proofreading the cell chapter. Erhard Conrad introduced me to the intricacies of PECVD and the deposition cluster tool, kept the system running under all circumstances, and contributed countless a-Si:H depositions. Kerstin Jacob cleaned all silicon substrates and did texturing as well as photolithography for solar cells and diode structures. Anja Scheu performed metal evaporation and helped with wet-chemical processing. Martin Muske and Karola Klimm deposited ZnO, while Dagmar Patzek helped with metalization and performed conductivity measurements. Heike Angermann provided auxiliary wet-chemical treatment of silicon surfaces, while Tobias Hänel performed quantum efficiency measurements. Norbert Nickel performed deuterium effusion measurements.

Lars Korte, Caspar Leendertz, Manfred Schmidt, Erhard Conrad, Nicola Mingirulli and Jan Haschke of the a-Si:H/c-Si heterojunction team, as well as Florian Ruske, Klaus Lips, Alexander Schnegg and Rolf Stangl participated in countless inspiring discussions during daily lab life.

I would also like to thank the people who helped keeping the labs, the building and the work flow running and without whom no research would be possible. These are Thomas Lussky, who is the master of the MBE setup and who often provided assistance with PES measurements; Thorsten Seefeld, who built small experimental setups in his work shop; Andreas von Kozierowski, who equipped me with office supplies; and Marion Krusche, who helped me to survive HZB's bureaucracy.

Within this thesis, some experiments were carried out collaborating with other institutes, and I am much obliged to the people who were involved. Among these were Anja Dobrich and Thomas Hannappel from the Institute Materials for photovoltaics at HZB as well as Karsten Holldack of BESSY who provided their FTIRS setups and crucial assistance in performing the measurements. Florian Einsele and Wolfhard Beyer of Forschungszentrum Jülich performed hydrogen effusion measurements and participated in helpful discussions. Otwin Breitenstein at the Max-Planck-Institute for Microstructure Physics provided DLIT measurements and sharpened my perception concerning current inhomogeneities. I further appreciate a discussion with Siegfried Hofmann of the Max-Planck-Institute for Metals Research on the MRI analysis of SIMS data.

I acknowledge inspiring discussions with many researchers at conferences or workshops, including but not limited to Delfina Muñoz of INES, Stefaan de Wolf of EPFL, Jean-Paul Kleider, Wilfried Favre and Marie Gueunier-Farret of LGEP, Pere Roca I Cabarrocas of LPICM, Rafel Ferré and Nils-Peter Harder of ISFH, Damian Pysch of Fraunhofer ISE and Mario Tucci of ENEA.

I particularly appreciated the pleasant working atmosphere at the Institute Silicon Photovoltaics which made (most of) the preparation of this thesis an enjoyable experience. I particularly thank Caspar, Mark, Lars, Nico, Enno, Hannes, Robert, the two Tobias, Gerald and Stefanie for being around, helping to keep up my spirit and providing all the jokes that make working life agreeable.

Finally, I would like to express my deepest thanks to my wife Sybille for her unfailing support and encouragement, to my son Ben just for existing, and to my parents for the caring support during my entire educational career.